

**High Performance Silicon Photonic Filters for Dense
Wavelength-Division Multiplexing Applications**

by

Robert Boeck

B.A.Sc., The University of British Columbia, 2009

M.A.Sc., The University of British Columbia, 2011

A DISSERTATION SUBMITTED IN PARTIAL FULFILLMENT
OF THE REQUIREMENTS FOR THE DEGREE OF

Doctor of Philosophy

in

THE FACULTY OF GRADUATE AND POSTDOCTORAL
STUDIES

(Electrical and Computer Engineering)

The University of British Columbia
(Vancouver)

April 2016

© Robert Boeck, 2016

Abstract

This dissertation presents theoretical and experimental results for silicon optical ring resonator filters that meet many of the typical commercial specifications for dense wavelength-division multiplexing (DWDM) filters. First, we theoretically demonstrate a silicon quadruple Vernier racetrack resonator that meets 4-port filter commercial specifications for a clear window of 0.08 nm and a channel spacing of 0.8 nm while being tolerant to typical fabrication variations. Next, we experimentally demonstrate a silicon quadruple Vernier racetrack resonator that meets many 3-port filter commercial specifications for a clear window of 0.048 nm and a channel spacing of 0.8 nm. Then, enhanced resonant tuning range using the Vernier effect is theoretically and experimentally demonstrated using a thermally tunable silicon quadruple Vernier racetrack resonator. Also, we sent 12.5 Gbps data through a thermally tunable silicon quadruple Vernier racetrack resonator and show open eye diagrams in both the drop port and through port of the filter, even within one of the minor through port notches. We then present theoretical and experimental results on a high performance silicon double microring resonator filter using Mach-Zhender interferometer-based coupling that meets numerous 3-port filter commercial specifications for a clear window of 8 GHz and a channel spacing of 200 GHz as well as having an FSR larger than the span of the C-band and low through port passband dispersion. Next, we present a FSR-eliminated silicon Vernier racetrack resonator filter. We demonstrate the performance of this filter both theoretically and experimentally. The FSR of this filter is eliminated by using contra-directional grating couplers (contra-DCs) to suppress all but one of the notches and peaks of the filter's spectra. Lastly, a process calibration procedure is demonstrated that accurately determines the coupling coefficients of fabricated

contra-DCs and is used to design a FSR-eliminated silicon Vernier racetrack resonator filter that meets 3-port filter commercial specifications for a clear window of 13 GHz and a channel spacing of 200 GHz. This filter also has low drop port dispersion and low dispersion within the passbands of the through port.

Preface

The content of this dissertation is mostly based on the following eight publications and I am first author on each of them. Additionally, Michael Caverley performed the measurements shown in Figures 4.5(a) and 4.5(b), helped with Figures 1.3 and 1.4, and provided valuable feedback regarding this dissertation.

1. R. Boeck, L. Chrostowski, and N. A. F. Jaeger, “Sensitivity analysis of silicon-on-insulator quadruple Vernier racetrack resonators,” *Optical Engineering*, vol. 54, no. 11, p. 117102, Nov. 2015. Parts of this paper, verbatim and modified, can be found in Chapters 1.2, 1.3, 2.1, 2.2, 2.3, and was used in Chapters 1.3 and 7.2. ©SPIE, 2015, by permission.

I and Dr. Nicolas A. F. Jaeger came up with this idea to investigate whether Vernier ring resonators could meet commercial specifications under fabrication variations. Dr. Lukas Chrostowski provided insight into fabrication variations and methods for analyzing those devices taking into account such variations. I performed the modelling and analysis and I was the main contributor in writing the manuscript. Dr. Nicolas A. F. Jaeger helped me write the paper and helped determine the technical content and direction of the research. Dr. Lukas Chrostowski helped edit the drafts of the paper, provided additional insights, and aided with the numerical modelling.

Dr. Miguel Ángel Guillén Torres and Dr. Ives Macêdo provided useful discussions and helped with initial simulation efforts regarding directional couplers. Also, Michael Caverley provided useful suggestions. In accordance with SPIE policy, a majority of this paper was taken from an SPIE Proceedings. This Proceedings is listed here as the fifth paper in the preface.

2. R. Boeck, M. Caverley, L. Chrostowski, and N. A. F. Jaeger, “Process calibration method for designing silicon-on-insulator contra-directional grating couplers,” *Optics Express*, vol. 23, no. 8, pp. 10573-10588, Apr. 2015. This paper, verbatim and modified, can be found in Chapter 6, Appendix C, Appendix D, and was used in Chapter 1.3. ©Optical Society of America, 2015, by permission.

I came up with the idea for the project, was in charge of the theoretical analysis, created the mask layout of the devices, directed the measurements and was in charge of interpreting the measured results, and I was the main contributor in writing the manuscript. Michael Caverley provided the idea and script for determining the group delay and dispersion of the contra-DC by using the Hilbert transform. Michael Caverley was in charge of the derivation of the minimum bandwidth equation, helped with the derivation of the average propagation constant mismatch, was in charge of doing the measurements, helped with MATLAB[®] coding and verification of my results, and helped with writing the paper. Dr. Nicolas A. F. Jaeger helped me write the paper and helped determine the technical content and direction of the research. Dr. Lukas Chrostowski helped edit the final drafts of the paper, provided additional insights, aided with the numerical modelling, and coordinated the electron beam fabrication and developed the process design kit for this process.

The devices were fabricated at the University of Washington by Richard Bojko. Han Yun provided a mask layout script for creating the contra-directional grating couplers. Yun Wang designed the fibre grating couplers. Some of the fabricated devices were measured by Fan Zhang. Dr. Wei Shi provided help with regards to contra-DC theory and modelling. Jonas Flueckiger provided useful discussions and technical assistance with using the mask layout software, Pyxis, by Mentor Graphics. Dr. Miguel Ángel Guillén Torres provided useful discussions.

3. R. Boeck, M. Caverley, L. Chrostowski, and N. A. F. Jaeger, “Silicon quadruple series-coupled Vernier racetrack resonators: experimental signal quality,” in *Optical Fiber Communication Conference, OSA Technical Digest (online)* (Optical Society of America, 2015), paper W2A.8. This paper, verbatim and modified, can be found in Chapter 3.2. ©Optical Society of America, 2015, by permission.

I came up with the idea for the project, created the mask layout of the device, directed the measurements, was in charge of thermally tuning the device, and was

in charge of interpreting the measured results. I was the main contributor in writing the manuscript. Michael Caverley performed the measurements, provided the script for determining the group delay and dispersion of the device by using the Hilbert transform, and helped with writing the paper. Dr. Nicolas A. F. Jaeger helped me write the paper and helped with the technical content and direction of the research. Dr. Lukas Chrostowski provided useful discussions, design review, feedback on the layout, helped edit the final drafts of the paper and coordinated the IME fabrication and developed the process design kit for this process.

The devices were fabricated at IME and Dr. Andy Knights provided the process specification. Yun Wang designed the fiber grating couplers. Dr. Alina Kulpa took the microscope image of the device. Jonas Flueckiger provided technical assistance with using the mask layout software, Pyxis, by Mentor Graphics.

4. R. Boeck, M. Caverley, L. Chrostowski, and N. A. F. Jaeger, “Experimental demonstration of a silicon-on-insulator high-performance double microring filter using MZI-based coupling,” *Optics Letters*, vol. 40, no. 2, pp. 276-279, Jan. 2015. This paper, verbatim and modified, can be found in Chapter 4 and was used in Chapter 1.3. ©Optical Society of America, 2015, by permission.

I came up with the idea for the project, was in charge of the theoretical analysis, created the mask layout of the devices, directed the measurements and was in charge of interpreting the measured results, and I was the main contributor in writing the manuscript. Michael Caverley was in charge of doing the measurements, helped verify my theoretical and experimental results, and helped with writing the paper. Dr. Nicolas A. F. Jaeger helped me write the paper and helped determine the technical content and direction of the research. Dr. Lukas Chrostowski helped edit the final drafts of the paper, provided additional insights, aided with the numerical modelling, and coordinated the electron beam fabrication and developed the process design kit for this process.

The devices were fabricated at the University of Washington by Richard Bojko. Jonas Flueckiger provided technical assistance with using the set-up and mask layout software, Pyxis, by Mentor Graphics. Dr. Wei Shi provided assistance with using the mask layout software. Yun Wang designed the fibre grating couplers.

5. R. Boeck, L. Chrostowski, and N. A. F. Jaeger, “Theoretical sensitivity analysis of quadruple Vernier racetrack resonators designed for fabrication on the silicon-on-insulator platform,” *Proc. SPIE 9288, Photonics North 2014*, pp. 928812, 2014. Parts of this paper, verbatim and modified, can be found in Chapters 1.2, 1.3, 2.1, 2.2, 2.3, and was used in Chapters 1.3 and 7.2. ©SPIE, 2014, by permission.

I and Dr. Nicolas A. F. Jaeger came up with this idea to investigate whether Vernier ring resonators could meet commercial specifications under fabrication variations. Dr. Lukas Chrostowski provided insight into fabrication variations and methods for analyzing those devices taking into account such variations. I performed the modelling and analysis and I was the main contributor in writing the manuscript. Dr. Nicolas A. F. Jaeger helped me write the paper and helped determine the technical content and direction of the research. Dr. Lukas Chrostowski helped edit the drafts of the paper, provided additional insights, and aided with the numerical modelling.

Dr. Miguel Ángel Guillén Torres and Dr. Ives Macêdo provided useful discussions and helped with initial simulation efforts regarding directional couplers.

6. R. Boeck, W. Shi, L. Chrostowski, and N. A. F. Jaeger, “FSR-eliminated Vernier racetrack resonators using grating-assisted couplers,” *IEEE Photonics Journal*, vol. 5, no. 5, pp. 2202511, Oct. 2013. This paper, verbatim and modified, can be found in Chapter 5. Also, the modelling methods in Chapter 6.3 are taken from this paper. ©IEEE 2013, by permission.

I came up with the idea for the project, performed the theoretical analysis, created the mask layout of the device, performed the measurements using an automated fibre array setup, and I was the main contributor in writing the manuscript. Dr. Wei Shi provided insight into how to design contra-directional grating couplers and integrating them with racetrack resonators, provided MATLAB[®] code for modelling a single racetrack resonator with contra-directional couplers which I modified for my device, provided sentences for the paper with regards to anti-reflection gratings, and provided suggestions and helped edit the paper. Dr. Nicolas A. F. Jaeger helped me write the paper and helped determine the technical content and direction of the research. Dr. Nicolas A. F. Jaeger and Dr. Lukas Chrostowski suggested the original motivation of using contra-DCs in a ring resonator as

a means of eliminating the FSR. Dr. Lukas Chrostowski provided design review, feedback on the layout, helped edit the final drafts of the paper, provided additional insights, aided with the numerical modelling, and coordinated the electron beam with metallization fabrication and developed the process design kit for this process.

The device was fabricated at the University of Washington by Richard Bojko and Dr. Edgar Huante-Ceron and Dr. Andy Knights did the metallization. Yun Wang designed the fibre grating couplers. Dr. Alina Kulpa took the microscope image of the device. Jonas Flueckiger provided technical assistance with using the mask layout software, Pyxis, by Mentor Graphics and using the measurement set-up. Han Yun provided a mask layout script for creating the contra-directional grating couplers. The automated fibre array setup was created by Jonas Flueckiger and Charlie Lin.

7. R. Boeck, L. Chrostowski, and N. A. F. Jaeger, “Thermally tunable quadruple Vernier racetrack resonators, *Optics Letters*, vol. 38, no. 14, pp. 2440-2442, Jul. 2013. This paper, verbatim and modified, can be found in the Chapter 3.1, the introduction paragraph to Chapter 3, and was used in Chapter 1.3. ©Optical Society of America, 2013, by permission.

I came up with the idea for the project, performed the theoretical analysis, created the mask layout of the devices, measured the devices, and I was the main contributor in writing the manuscript. Dr. Nicolas A. F. Jaeger helped me write the paper and helped determine the technical content and direction of the research. Dr. Lukas Chrostowski provided design review, feedback on the layout, helped edit the final drafts of the paper, provided additional insights, aided with the numerical modelling, and coordinated the electron beam with metallization fabrication and developed the process design kit for this process.

The device was fabricated at the University of Washington by Richard Bojko and Dr. Edgar Huante-Ceron and Dr. Andy Knights did the metallization. Jonas Flueckiger gave technical assistance with using the mask layout software. Yun Wang designed the fiber grating couplers. Jonas Flueckiger and Charlie Lin created the automated fibre array set-up used to measure the devices. Dr. Alina Kulpa took the microscope image of the device.

8. R. Boeck, J. Flueckiger, L. Chrostowski, and N. A. F. Jaeger, “Experimental performance of DWDM quadruple Vernier racetrack resonators,” *Optics Express*, vol. 21, no. 7, pp. 9103-9112, Apr. 2013. This paper, verbatim and modified, can be found in Chapter 2.4 and the introduction paragraph of Chapter 2 and Appendix A. ©Optical Society of America, 2013, by permission.

I came up with the idea for the project, performed the theoretical analysis, created the mask layout of the devices, directed the measurements, and I was the main contributor in writing the manuscript. Dr. Nicolas A. F. Jaeger helped me write the paper and helped determine the technical content and direction of the research. Dr. Lukas Chrostowski provided design review, feedback on the layout, helped edit the final drafts of the paper, provided additional insights, aided with the numerical modelling, and coordinated the electron beam fabrication and developed the process design kit for this process. Jonas Flueckiger was in charge of measuring the device, giving technical assistance with using the mask layout software as well as proofreading and providing suggestions for the paper.

The device was fabricated at the University of Washington by Richard Bojko and Yun Wang designed the fibre grating couplers. Jonas Flueckiger and Charlie Lin created the automated fibre array set-up.

Table of Contents

Abstract	ii
Preface	iv
Table of Contents	x
List of Tables	xiii
List of Figures	xv
List of Abbreviations	xxiii
Acknowledgments	xxv
1 Introduction	1
1.1 Silicon Photonics: Potential Disruptor for Optical Interconnects Markets	1
1.2 Optical DWDM Filters	6
1.2.1 Inter-Channel Cross-Talk and Intra-Channel Cross-Talk	7
1.2.2 DWDM Filter Specifications	8
1.2.3 Optical Filter Dispersion	12
1.3 Methods to Extend the FSR of Ring Resonators	13
1.3.1 Ring Resonators Exhibiting the Vernier Effect	17
1.3.2 Ring Resonators with Mach-Zehnder Interferometer-Based Coupling	24
1.3.3 Ring Resonators with Contra-Directional Grating Couplers	26

1.4	Objectives	30
2	Silicon-On-Insulator Quadruple Vernier Racetrack Resonators . . .	31
2.1	Design of Silicon Quadruple Vernier Racetrack Resonators	32
2.2	Performance Optimization	34
2.3	Fabrication Sensitivity	39
2.4	Experimental Results	49
3	Thermally Tunable Silicon-On-Insulator Vernier Racetrack Resonators	55
3.1	Thermally Tunable Silicon Quadruple Vernier Racetrack Resonators	56
3.2	Silicon-On-Insulator Quadruple Vernier Racetrack Resonators: Ex- perimental Signal Quality	61
4	High Performance Silicon-On-Insulator Double Microring Filter Us- ing MZI-Based Coupling	66
4.1	Theory and Design	67
4.2	Theoretical Results	69
4.3	Experimental Results	71
5	FSR-Eliminated Silicon-On-Insulator Vernier Racetrack Resonators Using Grating-Assisted Couplers	75
5.1	Theory	76
5.2	Experimental Results	87
6	Process Calibration Method for Designing Silicon-On-Insulator Contra- Directional Grating Couplers	92
6.1	Contra-DC Theory and Process Calibration Method	93
6.2	Experimental Results	99
6.3	Example of Using the Process Calibration Method in the Filter De- sign Process	108
7	Conclusion and Future Work	112
7.1	Conclusion	112
7.2	Future Work	115

Bibliography	118
Appendices	172
A Derivation of the Transfer Functions of a Quadruple Series-Coupled Racetrack Resonator Filter	172
B Derivation of the Transfer Functions of a Double Microring Resonator Filter with MZI-Based Coupling	177
C Derivation of the Average Propagation Constant Mismatch of a Contra-Directional Grating Coupler	181
D Derivation of the Minimum Bandwidth of a Contra-Directional Grating Coupler	184

List of Tables

Table 1.1	List of companies involved in silicon photonics [1, 7–73]. . . .	3
Table 1.2	Target specifications for 3-port and 4-port filters with channel spacings of 100 GHz.	11
Table 2.1	One of our device’s modelled results as compared to the target specifications. ©SPIE, 2015, by permission [85].	37
Table 2.2	Width tolerance for (gap 1, gap 2, gap 3) = (150 nm, 350 nm, 390 nm). Bolded parameter values do not meet their commercial specifications. ©SPIE, 2015, by permission [85].	44
Table 2.3	Width tolerance for (gap 1, gap 2, gap 3) = (150 nm, 360 nm, 410 nm). Bolded parameter values do not meet their commercial specifications. ©SPIE, 2015, by permission [85].	45
Table 2.4	Width tolerance for (gap 1, gap 2, gap 3) = (150 nm, 350 nm, 390 nm). ©SPIE, 2015, by permission [85].	46
Table 2.5	Height tolerance for (gap 1, gap 2, gap 3) = (150 nm, 350 nm, 390 nm). ©SPIE, 2015, by permission [85].	47
Table 2.6	Propagation loss tolerance for (gap 1, gap 2, gap 3) = (150 nm, 350 nm, 390 nm). Bolded parameter value does not meet its commercial specification. ©SPIE, 2015, by permission [85].	48
Table 2.7	Theoretical and target 3-port filter specifications [96].	50
Table 2.8	Experimental and target 3-port filter specifications [96].	54
Table 4.1	Target specifications for 200 GHz optical filters [105].	69
Table 4.2	Theoretical filter results [105].	71

Table 4.3	Experimental filter results [105].	73
Table 5.1	Drop port and through port insertion loss for single racetrack resonators with gratings, cascaded Vernier racetrack resonators with and without gratings, and grating-coupled cascaded identical racetrack resonators. ©2013 IEEE, by permission [97].	85
Table 5.2	Spectral characteristics for single racetrack resonators with gratings, cascaded Vernier racetrack resonators with and without gratings, and grating-coupled cascaded identical racetrack resonators. ©2013 IEEE, by permission [97].	86
Table 5.3	Experimental results of grating-coupled cascaded Vernier racetrack resonator. ©2013 IEEE, by permission [97].	90
Table 6.1	Modelled results and target specifications for 200 GHz 3-port filters (table modified from [105]).	111
Table 7.1	Comparison of FSR extension methods as implemented in dissertation (the benefits are bolded).	114

List of Figures

Figure 1.1	(a) The number of companies involved in silicon photonics based on market cap categories.	4
Figure 1.2	Diagram of a commercial 4-port optical add-drop filter consisting of two 3-port optical filters [86, 87].	7
Figure 1.3	A diagram illustrating inter-channel cross-talk and intra-channel cross-talk using a 4-port optical add-after-drop filter.	8
Figure 1.4	Diagrams illustrating (a) a method to reduce inter-channel cross-talk by changing the filter's drop port lineshape to have a faster transition from passband to stopband and a smaller bandwidth and (b) a method to reduce intra-channel cross-talk by changing the filter's through port lineshape to have a larger difference, in dB, between the passband and the stopband.	12
Figure 1.5	(a) Schematic diagram of a 4-port ring resonator optical add-drop filter and (b) example through port and drop port spectra when light is only injected into the input port.	14
Figure 1.6	Schematic diagram of two 3-port ring resonator filters cascaded together to form a 4-port optical add-after-drop filter. . .	15
Figure 1.7	Diagram that shows the 45 channels within the C-band that are used in DWDM applications for a channel spacing of 100 GHz (the location of each channel is taken from ITU-T Recommendation G.694.1 [92, 110]). The FSR of a ring resonator should be larger than the wavelength span between channel 1 and channel 45.	16

Figure 1.8	Schematic diagram of a double Vernier racetrack resonator (figure adapted from [85]).	17
Figure 1.9	The number of publications from 1986 to 2015 which discuss resonators that exhibit the Vernier effect [84, 85, 96, 97, 107, 111–114, 126–429].	19
Figure 1.10	Schematic diagram of a Vernier device consisting of four race-track resonators (see Refs. 96, 126, 140–143, 149, 150 for results on similar resonators). ©SPIE, 2015, by permission [85].	19
Figure 1.11	(a) Schematic diagram of a Vernier filter consisting of two racetrack resonators (figure adapted from [85]).	21
Figure 1.12	(a) Drop port spectral responses for single silicon ring resonators, “Ring 1” and “Ring 2”, that are not coupled together .	23
Figure 1.13	(a) Schematic diagram of a series-coupled double ring resonator, (b) schematic diagram of a MZI coupler, and (c) schematic diagram of a double ring resonator filter that uses MZI-BC (modified from [105]).	25
Figure 1.14	(a) Example through port and drop port spectral response of a series-coupled double ring resonator. (b) Example output responses of an MZI coupler when light is only injected into input port “In 1”. (c) Example through port and drop port spectral response of a double ring resonator filter that uses MZI-BC.	26
Figure 1.15	(a) Schematic diagram of a typical design of a contra-DC and (b) a close-up view of a portion of a typical design of a contra-DC (modified version from [435]).	27
Figure 1.16	(a) Effective index versus wavelength where the red line is the effective index of waveguide “b”, the green line is the effective index of waveguide “a”, and the blue line is the average effective index. (b) Example of a through port power transmission factor response (red line) and drop port power coupling factor response (green line) for a silicon contra-DC.	29
Figure 1.17	The number of publications from 2005 to 2015 which discuss silicon contra-DCs [97, 434–471].	29

Figure 2.1	Schematic of a Vernier filter consisting of four racetrack resonators (see Refs. 96, 126, 140–143, 149, 150 for results on similar resonators). ©SPIE, 2015, by permission [85].	34
Figure 2.2	For light injected at the input port, (a) shows the theoretical drop port and through port responses (solid lines correspond to D1 and dashed lines correspond to D2) which show large IPSs and FSRs larger than the span of the C-band	35
Figure 2.3	For light injected at the input port, (a) shows the drop port dispersions within the region of the passband, and (b) the largest through port dispersions within one of through port passbands for devices D1 and D2. ©SPIE, 2015, by permission [85]. . .	36
Figure 2.4	(a) Spectral response at through port and drop port when light is injected into the input port and the add port of the device, respectively. (b) shows that the major notch within the stop-band changes depending on whether the light is injected into the input port or add port. (c) shows that the passband spectrum changes depending on whether the light is injected into the input port or add port. ©SPIE, 2015, by permission [85]. .	38
Figure 2.5	Dispersion at the through port and the drop port when light is injected into the input port and the add port of the device, respectively. (b) A zoom-in of Figure 2.5(a) in the region of one of the passbands. ©SPIE, 2015, by permission [85]. . . .	38
Figure 2.6	For light injected at the input port, (a) shows the sensitivity of the spectral response to changes in the waveguide width for a height of 220 nm and a loss of 2.4 dB/cm	43
Figure 2.7	Schematic of our quadruple series-coupled racetrack resonators exhibiting the Vernier effect. ©Optical Society of America, 2013, by permission [96].	49
Figure 2.8	(a) Theoretical spectral response. (b) A “zoom-in” of the major resonance. ©Optical Society of America, 2013, by permission [96].	51
Figure 2.9	(a) Measured through port and drop port spectral response. . .	53

Figure 3.1	(a) Shows the schematic of the quadruple Vernier racetrack resonator and (b) shows the fabricated device. ©Optical Society of America, 2013, by permission [149].	57
Figure 3.2	(a) Shows the theoretical through port and drop port spectra and (b) shows a major peak in the drop port response and a major notch in the through port response. ©Optical Society of America, 2013, by permission [149].	58
Figure 3.3	(a) Shows the experimental through port and drop port spectra and (b) shows a major peak of the drop port response and a major notch of the through port response. ©Optical Society of America, 2013, by permission [149].	60
Figure 3.4	(a) Shows the theoretical drop port spectral responses for various temperature changes applied to racetrack resonators R3 and R4 and (b) shows the experimental drop port spectral responses for various changes in the voltage applied to the heaters on top of racetrack resonators R3 and R4. ©Optical Society of America, 2013, by permission [149].	60
Figure 3.5	(a) Schematic diagram of the Vernier filter (see [84, 96, 127, 140–142, 149]) and (b) a microscope image of the fabricated filter showing the integrated heaters. ©Optical Society of America, 2015, by permission [150].	62
Figure 3.6	(a) Measured spectra from the in port to the drop port as well as the in port to the through port of our filter in the region of the major peak/notch before and after thermal tuning	63
Figure 3.7	(a) Eye diagram measured for data passing from the in port to the drop port at a wavelength of 1532.636 nm. Eye diagrams for data passing from the in port to the through port at (b) 1543.018 nm, (c) 1545.153 nm, and (d) 1545.247 nm. ©Optical Society of America, 2015, by permission [150]. . .	65
Figure 4.1	Schematic of the device (either the add port or the drop port is used and the other is terminated when used as a 3-port device). ©Optical Society of America, 2015, by permission [105]. . .	68

Figure 4.2	(a) Theoretical drop port and through port response and (b) zoom-in of Figure 4.2(a). ©Optical Society of America, 2015, by permission [105].	70
Figure 4.3	Dispersion of (a) the drop port within the passband region and (b) the region near the suppressed through port notch. ©Optical Society of America, 2015, by permission.	71
Figure 4.4	(a) Experimental drop port and through port response and (b) zoom-in of Figure 4.4(a). ©Optical Society of America, 2015, by permission [105].	73
Figure 4.5	(a) Experimental drop port dispersion (vertical dashed lines indicate width of clear window) and (b) experimental through port dispersion within the through port passband.	73
Figure 5.1	(a) Schematic of a section of the contra-DC and (b) schematic of the grating-coupled cascaded Vernier racetrack resonator. ©2013 IEEE, by permission [97].	78
Figure 5.2	(a) $ \kappa ^2$ versus wavelength for the contra-directional (blue-solid) and co-directional (black-dash) couplers. (b) $ t ^2$ versus wavelength for the contra-directional (red-solid) and co-directional (black-dash) couplers. ©2013 IEEE, by permission [97].	80
Figure 5.3	(a) Drop port spectral response comparison between single grating-coupled racetrack resonator with length L_a (green-solid) and L_b (red-dash)	82
Figure 5.4	(a) Drop port spectral response and phase and (b) group delay and dispersion of our grating-coupled cascaded Vernier racetrack resonator. ©2013 IEEE, by permission [97].	83

Figure 5.5	(a) Through port spectral response comparison between grating-coupled cascaded racetrack resonator (blue-solid) and cascaded racetrack resonator without gratings (black-dash), (b) a “zoom-in” of the major notch in Figure 5.5(a), (c) through port spectral response comparison between grating-coupled single (response same as cascaded configuration) racetrack resonator with lengths L_a and L_b , and (d) a “zoom-in” of the major notch in Figure 5.5(c). ©2013 IEEE, by permission [97].	83
Figure 5.6	Optical microscope image of the fabricated device. ©2013 IEEE, by permission [97].	87
Figure 5.7	(a) Experimental drop port (solid) and through port (dashed) responses when the voltage to the heater for racetrack resonator “a” is 0 V (red), 4V (green), 5.8 V (black), and 7 V (blue).	89
Figure 6.1	(a) Diagram of a contra-DC. (b) A close-up view of a portion of a contra-DC (figure was adapted from [97]). ©Optical Society of America, 2015, by permission [435].	94
Figure 6.2	(a) Diagram depicting some of the relevant contra-DC parameters as functions of $\Delta\beta$. (b) Experimental drop port spectrum of one of our devices as a function of $\Delta\beta$. ©Optical Society of America, 2015, by permission [435].	97
Figure 6.3	Experimental drop port spectra for the devices from (a) “run 1,” (c) “run 2,” and (e) “run 3” with gap distances equal to 140 nm, 220 nm, 340 nm, and 400 nm. Experimental through port spectra for the devices from (b) “run 1,” (d) “run 2,” and (f) “run 3” with gap distances equal to 140 nm, 220 nm, 340 nm, and 400 nm. ©Optical Society of America, 2015, by permission [435].	100

Figure 6.4	(a) Experimental bandwidth at FWHM versus gap distance and (b) extracted coupling coefficient versus gap distance using the FWHM method. (c) Experimental bandwidth at FWHM versus corrugation width and (d) extracted coupling coefficient versus corrugation width for devices from “run 1” with a fixed gap distance of 280 nm using the FWHM method. ©Optical Society of America, 2015, by permission [435].	102
Figure 6.5	Comparison between the FWHM method, the null method, and the curve-fit method to determine $ \kappa $ for (a) “run 1,” (b) “run 2,” and (c) “run 3.” (d) Drop port spectrum of a contra-DC with a gap distance of 300 nm from “run 2,” which is chosen to illustrate that there can be multiple possible choices for the location of the first null to the left of the main lobe (the red dots indicate possible choices for the null location). ©Optical Society of America, 2015, by permission [435].	103
Figure 6.6	Theoretical predicted minimum bandwidth at FWHM versus coupling length including experimental data points from the devices with gap distances of 400 nm from the three fabrication runs. ©Optical Society of America, 2015, by permission [435].	104
Figure 6.7	(a) Experimental and simulated (using the extracted $ \kappa $ obtained using the FWHM method) drop port and through port spectra for a contra-DC (from “run 2”) with a gap distance equal to 140 nm.	106
Figure 6.8	Comparison between the experimental and the simulated (using extracted $ \kappa $ s determined from the FWHM method) (a) maximum power coupling factor and (b) minimum power transmission factor versus gap distance. ©Optical Society of America, 2015, by permission [435].	107

Figure 6.9	Comparison between the experimental through port (a) group delay response and (b) dispersion response that were determined using the Hilbert transform method and the simulated results that were determined using the extracted $ \kappa $ of 19882 m^{-1} as well as the measured results using the OVA. ©Optical Society of America, 2015, by permission [435].	108
Figure 6.10	Schematic diagram of an optimized 3-port grating-assisted Vernier filter (figure has been adapted from [97]).	109
Figure 6.11	(a) Through port spectral response and drop port spectral response, (b) a zoom-in within the region of the major peak/notch, (c) drop port dispersion within the wavelength region of the major peak, and (d) through port dispersion within the wavelength region corresponding to the passband to the left of the major notch of an optimized 3-port grating-assisted Vernier filter.	110
Figure 7.1	(a) Through port passband and (b) drop port passband comparison, when light is injected into the input port and when light is injected into the add port, respectively, of a 4-port quadruple Vernier racetrack resonator, for propagation losses of 2.4 dB/cm and 0.5 dB/cm.	116
Figure C.1	Diagram depicting some of the relevant parameters used in our derivation. ©Optical Society of America, 2015, by permission [435].	183

List of Abbreviations

WDM	wavelength-division multiplexing
cap	capitalization
ADR	American depositary receipt
USD	United States dollar
CWDM	coarse wavelength-division multiplexing
MZI	Mach-Zehnder interferometer
DWDM	dense wavelength-division multiplexing
MUX	multiplexer
DEMUX	demultiplexer
ITU	International Telecommunication Union
AWG	arrayed waveguide grating
FSR	free spectral range
IL	insertion loss
IPS	interstitial peak suppression
EC	express channel
NRZ	non-return-to-zero
SOI	silicon-on-insulator
CMOS	complementary metal-oxide-semiconductor
MZI-BC	Mach-Zehnder interferometer-based coupling
FDTD	finite-difference time-domain

contra-DC	contra-directional grating coupler
TE	transverse electric
TM	transverse magnetic
CIFS	coupling-induced frequency shift
BW	bandwidth
IME	Institute of Microelectronics
PRBS	pseudorandom binary sequence
MRR	microring resonator
OADM	optical add-drop multiplexer
FWHM	full-width-at-half-maximum
SEM	scanning electron microscope
OVA	Optical Vector Analyzer

Acknowledgments

I would like to thank my father, Max, for his support at every step of this journey and, in memoriam, my mother, Ildiko, who inspired, encouraged, and taught me to pursue excellence in all areas of my life.

Additionally, I would like to thank Dr. Nicolas A. F. Jaeger and Dr. Lukas Chrostowski for their supervision. Specifically, I am incredibly grateful for the guidance and mentorship that Dr. Jaeger has provided me. I would also like to thank Michael Caverley, Dr. Wei Shi, Jonas Flueckiger, Dr. Miguel Ángel Guillén Torres, Yun Wang, Han Yun, Charlie Lin, Hasitha Jayatilleka, Dr. Xu Wang, Kyle Murray, Dr. Alina Kulpa, Fan Zhang, and Dr. Ives Macêdo. Also, I would like to thank Richard Bojko at the University of Washington for fabricating many of the devices that are presented within this dissertation as well as Dr. Edgar Huante-Ceron and Dr. Andy Knights at McMaster University for the metallization process.

I would like to thank Dr. Edmond Cretu for being on my supervisory committee as well as the other member of my qualifying and departmental examining committees, Dr. Shahriar Mirabbasi as Heads Nominee and Drs. Konrad Walus and Alireza Nojeh for serving as the Chairs. Also, I thank the External Examiner, Dr. Vittorio Passaro, the University Examiners, Drs. William G. Dunford and Anasavarapu Srikantha Phani, and the Chair, Dr. Antony Hodgson, for serving as examining committee members for my Final Doctoral Examination.

Also, I acknowledge the Natural Sciences and Engineering Research Council of Canada, the SiEPIC program, CMC Microsystems, Lumerical Solutions, Inc., and Mentor Graphics. Part of this work was conducted at the University of Washington Nanofabrication Facility, a member of the NSF National Nanotechnology Infrastructure Network.

Chapter 1

Introduction

1.1 Silicon Photonics: Potential Disruptor for Optical Interconnects Markets

Silicon photonics has emerged as an attractive alternative to on-chip copper interconnects as well as to currently used wavelength-division multiplexing (WDM) components (see [1]). In 2013, the application that had the largest market for silicon photonics was telecommunications [2] and in 2015 the largest market is data communications [1]. In 2014, WDM silicon photonic filters had the largest share of the market as compared to other components, such as silicon modulators, and the demand for these filters is expected to grow rapidly in the years to come [2]. Yole Développement has stated that the silicon photonics market sales are expected to quadruple between 2010-2017 [3].

Due to the enormous potential that silicon photonics has to be a technology disruptor, numerous companies are involved in the design and/or manufacturing of silicon photonic devices and circuits, as well as selling software that can be used for the modelling and layout of silicon photonic circuits for a variety of applications that include telecommunications, data communications, and sensing, as listed in Table 1.1. Figure 1.1(a) provides a break-down of the 77 companies involved in silicon photonics that are listed in Table 1.1. The break-down is based on the number of companies that are not publicly traded (private) as well as based on the market capitalization (cap) of publicly traded companies (all sectors of each

company). The market cap is categorized as micro cap, small cap, mid cap, and large cap [4]. Micro cap is defined as a market cap between 50 million dollars and 300 million dollars, small cap is defined as a market cap between 300 million dollars and 2 billion dollars, mid cap is defined as a market cap between 2 billion dollars and 10 billion dollars, and large cap is defined as a market cap greater than 10 billion dollars [4]. Figure 1.1(a) shows that, currently, there are significantly more private companies (52) involved in silicon photonics than publicly traded companies (25). The market cap provides insight into the sentiment that investors have with regards to a particular company [5, 6]. Figure 1.1(b) shows the market cap of the 25 publicly traded companies involved in silicon photonics. The total market cap of these companies, as of January 3, 2016, is about 1 trillion USD, which indicates the overall, positive sentiment that investors have towards these companies [5, 6]. Furthermore, this positive investor sentiment [5, 6] translates into an advantageous situation with regard to the progress of this technology, as it is desirable to have companies with excellent track records involved in silicon photonics research and development.

Table 1.1: List of companies involved in silicon photonics [1, 7–73].

<p>Acacia Communications, Inc. Accelink Technologies Co., Ltd. Acorn Technologies AEPONYX, Inc. Alcatel-Lucent S. A.^a Analog Photonics LLC APIC Corp. Apollo Photonics, Inc. Applied NanoTools, Inc. Aurrion, Inc. Avago Technologies Ayar Labs BrPhotonics Produtos Optoeletrônicos LTDA^b Caliopa^c Centera Photonics, Inc. Chiral Photonics, Inc. Cisco Systems, Inc. Compass-EOS COMSOL, Inc. Coriant^d DAS Photonics DermaLumics S.L. EM Photonics, Inc. Ericsson Etaphase, Inc. Finisar Corp.</p>	<p>Fujitsu Ltd.^e Genalyte, Inc. Hamamatsu Photonics K. K. Hewlett-Packard Company^f IBM Infinera Corp. Inphi Corp. Innolume GmbH Intel JCMwave GmbH Kaia Corp. Luceda Photonics Lumerical Solutions, Inc. Luxmux Technology Corp. Luxtera, Inc. M/A-COM Technology Solutions Holdings, Inc. Magic Leap, Inc. Maple Leaf Photonics LLC Mellanox Technologies Mentor Graphics Corp. Morton Photonics, Inc. NEC Corp. NeoPhotonics Corp. Novati Technologies^g Oclaro, Inc. Omega Optics, Inc.</p>	<p>One Silicon Chip Photonics, Inc. Optic2Connect Pte. Ltd. Optiwave Systems, Inc. Oracle Corp. Phoenix B.V. Photline Technologies^h Photon Design, Inc. PhotonIC Corp. PLCC2 LLC RANOVUS, Inc. Rockley Photonics Samsung Electronics Co., Ltd. Samtec, Inc. Sandia Corp.ⁱ Shanghai Industrial μTechnology Research Institute Co., Ltd. Sicoya GmbH SiFive SiFotonics Technologies Co., Ltd. Skorpis Technologies, Inc. STMicroelectronics Synopsys, Inc. TeraXion, Inc. VLC Photonics S.L. VPIphotonics Inc. VTT Memsfab Ltd.</p>
---	---	--

^aOwns Bell Labs [50].

^bOwned by CPqD, 51%, and GigOptix, Inc., 49% [73].

^cOwned by Huawei Technologies Co. Ltd. [31].

^dFounded by Marlin Equity Partners [74].

^e Owns Fujitsu Laboratories Ltd. Fujitsu Laboratories of America, Inc., is owned by Fujitsu Laboratories Ltd. [18].

^f Has now split into two publicly traded companies: HP Inc. and Hewlett Packard Enterprise [75].

^gOwned by Tezzaron Semiconductor Corp. [76].

^h Now called iXBlue Photonics (originally two companies, Photline Technologies and iXFiber) and owned by iXBlue [77].

ⁱOwned by Lockheed Martin Corp. [33].

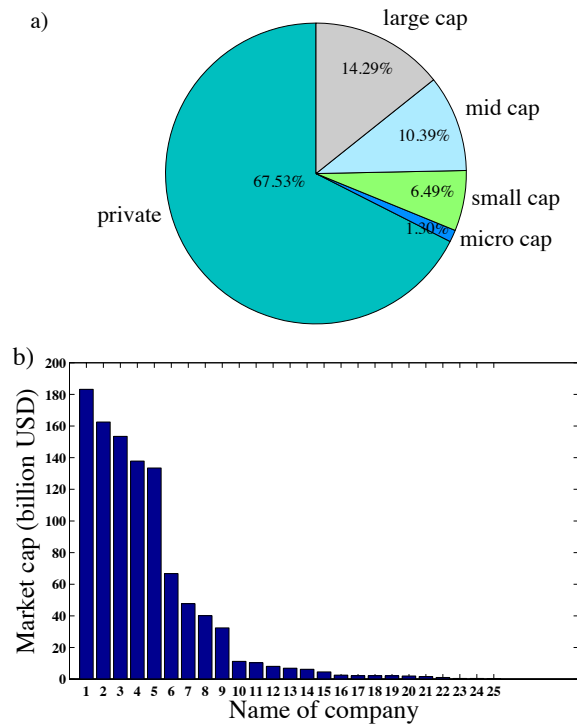


Figure 1.1: (a) The number of companies involved in silicon photonics based on market cap categories. It should be noted that if a private company is owned by a publicly traded company, only the publicly traded company is included in this chart. We have included HP, Inc., and Hewlett Packard Enterprise as a single large cap entity. (b) The market cap values, as of January 3, 2016, for companies involved in silicon photonics where: 1 = Samsung Electronics Co., Ltd., 2 = Intel, 3 = Oracle Corp., 4 = Cisco Systems, Inc., 5 = IBM, 6 = Lockheed Martin Corp., 7 = the combined market caps for HP, Inc., and Hewlett Packard Enterprise, 8 = Avago Technologies, 9 = Ericsson [American depository receipt, ADR], 10 = Alcatel-Lucent S. A., [ADR], 11 = Fujitsu Ltd. [ADR], 12 = NEC Corp., 13 = Synopsys, Inc., 14 = STMicroelectronics [ADR], 15 = Hamamatsu Photonics K. K., 16 = Infinera Corp., 17 = M/A-COM Technology Solutions Holdings, Inc., 18 = Mentor Graphics Corp., 19 = Accelink Technologies Co., Ltd., 20 = Mellanox Technologies, 21 = Finisar Corp., 22 = Inphi Corp., 23 = NeoPhotonics Corp., 24 = Oclaro, Inc., and 25 = GigOptix, Inc. The market cap values were obtained from <https://www.google.com/finance> and currency conversions to USD were calculated using <http://www.xe.com/currencyconverter/>.

The on-chip integration of high-yield silicon photonics interconnect components such as lasers, modulators, WDM filters, and photodetectors is essential for the deployment of this technology in telecommunications and data communications applications. Numerous companies have demonstrated integrated silicon photonic chips, such as IBM [56], Intel [55], Oracle Corp. [78], Hewlett-Packard Company [52], Luxtera, Inc. [65, 79], Aurrion, Inc. [56], and Acacia Communications, Inc., [80]. For example, recently, IBM in collaboration with Aurrion, Inc., have integrated tunable lasers, electro-absorption modulators, and multiplexers to create a four channel silicon photonic transmitter where each channel had a data rate of 28 Gbps [56]. Also, Hewlett-Packard Company in collaboration with Innolume GmbH have recently integrated silicon microring modulators with a quantum dot-based comb laser for the creation of a five channel silicon photonic transmitter [52]. Intel has recently demonstrated the integration of hybrid silicon lasers, modulators, multiplexer and demultiplexer filters, and SiGe photodetectors to create a coarse wavelength-division multiplexing (CWDM) four channel (12.5 Gbps per channel) packaged silicon photonic transmitter and receiver [55]. Intel has also demonstrated a 1310 nm silicon photonic transceiver operating at a data rate of 25 Gbps [55]. Oracle Corp. has demonstrated a packaged, eight channel (10 Gbps per channel), WDM silicon photonic transceiver that included ring modulators, demultiplexer ring resonators, and Ge photodiodes [78]. In 2012, Luxtera, Inc., announced that it had sold one million 10 Gbit channel silicon photonics products [65] and they have recently demonstrated a packaged silicon photonic transceiver operating at an aggregate data rate of 104 Gbps [79]. Acacia Communications, Inc., have also demonstrated integrated silicon photonics by creating a 100 Gbps coherent silicon photonic transceiver [80], and recently they announced their intention for an initial public offering in 2016 [81]. The fact that there are numerous companies involved in various aspects of silicon photonics technology provides clear evidence that silicon photonics is becoming widely accepted as the next technology for data interconnects as well as for the WDM filters currently deployed in telecommunication applications.

Multiplexer/demultiplexer filters and modulators have been utilized in a number of the integrated silicon photonics chips mentioned above. There are a number of waveguide-based structures that have been used by these companies to create

filters and/or modulators, such as ring resonators [52, 78] and Mach-Zehnder interferometers (MZIs) [53, 80]. Specifically, there are numerous companies currently involved in research and development of ring resonator-based silicon photonics, see for example, Oracle Corp. [54, 78], Coriant [49], Ericsson [82], Hewlett-Packard Company [52], Samsung Electronics Co., Ltd. [8], Alcatel-Lucent S. A. [50], Sandia Corp. [33], RANOVUS [60], Chiral Photonics, Inc. [35], and Fujitsu Laboratories Ltd. [83]. The fact that numerous companies are involved in silicon photonic ring resonator research provides concrete evidence that ring resonators are seen, from an industry perspective, as desirable components for next generation data interconnects. Furthermore, the fact that WDM silicon photonic filters had the largest share of the silicon photonics market in 2014 [2] provides additional evidence that silicon photonic ring resonators are a promising area for research and development, since one of the main components that can be created using ring resonators are silicon photonic filters for WDM applications.

The focus of this dissertation is the design and experimental demonstration of silicon photonic ring resonator-based filters for dense wavelength-division multiplexing (DWDM) applications. Therefore, it is important to know what the typical commercial filter specifications are to ensure that adequate filter operation in DWDM applications is achieved. In Chapter 1.2, I will present the typical commercial specifications for DWDM 3-port optical filters and 4-port optical add-drop filters, as well as the definition for each specification.

1.2 Optical DWDM Filters

¹ There are three main types of optical filters used in DWDM applications, which are optical multiplexer filters (MUXs), optical demultiplexer filters (DEMUXs), and optical add-drop filters. The MUX consists of three ports which are the input port, the add port, and the through port. The MUX allows signals to be merged onto the same optical link by routing them from the add port to the through port. The DEMUX consists of three ports which are the input port, the drop port, and the through port. The DEMUX allows signals to be separated by routing them from the input port to the drop port. The optical add-drop filter consists of four ports

¹Parts of Chapter 1.2 are taken from [84, 85].

which are the input port, the drop port, the add port, and the through port. Optical add-drop filters function as both MUXs and as DEMUXs. It should be noted here that some commercially available DWDM 4-port optical add-drop filters consist of a 3-port DEMUX cascaded to a 3-port MUX to form a 4-port optical add-after-drop filter as shown in Figure 1.2 [86, 87]. In the example shown in Figure 1.2, the input has three different signals at three different wavelengths, λ_1 , λ_2 , and λ_3 . The first 3-port filter passes the data at λ_2 and λ_3 to the through port and the data at λ_1 is routed to the drop port. The input to the second 3-port filter is now λ_2 and λ_3 . New data at λ_1 is then routed from the add port to the through port of the second three-port filter where it is combined with the data at λ_2 and λ_3 .

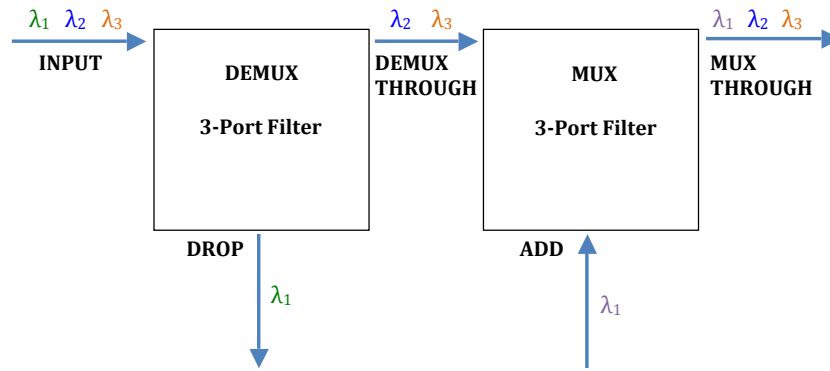


Figure 1.2: Diagram of a commercial 4-port optical add-drop filter consisting of two 3-port optical filters [86, 87].

1.2.1 Inter-Channel Cross-Talk and Intra-Channel Cross-Talk

Ideally, a DEMUX will drop one of the input wavelengths and pass it to its drop port and a MUX will add a new wavelength and pass it to its through port (the DEMUX through port is the input port of the MUX). In Figure 1.2, the signals to be removed and added are at λ_1 . The rest of the signals pass through the filters without any distortion. However, in reality a filter has a wavelength-dependent spectral response which makes the selection of only one signal dependent on the filter's lineshape. In the following example shown in Figure 1.3, we use a 4-port optical add-after-drop filter where each filter has a wavelength-dependent spectral response. Here, the input has 5 signals at wavelengths λ_1 to λ_5 , and we wish to

separate out the signal at λ_3 and route it to the drop port of the filter. However, the filter will also route a small portion of the signals in the neighbouring channels to the drop port, which will lead to inter-channel cross-talk at the photodetector between the target signal at λ_3 and the small portions of the signals at λ_2 and λ_4 [88–90]. The rest of the signals that are passed to the through port will be affected by the filter’s wavelength dependent spectral response as well, which can lead to signal distortion. Here, we can see that the intensities of the signals at λ_2 and λ_4 are slightly reduced when they are passed to the DEMUX through port. Also, a small portion of the signal at λ_3 will be routed to the DEMUX through port. If a new signal at λ_3 is required to be routed to the MUX through port, the partially passed signal at λ_3 will generate intra-channel cross-talk between it and the new signal at λ_3 at the eventual photodetector [88–90].

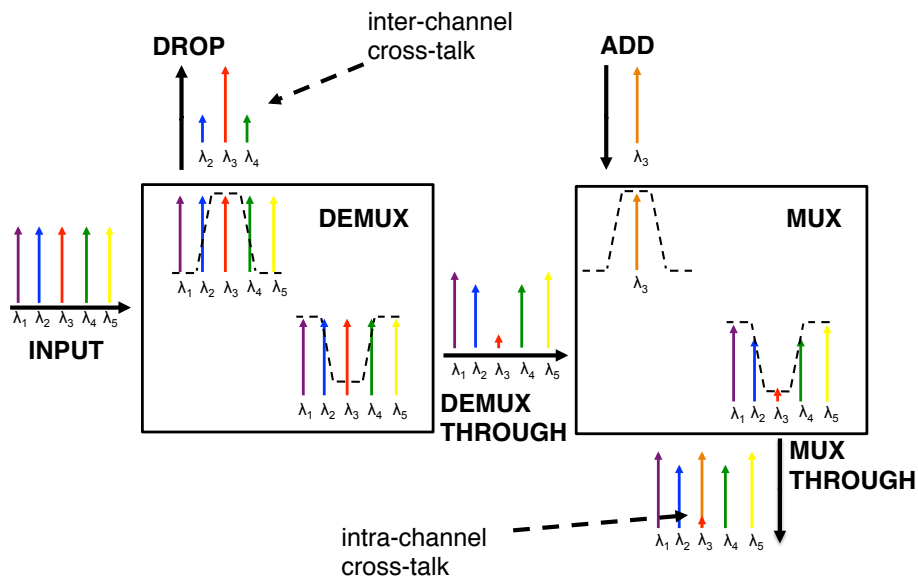


Figure 1.3: A diagram illustrating inter-channel cross-talk and intra-channel cross-talk using a 4-port optical add-after-drop filter.

1.2.2 DWDM Filter Specifications

Filters used in DWDM applications have performance specifications listed within their datasheets, which are provided by the telecommunication vendors. These

performance specifications provide businesses with the information needed to determine whether the filters are suitable for integration within their infrastructure. The performance specifications are determined within the clear windows of the channels [91, 92]. Here, the clear window (which can be found in [91, 92]) is assumed to have the same definition as the channel wavelength range that is defined by the International Telecommunication Union (ITU) [93, 94]; the clear window is the necessary wavelength span that is needed for the signal to go through a filter taking into account everything that affects the signal's frequency/spectrum such as transmitter temperature drift and data rate bandwidth [91, 94]. Since many filters have a periodic spectral response, such as arrayed waveguide gratings, AWGs, [95] and ring resonator filters, the period, or free spectral range (FSR), should be larger than the span of wavelengths to be covered. For example, in a typical telecommunications application the C-band covers 35.09 nm from 1528.77 nm to 1563.86 nm [96]. Hence, we have chosen the specification for the FSR to be greater than or equal to the span of the C-band plus one adjacent channel [96]. Since there are 45 channels within the C-band (100 GHz channel spacing), the number of channels to both the left and right of the desired channel is chosen to be 44, unless otherwise specified. Here, we have defined the centre wavelength value (this is the wavelength at which the clear window is centred) of the major peak within the channel of interest to be the arithmetic mean wavelength between the -3 dB points (referenced at the maximum transmission of the major peak).

Next, the definitions for the drop port performance specifications are provided. The maximum drop port insertion loss, IL_{drop} , or maximum channel insertion loss, is defined as the the minimum transmission within the clear window (the channel wavelength range) of the desired channel with respect to 0 dB [92, 93, 97]. The ripple, R_{depth} , is defined as the difference between the maximum and minimum drop port transmission within the clear window of the desired channel [92, 93, 97]. The adjacent channel isolation, A_i , is defined as the difference between the minimum and maximum drop port transmission within the clear window of the desired channel and the adjacent channels, respectively [93, 97]. The non-adjacent channel isolation, nA_i , is defined as the difference between the minimum and maximum drop port transmission within the clear window of the desired channel and all non-adjacent channels (we have defined this for the 43 non-adjacent channels to the left

and right of the desired channel), respectively [93, 97]. The interstitial peak suppression (IPS) is defined as the difference between the minimum drop port transmission within the clear window of the desired channel and the maximum drop port transmission of the largest interstitial peak to the left and right of the major drop port peak at which another channel might be located. Devices with larger A_i , nA_i , and IPS will have less inter-channel cross-talk.

Next, the definitions for the through port performance specifications are provided. The express channel isolation, EC_i , or channel extinction, of the through port is defined as the difference between the minimum and maximum transmission within the clear windows of the adjacent channels and the non-adjacent channels and the clear window of the desired channel, respectively [93, 97]. Here, EC_i will not include non-adjacent channels (which is how Alliance Fiber Optic Products, Inc., [98] defined their specification that they named pass channel residual at express port) [97]. Devices with larger EC_i will have less intra-channel cross-talk. The minimum transmission within the adjacent and non-adjacent clear windows (44 channels to the left and right of the desired channel) of the through port with respect to 0 dB is defined as the maximum through port insertion loss, IL_{thru} [97]. $IL_{\text{thru-m}}$ is the minimum through port transmission with respect to 0 dB at any wavelength within the passbands of the through port at which another channel might be located.

Table 1.2 shows the performance specifications that need to be met for DWDM 3-port and 4-port optical filters with channel spacings of 100 GHz. The specifications used here are based on data sheets from telecom vendors for long-haul applications. I have done this with the assumption that filters that can meet long-haul specifications will meet short-haul specifications.

Table 1.2: Target specifications for 3-port and 4-port filters with channel spacings of 100 GHz.

Parameter	3-Port Target	4-Port Target
FSR (nm)	≥ 35.89 [96]	≥ 35.89 [96]
A_i (dB)	≥ 25 [99, 100], 30 [101]	≥ 25 [87, 102]
nA_i (dB)	≥ 35 [101], 40 [99, 100]	≥ 40 [87, 102]
IPS (dB)	≥ 35 [101], 40 [99, 100]	≥ 40 [87, 102]
IL_{drop} (dB)	≤ 1.6 [101], 1.2 [99], 0.9 [100]	≤ 1.2 [87, 102]
R_{depth} (dB)	≤ 0.5 [99]	≤ 0.3 [102]
EC_i (dB)	≥ 10 [99], 12 [100]	≥ 25 [87, 102]
IL_{thru} (dB)	≤ 0.7 [101], 0.5 [99], 0.45 [100]	≤ 1.0 [87, 102]
$IL_{\text{thru-m}}$ (dB)	≤ 0.7 [101], 0.5 [99], 0.45 [100]	≤ 1.0 [87, 102]

As previously shown, the filter’s drop port spectral response leads to inter-channel cross-talk between the partially selected signals at λ_2 and λ_4 and the signal at λ_3 . However, a filter’s through port and drop port spectra can be designed to minimize intra-channel cross-talk and inter-channel cross-talk, respectively. For example, inter-channel cross-talk can be reduced if a filter’s drop port spectral response has a faster transition from passband to stopband and a smaller bandwidth as shown in Figure 1.4(a). Intra-channel cross-talk can be reduced if the difference, in dB, between the passband and the stopband of the through port response is increased as shown in Figure 1.4(b). For more information on cross-talk and its mitigation, see Chapters 2 to 6 and Refs. 88–90.

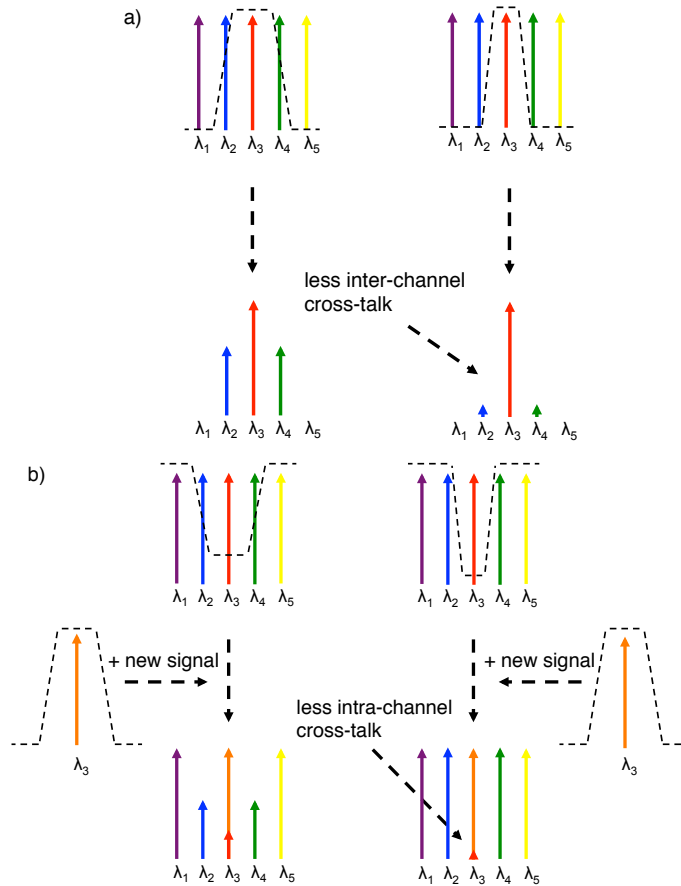


Figure 1.4: Diagrams illustrating (a) a method to reduce inter-channel cross-talk by changing the filter’s drop port lineshape to have a faster transition from passband to stopband and a smaller bandwidth and (b) a method to reduce intra-channel cross-talk by changing the filter’s through port lineshape to have a larger difference, in dB, between the passband and the stopband.

1.2.3 Optical Filter Dispersion

For a specific optical link, there is a maximum dispersion that is acceptable [103]. For example, Ref. 103 states that for a 2.5 Gbps non-return-to-zero (NRZ) optical link operating at 1550 nm with a power penalty of 1 dB the maximum dispersion that can be tolerated is 18817 ps/nm [103]. If the data rate is increased to 10 Gbps or 40 Gbps, then the maximum dispersion that can be tolerated is 1176 ps/nm or

73.5 ps/nm, respectively [103]. Also, for components used in an optical link, such as an optical add-drop filter, there is an application-dependent maximum dispersion, for example, ± 30 ps/nm [104]. Since the through port dispersions of some of our designed filters are much larger than ± 30 ps/nm [104], this will cause a reduction in the number of these devices that can be used in an optical link as well as a reduction in the total length of the fibre that can be used. However, while some of the filters presented in this dissertation may not be useful for long haul, they should still be suitable for metro and on-chip applications. For example, let's say that an optical add-drop filter has a dispersion of 500 ps/nm and the maximum allowable dispersion is 1176 ps/nm (for a data rate of 10 Gbps) [103] and the optical link uses single-mode fibre with a dispersion coefficient of 17 ps/nm/km [103], then the maximum optical fibre length that can be used is almost 40 km (for an example that uses a filter dispersion of ± 30 ps/nm, see Appendix II.2 in Ref. 104).

References 92 and 91 define dispersion as the maximum dispersion within the clear window of any channel. Here, we will define the maximum drop port dispersion, D_{drop} , as the maximum positive or negative dispersion within the desired channel's clear window [105]. The maximum through port dispersion, D_{thru} , is defined as the maximum positive or negative dispersion at the through port within any of the clear windows of the adjacent and non-adjacent channels [105]. $D_{\text{thru-m}}$ is defined as the maximum positive or negative dispersion at any wavelength within the passbands of the through port at which another channel might be located.

1.3 Methods to Extend the FSR of Ring Resonators

² Silicon-on-insulator (SOI) ring resonator DWDM optical filters offer advantages as compared to commercially available DWDM optical filters; ring resonators are compact and CMOS-compatible [106]. Thus, there has been substantial research into the design and fabrication of ring resonators, for example, see [8, 33, 35, 49, 50, 52, 54, 60, 78, 82, 83]. When using ring resonators for DWDM applications, a single ring resonator can be used as a 4-port optical add-drop filter, as shown in Figure 1.5(a). An example through port spectral response and drop port spectral response are shown in Figure 1.5(b) for broadband illumination at the input port

²Parts of Chapter 1.3 are taken from [84, 85].

with no other light injected into the device (total length of ring resonator is 45.416 μm [85], bus-to-ring field coupling factor is 0.2, and propagation loss is 3 dB/cm). The transfer functions for a single ring resonator can be found in [107].

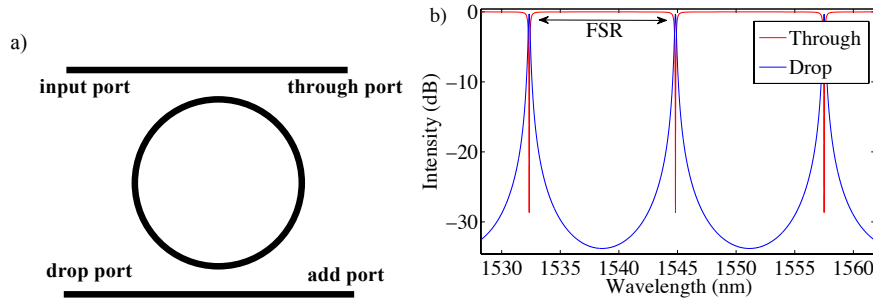


Figure 1.5: (a) Schematic diagram of a 4-port ring resonator optical add-drop filter and (b) example through port and drop port spectra when light is only injected into the input port.

Alternatively, one can use two sets of ring resonators, as shown in Figure 1.6, to create a 4-port optical add-after-drop filter (see, for example, [108, 109]). The benefit of using the add-after-drop configuration is that the EC_i specification for each individual filter (≥ 10 dB [99], 12 dB [100]) is less than it would be if we used just one filter (≥ 25 dB [87, 102]) for the add-drop functionality. EC_i is defined within the clear window [85] and, therefore, it is possible to increase the clear window for the add-after-drop configuration since the EC_i specification is less than for the 4-port add-drop filter (see Table 1.2). However, the add-after-drop configuration is more complex and less compact since more ring resonators are needed.

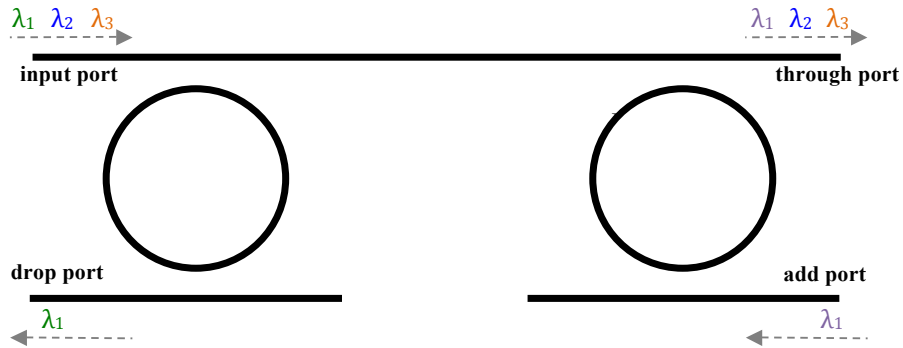


Figure 1.6: Schematic diagram of two 3-port ring resonator filters cascaded together to form a 4-port optical add-after-drop filter.

In DWDM applications that require 100 GHz channel spacings, the C-band consists of 45 channels (191.7 THz to 196.1 THz with 100 GHz channel spacing) that are utilized in data transmission [92, 96] and the centre frequency of each of these channels is determined by the ITU [92, 110], as shown in Figure 1.7. If the FSR of a ring resonator is smaller than or equal to the span of the C-band, then signals that are operating at frequencies within the C-band may also correspond to the locations of the filter's resonances that are within the C-band and, thus, the signals will be multiplexed or demultiplexed by the same device [111]. Thus, the FSR of a ring resonator should be larger than the span of the C-band [111], see Figure 1.7. In Chapters 1.3.1 to 1.3.3, three methods to extend the FSRs of ring resonators will be presented, which provide a desirable alternative to the conventional way of increasing the FSR, *i.e.*, the FSRs of ring resonators are inversely proportional to the total lengths of the resonators [111].

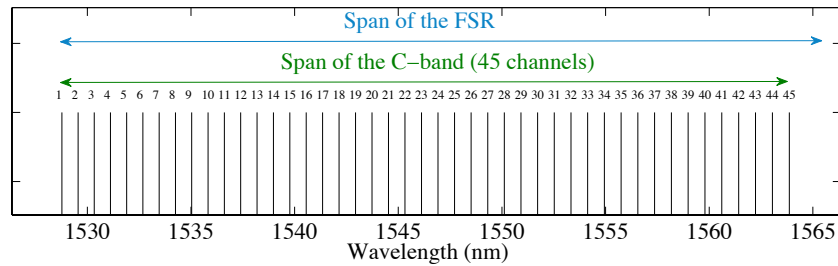


Figure 1.7: Diagram that shows the 45 channels within the C-band that are used in DWDM applications for a channel spacing of 100 GHz (the location of each channel is taken from ITU-T Recommendation G.694.1 [92, 110]). The FSR of a ring resonator should be larger than the wavelength span between channel 1 and channel 45.

Some of the previous filters, such as [112–115], on the silicon photonics platform have met many of the current commercial telecom filter specifications that can be found in vendor datasheets. However, no one has reported on fabricated silicon photonic filters that meet all the specifications that can be found in current telecom vendor datasheets (including FSRs larger than the span of the C-band) for a given clear window and channel spacing. Due to my prior experience with silicon photonic resonators, I hypothesized that silicon photonic devices can meet commercial specifications. In particular, my experience with extending the FSR by using multiple rings and the Vernier effect inspired me to explore this area more fully. Thus, one of the main aspects of this dissertation is to theoretically demonstrate silicon photonic filters that meet the current commercial specifications found in vendor datasheets as well as provide experimental evidence that such performance is realizable on the silicon photonics platform. The main design features that are investigated in this dissertation to enable the creation of silicon photonics filters with desirable performance are: FSR extension methods; resonant peak/notch suppression; through port dispersion analysis; and wavelength tuning methods. Focusing on these design features as well as current fabrication technology constraints (*e.g.*, minimum feature sizes, propagation losses, etc.), silicon photonic filters have been both theoretically and experimentally demonstrated. The design methodology to create these filters consisted of using analytic models to gain insight into the filters' operation. This was followed by numerical design and optimization using

both compact models (MATLAB[®]) and commercial models (MODE Solutions and FDTD Solutions by Lumerical Solutions, Inc.).

1.3.1 Ring Resonators Exhibiting the Vernier Effect

Filters should be designed to meet typical commercial specifications within the clear windows [91, 92] of the C-band channels. Popović *et al.* experimentally demonstrated a quadruple microring resonator filter, in silicon, that meets telecom specifications [115]. However, the FSR was only 16 nm [115]. Others have experimentally demonstrated series-coupled silicon ring resonators [116–125] that do not exhibit the Vernier effect. The spectral response of a ring resonator filter is periodic and the distance between two resonant peaks is defined as the FSR [126, 127]. If we wish to have a large FSR (*i.e.*, greater than the span of the C-band), then very small microring resonators would be required [126–128]. The Vernier effect can be used to extend the FSR to larger than the span of the C-band without needing to use very small microring resonators, *i.e.*, radii of about less than 3 μm [107]. The extended FSR is achieved by using two coupled ring resonators in which the optical path lengths are not all the same, for example, in our Figure 1.8 “Ring 1” and “Ring 2” do not have the same optical path lengths [107, 126–129]. The extended FSR, $\text{FSR}_{\text{extend}}$, occurs when $\text{FSR}_{\text{extend}} = m_1 \text{FSR}_1 = m_2 \text{FSR}_2$ where m_1 and m_2 are co-prime integers, FSR_1 is the FSR of “Ring 1”, and FSR_2 is the FSR of “Ring 2” [107, 129].

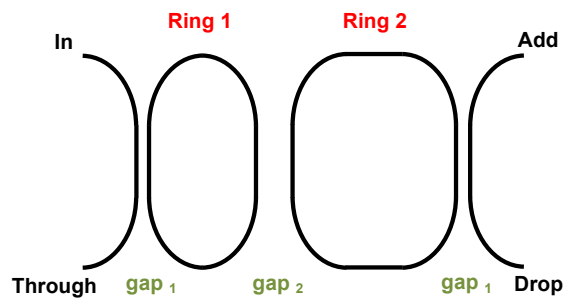


Figure 1.8: Schematic diagram of a double Vernier racetrack resonator (figure adapted from [85]).

Figure 1.9 shows the approximate number of publications (theses, conference papers, journal papers, patents, and books) from 1986 to 2015 which discuss res-

onators exhibiting the Vernier effect, which clearly shows that research involving the Vernier effect and resonators has increased substantially over the years. The main three areas of research from 1986 to 2015 regarding Vernier resonators have been filters for optical communications applications [96], tunable lasers [130], and sensors [131]. Vernier resonators have been demonstrated in a variety of materials such as single-mode fibre [132], $\text{Ta}_2\text{O}_5\text{-SiO}_2$ [133], Hydrex [134], SiON [135], Si_3N_4 [136], and Si [137]. Popović demonstrated, theoretically, a high performance ring resonator-based filter exhibiting the Vernier effect [112, 138]. In 2008, researchers at Pirelli Labs presented theoretical and experimental results on silicon Vernier microring resonators [113]. Socci *et al.* [114] have presented theoretical results showing that silicon series-coupled double Vernier ring resonators cascaded together can be used to create high performance filters. There have been two companies, Lambda Crossing [139] and Little Optics, Inc., [134, 139] that have created Vernier filters using series-coupled double ring resonators cascaded together and series-coupled quintuple ring resonators cascaded together, respectively. To achieve large bandwidths and large IPSs, four coupled ring resonators in which the optical path lengths are not all the same can be used [96, 140–143]. For example, in our Figure 1.10 “Ring 1” and “Ring 2” do not have the same optical path lengths as “Ring 3” and “Ring 4” have [126–128]. Series-coupled quadruple Vernier ring resonators have been demonstrated both theoretically [84, 85, 96, 126, 140–149] and experimentally [96, 149, 150], which includes five publications [84, 85, 96, 149, 150] that are presented within this dissertation.

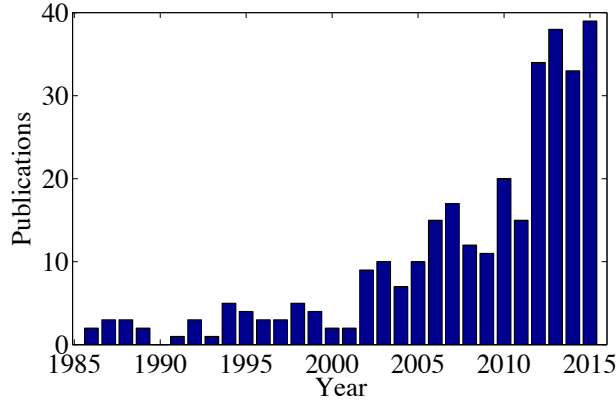


Figure 1.9: The number of publications from 1986 to 2015 which discuss resonators that exhibit the Vernier effect [84, 85, 96, 97, 107, 111–114, 126–429].

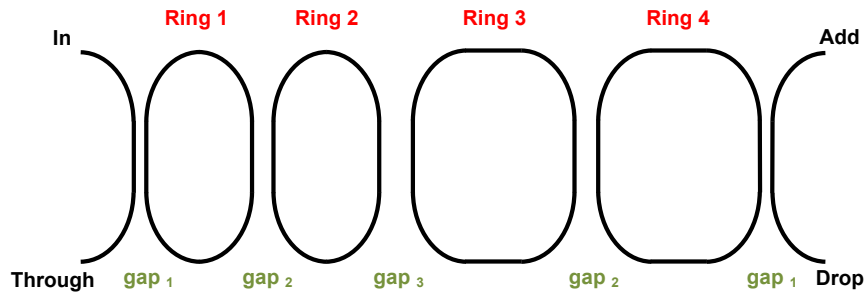


Figure 1.10: Schematic diagram of a Vernier device consisting of four race-track resonators (see Refs. 96, 126, 140–143, 149, 150 for results on similar resonators). ©SPIE, 2015, by permission [85].

To explain how the Vernier effect works we will model a double Vernier race-track resonator. We chose “Ring 1” to have a total length, L_1 , of $45.416 \mu\text{m}$ [85] and “Ring 2” to have a total length, L_2 , of $60.555 \mu\text{m}$ [85], such that $m_2/m_1 = L_2/L_1$ [107, 129] where $m_1 = 3$ and $m_2 = 4$. The propagation loss was chosen to be 3 dB/cm, the bus-to-ring field coupling factor is 0.6, the ring-to-ring field coupling factor is 0.2, the strip waveguides have widths of 500 nm and heights of 220 nm, and the waveguides have an oxide cladding. The transfer functions for a double series-coupled ring resonator can be found in [107].

Figure 1.11(b) shows the drop port spectral response for single ring resonators “Ring 1” and “Ring 2” that are not coupled together in which we can see that, at certain wavelengths, the peaks are aligned and at all other wavelengths the peaks are not aligned. If “Ring 1” and “Ring 2” are coupled together, as shown in Figure 1.11(a), major peaks will occur where the individual peaks seen Figure 1.11(b) are aligned and all the other peaks, minor peaks, will be suppressed as shown in Figure 1.11(c). Also, the through port spectral response has an extended FSR due to the suppressed minor notches located between the major notches, as shown in Figure 1.11(d). The drop port dispersion within the wavelength region of one of the major peaks is shown in Figure 1.11(e). Since within the through port passbands light will still resonate at certain wavelengths, as indicated by the minor notches in Figure 1.11(d), there will be wavelength-dependent dispersions within these locations [85], as shown in Figure 1.11(f).

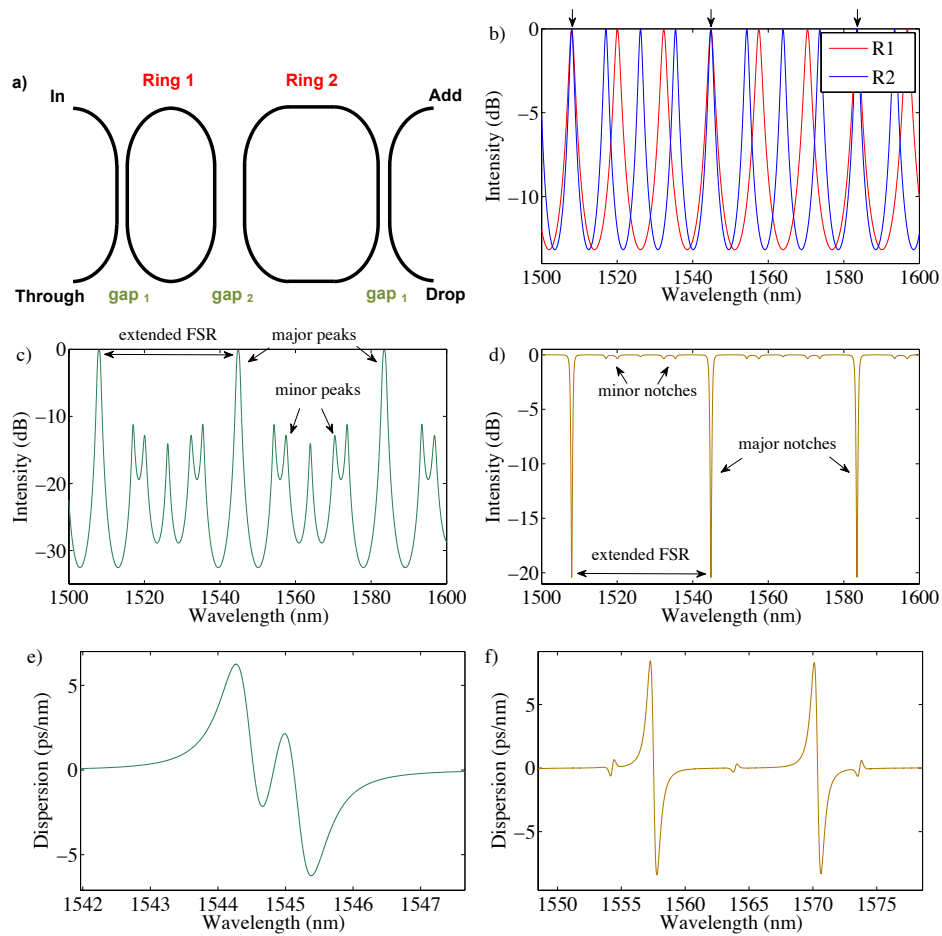


Figure 1.11: (a) Schematic diagram of a Vernier filter consisting of two race-track resonators (figure adapted from [85]). (b) Drop port spectral responses for single silicon ring resonators, “Ring 1” and “Ring 2”, that are not coupled together which show that their peaks are aligned at certain wavelengths (indicated by the arrows) and at other wavelengths their peaks are not aligned. (c) The drop port spectral response and (d) the through port spectral response after serially coupling “Ring 1” and “Ring 2” together (light only injected into the input port), which clearly shows that the FSR is extended. The wavelength-dependent dispersion at (e) the drop port within the wavelength region corresponding to the location of one of the major peaks and at (f) the through port within the wavelength region corresponding to the location of the through port passband to the right of one of the major notches.

It is desirable to be able to thermally tune a ring resonator filter to any channel within the C-band [134, 430]. Such tuning can be achieved using ring resonators that exhibit the Vernier effect and require smaller changes in temperature as compared to the temperature change required to tune across the C-band when using ring resonators that do not exhibit the Vernier effect [134, 149, 301, 430]. To explain how the Vernier effect can be used to increase the tuning range of a ring resonator filter, the drop port spectral responses of single ring resonators “Ring 1” and “Ring 2” (using the relevant parameters found in [85, 149]) that are not coupled together will be compared to the spectral response when a temperature change of 46 °C ($dn/dT = 1.86 \times 10^{-4} \text{ }^\circ\text{C}^{-1}$ [431]) is applied to “Ring 2”. Figure 1.12(a) shows the drop port spectral responses for “Ring 1” (solid blue line) and for “Ring 2” (solid red line) prior to changing the temperature of “Ring 2”. The resonances of the two drop port spectral responses are aligned at $\lambda = 1544.824 \text{ nm}$. When a temperature change, ΔT_2 , of 46 °C is applied to “Ring 2”, the resonances of the two drop port spectral responses are now aligned at $\lambda = 1557.497 \text{ nm}$. If both resonators were tuned by 46 °C the common peaks would only shift by about 3.2 nm whereas by tuning only one ring the common peaks have jumped by about 12.7 nm. Figure 1.12(b) shows the drop port spectral responses when “Ring 1” and for “Ring 2” are serially coupled together, now exhibiting the Vernier effect. The drop port spectral response prior to changing the temperature of “Ring 2” is shown by the solid green line and the spectrum after changing the temperature of “Ring 2” by 46 °C is shown by the solid blue line. The location of the major peak (*i.e.*, the common peak) is now centred at a new wavelength, which is about 12.7 nm away from where the major peak was originally located. For comparison, the spectral response when the temperature change applied to both rings is 46 °C is given by the dashed black line. This demonstrates the benefit of using the Vernier effect.

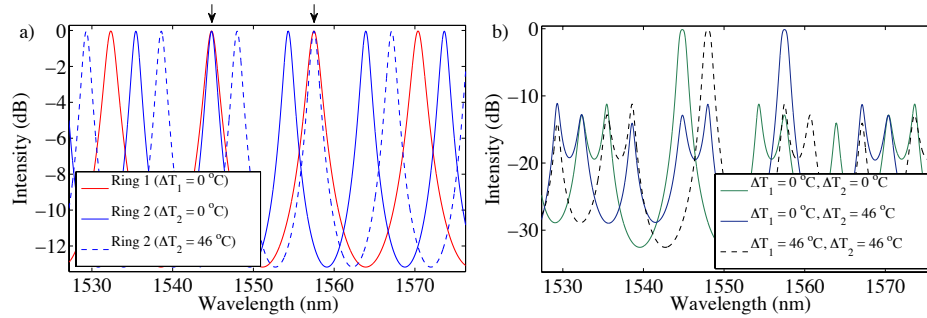


Figure 1.12: (a) Drop port spectral responses for single silicon ring resonators, “Ring 1” and “Ring 2”, that are not coupled together when $\Delta T_1 = 0^\circ\text{C}$ (solid blue line) and $\Delta T_2 = 0^\circ\text{C}$ (solid red line) as well as when $\Delta T_1 = 0^\circ\text{C}$ and $\Delta T_2 = 46^\circ\text{C}$ (dashed blue line). The arrows indicate before and after changing the temperature applied to “Ring 2”. (b) The drop port spectral responses after serially coupling “Ring 1” and “Ring 2” together when $\Delta T_1 = 0^\circ\text{C}$ and $\Delta T_2 = 0^\circ\text{C}$ (solid green line) as well as when $\Delta T_1 = 0^\circ\text{C}$ and $\Delta T_2 = 46^\circ\text{C}$ (solid blue line). Also, the drop port spectral response when $\Delta T_1 = 46^\circ\text{C}$ and $\Delta T_2 = 46^\circ\text{C}$ (dashed black line) is provided, which clearly shows the limited tuning range as compared to when the temperature change of 46°C is applied to only “Ring 2”.

1.3.2 Ring Resonators with Mach-Zehnder Interferometer-Based Coupling

Another method to expand the FSR is to use identical series-coupled ring resonators with Mach-Zehnder interferometer-based coupling (MZI-BC) [105, 432, 433]. The amount of coupling from the bus waveguides to the ring resonators is determined by the periodic responses of the input MZI [105, 432, 433]. If the difference in the branch lengths is equal to half the total length of the ring resonator then the MZI has an FSR that is twice the FSR of the ring resonator [105, 432, 433]. Thus, it is possible to double the FSR of the ring resonator since the nulls of the MZI couplers' responses are located at some of the wavelengths at which the rings resonate [105, 432, 433].

Next, an example is provided to show how an MZI coupler can be used to extend the FSR of ring resonators. The transfer functions can be found in Appendix B. Figure 1.13(a) shows a schematic diagram of a series-coupled double ring resonator without MZI-BC. Figure 1.13(b) shows a schematic diagram of an MZI coupler and Figure 1.13(c) shows a schematic diagram of a double ring resonator filter that uses MZI-BC. In this example, the following parameters were used for modelling: the propagation loss was chosen to be 3 dB/cm; the power coupling factors and power transmission factors at $\lambda = 1550$ nm have been modelled in 3D FDTD and, thus, include coupling losses (the values were taken from [105]); the silicon strip waveguide widths and heights are 500 nm and 220 nm, respectively, and the waveguides have a top oxide cladding; the lengths of the microring resonators and branch lengths, L_{mzi-1} and L_{mzi-2} , of the MZIs were taken from [105]. In this example, the value of the bus-to-ring field coupling factor, κ_b , is equal to the value of the MZI field coupling factor, κ_{mzi} .

Figure 1.14(a) shows the through port and drop port spectral responses of the series-coupled double ring resonator filter. Figure 1.14(b) shows the MZI coupler response from the input port, "In 1" to the output port, "Out 1", as well as from the input port, "In 1" to the output port "Out 2" [see Figure 1.13(b)] when no light is injected into input port "In 2". The responses are periodic and the MZI's FSR is twice that of the FSR shown in Figure 1.14(a). Figure 1.14(c) shows the through port and drop port spectral response of a double ring resonator filter that uses MZI-BC. The response has an extended FSR due to the suppression of the resonances

that align with the nulls of the MZI coupler's response [105, 432, 433]. This type of device has been demonstrated in silicon [105, 433] (including one of our own papers [105]) and silicon nitride [432]. These devices can be designed to also have minimal dispersion within the passbands of the through port [105, 432] while meeting numerous commercial 3-port filter specifications, as shown in Chapter 4.

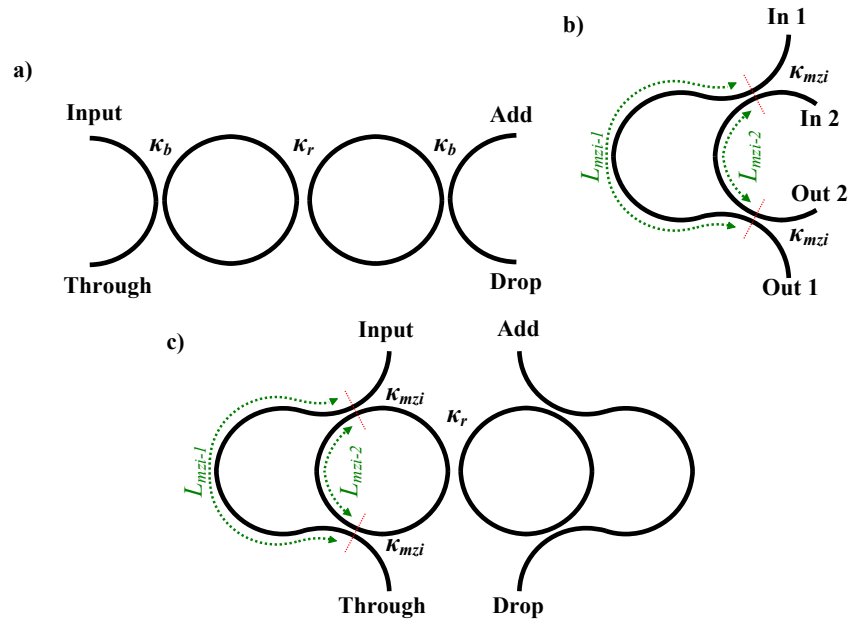


Figure 1.13: (a) Schematic diagram of a series-coupled double ring resonator, (b) schematic diagram of a MZI coupler, and (c) schematic diagram of a double ring resonator filter that uses MZI-BC (modified from [105]).

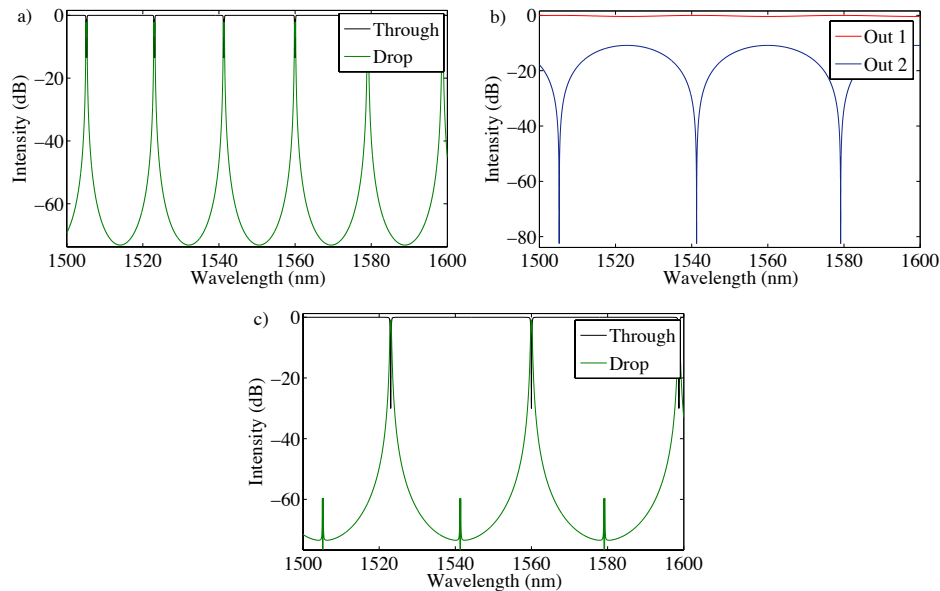


Figure 1.14: (a) Example through port and drop port spectral response of a series-coupled double ring resonator. (b) Example output responses of an MZI coupler when light is only injected into input port “In 1”. (c) Example through port and drop port spectral response of a double ring resonator filter that uses MZI-BC.

1.3.3 Ring Resonators with Contra-Directional Grating Couplers

Vernier ring resonators typically consist of very broadband wavelength-dependent directional couplers and, although MZI-BC directional couplers are highly wavelength dependent, both Vernier ring resonators and ring resonators with MZI-BC still have (extended) FSRs [105]. However, there is another type of directional coupler that is highly wavelength dependent which is the contra-directional grating coupler (contra-DC) [97, 434]. A contra-DC can eliminate the FSR of a ring resonator when the maximum reflectivity of the contra-DC occurs at the same wavelength as one of the resonances of the ring resonator [97, 434]. Furthermore, the extended FSRs of cascaded Vernier racetrack resonators can also be eliminated by using contra-DCs [97], which will be presented in Chapter 5. However, a drawback in using grating-assisted Vernier racetrack resonators is the enhanced resonant wavelength tuning range achievable by using the Vernier effect is not possible due to the highly wavelength-dependent responses of contra-DCs.

Contra-DCs can be created by adding corrugations to the inner sidewalls of two waveguides that are in close proximity to one another [97, 434, 435], as shown in Figure 1.15, and can be used as either 3-port couplers (only light injected into the input ports) or as 4-port couplers (light injected into both the input ports and the add ports). The amount of light that is reflected from the input port to the drop port is highly wavelength dependent due to the presence of the corrugations [97, 434, 435]. When the propagation constant mismatch equation equals zero, *i.e.*, $\Delta\beta = \beta_a + \beta_b - m\frac{2\pi}{\Lambda} = 0$, where β_a is the propagation constant of waveguide “a”, β_b is the propagation constant of waveguide “b”, m is an integer (which here, equals 1), and Λ is the grating period, there is maximum reflectivity at λ_D at the drop port of the contra-DC [434].

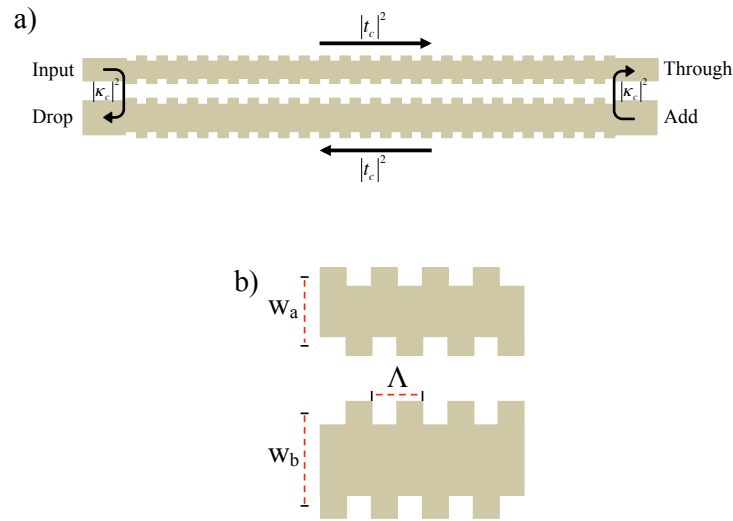


Figure 1.15: (a) Schematic diagram of a typical design of a contra-DC and (b) a close-up view of a portion of a typical design of a contra-DC (modified version from [435]).

Besides the inter-waveguide reflections that occur using a contra-DC, each individual waveguide has intra-waveguide reflections [97, 434]. The intra-waveguide reflections for waveguide “a” are centred at λ_a which can be determined by solving Eq. 1.2 for λ [434],

$$\beta_a(\lambda) + \beta_a(\lambda) - \frac{2\pi}{\Lambda} = 0, \quad (1.1)$$

$$\frac{4\pi n_a(\lambda)}{\lambda} - \frac{2\pi}{\Lambda} = 0, \quad (1.2)$$

where n_a is the effective index of waveguide “a”. The intra-waveguide reflections for waveguide “b” are centred at λ_b which can be determined by solving Eq. 1.4 for λ [434],

$$\beta_b(\lambda) + \beta_b(\lambda) - \frac{2\pi}{\Lambda} = 0, \quad (1.3)$$

$$\frac{4\pi n_b(\lambda)}{\lambda} - \frac{2\pi}{\Lambda} = 0, \quad (1.4)$$

where $n_b(\lambda)$ is the effective index of waveguide “b”. The inter-waveguide reflections are centred at λ_D which can be determined by solving Eq. 1.6 for λ [434],

$$\beta_a(\lambda) + \beta_b(\lambda) - \frac{2\pi}{\Lambda} = 0, \quad (1.5)$$

$$\frac{2\pi n_a(\lambda)}{\lambda} + \frac{2\pi n_b(\lambda)}{\lambda} - \frac{2\pi}{\Lambda} = 0. \quad (1.6)$$

Figure 1.16(a) shows an example of how to determine the centre wavelength location of the intra-waveguide reflections and the inter-waveguide reflections [434] based on silicon dioxide cladded, silicon strip waveguides with heights of 220 nm and with widths of 450 nm for waveguide “a” and 550 nm for waveguide “b” [435]. If light is only injected into the input port, the through port will see notches located at λ_a and λ_D . If light is only injected into the add port, the drop port will see notches located at λ_b and λ_D . Since in Figure 1.15 we added anti-reflection gratings to the external sidewalls of waveguides “a” and “b” [97, 435, 436], the intra-waveguide reflections, located at λ_a and λ_b in Figure 1.16(a), are suppressed. Figure 1.16(b) shows the power coupling factor, $|\kappa_c|^2$, and power transmission factor, $|t_c|^2$, versus wavelength, when light is only injected into the input port, in which we can clearly

see that the maximum intensity at the drop port occurs at the wavelength corresponding to λ_D in Figure 1.16(a). For the simulated spectra in Figure 1.16(b), the coupling length is $159\ \mu\text{m}$, the propagation loss is $3\ \text{dB/cm}$, the period is $318\ \text{nm}$, the period number is 500 , and the coupling coefficient is $10000\ \text{m}^{-1}$. There have been numerous publications on silicon contra-DCs from 2005 to 2015, as shown in Figure 1.17, including theoretical and experimental demonstrations of integrating contra-DCs into the coupling regions of ring resonators [97, 434, 437–441].

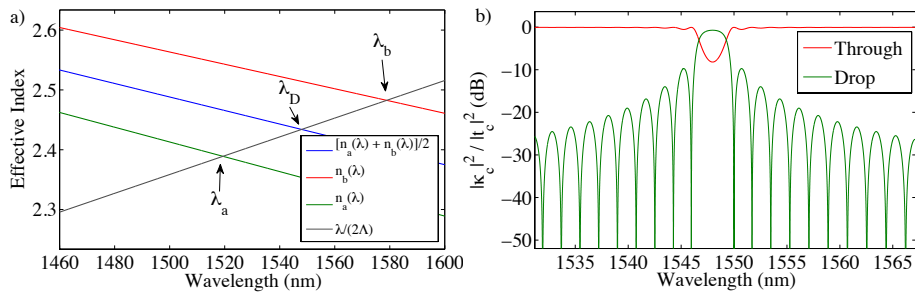


Figure 1.16: (a) Effective index versus wavelength where the red line is the effective index of waveguide “b”, the green line is the effective index of waveguide “a”, and the blue line is the average effective index. (b) Example of a through port power transmission factor response (red line) and drop port power coupling factor response (green line) for a silicon contra-DC.

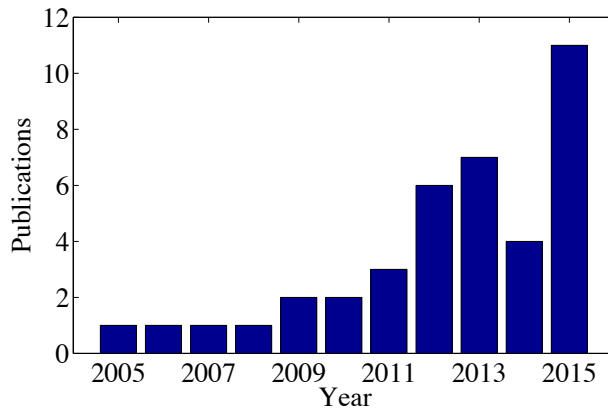


Figure 1.17: The number of publications from 2005 to 2015 which discuss silicon contra-DCs [97, 434–471].

1.4 Objectives

The objective of this dissertation is to demonstrate high performance silicon photonic filters that meet many typical commercial DWDM long-haul specifications as well as demonstrate a new silicon photonic filter that has its FSR eliminated. Specifically, my research explores a variety of methods that increase the number of channels that can be multiplexed and/or demultiplexed for DWDM applications.

In Chapter 1, I have presented an overview of the current state of silicon photonics with regard to private and publicly-traded companies. I also provided an overview of optical DWDM filters and their typical commercial specifications. Then, I provided an overview of three methods to extend the FSR, which are Vernier ring resonators, ring resonators with MZI-BC, and ring resonators with contra-DCs. In Chapter 2, I present theoretical results for silicon quadruple Vernier racetrack resonators that meet 4-port filter commercial specifications [84, 85]. I also present our theoretical results for a silicon quadruple Vernier racetrack resonator that meets 4-port filter commercial specifications while being tolerant to typical fabrication variations [84, 85]. Next, I discuss our theoretical and experimental results on a silicon quadruple Vernier racetrack resonator that meets many 3-port filter commercial specifications [96]. In Chapter 3, I present our results on thermally tunable silicon Vernier racetrack resonators. Specifically, I present our theoretical and experimental results on thermally tunable silicon quadruple Vernier racetrack resonators [149, 150]. In Chapter 4, I discuss our theoretical and experimental results for a high performance silicon double microring filter using MZI-BC that meets numerous 3-port filter commercial specifications and has an FSR larger than the span of the C-band [105]. In Chapter 5, I discuss our theoretical and experimental results on cascaded grating-assisted silicon Vernier racetrack resonators that have no FSRs due to the use of contra-DCs [97]. In Chapter 6, I present a new process calibration technique to determine the coupling coefficients of fabricated contra-DCs [435]. In Chapter 7, I present conclusions and suggestions for future work.

Chapter 2

Silicon-On-Insulator Quadruple Vernier Racetrack Resonators

¹Ideally, one would like a box-like drop port spectral response, which can be achieved using series-coupled ring resonators [190]. Increasing the number of series-coupled rings, allows one to increase the clear window (channel bandwidth) and thus the data rate that the filter can handle. There have been a number of papers that have discussed the benefits of increasing the number of ring resonators to four to enable large IPSs, see, for example [140–143]. However, prior to our work, no one has experimentally demonstrated the Vernier effect in more than three series-coupled rings and no one has experimentally shown whether series-coupled Vernier ring resonators can be used to meet many of the typical commercial DWDM filter specifications that can be found in vendor datasheets. Timotijevic *et al.* [137] demonstrated double Vernier SOI series-coupled ring resonators which had an FSR larger than the span of the C-band but minimal IPS. Fegadolli *et al.* [317] fabricated thermally tunable double Vernier SOI series-coupled ring resonators exhibiting the Vernier effect in the through port and drop port. Romagnoli *et al.* [113] experimentally demonstrated thermally tunable silicon double Vernier ring resonators, however, their IPS does not meet its typical commercial specification. Mancinelli *et al.* [290] used double Vernier SOI series-coupled resonators that had an extended FSR of 20 nm. Prabhathan *et al.* [301] fabricated double SOI cascaded ring res-

¹A version of this paragraph has been published in [96].

onators exhibiting the Vernier effect at the drop port for use as a thermally tunable wavelength selective switch. The authors’ device had an FSR of approximately 50 nm and a drop port out-of-band extinction greater than 15 dB [301]. However, ring resonators in cascaded configurations only exhibit the Vernier effect in the drop port response and not the through port response [415]. Yanagase *et al.* [190] have shown triple-ring resonators exhibiting the Vernier effect, where the coupling was done vertically and the material used for the waveguides was Ta₂O₅-SiO₂. However, their devices show minimal IPS and their extended FSR was less than the span of the C-band. Also, they do not show the through port responses. Previously published research, both experimental and theoretical, show the benefit (FSR expansion) of using the Vernier effect within series-coupled ring resonators, as compared to the case where each resonator is identical. However, prior to our research results, there have been only a few publications regarding Vernier ring resonators meeting commercial specifications as regards to the IPS (see [112–114, 134, 141–143]). Here, we theoretically and experimentally demonstrate that it is, in fact, possible to meet many drop port and through port commercial filter specifications when using silicon quadruple series-coupled racetrack resonators exhibiting the Vernier effect including the necessary IPS and FSR.

2.1 Design of Silicon Quadruple Vernier Racetrack Resonators

²The quadruple Vernier racetrack resonator has four racetrack resonators each with a radius, r , of 5 μm and a coupling length, L_c , of 7 μm . The two larger racetrack resonators, “Ring 3” and “Ring 4”, have additional straight segments, L , equal to 7.5693 μm (see Figure 2.1). The ratio of the total length of the smaller racetrack resonator, “Ring 1” or “Ring 2”, to the total length of the larger racetrack resonator, “Ring 3” or “Ring 4” is 3/4 (this ratio can also be found in Refs. 97, 126). The nominal widths and heights of the SOI strip waveguides are 500 nm and 220 nm, respectively. There is also a silicon dioxide cladding on top of the waveguides. The propagation loss was chosen to be 2.4 dB/cm (losses of 2.4 ± 0.3 dB/cm for SOI channel waveguides are reported in Ref. 472). Also, some of these parameters

²A version of Chapter 2.1 has been published in [84, 85].

were taken from Refs. 96 and 149 and the through port and drop port transfer functions can be found in Appendix A.

To determine the through port and drop port spectral responses of our modelled devices, we need to determine the real, wavelength dependent, point field coupling factors, κ s, and transmission factors, t s for each racetrack resonator's directional couplers. To simplify our modelling of the directional coupler, we used straight waveguides to obtain κ and t , on the assumption that changes in κ and t due to changes in the waveguide widths, heights, and gap occur, predominantly, in the straight waveguide sections of the couplers and that, to fabricate the devices studied herein that meet the commercial specifications one could modify the gaps of the straight sections of the actual couplers to compensate for the contributions of the bend regions. κ and t were determined by calculating the even and odd effective indices of the straight sections of the directional couplers [96, 97, 107, 111, 129, 149, 470, 473] using MODE Solutions by Lumerical Solutions, Inc. The even and odd effective indices were then curve-fitted to third-order polynomials in MATLAB[®]. Also, a third-order polynomial curve-fit was used for the strip waveguide effective indices, which were calculated using MODE Solutions. Figure 2.1 shows the schematic of the Vernier filter.

In our simulations, the waveguide effective indices used are for the fundamental quasi-TE modes of the strip waveguides. If the polarization is changed, the performance of the Vernier resonators will change. For quasi-TM polarization, the mode is less confined within the waveguide core and, as a result, the effective index will be smaller as compared to the effective index for a quasi-TE mode [470]. Therefore, the resonance condition for a racetrack resonator will be polarization dependent. Since our Vernier filters consist of racetrack resonators, the wavelengths at which the major and minor peaks and notches occur will be polarization dependent. With regards to the directional couplers, since quasi-TM modes are less confined within the waveguide cores, the field coupling factors will be larger than the field coupling factors for quasi-TE modes [474]. Since our Vernier filters include directional couplers, the spectra of our filters will be further affected by the polarization dependence of the field coupling factors.

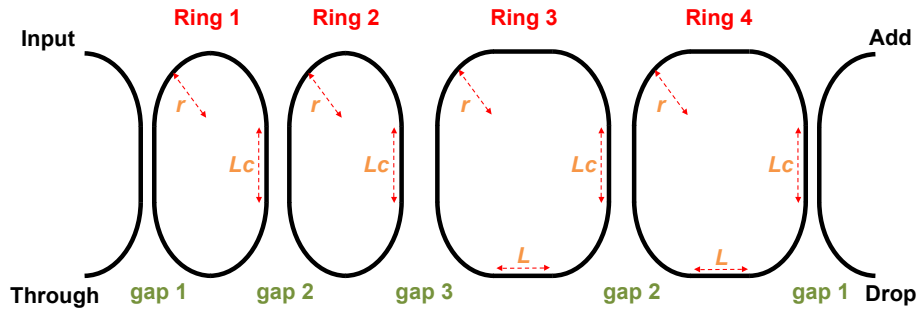


Figure 2.1: Schematic of a Vernier filter consisting of four racetrack resonators (see Refs. 96, 126, 140–143, 149, 150 for results on similar resonators). ©SPIE, 2015, by permission [85].

2.2 Performance Optimization

³We set “gap 1” to be 150 nm (we have assumed that the minimum fabrication gap distance is 150 nm) and then varied “gap 2” and “gap 3”. The spectral responses shown in Figure 2.2 (where we inject light into the input port) in solid lines correspond to the device, D1, which has gap distances “gap 1”, “gap 2”, and “gap 3” equal to 150 nm, 350 nm, and 390 nm, respectively. The spectral responses shown in Figure 2.2 (where we inject light into the input port) in dashed lines correspond to the device, D2, which has gap distances “gap 1”, “gap 2”, and “gap 3” equal to 150 nm, 360 nm, and 410 nm, respectively. These devices meet all of the 4-port filter specifications listed in Table 1.2. The field coupling factors at 1550 nm (here, to show the wavelength dependency of the field coupling factors we provide the slopes, $d\kappa/d\lambda$, at $\lambda = 1550$ nm) for gap distances of 150 nm, 350 nm, 360 nm, 390 nm, and 410 nm, are 0.44422 ($d\kappa/d\lambda = 0.00158 \text{ nm}^{-1}$), 0.07856 ($d\kappa/d\lambda = 0.00047 \text{ nm}^{-1}$), 0.07209 ($d\kappa/d\lambda = 0.00044 \text{ nm}^{-1}$), 0.05570 ($d\kappa/d\lambda = 0.00036 \text{ nm}^{-1}$), and 0.04692 ($d\kappa/d\lambda = 0.00031 \text{ nm}^{-1}$), respectively. Figure 2.2(a) shows that the FSR is larger than the span of the C-band and that the IPS for each device is greater than 40 dB, which meets their performance specification. Figure 2.2(b) is a “zoom-in” of the major resonant peaks that are located within the C-band. Figure 2.2(c) is a zoom-in of the through port spectral responses to the left of the major notches. Fig-

³A version of Chapter 2.2 has been published in [84, 85].

ures 2.3(a) and 2.3(b) show the wavelength-dependent drop port dispersion within the drop port passband region and the largest wavelength dependent through port dispersion within one of the passbands, respectively, for D1 and D2. It is important to note that the through port passbands have minor notches in their intensity spectra [96, 112, 114, 126, 127, 138, 149, 150] and large dispersions within the wavelength region where these minor notches are located [112, 138, 150, 231, 432]. These minor notches are the result of coupling of ring resonators with different optical lengths (*i.e.*, the Vernier effect) [96, 112, 114, 126, 127, 138, 149, 150].

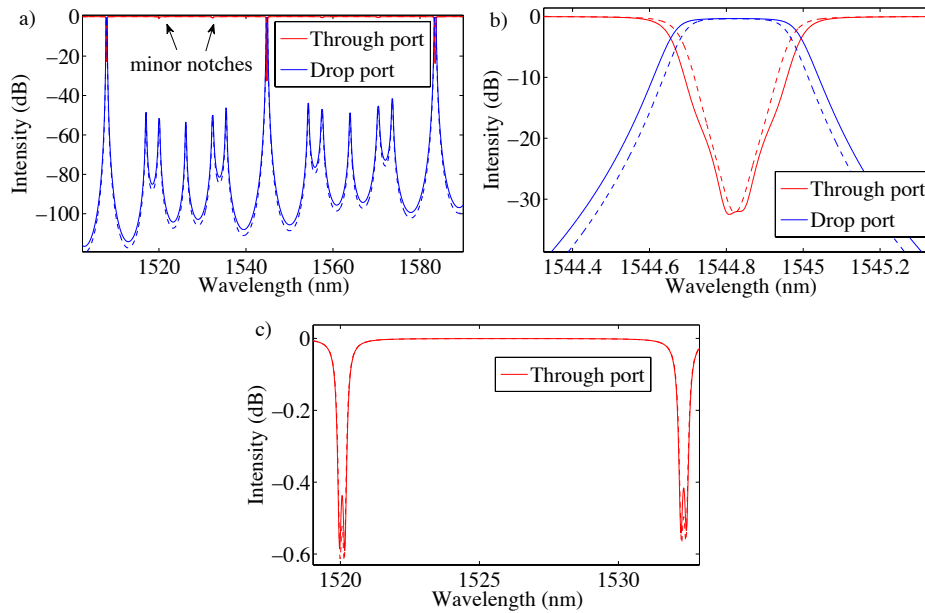


Figure 2.2: For light injected at the input port, (a) shows the theoretical drop port and through port responses (solid lines correspond to D1 and dashed lines correspond to D2) which show large IPSs and FSRs larger than the span of the C-band, (b) shows flat drop port passbands and large notches within the through port stopbands, and (c) shows minor notches within the through port passbands. The two devices meet the 4-port filter specifications listed in Table 1.2. ©SPIE, 2015, by permission [85].

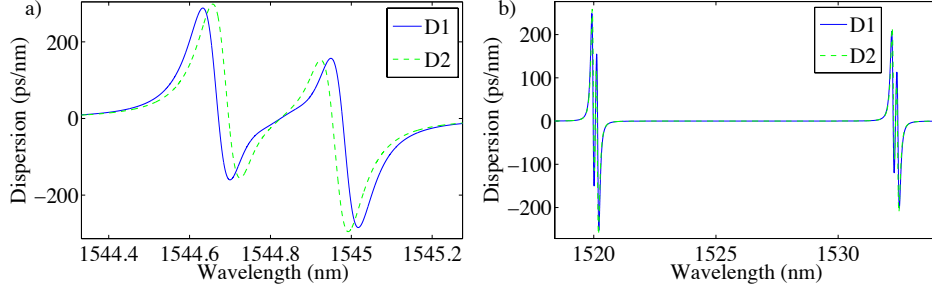


Figure 2.3: For light injected at the input port, (a) shows the drop port dispersions within the region of the passband, and (b) the largest through port dispersions within one of through port passbands for devices D1 and D2. ©SPIE, 2015, by permission [85].

For example, if we look at the device with gap distances “gap 1”, “gap 2”, and “gap 3” that are 150 nm, 350 nm, and 390 nm, respectively, the modelling results listed in Table 2.1 meet all of the 4-port filter specifications listed in Table 1.2. In Table 2.1, there are two different FSR values listed. The reason we give two values is that, provided that the group index of the waveguide forming a ring resonator is constant, then the FSR is periodic in frequency but not in wavelength. When measured against wavelength, the FSR depends on which resonant peaks are chosen for measuring it [107]. Here, we have chosen a resonant peak and give the FSRs measured to both the adjacent shorter wavelength peak and to the adjacent longer wavelength peak. It should be noted that, if we injected light into the add port of our Vernier resonator, the spectrum measured at the through port due to this light will be the same as if we injected light into the input port and measured the spectrum at the drop port (see experimental results in Ref. 150). Therefore, the add port to through port parameters are defined in a similar way as the input port to drop port parameters (we will refer to both cases using the parameter symbols, A_i , nA_i , IPS , IL_{drop} , R_{depth} , and D_{drop}). However, if we injected light into the add port of our Vernier resonator, the spectrum measured at the drop port due to this light will not be the same as if we injected light into the input port and measured the spectrum at the through port (see experimental results in Ref. 150). Thus, for light injected at the add port, the parameters, EC_d , IL_d , IL_{d-m} , D_d , and D_{d-m} are defined in a similar way as EC_i , IL_{thru} , $IL_{\text{thru-m}}$, D_{thru} , and $D_{\text{thru-m}}$ are defined, respectively.

Also, Minoli stated that the clear window is typically 25% of the channel spacing [92]. However, in our modelling, the clear window (or channel wavelength range) was chosen to be 10% of the channel spacing. The channel spacing was chosen to be 0.8 nm, and hence, the clear window was chosen to be 0.08 nm (similar to the numbers given in Ref. 475). Figures 2.4 and 2.5, respectively, show that the spectral response and dispersion change depending on whether the light is injected into the input port or injected into the add port. For light injected at the input port, D_{thru} and $D_{\text{thru-m}}$ are -150 ps/nm and -253 ps/nm, respectively. For light injected at the add port, D_d and D_{d-m} are -247 ps/nm and +480 ps/nm, respectively. D_{drop} is ± 26 ps/nm when light is injected into the input port as well as when light is injected into the add port.

Table 2.1: One of our device’s modelled results as compared to the target specifications. ©SPIE, 2015, by permission [85].

Parameter	Modelling Result	Target
FSR (nm)	36.85 ^a /38.66 ^b	≥ 35.89 [96]
A_i (dB)	54.0	≥ 25 [87, 102]
nA_i (dB)	41.2	≥ 40 [87, 102]
IPS (dB)	41.2	≥ 40 [87, 102]
IL_{drop} (dB)	0.4	≤ 1.2 [87, 102]
R_{depth} (dB)	0.0	≤ 0.3 [102]
EC_i/EC_d (dB)	28.0/29.1	≥ 25 [87, 102]
IL_{thru}/IL_d (dB)	0.6/0.6	≤ 1.0 [87, 102]
$IL_{\text{thru-m}}/IL_{d-m}$ (dB)	0.6/0.8	≤ 1.0 [87, 102]

^aThe FSR to the left of the major peak

^bThe FSR to the right of the major peak

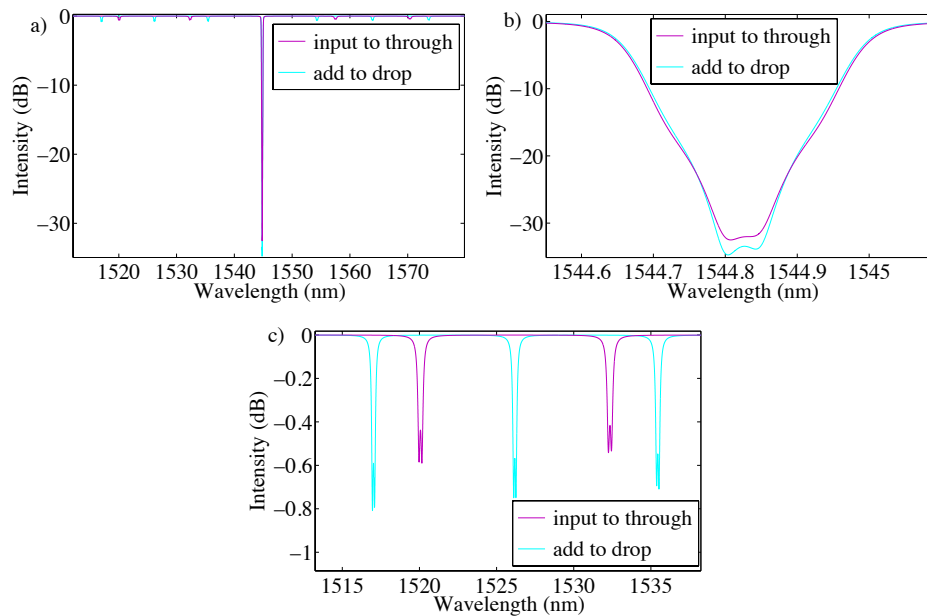


Figure 2.4: (a) Spectral response at through port and drop port when light is injected into the input port and the add port of the device, respectively. (b) shows that the major notch within the stopband changes depending on whether the light is injected into the input port or add port. (c) shows that the passband spectrum changes depending on whether the light is injected into the input port or add port. ©SPIE, 2015, by permission [85].

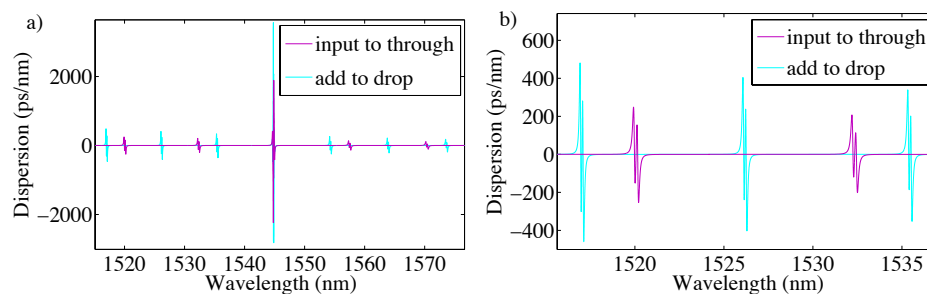


Figure 2.5: Dispersion at the through port and the drop port when light is injected into the input port and the add port of the device, respectively. (b) A zoom-in of Figure 2.5(a) in the region of one of the passbands. ©SPIE, 2015, by permission [85].

It is also important to understand that there are many unknown variables within the fabrication process which make matching designed results to experimental results difficult. These unknowns include the heights and the widths of the waveguides [129] and optical proximity effects in the coupling regions causing the waveguide widths to change [476]. In the next section we will analyze the effects of changing the waveguide widths and the corresponding gap distances for devices D1 and D2. We will then analyze the effects of independently changing the waveguide height and the propagation loss for one of these quadruple Vernier racetrack resonators.

2.3 Fabrication Sensitivity

⁴The sensitivity to fabrication errors is important in determining whether the actual device will, in fact, work as designed, given the inherent errors expected during the fabrication process. There are numerous publications regarding the fabrication sensitivities of silicon photonic devices [112, 472, 476–492]. Krishnamoorthy *et al.* has stated that the inter-wafer silicon thickness variation on a SOI wafer can be up to ± 5 nm [481]. Recent advances in optical lithography have enabled improvements in the waveguide width variations by using 193 nm immersion lithography [488]. Selvaraja *et al.* [488] have demonstrated a “ 3σ ” silicon waveguide width variation of 7.95 nm. Hence, we have decided to vary the strip waveguide widths by ± 10 nm to capture virtually all possible variations for devices D1 and D2. MODE Solutions by Lumerical Solutions, Inc., was used to determine the effective index for waveguide widths of 490 nm, 500 nm, and 510 nm with fixed heights of 220 nm as well as the even and odd supermode effective indices of the straight portions of the directional couplers. When calculating these supermode effective indices, we allowed for the changes in gap distances resulting from the changes in the waveguide widths (we assume that the centre-to-centre distance between the waveguides of the coupler regions remain constant). Tables 2.2 and 2.3 show the results for waveguide widths of 490 nm, 500 nm, and 510 nm for devices D1 and D2, respectively, when the waveguide height is fixed at 220 nm and the propagation loss is fixed at 2.4 dB/cm. The field coupling factors at 1550 nm (here, to show the

⁴A version of Chapter 2.3 has been published in [84, 85].

wavelength dependency of the field coupling factors we provide the slopes, $d\kappa/d\lambda$, at 1550 nm) for directional couplers with waveguide widths of 490 nm, heights of 220 nm, and nominal gap distances (gap distances prior to varying the waveguide widths) of 150 nm, 350 nm, 360 nm, 390 nm, and 410 nm, are 0.43906 ($d\kappa/d\lambda = 0.00161 \text{ nm}^{-1}$), 0.07939 ($d\kappa/d\lambda = 0.00048 \text{ nm}^{-1}$), 0.07290 ($d\kappa/d\lambda = 0.00045 \text{ nm}^{-1}$), 0.05648 ($d\kappa/d\lambda = 0.00037 \text{ nm}^{-1}$), and 0.04766 ($d\kappa/d\lambda = 0.00032 \text{ nm}^{-1}$), respectively. The field coupling factors at 1550 nm (as well as their slopes, $d\kappa/d\lambda$, at 1550 nm) for directional couplers with waveguide widths of 500 nm, heights of 220 nm, and nominal gap distances of 150 nm, 350 nm, 360 nm, 390 nm, and 410 nm, are 0.44422 ($d\kappa/d\lambda = 0.00158 \text{ nm}^{-1}$), 0.07856 ($d\kappa/d\lambda = 0.00047 \text{ nm}^{-1}$), 0.07209 ($d\kappa/d\lambda = 0.00044 \text{ nm}^{-1}$), 0.05570 ($d\kappa/d\lambda = 0.00036 \text{ nm}^{-1}$), and 0.04692 ($d\kappa/d\lambda = 0.00031 \text{ nm}^{-1}$), respectively. The field coupling factors at 1550 nm (as well as their slopes, $d\kappa/d\lambda$, at 1550 nm) for directional couplers with waveguide widths of 510 nm, heights of 220 nm, and nominal gap distances of 150 nm, 350 nm, 360 nm, 390 nm, and 410 nm, are 0.45162 ($d\kappa/d\lambda = 0.00155 \text{ nm}^{-1}$), 0.07813 ($d\kappa/d\lambda = 0.00045 \text{ nm}^{-1}$), 0.07163 ($d\kappa/d\lambda = 0.00042 \text{ nm}^{-1}$), 0.05521 ($d\kappa/d\lambda = 0.00034 \text{ nm}^{-1}$), and 0.04643 ($d\kappa/d\lambda = 0.00030 \text{ nm}^{-1}$), respectively. The EC_i and EC_d (indicated in the tables with bold values) for all of the devices with widths of 490 nm do not meet the commercial specification of 25 dB. However, all of the other commercial 4-port filter specifications listed in Table 1.2 are still met. By inspection of Tables 2.2 and 2.3, we believe that Table 2.2 is the best choice since it shows the best combination of EC_i and EC_d values for widths of 490 nm and 500 nm. Therefore, we believe that the device from Table 2.2 is the best one. Having chosen this device, we then looked to see what width variation it could tolerate. Table 2.4 shows the results for this device when the waveguide widths are 494 nm, 502 nm, and 510 nm. The field coupling factors at 1550 nm (as well as their slopes, $d\kappa/d\lambda$, at 1550 nm) for directional couplers with waveguide widths of 494 nm, heights of 220 nm, and nominal gap distances of 150 nm, 350 nm, and 390 nm are 0.44081 ($d\kappa/d\lambda = 0.00160 \text{ nm}^{-1}$), 0.07900 ($d\kappa/d\lambda = 0.00048 \text{ nm}^{-1}$), and 0.05613 ($d\kappa/d\lambda = 0.00036 \text{ nm}^{-1}$), respectively. The field coupling factors at 1550 nm (as well as their slopes, $d\kappa/d\lambda$, at 1550 nm) for directional couplers with waveguide widths of 502 nm, heights of 220 nm, and nominal gap distances of 150 nm, 350 nm, and 390 nm are 0.44546 ($d\kappa/d\lambda = 0.00157 \text{ nm}^{-1}$), 0.07844 ($d\kappa/d\lambda = 0.00046 \text{ nm}^{-1}$), and 0.05558 ($d\kappa/d\lambda =$

0.00035 nm⁻¹), respectively. We can clearly see that all commercial specifications are met for this device with a width tolerance of ± 8 nm when designed for widths of 502 nm (*i.e.*, this is approximately twice the 3σ variation given above). Hence, we chose waveguide widths of 502 nm for all subsequent modelling of this device. Figure 2.6(a) shows the spectral results (where light was injected only into the input port), for the chosen device, for waveguide widths of 494 nm, 502 nm, and 510 nm. It can be clearly seen that a change in the waveguide width shifts the central wavelength by a few nanometers due to the changes in the effective indices. Also, it is interesting to note that the FSR increases when the waveguide width increases.

We now look at how the spectral characteristics are affected by changes in the waveguide height. Table 2.5 shows the height variation analysis results for heights of 210 nm, 220 nm, and 230 nm when the waveguide widths are 502 nm and the propagation loss is 2.4 dB/cm. The field coupling factors at 1550 nm (as well as their slopes, $d\kappa/d\lambda$, at 1550 nm) for directional couplers with waveguide widths of 502 nm, heights of 210 nm, and nominal gap distances of 150 nm, 350 nm, and 390 nm are 0.47215 ($d\kappa/d\lambda = 0.00166$ nm⁻¹), 0.08669 ($d\kappa/d\lambda = 0.00052$ nm⁻¹), and 0.06189 ($d\kappa/d\lambda = 0.00040$ nm⁻¹), respectively. The field coupling factors at 1550 nm (as well as their slopes, $d\kappa/d\lambda$, at 1550 nm) for directional couplers with waveguide widths of 502 nm, heights of 230 nm, and nominal gap distances of 150 nm, 350 nm, and 390 nm are 0.42229 ($d\kappa/d\lambda = 0.00149$ nm⁻¹), 0.07160 ($d\kappa/d\lambda = 0.00042$ nm⁻¹), and 0.05038 ($d\kappa/d\lambda = 0.00032$ nm⁻¹), respectively. The results show that, even with a variance in height of ± 10 nm, all of the commercial filter specifications are still met (which is twice the ± 5 nm variation given above). Close inspection of Figures 2.6(a) and 2.6(b) shows that for the same change in height or width, height changes cause greater shifts in the centre wavelength than width changes. However, EC_i is relatively insensitive to the chosen changes in height.

Upon analyzing the field coupling factor values presented in this chapter, the field coupling factor is significantly more sensitive to a change in the waveguide heights of the directional coupler as compared to changes in the waveguide widths of the directional coupler. For example, if we change the waveguide widths from 490 nm to 510 nm for a directional coupler with a nominal gap distance of 150 nm, the field coupling factor would increase by 2.86% at a wavelength of 1550 nm. However, a change in the waveguide heights from 210 nm to 230 nm for a

directional coupler with waveguide widths of 502 nm and a nominal gap distance of 150 nm would result in the field coupling factor decreasing by 10.56% at a wavelength of 1550 nm.

In the waveguide width and height analysis, we used a constant propagation loss of 2.4 dB/cm. To account for variations in the propagation loss, Table 2.6 shows the propagation loss analysis results for losses of 1.4 dB/cm, 2.4 dB/cm, and 3.4 dB/cm for waveguide widths and heights of 502 nm and 220 nm, respectively. The maximum propagation loss considered is 3.4 dB/cm, due to IL_d being equal to 1.0 dB (which is the maximum value for meeting its commercial specification). It should be noted, however, that IL_{d-m} is 1.1 dB. If the spectrum were to shift, it is possible that IL_d might exceed the 1.0 dB specification as well were the propagation loss to reach 3.4 dB/cm. Nevertheless, we note that reported loss values for SOI channel waveguides are 2.4 ± 0.3 dB/cm and 2.35 ± 0.33 dB/cm in Refs. 472 and 492, respectively, and that our calculations show that as long as the propagation loss is less than or equal to 3.0 dB/cm, all the specifications will be met. Figure 2.6(c) shows the sensitivity of IL_{thru-m} to a change in propagation loss.

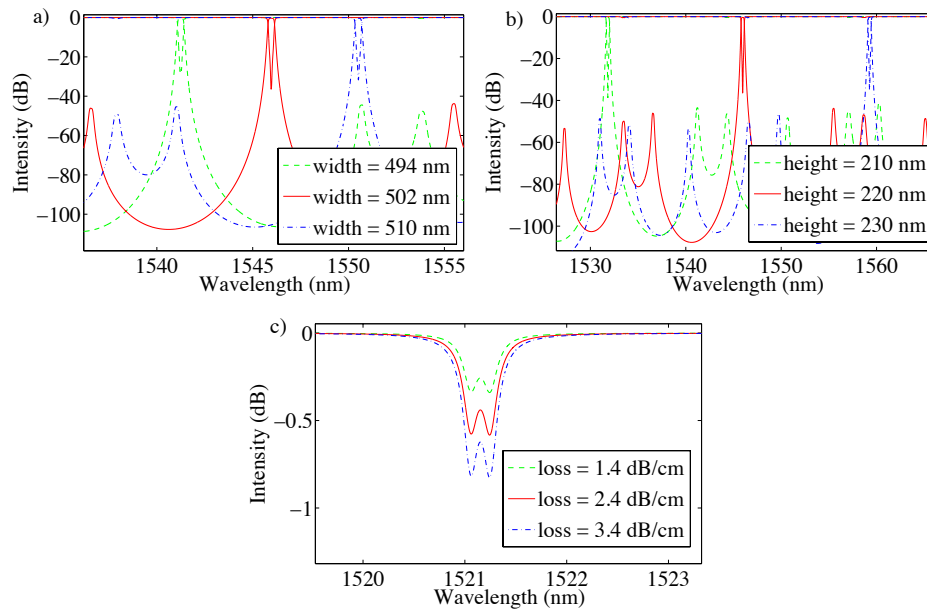


Figure 2.6: For light injected at the input port, (a) shows the sensitivity of the spectral response to changes in the waveguide width for a height of 220 nm and a loss of 2.4 dB/cm, (b) shows the sensitivity of the spectral response to changes in the height for a width of 502 nm and a loss of 2.4 dB/cm, and (c) shows the sensitivity of the spectral response to changes in loss for a width of 502 nm and a height of 220 nm. It should be noted that some of these parameters were taken from Ref. 96 and Ref. 149. ©SPIE, 2015, by permission [85].

Table 2.2: Width tolerance for (gap 1, gap 2, gap 3) = (150 nm, 350 nm, 390 nm). Bolded parameter values do not meet their commercial specifications. ©SPIE, 2015, by permission [85].

Parameter	Width (nm) = 490	500	510
FSR (nm)	36.43 ^a /38.20 ^b	36.85 ^a /38.66 ^b	37.26 ^a /39.11 ^b
A _i (dB)	55.7	54.0	52.2
nA _i (dB)	51.5	41.2	42.7
IPS (dB)	41.9	41.2	40.3
IL _{drop} (dB)	0.4	0.4	0.4
R _{depth} (dB)	0.0	0.0	0.0
EC _i /EC _d (dB)	22.9/23.4	28.0/29.1	25.3/25.0
IL _{thru} /IL _d (dB)	0.2/0.8	0.6/0.6	0.4/0.7
IL _{thru-m} /L _{d-m} (dB)	0.6/0.9	0.6/0.8	0.6/0.8
D _{drop} (ps/nm)	±32	±26	-23
D _{thru} /D _d (ps/nm)	-119/+313	-150/-247	+177/-388
D _{thru-m} /D _{d-m} (ps/nm)	-297/+564	-253/+480	-215/+406

^aThe FSR to the left of the major peak

^bThe FSR to the right of the major peak

Table 2.3: Width tolerance for (gap 1, gap 2, gap 3) = (150 nm, 360 nm, 410 nm). Bolded parameter values do not meet their commercial specifications. ©SPIE, 2015, by permission [85].

Parameter	Width (nm) = 490	500	510
FSR (nm)	36.43 ^a /38.20 ^b	36.85 ^a /38.66 ^b	37.26 ^a /39.11 ^b
A _i (dB)	58.7	57.0	55.3
nA _i (dB)	54.6	42.7	44.2
IPS (dB)	43.4	42.7	41.8
IL _{drop} (dB)	0.4	0.4	0.4
R _{depth} (dB)	0.0	0.0	0.0
EC _i /EC _d (dB)	22.4/23.4	25.3/25.7	25.9/25.0
IL _{thru} /IL _d (dB)	0.2/0.8	0.6/0.6	0.5/0.7
IL _{thru-m} /IL _{d-m} (dB)	0.7/0.9	0.6/0.8	0.6/0.8
D _{drop} (ps/nm)	±48	±43	-41
D _{thru} /D _d (ps/nm)	-102/+255	-144/-261	+186/-409
D _{thru-m} /D _{d-m} (ps/nm)	-305/+578	-262/+496	-225/+425

^aThe FSR to the left of the major peak

^bThe FSR to the right of the major peak

Table 2.4: Width tolerance for (gap 1, gap 2, gap 3) = (150 nm, 350 nm, 390 nm). ©SPIE, 2015, by permission [85].

Parameter	Width (nm) = 494	502	510
FSR (nm)	36.60 ^a /38.38 ^b	36.93 ^a /38.75 ^b	37.26 ^a /39.11 ^b
A _i (dB)	55.0	53.6	52.2
nA _i (dB)	45.8	41.1	42.7
IPS (dB)	41.7	41.0	40.3
IL _{drop} (dB)	0.4	0.4	0.4
R _{depth} (dB)	0.0	0.0	0.0
EC _i /EC _d (dB)	25.4/26.1	28.0/28.7	25.3/25.0
IL _{thru} /IL _d (dB)	0.4/0.8	0.5/0.7	0.4/0.7
IL _{thru-m} /IL _{d-m} (dB)	0.6/0.8	0.6/0.8	0.6/0.8
D _{drop} (ps/nm)	-30	-26	-23
D _{thru} /D _d (ps/nm)	+216/-443	+146/+465	+177/-388
D _{thru-m} /D _{d-m} (ps/nm)	-279/+530	-245/+465	-215/+406

^aThe FSR to the left of the major peak

^bThe FSR to the right of the major peak

Table 2.5: Height tolerance for (gap 1, gap 2, gap 3) = (150 nm, 350 nm, 390 nm). ©SPIE, 2015, by permission [85].

Parameter	Height (nm) = 210	220	230
FSR (nm)	36.36 ^a /38.16 ^b	36.93 ^a /38.75 ^b	37.49 ^a /39.33 ^b
A _i (dB)	53.6	53.6	53.6
nA _i (dB)	50.8	41.1	43.7
IPS (dB)	40.7	41.0	41.3
IL _{drop} (dB)	0.4	0.4	0.4
R _{depth} (dB)	0.0	0.0	0.0
EC _i /EC _d (dB)	27.9/28.4	28.0/28.7	28.1/28.9
IL _{thru} /IL _d (dB)	0.2/0.7	0.5/0.7	0.5/0.7
IL _{thru-m} /IL _{d-m} (dB)	0.6/0.8	0.6/0.8	0.6/0.8
D _{drop} (ps/nm)	±25	-26	±26
D _{thru} /D _d (ps/nm)	-92/-219	+146/+465	+199/+280
D _{thru-m} /D _{d-m} (ps/nm)	-240/+456	-245/+465	-249/+472

^aThe FSR to the left of the major peak

^bThe FSR to the right of the major peak

Table 2.6: Propagation loss tolerance for (gap 1, gap 2, gap 3) = (150 nm, 350 nm, 390 nm). Bolded parameter value does not meet its commercial specification. ©SPIE, 2015, by permission [85].

Parameter	Loss (dB/cm) = 1.4	2.4	3.4
FSR (nm)	36.93 ^a /38.75 ^b	36.93 ^a /38.75 ^b	36.93 ^a /38.75 ^b
A _i (dB)	53.8	53.6	53.5
nA _i (dB)	41.1	41.1	41.0
IPS (dB)	41.1	41.0	41.0
IL _{drop} (dB)	0.2	0.4	0.5
R _{depth} (dB)	0.0	0.0	0.0
EC _i /EC _d (dB)	28.0/ 28.4	28.0/28.7	28.0/29.0
IL _{thru} /IL _d (dB)	0.3/0.4	0.5/0.7	0.7/1.0
IL _{thru-m} /IL _{d-m} (dB)	0.3/0.5	0.6/0.8	0.8/ 1.1
D _{drop} (ps/nm)	-26	-26	-26
D _{thru} /D _d (ps/nm)	+146/+464	+146/+465	+147/+466
D _{thru-m} /D _{d-m} (ps/nm)	-245/+464	-245/+465	-246/+466

^aThe FSR to the left of the major peak

^bThe FSR to the right of the major peak

We have presented silicon quadruple Vernier racetrack resonators designed to meet typical 4-port filter commercial specifications. Also, we have shown that we can design a device with a waveguide width of 502 nm and a height of 220 nm that is tolerant to ± 8 nm changes in the widths of the waveguides. This device also has a D_{drop} of -26 ps/nm and a D_{d-m} of +465 ps/nm. Then, one at a time, we varied the waveguide height and propagation loss. The device was also tolerant to a ± 10 nm change in height as well as tolerant to changes in propagation loss. Next, theoretical and experimental results on a silicon quadruple Vernier racetrack resonator that meets numerous 3-port filter commercial specifications is presented.

2.4 Experimental Results

⁵A schematic of our quadruple series-coupled racetrack resonator exhibiting the Vernier effect is shown in Figure 2.7 which is similar to that found in [126, 142, 143] (same arrangement of the resonators but different resonator lengths, field transmission and coupling factors, and propagation loss). Here, L_1 , L_2 , L_3 , and L_4 are the total lengths of racetrack resonators R1, R2, R3, and R4, respectively. L_c is the length of the straight coupling regions, r is the radius of the racetrack resonators, and L is the length of the straight sections (other than those in the coupling regions) for racetrack resonators R3 and R4. κ_1 , κ_2 , κ_3 , κ_4 , and κ_5 are the symmetric (real) point field coupling factors. t_1 , t_2 , t_3 , t_4 , and t_5 are the straight through (real) point field transmission factors.

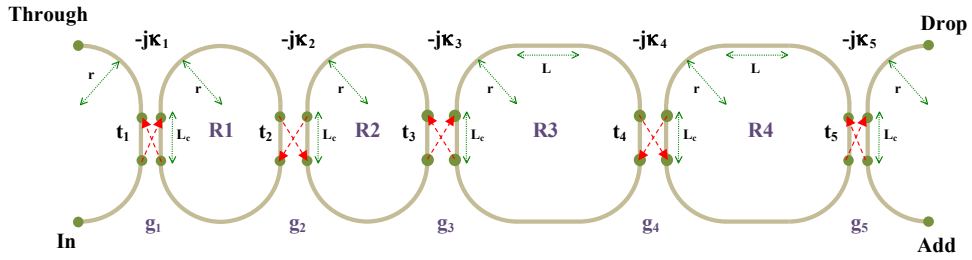


Figure 2.7: Schematic of our quadruple series-coupled racetrack resonators exhibiting the Vernier effect. ©Optical Society of America, 2013, by permission [96].

The following assumptions are made for the design: $L_{1,2} = 2\pi r + 2L_c$ and $L_{3,4} = (4/3)L_{1,2} = 2\pi r + 2L + 2L_c$, where $r = 5 \mu\text{m}$, $L_c = 7 \mu\text{m}$ and $L = 7.569 \mu\text{m}$. $\kappa_1 = \kappa_5$, $\kappa_2 = \kappa_4$, $t_1 = t_5$, and $t_2 = t_4$. The waveguides are SOI strip waveguides with a top silicon dioxide cladding having widths and heights of 502 nm and 220 nm, respectively. The propagation loss for each ring was assumed to be 2.4 dB/cm [492]. The modelling and analysis of the quadruple Vernier racetrack resonator was done using a mixture of numeric and analytic methods. Specifically, the effective index of the strip waveguides and the field coupling and transmission factors were determined using MODE Solutions by Lumerical Solutions, Inc., and everything else was done analytically. The gap distances are $g_1 = 125 \text{ nm}$, $g_2 = 350 \text{ nm}$, g_3

⁵A version of Chapter 2.4 has been published in [96].

= 410 nm, $g_4 = 350$ nm, and $g_5 = 125$ nm, respectively. The value of their field coupling and field transmission factors were determined by applying a third order polynomial curve-fit to the wavelength dependent even and odd effective indices. At 1550 nm, the field coupling factors are $\kappa_1 = \kappa_5 = 0.5446$, $\kappa_2 = \kappa_4 = 0.0771$, and $\kappa_3 = 0.0460$ and their slopes are $d\kappa_1/d\lambda = d\kappa_5/d\lambda = 1.72 \times 10^{-3} \text{ nm}^{-1}$, $d\kappa_2/d\lambda = d\kappa_4/d\lambda = 4.58 \times 10^{-4} \text{ nm}^{-1}$, $d\kappa_3/d\lambda = 3.03 \times 10^{-4} \text{ nm}^{-1}$. Also at 1550 nm, the effective index is 2.4464 and the slope is $-1.12 \times 10^{-3} \text{ nm}^{-1}$. The theoretical drop port and through port responses are shown in Figures 2.8(a) and 2.8(b). The derivation of the drop port and through port transfer functions can be found in Appendix A. We choose a 0.8 nm channel spacing and a 0.048 nm clear window centred at a desired wavelength. The spectral characteristics are determined within the clear windows of the desired channel and the 44 clear windows to the left and right of the desired channel. The FSR should be greater than or equal to 35.89 nm (the span of the C-band, 1528.77 nm to 1563.86 nm [92], plus one adjacent channel). The spectra (when light is only injected into the input port) shown in Figures 2.8(a) and 2.8(b) meet the typical commercial values for the target 3-port filter specifications as shown in Table 2.7 (bolded values). It should be noted that there is some variance in target values depending on the DWDM vendor. For example, [100] specifies an EC_i value of 12 dB whereas [99] specifies a value of 10 dB.

Table 2.7: Theoretical and target 3-port filter specifications [96].

Parameter	Theoretical	Target
FSR (nm)	36.93	\geq 35.89
A_i (dB)	52.7	\geq 25 [99, 100], 30 [101]
nA_i (dB)	40.4	\geq 35 [101], 40 [99, 100]
IPS (dB)	38.5	\geq 35 [101], 40 [99, 100]
R_{depth} (dB)	0.1	\leq 0.5 [99]
EC_i (dB)	11.1	\geq 10 [99], 12 [100]

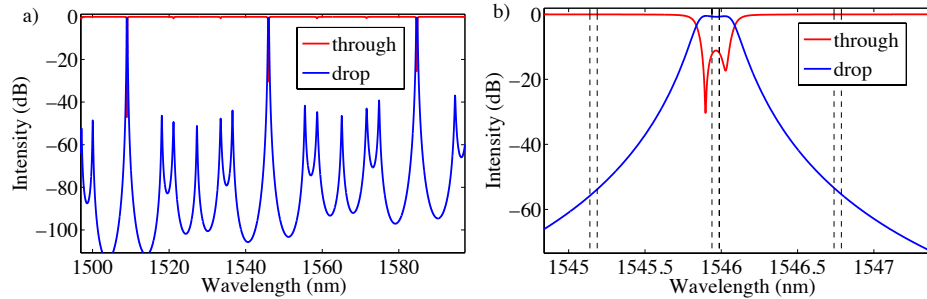


Figure 2.8: (a) Theoretical spectral response. (b) A “zoom-in” of the major resonance. ©Optical Society of America, 2013, by permission [96].

The device was fabricated at the University of Washington using electron beam lithography, as described in [493]. Figures 2.9(a) and 2.9(b) show the experimental through port and drop port responses of one of our silicon quadruple Vernier racetrack resonators. Figure 2.9(a) clearly shows significant IPS. The maximum through port insertion loss [98] and the drop port insertion loss [92, 98, 494] have not been included since we were unable to measure them accurately. The spectral characteristics meet numerous commercial 3-port filter specifications as shown in Table 2.8 (bolded values). The EC_i , R_{depth} , nA_i , and IPS are within 1.6 dB of the theoretical results. The experimental A_i is 37.2 dB whereas the theoretical A_i is 52.7 dB, which is likely due to the experimental filter line shape being asymmetric and to increased field coupling factors due to the bend regions of the couplers. To be able to simultaneously drop and add signals using just one instance of the device shown in Figure 2.7, the target values shown in Table 1.2 for 4-port filters would be needed. Specifically, the EC_i would need to be greater than or equal to 25 dB [87, 102]. The much larger notches within the pass band of the through port as compared to the theoretical results are possibly due to fabrication variations and coupling-induced frequency shifts (CIFs) [124, 495], which can be corrected by thermally tuning each racetrack resonator [124]. However, the notches are not located within any of the adjacent or non-adjacent channels as shown in Figures 2.9(c) and 2.9(d). The passband of the through port to the left of the major peak shows that there are actually 4 notches (two small notches and two large notches) as shown in Figure 5.7(c). However, our theoretical results showed that there are only two small notches as shown in Figure 2.8(a). The likely rea-

sons for this difference between the theory and experimental results are fabrication variations, in which the effective indices of the resonators are not all exactly the same, and CIFS. For example, if the effective index of racetrack resonator R1 is decreased by 0.003 [as shown in Figure 2.9(e)] each of the notches separates into 2 notches (one small and one large), where the larger notch is located to the right of the smaller notch [as shown in Figure 2.9(f)], which is in agreement with the experimental results. In addition to the device presented here, we fabricated 48 other devices in which the gap distances were varied. The device presented here showed the best performance. However, future designs based on this device can be made to be thermally tunable to compensate for fabrication variations and effects such as CIFS.

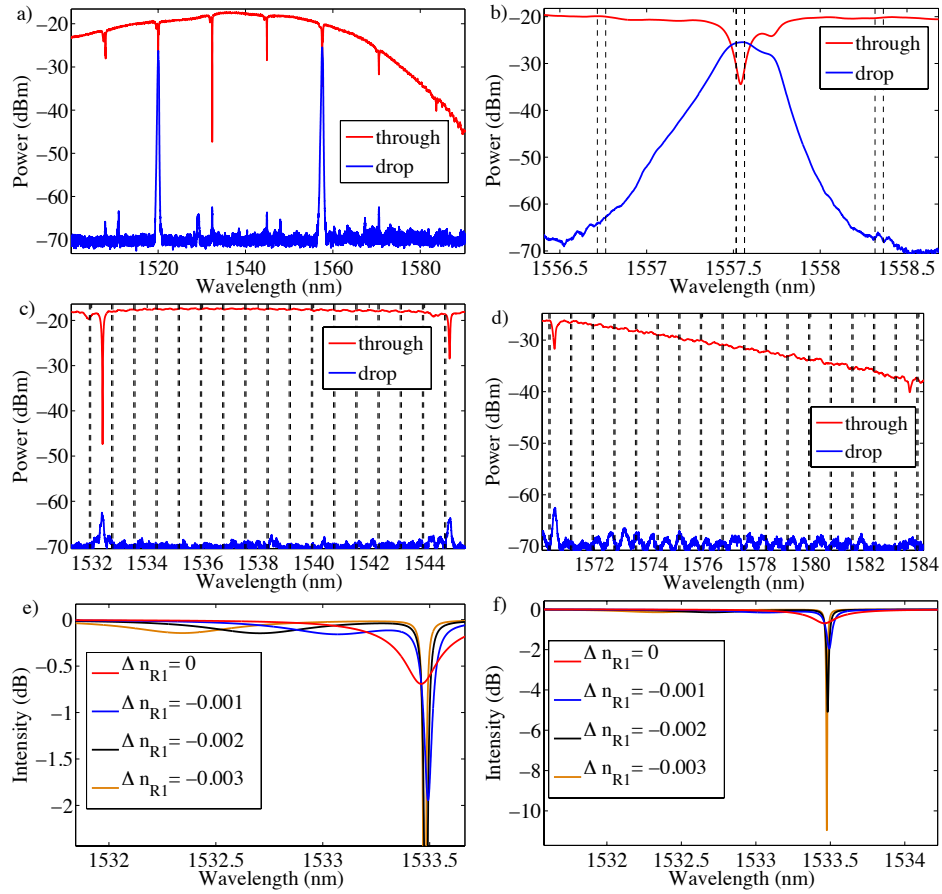


Figure 2.9: (a) Measured through port and drop port spectral response. (b) zoom-in of the measured major resonance. (c) Zoom-in of the measured through port passband to the left of the major peak. (d) Zoom-in of the measured through port passband to the right of the major peak. (e) Zoom-in of the theoretical notch splitting when the effective index of racetrack resonator R1 decreases and (f) zoom-out of Figure 2.9(e) (showing the increase in notch depth as the effective index of racetrack resonator R1 decreases). ©Optical Society of America, 2013, by permission [96].

Table 2.8: Experimental and target 3-port filter specifications [96].

Parameter	Experimental	Target
FSR (nm)	37.52	\geq 35.89
A_i (dB)	37.2	\geq 25 [99, 100], 30 [101]
nA_i (dB)	39.7	\geq 35 [101], 40 [99, 100]
IPS (dB)	36.9	\geq 35 [101], 40 [99, 100]
R_{depth} (dB)	0.2	\leq 0.5 [99]
EC_i (dB)	10.2	\geq 10 [99], 12 [100]

In summary, we have experimentally shown that it is possible to meet numerous 3-port DWDM filter commercial requirements using silicon quadruple series-coupled racetrack resonators exhibiting the Vernier effect. We have demonstrated a Vernier filter having a FSR greater than the span of the C-band (37.52 nm), a ripple of 0.2 dB, an adjacent channel isolation of 37.2 dB, a non-adjacent channel isolation of 39.7 dB, an interstitial peak suppression of 36.9 dB, and an express channel isolation of 10.2 dB. Next, I will discuss our work on thermally tunable silicon quadruple Vernier racetrack resonators.

Chapter 3

Thermally Tunable Silicon-On-Insulator Vernier Racetrack Resonators

¹ Thermal tuning of ring resonators is desirable since its effect on the effective index is large [496] and there is no excess loss versus current [497]. Thermally tunable identical series-coupled ring resonators have been fabricated [115, 124], however, an increase in temperature tends to shift the resonant wavelength by approximately 0.07 nm/°C, therefore, to tune the resonant wavelength by the span of the C-band (35.09 nm) would require a temperature change of several hundred degrees Celsius. Fortunately, the Vernier effect enables one to significantly enhance the resonant wavelength tuning range as compared to the range capable when using identical ring resonators [301]. Thermally tunable series [113, 212, 317] and cascaded [134, 301] coupled double ring resonator filters exhibiting the Vernier effect have been achieved previously. However, these devices show unacceptable spectral characteristics for typical DWDM applications such as low IPS [113, 301, 317], small extension of the FSR [212, 317], no extension of the FSR in the through port [134, 301], and many do not use the SOI platform [134, 212].

In this chapter, I present our results on thermally tunable silicon quadruple

¹A version of this paragraph has been published in [149].

Vernier racetrack resonators that exhibit an increased resonant wavelength tuning range as compared to resonators that do not utilize the Vernier effect. We also show that it is possible to transmit data through a silicon quadruple Vernier racetrack resonator.

3.1 Thermally Tunable Silicon Quadruple Vernier Racetrack Resonators

² Here, we present theoretical and experimental results on a thermally tunable silicon quadruple Vernier racetrack resonator. For the modelling and analysis of our Vernier racetrack resonator, we have used SOI strip waveguides with heights of 220 nm and widths of 502 nm, as well as a top SiO₂ cladding. The Si refractive index is wavelength dependent and can be fitted to experimental data using a Lorentz model [470]. Since the wavelength dependency of the refractive index of SiO₂ is minimal, we have assumed a constant refractive index of 1.4435. Also, we have used 2.4 dB/cm propagation loss in our modelling. This is consistent with the value of 2.35 ± 0.33 dB/cm recently reported by [492], for SOI strip waveguides with top SiO₂ claddings. The schematic of the quadruple Vernier racetrack resonator is shown in Figure 3.1(a), which has an asymmetric arrangement of resonators as described in [96, 126, 142, 143]. The fabricated device is shown in Figure 3.1(b).

²A version of Chapter 3.1 has been published in [149].

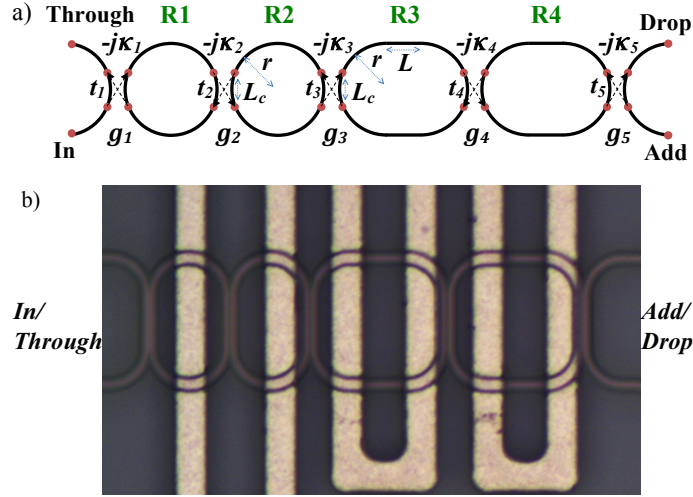


Figure 3.1: (a) Shows the schematic of the quadruple Vernier racetrack resonator and (b) shows the fabricated device. ©Optical Society of America, 2013, by permission [149].

$L_{1,2,3,4}$ are the total lengths of the racetrack resonators, κ_1 and κ_5 are the symmetric (real) point field coupling factors to the bus waveguides, $\kappa_{2,3,4}$ are the interring symmetric (real) point field coupling factors, and $t_{1,2,3,4,5}$ are the respective (real) point field transmission factors. The derivations of the transfer functions can be found in [96, 144] and Appendix A. The following simulations assume that $L_1 = L_2 = 2\pi r + 2L_c$ (where $r = 5 \mu\text{m}$ and $L_c = 7 \mu\text{m}$), $L_3 = L_4 = (4/3)L_1 = 2\pi r + 2L_c + 2L$ (where $L = 7.569 \mu\text{m}$), $\kappa_1 = \kappa_5$, $\kappa_2 = \kappa_4$, $t_1 = t_5$, and $t_2 = t_4$. The effective index and field coupling and transmission factors are wavelength dependent and were determined using MODE Solutions software by Lumerical Solutions, Inc. The field coupling and transmission factors were calculated by determining the even and odd effective indices. At the major resonance wavelength (1545.96 nm), the effective index for a single waveguide is 2.4509 and its slope is -0.0011 nm^{-1} . The gap distances g_1 , g_2 , g_3 , g_4 , and g_5 were chosen to be 148 nm, 348 nm, 388 nm, 348 nm, and 148 nm, respectively. At the major resonance wavelength, their respective field coupling factors (and slopes) are 0.4392 (0.0016 nm^{-1}), 0.0766 (0.0005 nm^{-1}), 0.0542 (0.0003 nm^{-1}), 0.0766 (0.0005 nm^{-1}), and 0.4392 (0.0016 nm^{-1}). We designed our device to have an EC_i greater than or equal to 25 dB [87, 102] for a clear

window of 0.1 nm at a centre wavelength of 1545.94 nm and a channel spacing of 0.8 nm, as shown in Figure 3.2(b), whereas our previous device had an EC_i of 11.1 dB for a clear window of 0.048 nm [96]. Also, minimal notches within the passbands of the through port and a large IPS is required, as shown in Figure 3.2(a). The 3-dB BW, IPS, FSR, and EC_i are 0.34 nm, 41.0 dB, 36.93 nm, and 25.7 dB, respectively, when light is only injected into the input port.

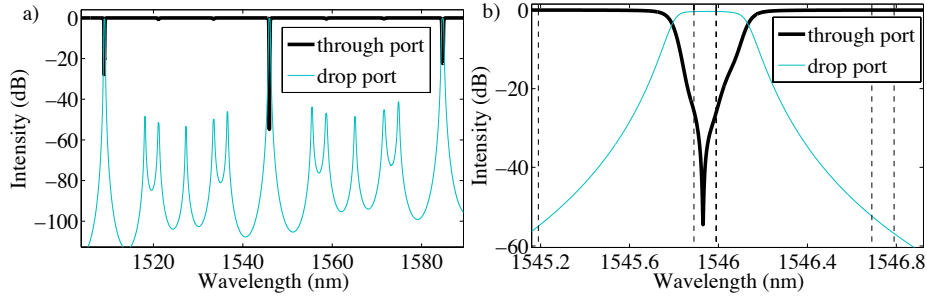


Figure 3.2: (a) Shows the theoretical through port and drop port spectra and (b) shows a major peak in the drop port response and a major notch in the through port response. ©Optical Society of America, 2013, by permission [149].

The device fabricated consisted of multiple e-beam lithography [493] and Cl_2 etch steps (to define the strip waveguides and shallow etch grating couplers), a 2 micron oxide deposition, followed by a 300 nm deposition of Al for the electrodes and metal heaters (5 μ m wide) above the waveguides. Figures 3.3(a) and 3.3(b) show the experimental through port and drop port responses of the device when no voltage is applied (light is only injected into the input port). The FSR (37.09 nm) is larger than the span of the C-band, the IPS is 24.5 dB for a clear window of 0.1 nm centred at $\lambda = 1549.468$ nm, and the 3-dB BW is 0.24 nm. It is also clear that the through port response shows suppression of the resonances within the passband. The minimum insertion loss (defined as the maximum transmission at the through port) of the device is approximately 12 dB, which is mainly due to the grating coupler loss (typically measured to be 10-12 dB), whereas other loss mechanisms are minimal such as mode-mismatch loss at the interfaces between straight sections and 90 degree bends of the racetrack resonators which, based on our simulation results, is approximately 0.008 dB per interface. Also, one can

clearly see that the major peak is much lower than the through port transmission and the major notch shows worse performance as compared to the theory which are likely due to fabrication variations and CIFSs which can be corrected for by finely tuning each ring resonator [124]. However, here we have focussed on the discrete wavelength tunability of our device (continuous tuning is possible as described in [301]). We applied the same voltage to racetrack resonators R3 and R4 to enable the Vernier effect switching mechanism. Figure 3.4(a) shows the theoretical results when the temperature difference between resonators R3 and R4, as compared to the temperature of resonators R1 and R2, is increased from 0 °C to 46 °C ($dn/dT = 1.86 \times 10^{-4} \text{ }^\circ\text{C}^{-1}$ [431]). We can clearly see the discrete switching of the major peak across a wavelength span of 12.70 nm, which corresponds to the FSR of a single racetrack resonator with the dimensions of one of our small resonators (*i.e.*, resonator R1 or R2). If we changed the temperatures of all of the racetrack resonators at the same time by 46 °C, the major peak would only shift by 3.17 nm. Thus, we can see one of the benefits of using the Vernier effect to tune the resonant wavelength. Figure 3.4(b) shows the experimental results in which we varied the voltage applied to the heaters on top of both racetrack resonators R3 and R4 from 0 V to 10.5 V. The major peak shifts discretely by 15.54 nm. When 10.5 V is applied, the major peak has an IPS of 32.7 dB for a clear window of 0.1 nm that is centred at $\lambda = 1565.062$ nm, a 3-dB BW of 0.45 nm, and an FSR of 37.66 nm. Except for a 2.84 nm increase in the resonant shift, which is possibly due to thermal crosstalk between the racetrack resonators [301] (resonators R1 and R2 are likely also being heated), the experimental Vernier switching mechanism seen here is in agreement with the theoretical results.

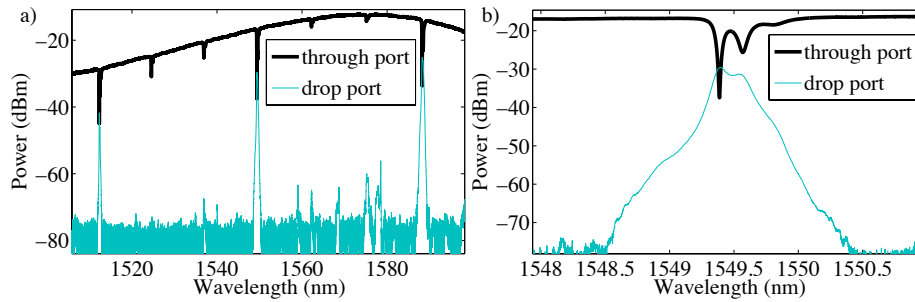


Figure 3.3: (a) Shows the experimental through port and drop port spectra and (b) shows a major peak of the drop port response and a major notch of the through port response. ©Optical Society of America, 2013, by permission [149].

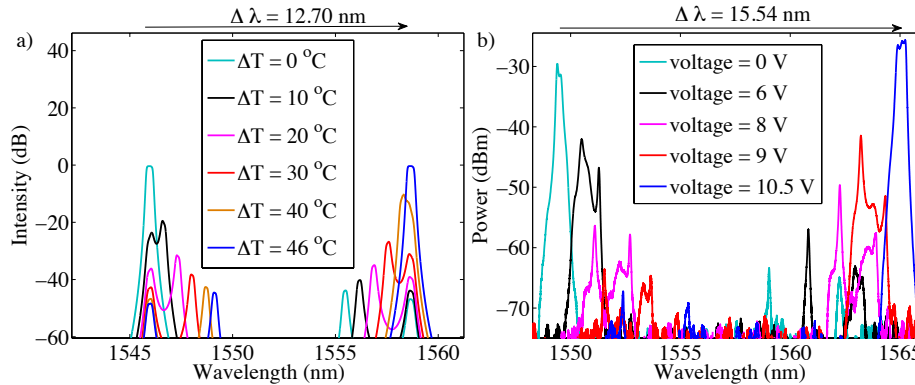


Figure 3.4: (a) Shows the theoretical drop port spectral responses for various temperature changes applied to racetrack resonators R3 and R4 and (b) shows the experimental drop port spectral responses for various changes in the voltage applied to the heaters on top of racetrack resonators R3 and R4. ©Optical Society of America, 2013, by permission [149].

In summary, we have demonstrated a thermally tunable silicon quadruple Vernier racetrack resonator. This device has an IPS of 32.7 dB, a 3-dB BW of 0.45 nm, and an extended FSR of 37.66 nm when 10.5 V is applied to the heaters on top of the two larger racetrack resonators. We were also able to shift the major peak by 15.54 nm. Next, I discuss our experimental results that demonstrate that it is possible to transmit data to the drop port of another one of our thermally tunable silicon quadruple Vernier racetrack resonators as well as to the through port in the location of one of the minor notches at a data rate of 12.5 Gbps.

3.2 Silicon-On-Insulator Quadruple Vernier Racetrack Resonators: Experimental Signal Quality

³One of the issues with using series-coupled Vernier ring resonators is that large dispersion can occur in the region of the suppressed notches of the through port [112, 231, 432]. Here, we experimentally demonstrate a thermally tunable silicon quadruple series-coupled Vernier racetrack resonator filter (similar to [149]) and show data transmission at 12.5 Gbps through the filter. Our results show that there is degradation of the signal quality through our filter in the region of a suppressed notch, however, the eye remained open.

A thermally tunable silicon quadruple series-coupled Vernier racetrack resonator filter was fabricated using optical lithography at the Institute of Microelectronics (IME) in Singapore. The filter had an oxide cladding and 3 μm wide TiN heaters were fabricated on top of the racetracks for the purpose of thermal tuning. The strip waveguides had widths of 500 nm and heights of 220 nm and the rest of the parameters can be seen in Figure 3.5(a) (some of these parameters can also be found in [84, 96, 149]). Figure 3.5(b) is an image of the fabricated filter. Fibre grating couplers were used for coupling light in/out of the device [498].

³A version of Chapter 3.2 has been published in [150].

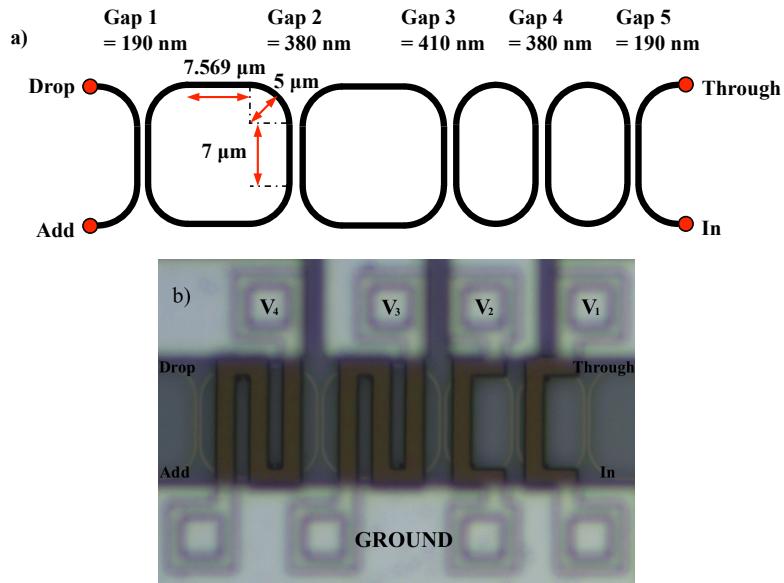


Figure 3.5: (a) Schematic diagram of the Vernier filter (see [84, 96, 127, 140–142, 149]) and (b) a microscope image of the fabricated filter showing the integrated heaters. ©Optical Society of America, 2015, by permission [150].

Figure 3.6(a) shows the in-port-to-through-port and in-port-to-drop-port spectral responses before and after thermal tuning. For thermal tuning, we applied voltages of $V_1 = 0.631$ V, $V_2 = 0.795$ V, $V_3 = 0.37$ V, and $V_4 = 1.07$ V [see Figure 3.5(b)]. The 3-dB BW after thermal tuning is 0.35 nm. Figure 3.6(b) shows a zoom-out of the spectra after thermal tuning which exhibits a large FSR of 37.87 nm and significant IPS. Figure 3.6(c) shows that the in-port-to-drop-port spectral response and the add-port-to-through-port spectral response are similar. In Figure 3.6(d) we can see that there are two relatively suppressed notches (the other three notches are more suppressed and are not visible) within the passband of the through port (in-port-to-through-port) and three relatively suppressed notches (the other two notches are more suppressed and are not visible) within the passband of the drop port (add-port-to-drop-port) which is consistent with the theoretical results in [84]. Figures 3.6(e) and 3.6(f) show the group delay and dispersion (see [112, 114, 140, 144]), respectively, from the in port to the drop port and from the add port to the through port. The group delay and dispersion were determined

using the Hilbert transform method [112, 499] (we used the MATLAB[®] Hilbert transform function [500]) and averaging was used to smooth the results.

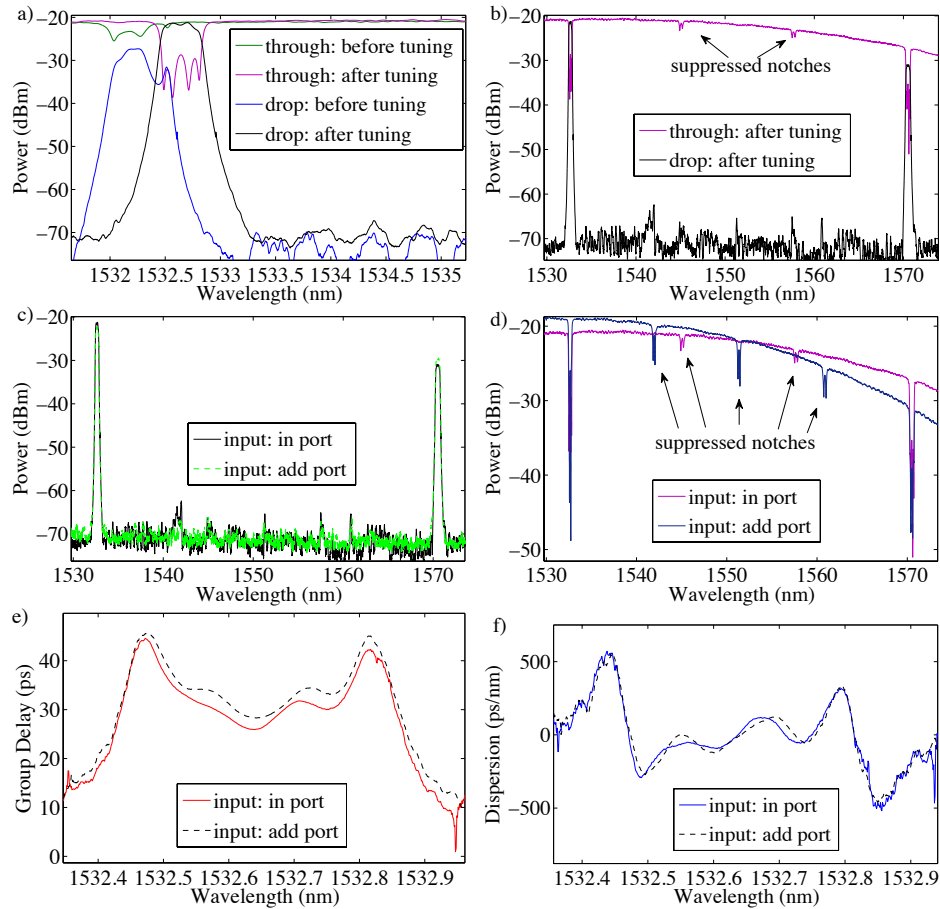


Figure 3.6: (a) Measured spectra from the in port to the drop port as well as the in port to the through port of our filter in the region of the major peak/notch before and after thermal tuning and (b) spectra of the filter after thermal tuning. (c) Shows the measured in-port-to-drop-port spectrum as well as the measured add-port-to-through-port spectrum after tuning. (d) Shows the measured in-port-to-through-port spectrum as well as the measured add-port-to-drop-port spectrum after tuning. (e) and (f) show the group delay (zero set arbitrarily) and the dispersion, respectively, from the in port to the drop port as well as from the add port to the through port after tuning. ©Optical Society of America, 2015, by permission [150].

To determine if data can pass through our filter without significant distortion, we performed eye diagram measurements (see [501]). Electrical data was generated using a bit pattern generator (data rate = 12.5 Gbps NRZ, PRBS $2^{31}-1$, mark ratio = 1/4) which was then sent to a 10 GHz lithium niobate Mach-Zhender interferometer modulator and a polarization controller to modulate the light coming from the laser and to control the polarization, respectively. After the data was passed through the quadruple Vernier racetrack resonator, an optical amplifier was used to amplify the signal and a tunable grating filter was used to minimize the noise. After the data was sent through a photodetector, a digital communication analyzer was used to measure the eye diagrams. The set-up is similar to the one shown in [501]. Figure 3.7(a) shows an open eye diagram when data is passed from the in port to the drop port of our device at a wavelength of 1532.636 nm. For the through port spectral response, the most important wavelength regions of interest are at the suppressed notches within the through port passband [see Figure 3.6(b)] since large dispersion occurs here [112, 231, 432]. Figures 3.7(b)-3.7(d) show eye diagrams when data is passed from the in port to the through port at different wavelengths within the through port passband. Figure 3.7(b) shows an open eye at a wavelength of 1543.018 nm, which is to the left of one of the relatively suppressed notches. Next we measured the eye at two different wavelengths, 1545.153 nm and 1545.247 nm, in the region of a relatively suppressed notch (*i.e.*, near 1545.074 nm which is in the middle of one of the notches). Both Figures 3.7(c) and 3.7(d) show signal degradation, as compared to Figure 3.7(b), however, both eyes are still open. Also, we can see that by changing the laser wavelength within the region of the suppressed notch we are able to obtain a more open eye at 1545.153 nm as compared to 1545.247 nm, which demonstrates that the signal quality can be tuned within the suppressed notch.

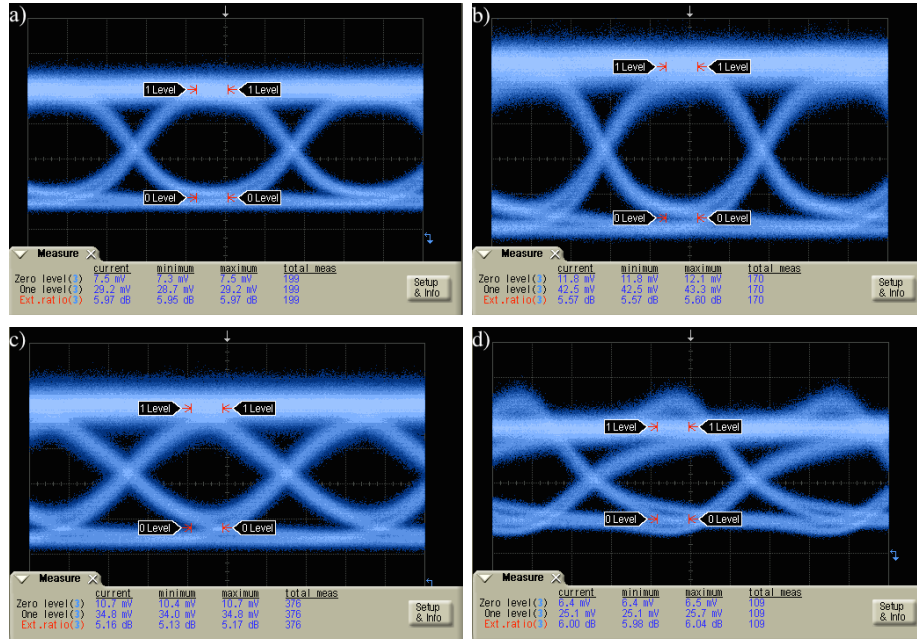


Figure 3.7: (a) Eye diagram measured for data passing from the in port to the drop port at a wavelength of 1532.636 nm. Eye diagrams for data passing from the in port to the through port at (b) 1543.018 nm, (c) 1545.153 nm, and (d) 1545.247 nm. ©Optical Society of America, 2015, by permission [150].

We have presented experimental results on a thermally tunable silicon quadruple series-coupled Vernier racetrack resonator filter. We have determined the group delay and dispersion of our filter and have shown successful data transmission at 12.5 Gbps, with open eyes, at a through port suppressed notch. Also, we have shown that the signal quality depends on where within the suppressed notch the data is transmitted.

In the next chapter, another method to extend the FSR using two identical series-coupled silicon microring resonators (MRRs) with MZI-BC will be presented, including improved resonant suppression exhibited by our fabricated device as compared to the suppression seen in [432]. The benefit of this approach to extending the FSR is that very low dispersion within the through port passbands can be achieved [432].

Chapter 4

High Performance Silicon-On-Insulator Double Microring Filter Using MZI-Based Coupling

¹One component of interest in optical interconnects is the optical add-drop filter for multiplexing and demultiplexing signals, which can be created using ring resonators [127]. Ring resonator-based filters have been shown to meet numerous commercial specifications. For example, Popović *et al.* showed that telecom specifications can be met using four series-coupled silicon MRRs [115] and Boeck *et al.* have shown that many key commercial specifications, for adding or dropping signals, can be met using silicon quadruple series-coupled Vernier racetrack resonators [96]. However, the challenge encountered when using ring resonators is that they have FSRs which limit the number of channels that can be used, thus, it is desirable to have a large FSR in order to have a large number of usable channels [127]. One method to increase the FSR is to use double MRRs with MZI-BC [432, 433] (see Figure 4.1).

Various configurations of series-coupled ring resonators that use MZI-BC have

¹A version of Chapter 4 has been published in [105].

been studied [112, 141, 175, 432, 433]. Here, we are going to focus on double MRRs with MZI-BC. Watts *et al.* demonstrated such a device using silicon nitride [432]. Their device had an FSR and resonant suppression of 40.8 nm and 19.5 dB, respectively [432]. Lira *et al.* experimentally demonstrated a thermally tunable SOI double MRR with MZI-BC which had an FSR of 19.2 nm and a resonant suppression of about 16 dB [433]. However, the suppressions demonstrated by [432] and [433] do not meet typical commercial specifications (*e.g.*, ≥ 35 dB [101]). While the Vernier effect can also be used to increase the FSR [84, 96, 97, 107, 112, 127, 128, 141], a double MRR with MZI-BC also increases the FSR while providing low through port dispersion near the suppressed through port notch [432]. Here we experimentally demonstrate a double MRR with MZI-BC for adding or dropping signals (*i.e.*, a 3-port device) on SOI, which is a CMOS compatible technology that is of considerable commercial interest, while giving a similar FSR and an improved resonant suppression as compared to the silicon nitride based device presented in [432]. Also, we show that our device meets many 3-port filter commercial specifications. We also present theoretical results on the maximum drop port dispersion, maximum drop port insertion loss, maximum through port dispersion, and maximum through port insertion loss. Also, experimental drop port and through port dispersions are presented. While we focus on 3-port filters, we can create a 4-port optical add-drop multiplexer (OADM) capable of simultaneously adding and dropping signals by cascading two 3-port filters together [108]. Therefore, one should be able to cascade two double MRR with MZI-BC filters at the through port (see [109]) to meet commercial specifications for adding and dropping signals.

4.1 Theory and Design

Our SOI device consists of two series-coupled MRRs and two sets of MZI couplers, as shown in Figure 4.1. The field coupling factor versus wavelength of a co-directional coupler (such as the coupling between the two MRRs, κ_r , or the coupling regions of the MZIs, κ_{mzi}) is relatively broadband. However, the MZI coupler enables the overall coupling to the ring to be periodic due to the length difference between the two MZI branches. It is possible to get resonant suppression

when the nulls and the peaks of the MZI are aligned, alternately, with the resonances of the rings, provided that the FSRs of the MZIs are twice that of the ring resonators' (see [112, 432, 433]).

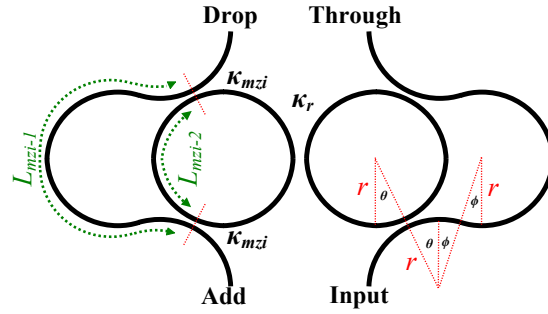


Figure 4.1: Schematic of the device (either the add port or the drop port is used and the other is terminated when used as a 3-port device). ©Optical Society of America, 2015, by permission [105].

Using an initial design, we placed 17 devices on our mask in which the gap distances were varied. In this initial design, the MZI-ring gap distances were chosen to be 150 nm and the gap distance between the rings was chosen to be 290 nm. We have chosen a device that gave good experimental results, then, for the purpose of comparing the measurement and design, we put the as-designed gap distances for the measured device into our model. In the modelling, we used the following: the SOI strip waveguide widths and heights are 500 nm and 220 nm, respectively, and there is a silicon dioxide top cladding; the radius, r , to the centre of the waveguide of each MRR is 4.9 μm ; the MZI-ring gap distance is 130 nm and the gap distance between the rings is 290 nm; the MZI-bus waveguide branch, L_{mzi-1} , has a length of 26.2037 μm and the MZI-ring branch, L_{mzi-2} has a length of 10.8099 μm (these lengths were chosen such that their difference is equal to half the circumference of the MRR [112, 432, 433]); and the propagation loss is assumed to be 2.4 dB/cm [84, 96]. Since the radius of each of the microring resonators is 4.9 μm , their FSRs are larger than half the width of the C-band. Since every alternate peak/notch is suppressed by the use of MZI-BC, the resulting spectra have FSRs greater than the span of the C-band. The power coupling and transmission factors were determined using 3-D FDTD and the effective indices were determined using a 2-D eigenmode

solver, both by Lumerical Solutions, Inc. The angles ϕ and θ for the MZI branches, which allow the device's required gap distances, radii of the microring resonators, and lengths of the MZI branches to be achieved, were determined using Eqs. 1 - 3 from [432] and are 18.2004° and 26.7996° , respectively.

The specifications of interest for the drop port response are IL_{drop} , R_{depth} , A_i , nA_i , IPS, and D_{drop} . The specifications of interest for the through port response are EC_i , IL_{thru} , $IL_{\text{thru-m}}$, and D_{thru} . Also, our filter needs to have an FSR greater than or equal to the width of the C-band plus one adjacent channel, *i.e.*, 36.72 nm (see [92, 110]). Some of the specifications that need to be met for adding or dropping signals, for a 200 GHz channel spacing, are listed in Table 4.1. The bolded values are the ones that the experimental results meet. The target specification for D_{drop} is $-30 \text{ ps/nm} \leq D_{\text{drop}} \leq +30 \text{ ps/nm}$, which is based on the example parameter value for a re-configurable OADM given in [104]. We have assumed that D_{thru} needs to meet a target specification of $-15 \text{ ps/nm} \leq D_{\text{thru}} \leq +15 \text{ ps/nm}$, which is half of the target specification for D_{drop} , since our device is for adding or dropping signals. Here, we chose a clear window of 8 GHz, based on our experimental results, and we looked at the relevant channels when determining the nA_i and IL_{thru} in the measured wavelength range (1520 nm to 1580 nm).

Table 4.1: Target specifications for 200 GHz optical filters [105].

Parameter	Target value
FSR (nm)	\geq 36.72
A_i (dB)	\geq 25 [502, 503], 30 [101]
nA_i (dB)	\geq 35 [101], 40 [502, 503]
IPS (dB)	\geq 35 [101], 40 [502, 503]
R_{depth} (dB)	\leq 0.5 [502]
EC_i (dB)	\geq 10 [502], 12 [503]

4.2 Theoretical Results

The simulated through port and drop port spectra were determined using transfer functions that were derived using Mason's rule [128, 504] (see Appendix B). Figure 4.2(a) shows the theoretical spectra of the drop port and through port and

Figure 4.2(b) shows a zoom-in of the response in the location of the desired channel. We have increased the effective indices by a constant value of 0.01787, as compared to the effective indices obtained using the 2-D eigenmode solver assuming 25°C, to align the theoretical drop port peak to that of the experimental drop port peak (at 1529.551 nm). Table 4.2 shows that, as modelled, this device meets at least one of the specifications for each parameter listed in Table 4.1. Also, this device has a theoretical 3-dB BW of 0.30 nm. The 3-dB BW is dependent on the the choice of the gap distances, the propagation losses, and the optical path lengths of each of the microring resonators [107], as well as the overall coupling due to the MZIs [433]. Figures 4.3(a) and 4.3(b) show the theoretical drop port dispersion within the clear window of the desired channel and the largest through port dispersion located in the region of the suppressed notch near 1547.85 nm, respectively. D_{drop} is -21 ps/nm, which meets its target specification of $-30 \text{ ps/nm} \leq D_{\text{drop}} \leq +30 \text{ ps/nm}$ [104]. D_{thru} is $\pm 0 \text{ ps/nm}$ which meets its target specification of $-15 \text{ ps/nm} \leq D_{\text{thru}} \leq +15 \text{ ps/nm}$ (although there is no channel clear window in the region where the through port notch is suppressed [see Figure 4.3(b)], the maximum and minimum dispersion is $\pm 15 \text{ ps/nm}$). Our results are consistent with the statement in [432] that low through port dispersion near the suppressed notch can be achieved using this type of device. Also, the modelled value for IL_{drop} is 1.0 dB, IL_{thru} is 0.0 dB, and $IL_{\text{thru-m}}$ is 0.0 dB which meets typical commercial specification of $\leq 1.2 \text{ dB}$ [101], $\leq 0.6 \text{ dB}$ [101], and $\leq 0.6 \text{ dB}$ [101], respectively.

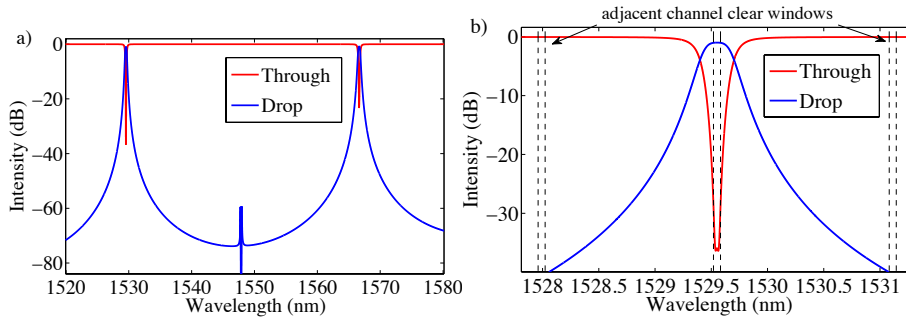


Figure 4.2: (a) Theoretical drop port and through port response and (b) zoom-in of Figure 4.2(a). ©Optical Society of America, 2015, by permission [105].

Table 4.2: Theoretical filter results [105].

Parameter	Modelling result
FSR (nm)	37.10
A_i (dB)	39.0
nA_i (dB)	38.3
IPS (dB)	58.5
R_{depth} (dB)	0.0
EC_i (dB)	28.7

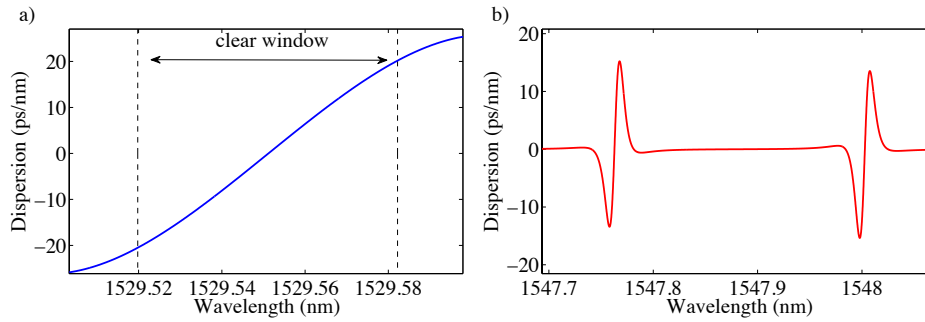


Figure 4.3: Dispersion of (a) the drop port within the passband region and (b) the region near the suppressed through port notch. ©Optical Society of America, 2015, by permission.

4.3 Experimental Results

17 devices were fabricated using e-beam lithography (see [493] for fabrication process) with the gap distances being varied. Figures 4.4(a) and 4.4(b) show the experimental drop port and through port responses for a good device. The FSR is 37.23 nm due to the doubling of the FSR achieved by the MZIs which suppress intermediate peaks and the 3-dB BW is 0.29 nm. Also, our device has an A_i , a nA_i and an IPS of at least 41.0 dB, 38.6 dB, and 37.5 dB, respectively, since we are unable to distinguish the filter shape within the noise floor. The clear window is 8 GHz and the channel spacing is 200 GHz. The clear window is centred at 1529.490 nm. The location and the width of the clear window were chosen to ensure that $R_{\text{depth}} \leq 0.5$ dB [502] and $EC_i \geq 10$ dB [502]. The splitting of the major notch seen in

Figure 4.4(b) is likely due to variations in the coupling factors and variations in the resonant wavelength of each of the microring resonators. Since we are using grating couplers to couple light into and out of our device [505], the shape of the grating coupler response affects the measured filter spectrum. Therefore, some of the parameter values can be difficult to determine accurately. In particular IL_{drop} , IL_{thru} , and $IL_{\text{thru-m}}$ are three such parameters and are not included in our experimental results for this reason. The maximum and minimum total device insertion loss measured at the through port, which includes two fibre grating couplers and routing waveguides, within the clear windows of the adjacent and non-adjacent channels are 27.9 dB and 22.8 dB, respectively. The maximum total device insertion loss measured at the drop port within the clear window of the desired channel is 27.9 dB. We measured our device within the wavelength range 1520 nm to 1580 nm, therefore, we looked at the 5 non-adjacent clear windows to the left of the major peak and the 21 non-adjacent clear windows to the right of the major peak when measuring the nA_i . Next, we measured the drop port dispersion (average of 200 measurements) within the region of the major peak as well as the through port dispersion (average of 200 measurements) within the wavelength span corresponding to the through port passband to the right of the major notch as shown in Figures 4.5(a) and 4.5(b), respectively. An Optical Vector AnalyzerTM *STe* by Luna Innovations, Inc., was used to measure the dispersion. The experimental through port passband dispersion is minimal which is in agreement with the statements made in [432] that low through port dispersion is possible using double MRR with MZI-BC.

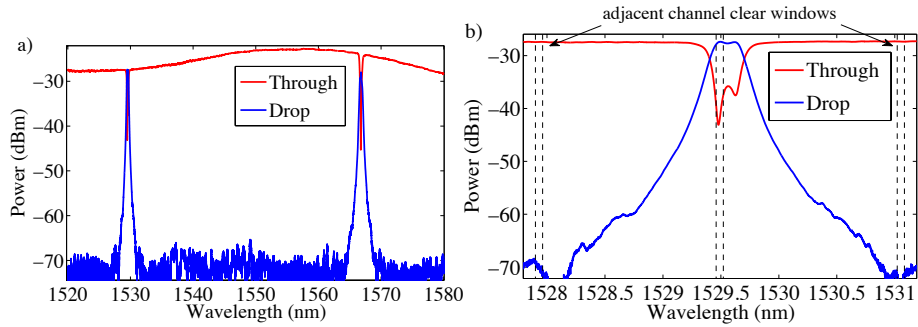


Figure 4.4: (a) Experimental drop port and through port response and (b) zoom-in of Figure 4.4(a). ©Optical Society of America, 2015, by permission [105].

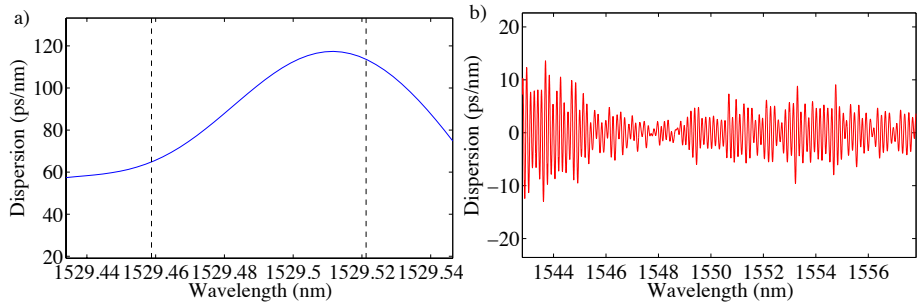


Figure 4.5: (a) Experimental drop port dispersion (vertical dashed lines indicate width of clear window) and (b) experimental through port dispersion within the through port passband.

Table 4.3: Experimental filter results [105].

Parameter	Experimental result
FSR (nm)	37.23
A_i (dB)	≥ 41.0
nA_i (dB)	≥ 38.6
IPS (dB)	≥ 37.5
R_{depth} (dB)	0.5
EC_i (dB)	10.0

As compared to [432] and [433], the IPS of our device meets its typical commercial specification. Also, our device's FSR, 37.23 nm, is comparable to the FSR in [432], 40.8 nm, both larger than the C-band, and our device's FSR is nearly double the FSR of [433]. We have provided the theoretical and experimental dispersion of our device which [432] and [433] do not provide. Our device is more compact (*i.e.*, smaller radii) as compared to the devices in [432] and [433], and our device is fabricated in 220 nm SOI, whereas the device in [432] is fabricated in silicon nitride. Although we have not included heaters on top of our device, as was done in [433], we varied the temperature of the entire chip that contained our device and determined that the spectral response shifts by 0.069 nm/°C.

In conclusion, we have experimentally demonstrated a high performance silicon double MRR with MZI-BC that meets many key 3-port filter commercial specifications for a 200 GHz channel spacing and a clear window of 8 GHz, which will be useful in DWDM and sensor applications. Even though the FSR can be extended using MZI-BC, an FSR still exists. In the next chapter, I will discuss a method to increase the IPS of cascaded Vernier ring resonators as well as eliminate the FSR by the use of contra-DCs instead of co-directional couplers (*i.e.*, couplers without gratings).

Chapter 5

FSR-Eliminated Silicon-On-Insulator Vernier Racetrack Resonators Using Grating-Assisted Couplers

¹Cascaded racetrack resonators exhibiting the Vernier effect have numerous benefits compared to single racetrack resonators, including an extended FSR in the drop port [134, 137, 216, 287, 301, 343, 415]. However, the through port spectral response does not have an increased FSR [343, 415], which can be problematic for certain DWDM applications. Fortunately, series-coupled racetrack resonators can exhibit the Vernier effect in both the drop port and the through port [96, 317, 415]. Numerous papers have presented theoretical [126–128, 142–144] results as well as experimental [96, 111, 129, 137, 157, 167, 190, 212, 290, 317] results for series-coupled Vernier resonators consisting of two [111, 127–129, 137, 142, 143, 157, 167, 212, 290, 317], three [126–128, 143, 190], and four [96, 126, 142–144] rings. Also, combinations of cascaded and series-coupled Vernier ring resonators have been theoretically analyzed [114]. Recently, Yan *et al.* [331] presented a novel configuration of microring resonators exhibiting the Vernier effect in which one

¹A version of Chapter 5 has been published in [97]. ©2013 IEEE, by permission.

ring resonator is directly coupled to four smaller ring resonators. Also, Vernier ring resonators have been used to create sensors [131, 286, 288, 416] and tunable lasers [203, 260]. Due to fabrication variations, the performance of the ring resonators may be significantly degraded. Thermal tuning of each individual ring resonator is needed to correct for the fabrication variations. A benefit of the cascaded configuration of ring resonators, as compared to the series-coupled configuration, is that the thermal cross-talk between resonators is reduced due to the increased distance between the rings [301]. Recently, Shi *et al.* [439] designed and fabricated a new single silicon racetrack resonator with contra-DCs within the coupling regions to suppress all but a single resonance in the drop port and the through port, which is due to the small bandwidth of the coupler. The suppression of minor peaks is greater than 8 dB [439]. Orlandi *et al.* [437] presented experimental results on a silicon racetrack resonator with gratings within the coupling regions but their device showed minimal suppression of peaks in the drop port. Also, Orlandi *et al.* [437] discussed and presented theoretical results on a modified version of their grating coupled racetrack resonator in which the input coupler has gratings but the output coupler does not. In this chapter, we demonstrate both theoretically and experimentally contra-directional grating-coupled cascaded racetrack resonators exhibiting the Vernier effect. The theoretical results show the elimination of the FSR (in both the drop port and the through port) as well as the improvement in the IPS at the drop port and the improvement in the through port insertion loss, IL_{thru} , as compared to the case in which no gratings were used. Our fabricated device shows an improvement in the suppression of minor peaks in the drop port as compared to the suppression shown by [439] and [437]. Our experimental results show an IPS of 24.3 dB and the elimination of the FSR in the drop port and through port.

5.1 Theory

We have decided to use SOI strip waveguides with a top oxide cladding for the FSR-eliminated grating-coupled cascaded Vernier racetrack resonator, since previous experimental results by Shi *et al.* [439] have shown promising results for individual grating-coupled racetrack resonators. The waveguide heights are 220 nm and the bus waveguide widths, w_b , and the racetrack resonator widths, w_r , are

450 nm and 550 nm, respectively. For the coupling regions that have co-directional coupling (no gratings), w_b and w_r are 550 nm and the gap distance is 280 nm. The gratings within the coupling regions are formed by corrugating the sidewalls as shown in Figure 5.1(a). The corrugation depths, c_b and c_r , for waveguides with widths of w_b and w_r , are defined as the extensions into the waveguides by $c_b/2$ and $c_r/2$ and into the gap by $c_b/2$ and $c_r/2$. The number of grating periods, P , is 110 and the perturbation period, Λ , is 311 nm, such that the drop port peak wavelength, λ_D , is very close to the resonance wavelength, λ_r , which corresponds to the major peak within the drop port spectrum of the cascaded Vernier racetrack resonator. The contra-DC was designed so that the value of the contra-directional power coupling factor, $|\kappa_c|^2$, and the contra-directional power transmission factor, $|t_c|^2$, would be very close to the value of the co-directional power coupling factor, $|\kappa|^2$, and power transmission factor, $|t|^2$, at λ_D when the losses in the couplers are taken into account. In order to suppress Bragg reflections back to the input port, an anti-reflection grating structure has been used, where additional gratings are formed on the external side-walls of the coupler [436] as shown in Figure 5.1(a). These external grating are out of phase with respect to the gratings inside the coupler region, which can significantly suppress back reflections through destructive interference [436].

The schematic of the grating-coupled cascaded Vernier racetrack resonator is shown in Figure 5.1(b), where “a” is the first racetrack, “b” is the second (larger) racetrack, and “tr” is the tapered routing section between the resonators, $Z_{a,b,tr}(\lambda) = \exp(-j\beta_{a,b,tr}(\lambda)L_{a,b,tr} - \alpha_{a,b,tr}L_{a,b,tr})$, $\beta_{a,b,tr}(\lambda) = 2\pi n_{eff_a,b,tr}(\lambda)/\lambda$, $n_{eff_a,b,tr}(\lambda)$ is the appropriate waveguide effective index, L_a and L_b are the total lengths of the racetrack resonators neglecting the lengths of the straight coupling regions, and α_a [m^{-1}] and α_b [m^{-1}] are the total field loss coefficients. L_{tr} and α_{tr} are the length and field loss coefficient of the tapered routing section between the two racetrack resonators. $\kappa_1(\lambda)$ and $\kappa_3(\lambda)$ are the symmetric complex field contra-directional coupling factors of the grating couplers of racetrack resonators “a” and “b”. $t_1(\lambda)$ and $t_3(\lambda)$ are the straight-through racetrack waveguide complex field transmission factors of the grating couplers of racetrack resonators “a” and “b”. $\bar{t}_1(\lambda)$ is the straight-through bus waveguide complex field transmission factor of the grating coupler of racetrack resonator “a”. The propagation constant in the expression for

$\bar{t}_1(\lambda)$ is different from that in the expression for $t_1(\lambda)$ since the bus waveguide and racetrack resonator widths are different. $\kappa_2(\lambda)$ and $\kappa_4(\lambda)$ are the symmetric complex field co-directional coupling factors of the waveguides. $t_2(\lambda)$ and $t_4(\lambda)$ are the straight-through complex field transmission factors of the waveguides.

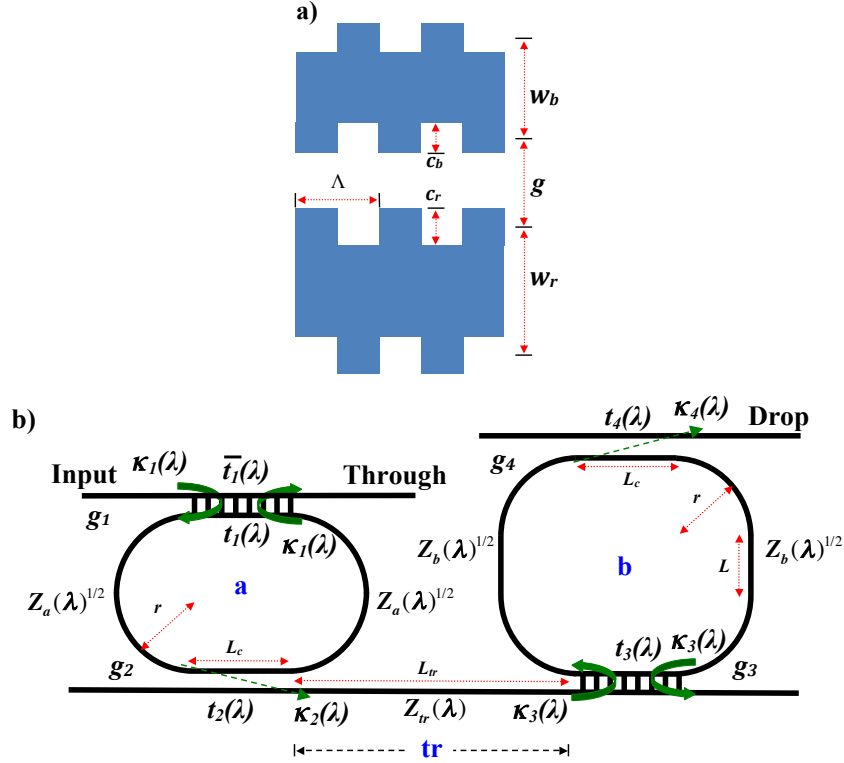


Figure 5.1: (a) Schematic of a section of the contra-DC and (b) schematic of the grating-coupled cascaded Vernier racetrack resonator. ©2013 IEEE, by permission [97].

The drop port and through port intensity responses of the grating-coupled cascaded Vernier racetrack resonator can be determined by multiplying Eq. 5.1 and Eq. 5.2 by their respective complex conjugates,

$$TF_{Drop}(\lambda) = \frac{\kappa_1(\lambda)\kappa_2(\lambda)Z_a(\lambda)^{1/2}}{1 - t_1(\lambda)t_2(\lambda)Z_a(\lambda)} \times Z_{tr}(\lambda) \times \frac{\kappa_3(\lambda)\kappa_4(\lambda)Z_b(\lambda)^{1/2}}{1 - t_3(\lambda)t_4(\lambda)Z_b(\lambda)}, \quad (5.1)$$

$$TF_{Through}(\lambda) = \frac{\kappa_1(\lambda)^2 t_2(\lambda) Z_a(\lambda) + \bar{t}_1(\lambda) (1 - t_1(\lambda) t_2(\lambda) Z_a(\lambda))}{1 - t_1(\lambda) t_2(\lambda) Z_a(\lambda)} \quad (5.2)$$

where,

$$\kappa_1(\lambda) = \kappa_3(\lambda) = \kappa_c(\lambda), \quad (5.3)$$

$$t_1(\lambda) = t_3(\lambda) = t_c(\lambda) e^{-j\beta_{a,b}(\lambda)L_c - \alpha_{a,b}L_c}, \quad (5.4)$$

$$\bar{t}_1(\lambda) = t_c(\lambda) e^{-j\bar{\beta}_a(\lambda)L_c - \bar{\alpha}_a L_c}, \quad (5.5)$$

$$\kappa_2(\lambda) = \kappa_4(\lambda) = -j \sin\left(\frac{\pi L_c}{2L_\pi(\lambda)}\right) e^{-j\beta_{a,b}(\lambda)L_c - \alpha_{a,b}L_c}, \quad (5.6)$$

$$t_2(\lambda) = t_4(\lambda) = \cos\left(\frac{\pi L_c}{2L_\pi(\lambda)}\right) e^{-j\beta_{a,b}(\lambda)L_c - \alpha_{a,b}L_c}. \quad (5.7)$$

The following design was chosen for all simulations: $L_a = 2\pi r$ (total length of the racetrack resonator not including the straight sections of the directional couplers), where $r = 4.65 \mu\text{m}$, and $L_c = \Lambda \times P$ where Λ and P are 311 nm and 110, respectively, $L_b = 2\pi r + 2L$, where $L = 16.27 \mu\text{m}$, β_a and β_b are for waveguide widths of 550 nm, $\bar{\beta}_a$ is for a waveguide width of 450 nm, and $L_\pi(\lambda)$ is the cross-over length. It should be noted that the ratio of the total length of resonator “b” to the total length of resonator “a” was chosen to be 4/3. Also, we assume that the propagation constants for the two racetrack resonators are identical (*i.e.*, the effective index is the same for all regions of each racetrack). The propagation loss seen from the input port to the through port, $\bar{\alpha}_a$ [m^{-1}], is 7.4 dB/cm [506], since the waveguide width is 450 nm. Also, the propagation loss for each ring is assumed to be 2 dB/cm, since their waveguide widths are 550 nm. We assume the optical attenuation due to the routing section between the two racetrack resonators is minimal and therefore the routing section is not included in our calculations. Finally, it is assumed that, since the waveguides within the coupling regions with gratings have different propagation constants, the co-directional coupling is minimal and is neglected in the model. In other words, only contra-directional coupling is considered within the regions with gratings.

To determine the complex field contra-directional coupling factors and the

straight-through complex field transmission factors of the gratings, the modelling method presented by Shi *et al.* was used [439, 461]. Here, we have chosen the coupling coefficient to be 12551 m^{-1} so that the contra-directional power coupling and power transmission factors are close to the values of the co-directional power coupling and power transmission factors at λ_D , as shown in Figure 5.2. To determine the symmetric complex field co-directional coupling and transmission factors, $L_\pi(\lambda)$ was determined using a numerical mode solver. The effective indices of the co-directional couplers and the waveguides were calculated at 11 wavelengths between 1500 nm and 1600 nm and curve-fitted to third-order polynomials from which all effective indices were obtained. Figures 5.2(a) and 5.2(b) show the wavelength dependent contra-directional and co-directional power coupling factors and the straight-through power transmission factors for the coupler with and without gratings.

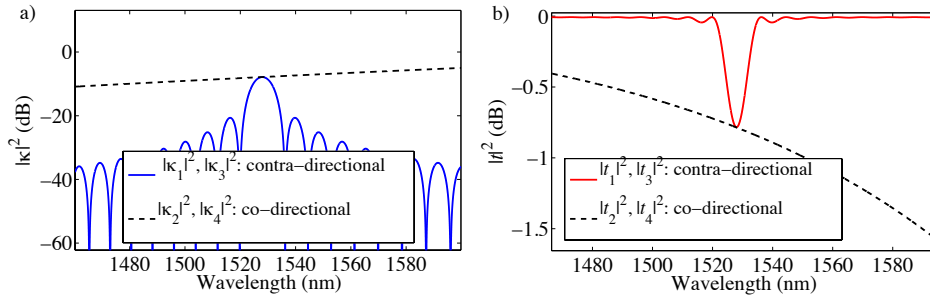


Figure 5.2: (a) $|\kappa|^2$ versus wavelength for the contra-directional (blue-solid) and co-directional (black-dash) couplers. (b) $|t|^2$ versus wavelength for the contra-directional (red-solid) and co-directional (black-dash) couplers. ©2013 IEEE, by permission [97].

Figure 5.3(a) shows the drop port responses for two independent single contra-directional grating-coupled racetrack resonators with lengths L_a (green-solid) and L_b (red-dash). The limited suppression of the peaks to the left and to the right of the major peaks for the single racetrack resonators are due to the bandwidth of the contra-DCs. Figure 5.3(b) shows the drop port responses for the cascaded configuration of these two racetrack resonators with (blue-solid) and without (black-dash) gratings. In the case where there are no gratings, we change the structure shown in Figure 5.1(b) such that the input port and the through port are exchanged with

each other as well as the drop port being placed at the spare output port. We can clearly see that the grating-coupled cascaded Vernier racetrack resonator spectrum shows increased suppression of all minor peaks as compared to the spectra of the other three devices. However, we also need to compare the response of the grating-coupled cascaded Vernier racetrack resonator to that of a grating-coupled cascaded identical racetrack resonator with lengths L_a as well as L_b . Figure 5.3(c) shows the drop port responses for grating-coupled cascaded Vernier (blue-solid) racetrack resonators as well as the response for identical (orange-dash) racetrack resonators with lengths L_a . Figure 5.3(d) shows the drop port responses for grating-coupled cascaded Vernier (blue-solid) racetrack resonators as well as the response for identical (light blue-dash) racetrack resonators with lengths L_b . In both cases, the Vernier effect causes an increase in suppression of all minor peaks as compared to the cases where identical racetrack resonators were used. The drop port spectrum and phase in the vicinity of the clear window of our grating-coupled cascaded Vernier racetrack resonator are shown in Figure 5.4(a). The group delay and the dispersion of our grating-coupled cascaded Vernier racetrack resonator are shown in Figure 5.4(b). Next, we compare the through port response for cascaded Vernier racetrack resonators with and without gratings, as shown in Figures 5.5(a) and 5.5(b). We can clearly see that using gratings is beneficial, since it significantly suppresses all but one of the resonances. The through port response for the grating-coupled cascaded identical racetrack resonator has the same response as that of a single contra-directional grating-coupled racetrack resonator when its dimensions are the same as one of the racetrack resonators in the cascaded configuration. In Figures 5.5(c) and 5.5(d), the through port responses for grating-coupled cascaded (single) identical racetrack resonator with lengths L_a as well as L_b are shown. It can be clearly seen that the response for the device with lengths L_a has more suppression of its minor notches as compared to the device with lengths L_b .

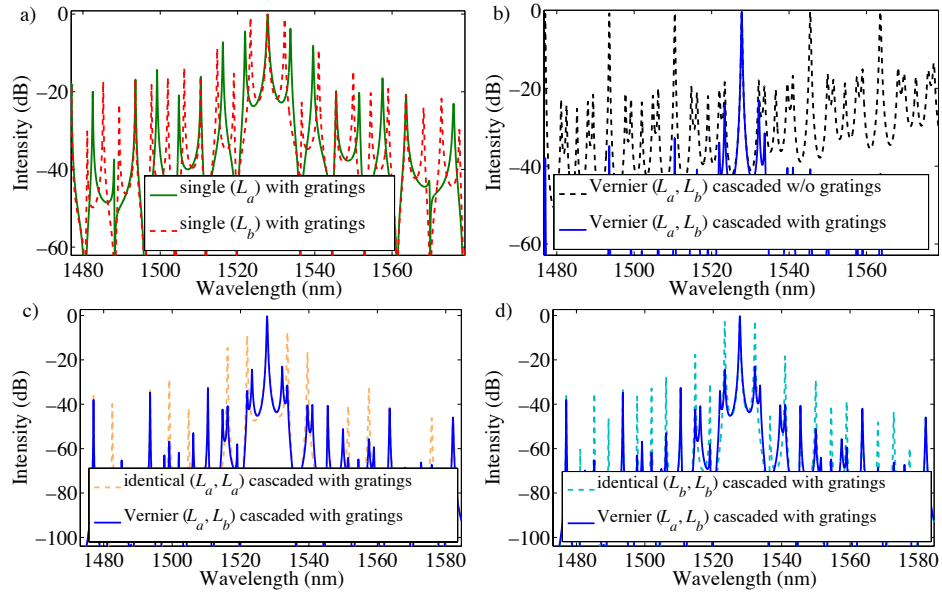


Figure 5.3: (a) Drop port spectral response comparison between single grating-coupled racetrack resonator with length L_a (green-solid) and L_b (red-dash), (b) coupled racetrack resonators with (blue-solid) and without (black-dash) contra-DCs, (c) drop port spectral response comparison between grating-coupled cascaded identical racetrack resonator with lengths L_a and grating-coupled cascaded Vernier racetrack resonator, and (d) drop port spectral response comparison between grating-coupled cascaded identical racetrack resonator with lengths L_b and grating-coupled cascaded Vernier racetrack resonator. ©2013 IEEE, by permission [97].

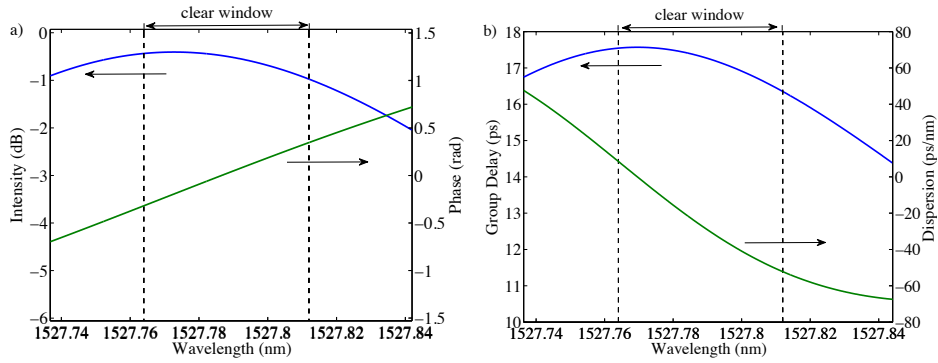


Figure 5.4: (a) Drop port spectral response and phase and (b) group delay and dispersion of our grating-coupled cascaded Vernier racetrack resonator. ©2013 IEEE, by permission [97].

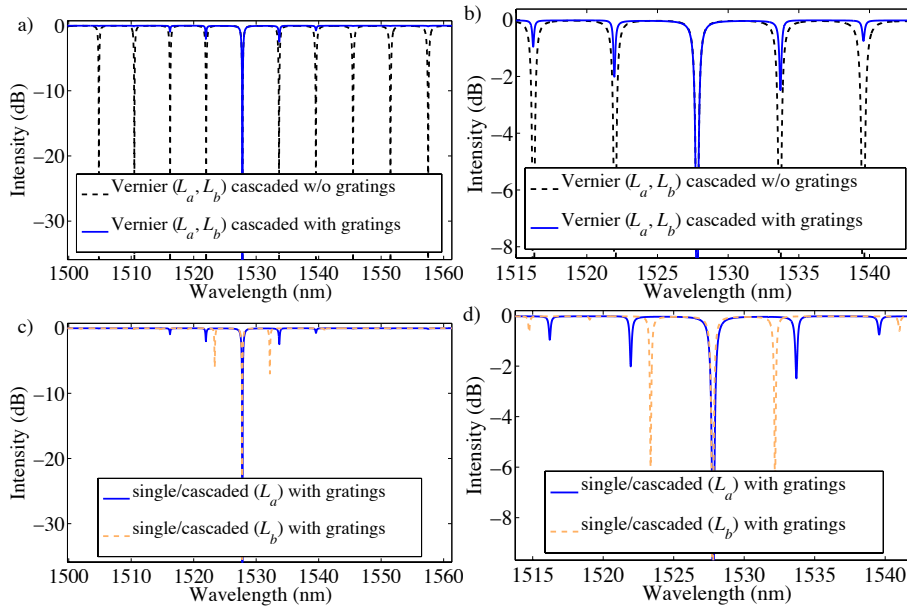


Figure 5.5: (a) Through port spectral response comparison between grating-coupled cascaded racetrack resonator (blue-solid) and cascaded racetrack resonator without gratings (black-dash), (b) a “zoom-in” of the major notch in Figure 5.5(a), (c) through port spectral response comparison between grating-coupled single (response same as cascaded configuration) racetrack resonator with lengths L_a and L_b , and (d) a “zoom-in” of the major notch in Figure 5.5(c). ©2013 IEEE, by permission [97].

All specifications are defined for a channel spacing of 0.8 nm, a clear window of 0.048 nm, and within the clear window of the desired channel as well as the clear windows of the 44 channels to the left and to the right of the desired channel (the number of channels within the ITU grid for the C-band is 45 [92]). Here, the clear window is centred at a wavelength value corresponding to the average wavelength value of the major peak between its -3 dB points and -20 dB points (referenced at the maximum intensity of the major peak) and of the major notch between its -3 dB points and -20 dB points (referenced at the maximum intensity of the major notch).

Tables 5.1 and 5.2 show the spectral characteristics of the single grating-coupled racetrack resonators with lengths L_a and L_b , the cascaded Vernier racetrack resonator with and without contra-directional gratings, and of the grating-coupled cascaded identical racetrack resonators. We can clearly see that the cascaded Vernier racetrack resonator with gratings shows a significant improvement in its FSR (in fact, there is no FSR), nA_i , IPS, IL_{thru} , and $IL_{\text{thru-m}}$ as compared to the response of the cascaded racetrack resonator without gratings. In the case of the cascaded configuration without gratings, the drop port shows an extended FSR of 17.30 nm and 17.70 nm to the left and right of the major peak, respectively, whereas the through port response only shows an FSR of 5.81 nm and 5.85 nm. However, the inclusion of the contra-directional gratings removes the FSR in both the drop port and the through port. Also, the grating-coupled cascaded Vernier racetrack resonator shows significant improvements in its A_i , nA_i , and IPS as compared to both of the single contra-directional grating-coupled racetrack resonator responses. Also, the grating-coupled cascaded Vernier racetrack resonator shows an improvement in the nA_i and IPS as compared to the responses of grating-coupled cascaded identical racetrack resonators. Thus, we can see the combined benefit of using contra-DCs and the Vernier effect within coupled racetrack resonators.

Table 5.1: Drop port and through port insertion loss for single racetrack resonators with gratings, cascaded Vernier racetrack resonators with and without gratings, and grating-coupled cascaded identical racetrack resonators. ©2013 IEEE, by permission [97].

Parameter	single (L_a) with gratings	single (L_b) with gratings	cascaded Vernier w/o gratings	cascaded iden- tical (L_a) with gratings	cascaded iden- tical (L_b) with gratings	cascaded Vernier with gratings
IL_{drop} (dB)	0.3	0.5	1.0	0.4	0.6	1.0
IL_{thru} (dB)	0.3	0.3	8.8	0.3	0.2	0.3
$IL_{\text{thru-m}}$ (dB)	2.5	7.0	40.9	2.5	7.0	2.5

Table 5.2: Spectral characteristics for single racetrack resonators with gratings, cascaded Vernier racetrack resonators with and without gratings, and grating-coupled cascaded identical racetrack resonators. ©2013 IEEE, by permission [97].

Parameter	single (L_a) with gratings	single (L_b) with gratings	cascaded Vernier w/o gratings	cascaded iden- tical (L_a) with gratings	cascaded iden- tical (L_b) with gratings	cascaded Vernier with gratings
FSR (nm)	N/A	N/A	5.81, 5.85	N/A	N/A	N/A
A_i (dB)	12.9	15.1	27.8	26.0	30.3	27.9
nA_i (dB)	11.3	12.5	0.1	23.6	25.8	33.9
IPS (dB)	3.4	0.6	N/A ^a	7.1	1.6	22.1
R_{depth} (dB)	0.2	0.3	0.6	0.2	0.3	0.6
EC_i (dB)	12.8	11.1	13.7	16.5	14.4	13.8

^aThere is no IPS since the wavelength range of the 44 channels to the left and right of the desired channel is larger than the filter's extended FSR.

5.2 Experimental Results

The device was fabricated using e-beam lithography [493] at the University of Washington and aluminum (300 nm thick) metallization for the heaters (5 μm wide) and electrodes was done at McMaster University. Figure 5.6 shows a microscope image of our device. Heaters were placed on each contra-directional coupling region to enable resonance tuning to correct for fabrication variations. The top oxide is 2 μm thick, the co-directional and contra-directional gap distances are 280 nm and 220 nm, w_b and w_r are 450 nm and 550 nm, the corrugation depths, c_b and c_r , for waveguides with widths of w_b and w_r are 30 nm and 40 nm, respectively. The tapered routing waveguide between the two racetrack resonators has a length of 74.912 μm .

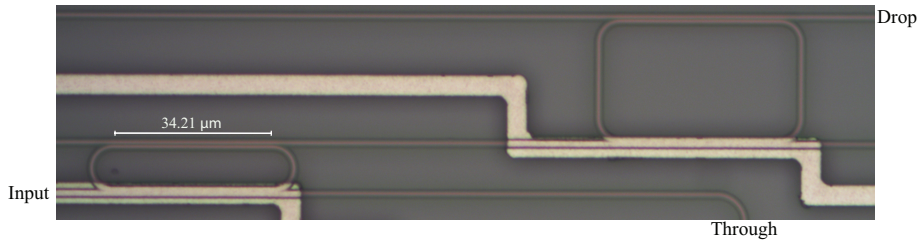


Figure 5.6: Optical microscope image of the fabricated device. ©2013 IEEE, by permission [97].

Figure 5.7(a) shows the experimental drop port and through port responses for applied voltages of 0 V, 4 V, 5.8 V, and 7 V to the contra-directional coupling region of racetrack resonator “a”. We can clearly see that applying a voltage of 5.8 V significantly improves the major peak of the drop port response; the maximum drop port peak intensity increases from -17.9 dB to -6.2 dB. Figure 5.7(b) shows the through port and drop port responses for this case. The drop port response has one major peak and all other peaks are suppressed and the through port response shows one major notch and all other notches have smaller notch depths (less than 2 dB) as compared to the depth of the major notch (5.9 dB). Thus we have experimentally confirmed that it is possible to eliminate the FSR in the drop port and through port. Next, we determine the A_i , nA_i , IPS , R_{depth} , and EC_i for a clear window of 0.048 nm centred at a wavelength of 1528.846 nm and a channel spacing of 0.8

nm. It should be noted that the minimum wavelength we measured the spectrum for is 1500 nm so only 36 channels to the left and 44 channels to the right of the desired channel were used in calculating the nA_i . Figure 5.7(c) shows a “zoom-in” of Figure 5.7(b) which includes vertical dashed lines that represent the clear window and channel spacing as well as labels for A_i , nA_i , IPS, and EC_i . Table 5.3 shows the experimental spectral characteristics of the grating-coupled cascaded Vernier racetrack resonator. The response of our device has no FSR in both the drop port and through port, which is in agreement with the theoretical result shown in Table 5.2 (we were unable to accurately determine the values for IL_{drop} , IL_{thru} , and $IL_{\text{thru-m}}$). Also, the device has a large IPS of 24.3 dB. Our grating-coupled cascaded Vernier racetrack resonator needs further improvement to give a value of the EC_i that is greater than or equal to 10 dB [99], of the R_{depth} that is less than or equal to 0.5 dB [99], of the nA_i that is greater than or equal to 35 dB [101], and of the IPS that is greater than or equal to 35 dB [101], so that this type of device can be used in typical DWDM applications. It should be noted that our device has an A_i of 30.5 dB (which is better than the 25 dB that can be found in data sheets for some commercial products [99]).

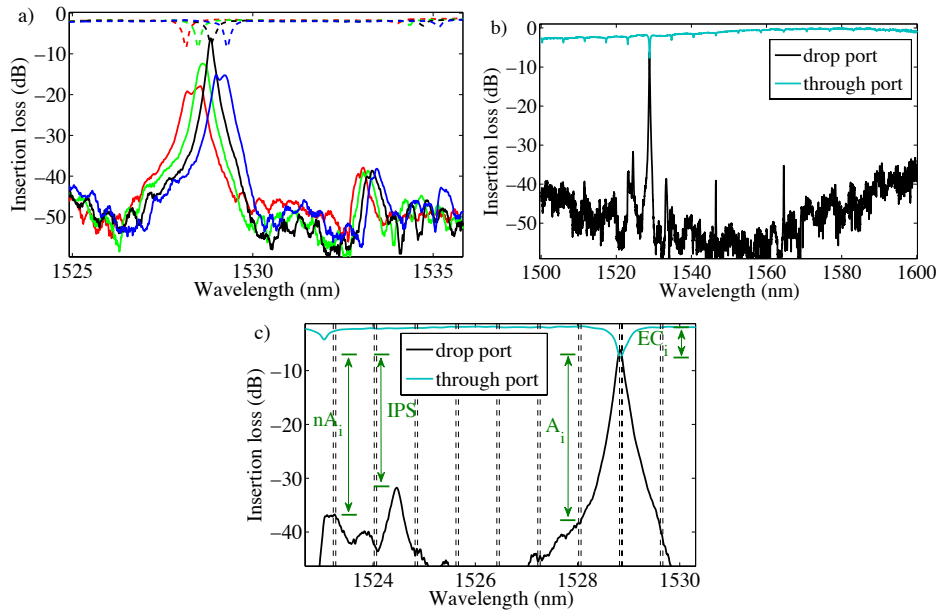


Figure 5.7: (a) Experimental drop port (solid) and through port (dashed) responses when the voltage to the heater for racetrack resonator “a” is 0 V (red), 4V (green), 5.8 V (black), and 7 V (blue). (b) the experimental drop port (black) and through port (light blue) spectra when a voltage of 5.8 V is applied to the heater of racetrack resonator “a”. (c) a zoom-in of Figure 5.7(b) with a 0.048 nm clear window and 0.8 nm channel spacing indicated by the dashed vertical lines. ©2013 IEEE, by permission [97].

Table 5.3: Experimental results of grating-coupled cascaded Vernier racetrack resonator. ©2013 IEEE, by permission [97].

Parameter	Measured value
FSR (nm)	N/A
A_i (dB)	30.5
nA_i (dB)	29.3
IPS (dB)	24.3
R_{depth} (dB)	1.2
EC_i (dB)	5.2

In summary, we have shown that using contra-DCs in cascaded racetrack resonators exhibiting the Vernier effect provides numerous advantages as compared to the responses of cascaded racetrack resonators exhibiting the Vernier effect without contra-DCs. The grating-coupled cascaded Vernier racetrack resonator studied here has a theoretical IPS of 22.1 dB whereas without the gratings there is no IPS since the wavelength range of the 44 channels to the left and right of the desired channel is larger than the filter's extended FSR. Also, the grating-coupled cascaded Vernier racetrack resonator has a theoretical $IL_{\text{thru-m}}$ of 2.5 dB whereas without the gratings $IL_{\text{thru-m}}$ is 40.9 dB. The reason why the $IL_{\text{thru-m}}$ is substantially improved is due to the suppression of all but one of the resonances in the through port, which is the result of the small bandwidth of the contra-DC. Also, there is no FSR in both the drop port and through port for the grating-coupled cascaded Vernier racetrack resonator whereas there is a 17.3 nm/17.7 nm extended FSR at the drop port and an FSR of 5.8 nm at the through port for the case without gratings. Also, we have presented experimental results which show that it is in fact possible to eliminate the FSR in the drop port as well as the through port. Our fabricated device also shows a large IPS of 24.3 dB. Thus, we are now able to use the cascaded configuration of the Vernier effect and not be limited to applications that only require a large FSR in the drop port.

The coupling coefficients of the contra-DCs are very important design param-

eters since they will have a major impact on the performance of the filter. Thus, it is essential that the contra-DC-based filter designs are based on accurate modelling which takes into account the impact of the fabrication process. In the next chapter, I will present a process calibration method that can be used to extract the coupling coefficients from fabricated contra-DCs, which can then be fed back into future designs.

Chapter 6

Process Calibration Method for Designing Silicon-On-Insulator Contra-Directional Grating Couplers

¹In communication applications that involve multiplexing and/or demultiplexing optical signals, maximizing the number of usable channels is essential for creating high data-rate interconnects [106, 111, 129]. Silicon contra-DCs are particularly useful in optical filtering applications because they do not have periodic spectral responses like ring resonator-based filters [97, 436, 439, 460–462, 466]. Silicon contra-DCs have been experimentally demonstrated in numerous publications [97, 434, 436–439, 459–468]. Although previous demonstrations of silicon contra-DCs have shown good results, it remains challenging to design a contra-DC’s bandwidth and have the “as-fabricated” device’s bandwidth, maximum power coupling factor, and minimum power transmission factor correspond to the design values, in the presence of lithography smoothing [470, 507]. Using a calibration procedure for the design process, a filter designer would be able to design a contra-DC such that the “as-designed” spectra closely matches the as-fabricated spectra.

¹A version of Chapter 6 has been published in [435].

In this chapter, we present a process calibration method which can be used to determine the absolute value of the coupling coefficient, $|\kappa|$, of a fabricated contra-DC by measuring its full-width-at-half-maximum (FWHM) bandwidth, $\Delta\lambda_{bw}$. Once $|\kappa|$ is known, the through port and drop port spectra can be simulated. We demonstrate the effectiveness of our FWHM method (similar to [457, 508]) by extracting the $|\kappa|$ s of contra-DCs that were fabricated using electron beam lithography [493] on three fabrication runs. Our FWHM method for extracting $|\kappa|$ provides more consistent results as compared to using the null bandwidth (see [470, 507, 509–511]) due to the fact that $\Delta\lambda_{bw}$ can be more easily determined. Also, as compared to using the null method, the $|\kappa|$ s extracted using our FWHM method are in general agreement with the values extracted by curve-fitting the drop port spectra. We then show that, using our FWHM method to extract $|\kappa|$, the simulated spectra agree well with the experimental spectra. Also, the simulated through port group delay and dispersion responses of a particular device are calculated using the extracted $|\kappa|$, which agree well with the Hilbert transform-determined and the measured group delay and dispersion responses. Using the process calibration method, we then design a 3-port grating-assisted Vernier filter that meets 3-port filter commercial specifications for a clear window of 13 GHz and a channel spacing of 200 GHz.

6.1 Contra-DC Theory and Process Calibration Method

First, we will discuss the theoretical aspects of contra-DCs and the contra-DC design we used in this chapter. The contra-DC design [Figures 6.1(a) and 6.1(b)] has two strip waveguides, waveguide “a” and waveguide “b,” which have different average waveguide widths, w_a and w_b , respectively [97]. The waveguides have the same height and are separated from each other by an average gap distance, g [97]. Each waveguide has periodic grating corrugations, with a grating period, Λ , defined in Figure 6.1(b), on the sidewalls located within the gap region [97]. The corrugation widths are labelled c_a and c_b for waveguide “a” and waveguide “b,” respectively [97]. The corrugations allow the coupler to act as a Bragg reflector with the strength of the inter-waveguide coupling determined by the inter-waveguide coupling coefficient, κ [97, 434, 436]. We have also included anti-reflection gratings on the external sidewalls of the waveguides to suppress the intra-waveguide Bragg reflections [97, 434, 436, 512].

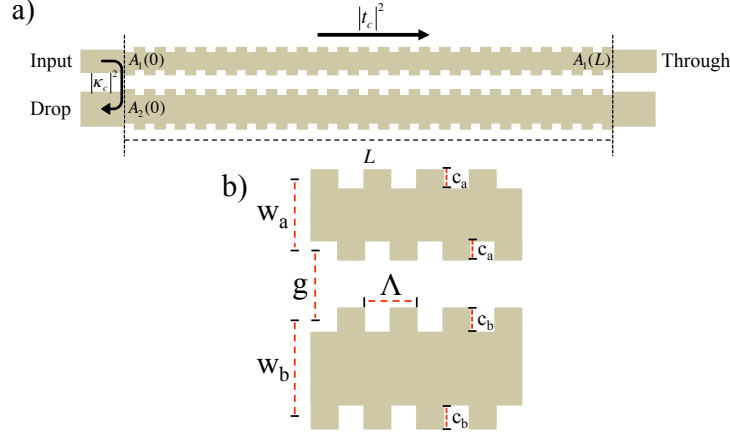


Figure 6.1: (a) Diagram of a contra-DC. (b) A close-up view of a portion of a contra-DC (figure was adapted from [97]). ©Optical Society of America, 2015, by permission [435].

The power transferred from the input port to the drop port of a contra-DC is given by the power coupling factor, $|\kappa_c|^2$, and the amount of power transferred to the through port is given by the power transmission factor, $|t_c|^2$, which can be calculated using the following equations,

$$|\kappa_c|^2 = \left| \frac{A_2(0)}{A_1(0)} \right|^2 = \frac{|\kappa|^2 \sinh^2(sL)}{s^2 \cosh^2(sL) + \left(\frac{\Delta\beta}{2}\right)^2 \sinh^2(sL)} \quad (6.1)$$

$$|t_c|^2 = \left| \frac{A_1(L)}{A_1(0)} \right|^2 = \frac{s^2}{s^2 \cosh^2(sL) + \left(\frac{\Delta\beta}{2}\right)^2 \sinh^2(sL)} \quad (6.2)$$

where $s^2 = |\kappa|^2 - \left(\frac{\Delta\beta}{2}\right)^2$, $\Delta\beta = \beta_a + \beta_b - m\frac{2\pi}{\Lambda}$, β_a and β_b are the propagation constants of waveguide “a” and waveguide “b” without corrugations with widths equal to w_a and w_b , respectively, L is the length of the coupler, and m is the grating order which equals 1 since we are using first-order gratings [513]. Equation 6.1 is the same as Eq. 13.5-19 in [513] and Eq. 1 in [461] and Eq. 6.2 can be determined from Eq. 13.5-16 in [513]. In this chapter, β_a and β_b are calculated by numerically determining the wavelength dependent effective indices of the waveguides using MODE Solutions by Lumerical Solutions, Inc., and curve-fitting them to third-order poly-

nomials [97]. The material model that was used for silicon included dispersion and was lossless [97, 111, 149, 470] and the refractive index for silicon dioxide was fixed at 1.4435 [97, 111, 149]. The inter-waveguide coupling coefficient, κ , is defined as the strength of the coupling of light from waveguide “a” to waveguide “b” within the contra-DC and traditionally has been calculated using the following equation [434, 459, 461, 465, 467, 512, 513],

$$\kappa = \frac{\omega}{4} \iint \xi_a^*(x,y) \cdot \epsilon_m(x,y) \xi_b(x,y) dx dy \quad (6.3)$$

where ω is the angular frequency, $\xi_a(x,y)$ is the transverse mode of waveguide “a,” $\xi_b(x,y)$ is the transverse mode of waveguide “b,” and $\epsilon_m(x,y)$ is the m^{th} component of the Fourier series expansion of the dielectric perturbation. However, this expression is appropriate for the weakly-guiding approximation and is not necessarily accurate for high-contrast nanophotonic waveguides. Using this equation, two different methods have been used to calculate $|\kappa|$ [434, 512]. The first method involves treating each waveguide as isolated [434, 461, 512–515]. In this method, $\xi_a(x,y)$ and $\xi_b(x,y)$, correspond to the modes of the isolated unperturbed waveguides [434, 461, 512–515]. The second method involves calculating the first and second-order transverse modes of the coupler (*i.e.*, supermode theory) [434, 465–467, 512, 514]. [507] and [470] have demonstrated that there is a large difference between the modelled results and experimental results for SOI Bragg gratings (see Figure 2.35 in [507] and Figure 4.43 in [470]). [461] showed good agreement between experimental results and simulated results for contra-DCs by using Eq. 6.3. However, cross-sectional SEM images were needed for calibration. Recently, [511] demonstrated a method to model Bragg gratings using 3-D FDTD simulations and Bloch boundary conditions which showed good agreement between theoretical and experimental results. However, the above-mentioned methods require knowledge of the effects of the lithography on the shape of the grating. One method to significantly reduce the difference between the modelled results and the experimental results is to take into account how the fabrication process affects the design of the device (*e.g.*, lithography smoothing) by using lithography simulation software, such as Mentor Graphics Calibre, and then simulating the structure using 3-D FDTD simulation software, such as FDTD Solutions by Lumerical Solutions, Inc.,

[470, 507]. However, this process is more complex since knowledge of fabrication process parameters are needed. In this chapter, we will demonstrate an experimental method to determine $|\kappa|$ by using $\Delta\lambda_{bw}$. With our experimental method, we can extract $|\kappa|$ without having to measure the effects of lithography directly, nor without resorting to the approximations in Equation 6.3.

There are three steps to extract $|\kappa|$. The first step is to determine $\Delta\lambda_{bw}$, which can be measured directly from the drop port spectrum. The second step is to determine the average propagation constant mismatch, $\delta\beta_{avg}$. To obtain $\delta\beta_{avg}$, we use the propagation constant differences, $\delta\beta_H$ and $\delta\beta_L$, where $\delta\beta_H$ is measured from the frequency that corresponds to the centre of the main lobe to the high-frequency half-maximum point and $\delta\beta_L$ is measured from the frequency that corresponds to the centre of the main lobe to the low-frequency half-maximum point (for a complete mathematical description see Appendix C). The magnitude of $\delta\beta_H$ and the magnitude of $\delta\beta_L$ are given in Eqs. 6.4 and 6.5, respectively, and defined graphically in Figure 6.2(a),

$$|\delta\beta_H| = \left(\frac{2\pi\Delta f_H}{c} \right) (n_{g,a}(f_0) + n_{g,b}(f_0)) = \left(\frac{2\pi\Delta\lambda_L}{\lambda_L\lambda_0} \right) (n_{g,a}(\lambda_0) + n_{g,b}(\lambda_0)) \quad (6.4)$$

$$|\delta\beta_L| = \left(\frac{2\pi\Delta f_L}{c} \right) (n_{g,a}(f_0) + n_{g,b}(f_0)) = \left(\frac{2\pi\Delta\lambda_H}{\lambda_H\lambda_0} \right) (n_{g,a}(\lambda_0) + n_{g,b}(\lambda_0)) \quad (6.5)$$

where $\Delta f_H = f_H - f_0$, $\Delta f_L = f_0 - f_L$, $\Delta\lambda_L = \lambda_0 - \lambda_L$, $\Delta\lambda_H = \lambda_H - \lambda_0$, f_0 and λ_0 are the frequency and wavelength corresponding to the centre frequency and centre wavelength (middle point between the FWHM points), respectively, f_H and λ_L correspond to the higher frequency FWHM point and the lower wavelength FWHM point, respectively, f_L and λ_H correspond to the lower frequency FWHM point and the higher wavelength FWHM point, respectively, $n_{g,a}$ and $n_{g,b}$ are the group indices of waveguide “a” and waveguide “b,” respectively, and c is the speed of light in a vacuum. Equations 6.4 and 6.5 are similar to Eq. 13.5-22 in [513] but here we include the effects of dispersion and use the group indices, since dispersion

affects the spectral response of contra-DCs (see [516]). To determine $\delta\beta_{avg}$, we take the average of Eqs. 6.4 and 6.5,

$$\delta\beta_{avg} = \frac{|\delta\beta_H| + |\delta\beta_L|}{2} = \frac{\pi\Delta\lambda_{bw}}{\lambda_L\lambda_H} (n_{g,a}(\lambda_0) + n_{g,b}(\lambda_0)) \quad (6.6)$$

where $\Delta\lambda_{bw} = \lambda_H - \lambda_L$. Here, for convenience, the wavelength dependent group indices are numerically determined using MODE Solutions by Lumerical Solutions, Inc., and curve-fitted to third-order polynomials. Equation 6.6 is similar to Eq. 31 in [508] but here we include the effects of dispersion and use the group indices. Figure 6.2(b) shows the experimental drop port spectrum of one of our fabricated contra-DCs, with a gap distance of 140 nm, as a function of $\Delta\beta$. The FWHM becomes $2\delta\beta_{avg}$ when the spectrum is plotted as a function of $\Delta\beta$. By plotting our spectral response as a function of $\Delta\beta$, we are able to directly measure $\delta\beta_{avg}$ from the spectral response without having to use Eq. 6.6. One may use either of these methods to determine $\delta\beta_{avg}$ but we will focus on the method that utilizes Eq. 6.6.

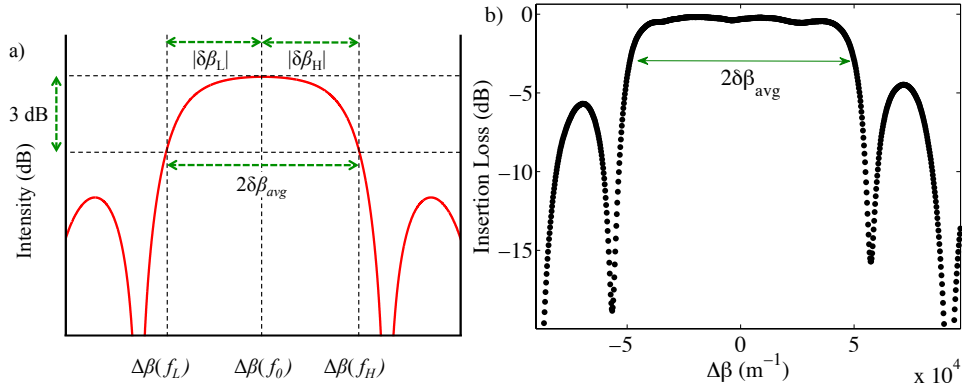


Figure 6.2: (a) Diagram depicting some of the relevant contra-DC parameters as functions of $\Delta\beta$. (b) Experimental drop port spectrum of one of our devices as a function of $\Delta\beta$. ©Optical Society of America, 2015, by permission [435].

The third step is to extract $|\kappa|$ by using Eq. 6.1 and Eq. 6.6. We replace $\Delta\beta$ in Eq. 6.1 with Eq. 6.6 as shown in the left-hand side of Eq. 6.7 where $s^2 = |\kappa|^2 - (\delta\beta_{avg}/2)^2$. Since Eq. 6.1 reduces to $\tanh^2(|\kappa|L)$ for $\Delta\beta = 0$ [513], we can find the FWHM intensity by dividing $\tanh^2(|\kappa|L)$ by 2 and finding the value of $|\kappa|$ that will

satisfy Eq. 6.7 for our value of $\delta\beta_{avg}$. [457, 508] use a similar method to extract the bandwidths of contra-DCs.

$$\frac{|\kappa|^2 \sinh^2(sL)}{s^2 \cosh^2(sL) + \left(\frac{\delta\beta_{avg}}{2}\right)^2 \sinh^2(sL)} = \frac{1}{2} \tanh^2(|\kappa|L) \quad (6.7)$$

It should be noted that there can be multiple solutions to Eq. 6.7 when the sidebands are greater than or equal to the half maximum intensity. The correct solution is the value of $|\kappa|$ that is largest.

An alternative method, using the nulls to determine $|\kappa|$, is to measure the bandwidth at the first nulls to the left and to the right of the main lobe and to use Eq. 6.8 (similar to [470, 507, 509, 517] and is a re-arrangement of the equation found in [510, 513]),

$$|\kappa| = \left[\frac{\delta\beta_{avg}^2}{4} - \frac{\pi^2}{L^2} \right]^{\frac{1}{2}}, \quad (6.8)$$

where $\delta\beta_{avg}$ is calculated using Eq. 6.6 but using the first null points instead of the FWHM points. [470, 511] have also used the null bandwidth to extract $|\kappa|$ but for SOI Bragg gratings. Also, another method to extract $|\kappa|$ is to curve-fit the drop port spectrum of the contra-DC using a nonlinear least-squares method. As we will show in the next section, the extracted $|\kappa|$ s from the curve-fit method and from the FWHM method are in general agreement with each other as compared to the values determined using the null method. However, the curve-fit method relies on an accurate normalization of the measured drop port spectrum (an issue which others have previously mentioned [518]) whereas the FWHM method does not require that the measured data be normalized. Both the FWHM method and the curve-fit method provide more consistent results than the null method does. Also, provided that $\delta\beta_{avg}$ can be accurately obtained, our FWHM method should be applicable to devices fabricated in other material platforms because the method is not platform dependent.

6.2 Experimental Results

Electron beam lithography was used to fabricate the SOI contra-DCs [493] and a silicon dioxide cladding layer was deposited on top of the devices. The silicon strip waveguide heights were all chosen to be 220 nm. The width of waveguide “a” was 450 nm and the width of waveguide “b” was 550 nm. The corrugation widths for waveguide “a” and “b” were 30 nm and 40 nm, respectively. These dimensions were taken from [97]. The grating period was chosen to be 312 nm and the number of periods was chosen to be 500. Therefore, the total length of each contra-DC was 156 μm . The gap distances were varied between 120 nm and 400 nm in 20 nm increments for a total of 15 devices. Fibre grating couplers were used for coupling light into and out of the devices [498, 505]. The contra-DCs were fabricated on three separate fabrication runs, “run 1,” “run 2,” and “run 3” at different times. Fully-etched fibre grating couplers [505] were used in “run 1” and “run 3” and shallow-etched fibre grating couplers [498] were used in “run 2.” The experimental drop port spectra of four of the devices from “run 1,” “run 2,” and “run 3” with gap distances equal to 140 nm, 220 nm, 340 nm, and 400 nm are shown in Figures 6.3(a), 6.3(c), and 6.3(e), respectively. The experimental through port spectra of four of the devices from “run 1,” “run 2,” and “run 3” with gap distances equal to 140 nm, 220 nm, 340 nm, and 400 nm are shown in Figures 6.3(b), 6.3(d), and 6.3(f), respectively. The fibre grating coupler response was removed from both the through port and drop port spectral responses by normalizing the spectra to the fibre grating response envelope in the through port spectral response.

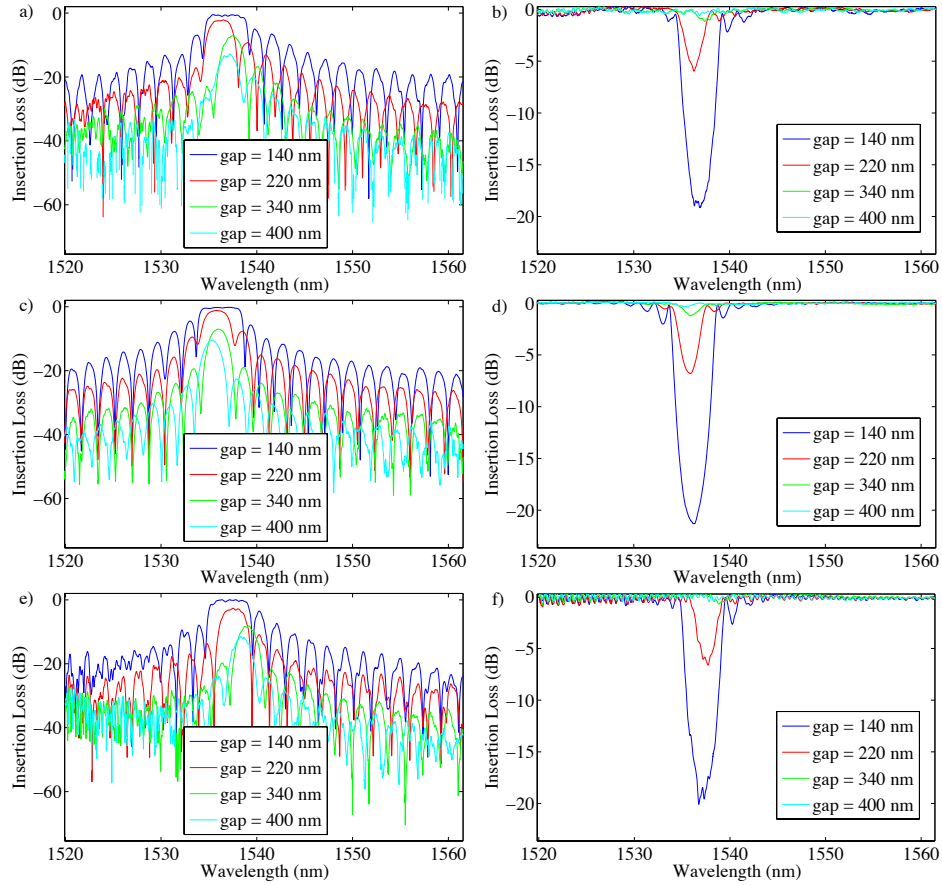


Figure 6.3: Experimental drop port spectra for the devices from (a) “run 1,” (c) “run 2,” and (e) “run 3” with gap distances equal to 140 nm, 220 nm, 340 nm, and 400 nm. Experimental through port spectra for the devices from (b) “run 1,” (d) “run 2,” and (f) “run 3” with gap distances equal to 140 nm, 220 nm, 340 nm, and 400 nm. ©Optical Society of America, 2015, by permission [435].

The relationship between the bandwidths of contra-DCs and their gap distances has been theoretically [459, 461] and experimentally [460, 461] demonstrated, and shows that, as the gap distance increases, the bandwidth decreases. Also, the relationship between $|\kappa|$ and the gap distance has been theoretically demonstrated, and shows that, as the gap distance increases, $|\kappa|$ exponentially decreases [466]. Here, we also experimentally demonstrate the relationship between $\Delta\lambda_{bw}$ and the gap

distance, which is in agreement with previously published results. Also, we experimentally demonstrate the relationship between $|\kappa|$ and the gap distance, which is in agreement with the theoretical results in [466]. Figures 6.4(a) and 6.4(b) show $\Delta\lambda_{bw}$ and the extracted $|\kappa|$ (extracted using our FWHM method) versus gap distance, respectively, for the contra-DCs fabricated on “run 1,” “run 2,” and “run 3.” As the gap distance increases, $\Delta\lambda_{bw}$ and $|\kappa|$ tend to decrease and $\Delta\lambda_{bw}$ reaches a minimum and for one of our devices, the device from “run 3” with a gap distance of 400 nm, we are not able to obtain a value for $|\kappa|$ since it goes to zero. We also fabricated contra-DCs on “run 1” with a fixed gap distance of 280 nm and varied the corrugation widths of waveguide “a” and waveguide “b.” Figures 6.4(c) and 6.4(d) show $\Delta\lambda_{bw}$ and the extracted $|\kappa|$ versus corrugation width, respectively, for corrugation widths of 30 nm to 150 nm in 20 nm increments for waveguide “a” and corrugation widths of 40 nm to 160 nm in 20 nm increments for waveguide “b.” As the corrugation width increases, $\Delta\lambda_{bw}$ [459, 461, 462] and $|\kappa|$ [466] increase.

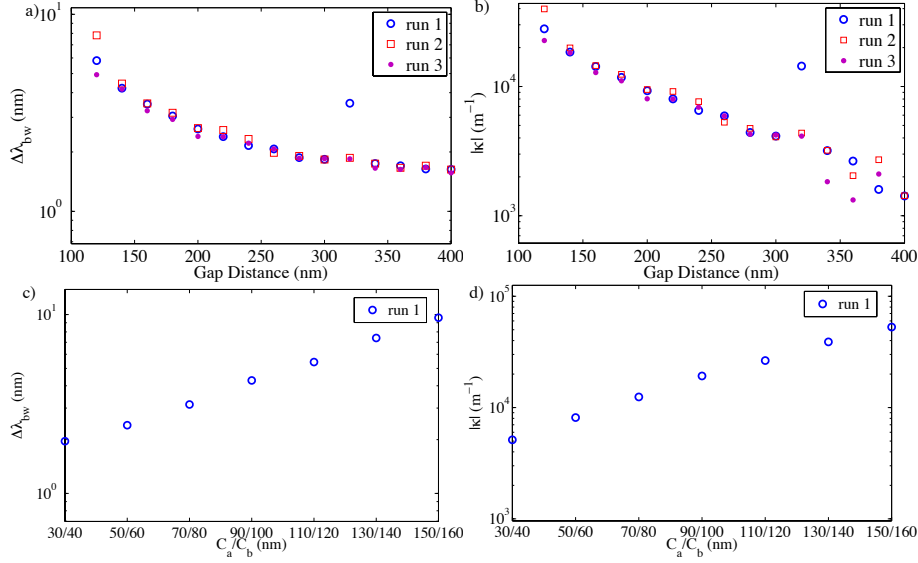


Figure 6.4: (a) Experimental bandwidth at FWHM versus gap distance and (b) extracted coupling coefficient versus gap distance using the FWHM method. (c) Experimental bandwidth at FWHM versus corrugation width and (d) extracted coupling coefficient versus corrugation width for devices from “run 1” with a fixed gap distance of 280 nm using the FWHM method. ©Optical Society of America, 2015, by permission [435].

Next, we provide a comparison between the $|\kappa|$ s extracted using the FWHM method [using Eqs. 6.6 and 6.7], the null method [using Eqs. 6.6 and 6.8], and the curve-fit method (using the *lsqcurvefit* function from MATLAB[®] [519]) from the devices made in three fabrication runs. Figures 6.5(a), 6.5(b), and 6.5(c) show the extracted $|\kappa|$ s using the three methods for “run 1,” “run 2,” and “run 3,” respectively. Upon inspection of Figures 6.5(a)-6.5(c), it is clear that the $|\kappa|$ s that were determined using the FWHM method and the curve-fit method exhibit nearly exponential trends, as expected. The $|\kappa|$ s extracted using the FWHM method and the curve-fit method are relatively close to each other as compared to the $|\kappa|$ s determined using the null method. The discrepancies seen in Figures 6.5(a)-6.5(c) using the null method are due to the difficulty in determining the locations of the nulls [*e.g.*, see Figure 6.5(d)]. Also, we were unable to determine the $|\kappa|$ s for five of the devices using the null method since there are no valid solutions to Eq. 6.8. For one

of the devices using the FWHM method we could only extract a zero solution for $|\kappa|$. With the curve-fit method, we were able to extract a non-zero value for $|\kappa|$ for each of the devices.

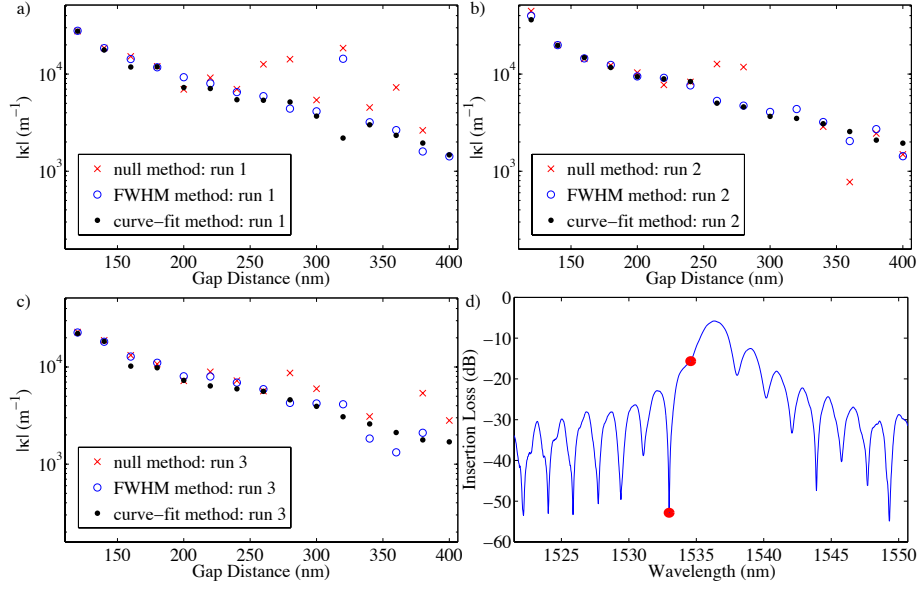


Figure 6.5: Comparison between the FWHM method, the null method, and the curve-fit method to determine $|\kappa|$ for (a) “run 1,” (b) “run 2,” and (c) “run 3.” (d) Drop port spectrum of a contra-DC with a gap distance of 300 nm from “run 2,” which is chosen to illustrate that there can be multiple possible choices for the location of the first null to the left of the main lobe (the red dots indicate possible choices for the null location). ©Optical Society of America, 2015, by permission [435].

Next, we demonstrate, for a given contra-DC with a fixed coupling length, that $\Delta\lambda_{bw}$ reaches a minimum value as $|\kappa|$ approaches zero ([517] also demonstrated this trend in Bragg gratings). To determine the theoretical minimum bandwidth, $\Delta\lambda_{bw-min}$, the following equation can be used (see Appendix D for the derivation),

$$\Delta\lambda_{bw-min} \approx \frac{2.783115\lambda_0^2}{\pi L [n_{g,a}(\lambda_0) + n_{g,b}(\lambda_0)]} \quad (6.9)$$

which is similar to the minimum bandwidth equation in [520] except that their equation is for a distributed Bragg reflector and does not account for dispersion.

Figure 6.6 shows how $\Delta\lambda_{bw-min}$ changes as the coupling length increases (the group indices were evaluated at 1535.33 nm). $\Delta\lambda_{bw-min}$ can be reduced by increasing the coupling length [520]. The device from “run 3” with a gap distance of 400 nm has a measured bandwidth below $\Delta\lambda_{bw-min}$ (due to the experimental results having ripples likely caused by the grating couplers), which could be the reason that there is no $|\kappa|$ solution other than zero for this device using the FWHM method.

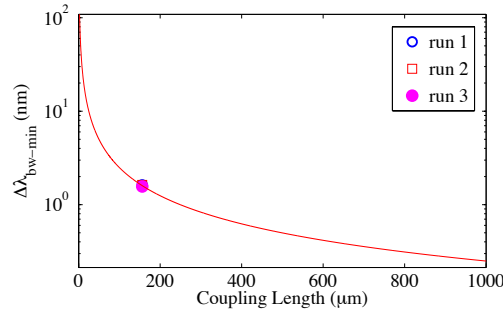


Figure 6.6: Theoretical predicted minimum bandwidth at FWHM versus coupling length including experimental data points from the devices with gap distances of 400 nm from the three fabrication runs. ©Optical Society of America, 2015, by permission [435].

Next, we show an example of using the extracted $|\kappa|$ (using the FWHM method) to closely match the simulated spectra to the experimental spectra of one of our contra-DCs. We have chosen one of our devices that showed a highly symmetric spectral response to the left and right of the centre of the main lobe for the comparison between the simulated results (using the extracted $|\kappa|$ determined from the FWHM method) and the experimental results. The device has a gap distance of 140 nm and is from “run 2.” The simulated spectra were plotted using Eqs. 6.1 and 6.2 and we have added 0.0147 to the modelled values of the effective indices for spectral alignment purposes. Figure 6.7(a) shows that the simulated through port and drop port spectra using the extracted $|\kappa|$ of 19882 m^{-1} from “run 2” closely match the experimental spectra. Figure 6.7(b) shows a comparison between the simulated spectra using the extracted $|\kappa|$ of 18466 m^{-1} from “run 1” and the experimental spectra from “run 2.” The results in Figure 6.7(b) show that, since there is close agreement between the two fabrication runs, using a previously extracted

$|\kappa|$ can be used to predict the spectral response of future fabricated devices with the same as-designed dimensions. Figures 6.7(c) and 6.7(d) show a comparison between the drop port spectra and through port spectra, respectively, from “run 1,” “run 2,” and “run 3” and the simulated spectra (we have aligned the measured spectra from “run 1,” “run 2,” “run 3,” and the simulated spectra to their respective centre wavelengths) using the average $|\kappa|$ of 18856 m^{-1} , calculated using the extracted $|\kappa|$ s from the three runs (*i.e.*, 18466 m^{-1} , 19882 m^{-1} , and 18219 m^{-1}).

Our method can also be used to predict the maximum power coupling factors, $\text{MAX}|\kappa_c|^2$ s, and the minimum power transmission factors, $\text{MIN}|t_c|^2$ s, of contra-DCs. In Figures 6.8(a) and 6.8(b) we show a comparison between the experimental and simulated (using the extracted $|\kappa|$ s determined from the FWHM method) $\text{MAX}|\kappa_c|^2$ s and $\text{MIN}|t_c|^2$ s versus gap distance, respectively, for the devices from “run 1,” “run 2,” and “run 3.” Experimental $\text{MIN}|t_c|^2$ s for the devices from “run 1” with gap distances of 320 nm, 380 nm, and 400 nm and for the devices from “run 3” with gap distances of 380 nm and 400 nm are not shown in Figure 6.8(b) since the main notches within their through port spectra were not visible. Simulated $\text{MAX}|\kappa_c|^2$ and $\text{MIN}|t_c|^2$ for the device from “run 3” with a gap distance of 400 nm is not shown since we were unable to extract a value for $|\kappa|$ other than zero. Also, the $\text{MAX}|\kappa_c|^2$ s determined using the curve-fit method are closer to the normalized measured results as compared to the $\text{MAX}|\kappa_c|^2$ s determined using the FWHM method. However, using the $|\kappa|$ s extracted by the FWHM method result in many of the simulated $\text{MIN}|t_c|^2$ s being closer to the measured results as compared to the $\text{MIN}|t_c|^2$ s determined using the curve-fit method. The likely reason that the FWHM method gives better results for $\text{MIN}|t_c|^2$, as compared to the values determined using the curve-fit method, is that the curve-fit method relies on an accurate normalization of the drop port spectrum.

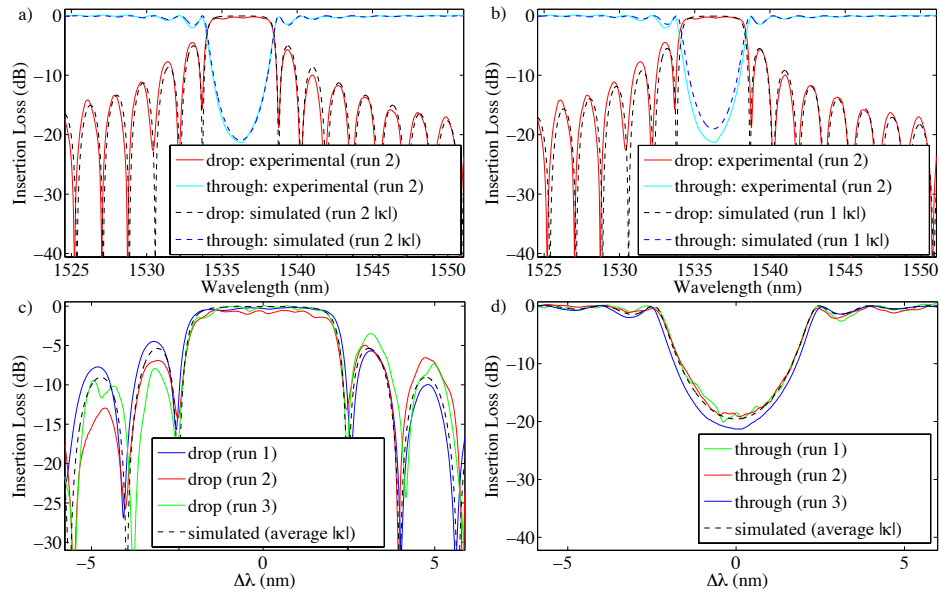


Figure 6.7: (a) Experimental and simulated (using the extracted $|\kappa|$ obtained using the FWHM method) drop port and through port spectra for a contra-DC (from “run 2”) with a gap distance equal to 140 nm. (b) Comparison between the experimental spectra from “run 2” and the simulated spectra using the extracted $|\kappa|$ of 18466 m^{-1} from “run 1” for contra-DCs with gap distances of 140 nm. Comparison between the experimental (c) drop port spectra and (d) through port spectra from “run 1,” “run 2,” and “run 3” and the simulated spectra using the average extracted $|\kappa|$ of 18856 m^{-1} from the three runs for contra-DCs with gap distances of 140 nm. ©Optical Society of America, 2015, by permission [435].

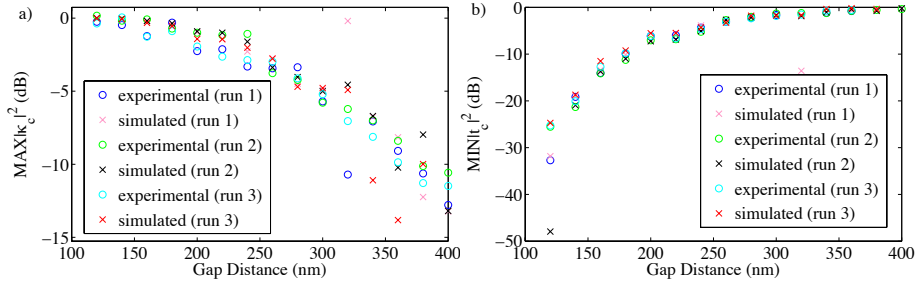


Figure 6.8: Comparison between the experimental and the simulated (using extracted $|\kappa|$ s determined from the FWHM method) (a) maximum power coupling factor and (b) minimum power transmission factor versus gap distance. ©Optical Society of America, 2015, by permission [435].

The group delay and the dispersion of a contra-DC is of interest because they give us an indication of the effect the contra-DC will have on a signal. Previously, it has been shown that the phase (and, therefore, the group delay and dispersion) of fibre Bragg gratings [499, 521, 522] and ring resonators [112, 501, 523, 524] can be determined using the Hilbert transform method. Specifically, the Hilbert transform method can be used to determine through port phase responses of Bragg gratings because the through port response is minimum phase [499, 521, 522]. Here, we use the Hilbert transform method [499] to determine the through port phase of a contra-DC from “run 2” with a gap distance of 140 nm (we use the *hilbert* function from MATLAB[®] [500]). Once the phase response is determined, the group delay [97, 525] and dispersion [97, 525, 526] can be calculated. Figures 6.9(a) and 6.9(b) show the group delay and dispersion responses, respectively, using the Hilbert transform method on the experimental through port spectrum from Figure 6.7(a) (the results shown were smoothed using moving averages) and are compared to the simulated responses that were determined for the $|\kappa|$ extracted using the FWHM method and the measured results (the average of 300 measurements) using an Optical Vector Analyzer[™] *STe* by Luna Innovations, Inc., (OVA). For the simulated results, we added an additional phase to account for the transit time of the device. The effective indices for this additional phase were calculated for a waveguide width of 450 nm using MODE Solutions by Lumerical Solutions, Inc. Similarly, we have added a 2.22 ps group delay offset to the Hilbert transform-determined

group delay. Also, a constant group delay offset was subtracted from the measured group delay for alignment to the simulated result. The Hilbert transform-determined through port group delay and dispersion results are in close agreement with the simulated results using the extracted $|\kappa|$ and the measured results using the OVA. Therefore, our FWHM method can also be used to predict the through port group delay response and the dispersion response of contra-DCs.

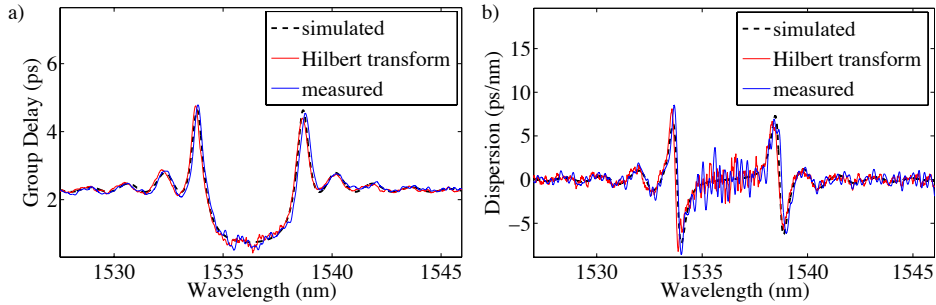


Figure 6.9: Comparison between the experimental through port (a) group delay response and (b) dispersion response that were determined using the Hilbert transform method and the simulated results that were determined using the extracted $|\kappa|$ of 19882 m^{-1} as well as the measured results using the OVA. ©Optical Society of America, 2015, by permission [435].

6.3 Example of Using the Process Calibration Method in the Filter Design Process

Here, a 3-port Vernier filter consisting of four silicon grating-assisted racetrack resonators (similar to the filter in [97]), as shown in Figure 6.10, is demonstrated theoretically. The arrangement of the racetrack resonators is similar to those found in [85, 126, 142], however, the racetrack resonators presented here are cascaded. The Vernier filter meets typical 3-port filter commercial specifications as well as low drop port and through port dispersions. The process calibration method presented in this chapter can be used to accurately determine the coupling coefficients of fabricated contra-DCs, and this method will be used to determine the gap distance that corresponds to the coupling coefficient of the contra-DC that is required for the filter to operate as desired.

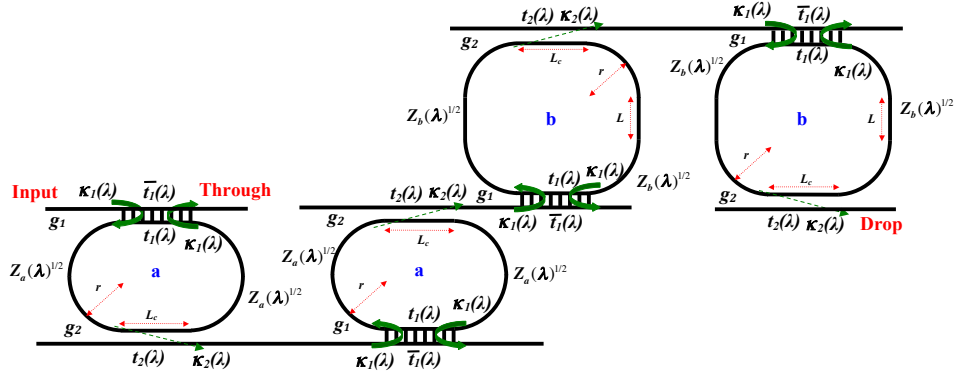


Figure 6.10: Schematic diagram of an optimized 3-port grating-assisted Vernier filter (figure has been adapted from [97]).

Simulation results for an optimized 3-port silicon grating-assisted Vernier racetrack resonator filter are presented. Figure 6.11(a) shows the theoretical spectra at the drop port and at the through port of an optimized 3-port grating-assisted Vernier filter that has the configuration shown in Figure 6.10. Figure 6.11(b) shows a zoom-in within the wavelength region of the major peak/notch where the clear window (indicated by the dashed vertical lines) is 13 GHz and the channel spacing is 200 GHz. This filter meets the target specifications that are bolded in Table 6.1. The drop port dispersion within the wavelength region near the desired channel's clear window is shown in Figure 6.11(c) and the through port dispersion within the wavelength region corresponding to the through port passband to the left of the major notch is shown in Figure 6.11(d). D_{drop} is +15 ps/nm and $D_{\text{thru-m}}$ is -4 ps/nm, which meet their typical requirements of $-30 \text{ ps/nm} \leq D_{\text{drop}} \leq +30 \text{ ps/nm}$ [105] and $-15 \text{ ps/nm} \leq D_{\text{thru-m}} \leq +15 \text{ ps/nm}$ [105], respectively. The method to model this grating-assisted Vernier racetrack resonator filter was based on [97]. The following parameter values were used in the simulation of the filter: the grating period was 312 nm [440]; the grating number was 182 [440]; the radius was 3 μm [440]; $L = 22.07 \mu\text{m}$; the routing length between each cascaded racetrack resonator was 20 μm ; the propagation loss was set to 3 dB/cm; κ was chosen to be 13000 m^{-1} ; the co-directional couplers without gratings consisted of silicon strip waveguides with widths of 550 nm and heights of 220 nm, a top oxide cladding, and gap distances of 280 nm [97]; the bend regions of the racetrack resonators had widths of

550 nm, heights of 220 nm, and were not included in the calculations of the field coupling factors and field transmission factors [97]; and the contra-DCs consisted of strip waveguides with average widths of 450 nm and 550 nm and heights of 220 nm [97]. Based on the extracted $|\kappa|$ s, using the FWHM method, shown in Figures 6.5(a)-6.5(c), the chosen κ of 13000 m^{-1} corresponds to a gap distance of about 170 nm.

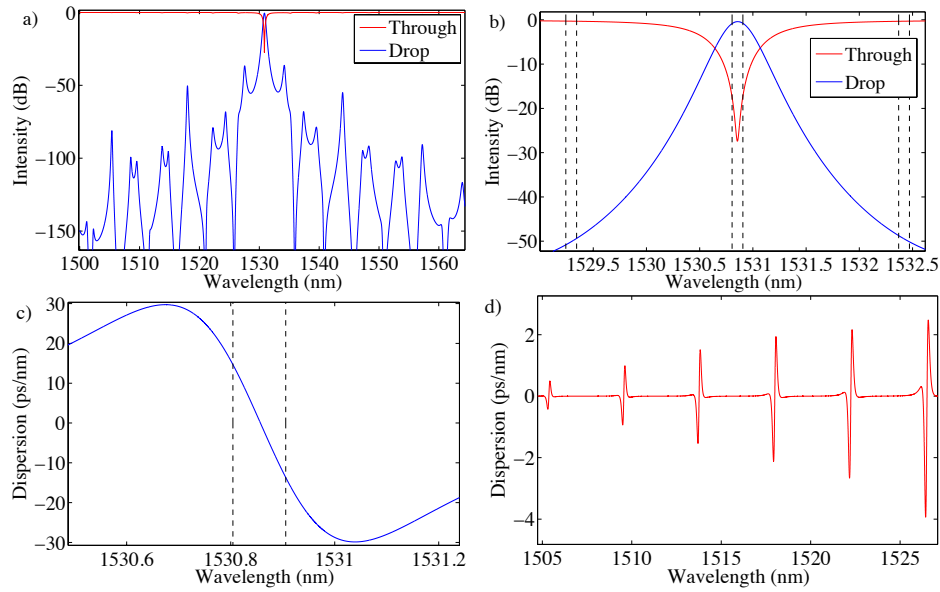


Figure 6.11: (a) Through port spectral response and drop port spectral response, (b) a zoom-in within the region of the major peak/notch, (c) drop port dispersion within the wavelength region of the major peak, and (d) through port dispersion within the wavelength region corresponding to the passband to the left of the major notch of an optimized 3-port grating-assisted Vernier filter.

Table 6.1: Modelled results and target specifications for 200 GHz 3-port filters (table modified from [105]).

Parameter	Modelled result	Target value
FSR (nm)	N/A	\geq 36.72
R_{depth} (dB)	0.5	\leq 0.5 [502]
A_i (dB)	47.9	\geq 25 [502, 503], 30 [101]
nA_i (dB)	38.9	\geq 35 [101], 40 [502, 503]
IPS (dB)	35.4	\geq 35 [101], 40 [502, 503]
IL_{drop} (dB)	0.9	\leq 0.8 [503], 1.0 [502], 1.2 [101]
EC_i (dB)	17.0	\geq 10 [502], 12 [503]
IL_{thru} (dB)	0.3	\leq 0.4 [503], 0.5 [502], 0.6 [101]
$IL_{\text{thru-m}}$ (dB)	0.5	\leq 0.4 [503], 0.5 [502], 0.6 [101]

In the filter design process, the ability to predict the performance of contra-DCs is invaluable. We have presented a method, the FWHM method, for determining the coupling coefficients of contra-DCs. To demonstrate the usefulness of our method, we fabricated SOI contra-DCs on three separate fabrication runs. Our FWHM method of extracting the coupling coefficient of contra-DCs can be used to predict the spectral response, group delay, and dispersion of subsequently fabricated devices. The FWHM method provides more consistent extracted coupling coefficient values as compared to the values extracted using the null method. Also, the FWHM method provides extracted coupling coefficient values of fabricated devices that are relatively close, as compared to using the null method, to the values extracted by curve-fitting the drop port spectra. However, the curve-fit method relies on the accurate normalization of the drop port spectrum whereas our FWHM method does not require normalization of the data, and our method is generally easier to implement. We have also shown that there is a minimum bandwidth that can be obtained by reducing the coupling coefficient, which needs to be considered when designing a contra-DC-based filter. We have presented an equation for this minimum bandwidth as a function of the length of the coupler. The method presented in this chapter can be used to calibrate the design process, enabling designers to accurately predict the as-fabricated contra-DC response.

Chapter 7

Conclusion and Future Work

7.1 Conclusion

The design of a variety of silicon photonic ring resonator filters for DWDM applications that allow for a large number of channels to be multiplexed and/or demultiplexed have been theoretically and experimentally demonstrated. Specifically, three methods to increase the FSR and, thus, increase the channel count, have been presented.

The first method utilized the Vernier effect to increase the FSR by coupling non-identical ring resonators together. First, silicon quadruple series-coupled ring resonators exhibiting the Vernier effect were theoretically shown to be able to meet typical 4-port filter commercial specifications as well as have FSRs larger than the span of the C-band. Also, experimental results on silicon quadruple series-coupled ring resonators exhibiting the Vernier effect have shown that it is possible to meet numerous 3-port commercial specifications, enhance the resonant tuning range, as well as the ability to transmit data through the device at 12.5 Gbps. The next method to increase the channel count is to use MZI-BC. Theoretical and experimental results on silicon series-coupled microring resonators with MZI-BC have been presented which showed that it is possible to meet numerous 3-port filter commercial specifications, have an FSR greater than the span of the C-band, and have low dispersion within the through port passbands. Although the FSR can be increased by using these two methods, ideally one would like to eliminate the

FSR. The third method utilized contra-DCs, which are highly wavelength selective couplers. Theoretical and experimental results on silicon cascaded Vernier racetrack resonators with integrated contra-DCs in the coupling regions have shown that it is possible to not only eliminate the FSR but also to increase the IPS as compared to the case in which co-directional couplers without gratings are used within all the coupling regions of the cascaded racetrack resonator filter. When using contra-DCs in the design of filters, it is important to accurately determine the coupling coefficients and, thus, we presented a process calibration method to determine the coupling coefficients of fabricated contra-DCs by measuring their FWHM bandwidths. Then, this process calibration method was used to design a silicon cascaded Vernier racetrack resonator with integrated contra-DCs, which met 3-port filter commercial specifications.

The three methods used to extend the FSRs of ring resonators (series-coupled Vernier ring resonators, MRRs with MZI-BCs, and cascaded Vernier ring resonators with contra-DCs) each have benefits and drawbacks, which are shown in Table 7.1. The comparison shown in Table 7.1 is based on the following features: FSR, wavelength tunability, thermal cross-talk, minor notch dispersion, filter shape, and filter application [fixed wavelength filter applications, limited wavelength tuning range filter applications (*i.e.*, less than C-band span), and C-band tuning range filter applications]. The benefits of series-coupled Vernier ring resonators are extend FSRs, enhanced wavelength tuning ranges, and flat-topped responses [149, 150]. However, series-coupled Vernier ring resonators typically have large dispersions within their through port minor notches [105, 112, 432]. Fortunately, low dispersion can be achieved using MRRs with MZI-BCs while extending the FSR and providing a flat-topped response [105, 432]. However, the current design within this dissertation cannot exhibit an enhanced wavelength tuning range. The last method, cascaded Vernier ring resonators with contra-DCs, has the desirable features that the FSRs are eliminated in the drop port and through port, reduced thermal cross-talks due to the cascaded configurations [97], and low minor notch dispersions. However, the drawbacks to this method are that the filters have no enhanced wavelength tuning ranges, and the filter responses are not flat-topped. With regard to the MZI-BC method, it may be possible to achieve the enhanced wavelength tuning range feature by reducing the FSRs of the MZIs, and, thus, the

Table 7.1: Comparison of FSR extension methods as implemented in dissertation (the benefits are bolded).

Method	FSR	Wavelength tunability	Thermal cross-talk	Minor notch dispersion	Flat-topped response	Application
Vernier rings (series) [105, 149, 150]	extended	enhanced	standard	large	yes	fixed, C-band tuning
MRRs with MZI-BC [105]	extended	standard*	standard	minimal	yes	fixed, limited tuning*
Vernier rings (cascade) with contra-DCs [97]	eliminated	standard	reduced	minimal	no	fixed, limited tuning

* Potential for enhanced wavelength tuning range.

MZI-BC method would be the most desirable method, since it would be the only method with, both, enhanced wavelength tuning ranges and minimal minor notch dispersions.

Overall, I have shown a variety of silicon photonic filters that meet commercial specifications including: first commercial specification-dependent sensitivity analysis of silicon Vernier ring resonators; first experimental demonstration of a silicon quadruple series-coupled Vernier racetrack resonator; first experimental demonstration of thermally tunable silicon quadruple series-coupled Vernier racetrack resonators; first experimental demonstration of a silicon MRR filter with MZI-BC that meets many of the typical commercial specifications; and the first demonstration of silicon cascaded Vernier racetrack resonators with integrated contra-DCs. Lastly, a superior process calibration method for contra-DC filter designs was presented.

7.2 Future Work

Experimental validation that silicon series-coupled Vernier racetrack resonators can meet all of the 4-port filter specifications, especially the express channel isolation, is still needed and the starting point would be to take the 4-port Vernier filter designs presented in Chapter 2 and model the directional couplers in 3-D FDTD; the bend regions of the couplers will increase the values of the coupling factors as compared to when the coupling factors are calculated using just the straight sections of the couplers, and, thus, the gap distances will have to be modified to achieve devices that exhibit similar performance to those presented in Chapter 2. Also, waveguide offsets can be introduced between the bent and straight regions of the racetrack resonators to reduce mode-mismatch losses [470]. The use of a fabrication process that results in lower waveguide losses would enable improvements in the performance of Vernier resonators. For example, the minor through port notches would be smaller since propagation losses can be dramatically reduced to as low as 0.5 dB/cm [527]. If we take the 4-port Vernier filter design from Chapter 2 with nominal gap distances, “gap 1”, “gap 2”, and “gap 3” equal to 150 nm, 350 nm, and 390 nm and reduce the propagation loss from 2.4 dB/cm to 0.5 dB/cm, then $IL_{\text{thru-m}}$ would reduce from 0.6 dB to 0.1 dB when light is injected into the

input port and $IL_{\text{thru-m}}$ would reduce from 0.8 dB to 0.2 dB when light is injected into the add port, as shown in Figures 7.1(a) and 7.1(b), respectively. An automated tuning and optimization method, such as the ones presented in [430, 528], can be used to create an automatically tunable silicon quadruple series-coupled Vernier racetrack resonator.

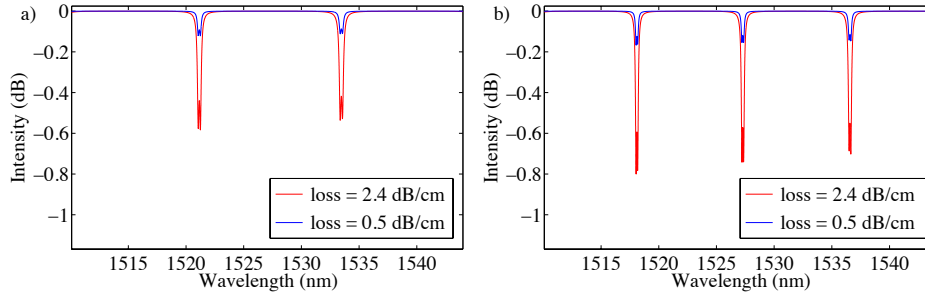


Figure 7.1: (a) Through port passband and (b) drop port passband comparison, when light is injected into the input port and when light is injected into the add port, respectively, of a 4-port quadruple Vernier racetrack resonator, for propagation losses of 2.4 dB/cm and 0.5 dB/cm.

With regard to the silicon double microring resonator with MZI-BC, adding heaters on top of the MZI-bus branches, as well as to each microring resonator, will enable it to operate as a wavelength tunable filter (as previously demonstrated in [433]) while meeting numerous commercial specifications. The integration of heaters will also help improve the performance of the device by enabling the ability to correct for fabrication variations. An automated tuning and optimization method, such as the ones presented in [430, 528], could be used with the silicon double microring resonator with MZI-BC.

With regard to the cascaded Vernier racetrack resonator that uses grating-assisted couplers, experimentally demonstrating the improved filter design that was presented in Chapter 6.3 is needed since such a device would be a desirable component in silicon photonic systems that require DWDM filters. To correct for fabrication variations, heaters can be placed on top of the contra-DCs as well as the portions of each of the racetrack resonators that are not within the coupling regions. Waveguide offsets can be introduced between the bent and straight regions of each racetrack resonator to reduce mode-mismatch losses [470]. Also, an automated tuning

and optimization method, such as the ones presented in [430, 528], could be used with the grating-assisted cascaded Vernier racetrack resonator.

Many of the filters presented in this dissertation have met numerous commercial filter specifications based on telecommunications vendor data sheets and, with ever-increasing improvements in the fabrication process, such filters could be commercializable. Thus, the silicon photonic DWDM filters presented in this dissertation have provided additional evidence that silicon photonics has the real potential to be a disruptive technology that transforms the telecommunications and data communications industries.

Bibliography

- [1] Future Market Insights, “Silicon Photonics Market: Global Industry Analysis and Opportunity Assessment 2015-2025,” [Online]. Available: <http://www.futuremarketinsights.com/reports/silicon-photonics-market>, (Jan. 15, 2016).
- [2] Markets and Markets, “Silicon Photonics Market by Product (Photonic Wavelength, Optical Modulators, Optical Interconnects, WDMF, LED, and Others), by Application (Telecommunication, Data Communication, and Others), and by Geography - Global Trends and Forecasts to 2014 - 2020,” [Online]. Available: <http://www.marketsandmarkets.com/Market-Reports/silicon-photonics-116.html>, (Jan. 15, 2016).
- [3] Yole Développement, “Silicon Photonics Market & Technologies 2011-2017: Big Investments, Small Business,” [Online]. Available: http://www.yole.fr/iso_upload/News/2012/PR_Silicon%20Photonics%20Big%20Investments%20Small%20Business_YOLE%20DEVELOPPEMENT_October%202012.pdf, (Jan. 15, 2016).
- [4] P. P. Drake and F. J. Fabozzi, *The Basics of Finance: An Introduction to Financial Markets, Business Finance, and Portfolio Management*. John Wiley & Sons, Inc., 2010.
- [5] M. S. Fridson and F. Alvarez, *Financial Statement Analysis: A Practitioner’s Guide, 4th Edition*. John Wiley & Sons, Inc., 2011.
- [6] iMinds, *Market Capitalisation: Money*. iMinds Pty Ltd., 2009.
- [7] Etaphase, Inc., “Etaphase successfully demonstrates fabrication of HUDS in silicon CMOS chip,” [Online]. Available: http://etaphase.com/2012/10/huds_silicon_cmos/, (Jan. 15, 2016).
- [8] H. Byun, J. Bok, K. Cho, K. Cho, H. Choi, J. Choi, S. Choi, S. Han, S. Hong, S. Hyun, T. J. Jeong, H.-C. Ji, I.-S. Joe, B. Kim, D. Kim, J. Kim,

J.-K. Kim, K. Kim, S.-G. Kim, D. Kong, B. Kuh, H. Kwon, B. Lee, H. Lee, K. Lee, S. Lee, K. Na, J. Nam, A. Nejadmalayeri, Y. Park, S. Parmar, J. Pyo, D. Shin, J. Shin, Y. hwack Shin, S.-D. Suh, H. Yoon, Y. Park, J. Choi, K.-H. Ha, and G. Jeong, "Bulk-Si photonics technology for DRAM interface [Invited]," *Photonics Research*, vol. 2, no. 3, pp. A25–A33, Jun. 2014.

- [9] Morton Photonics, Inc., [Online]. Available: <http://mortonphotonics.com>, (Jan. 15, 2016).
- [10] Kaiam Corp., "Kaiam Corporation Introduces a 40GB/S QSFP+ LR4 Transceiver with Integrated Optical Engines for Use in High Volume Applications at OFC 2014," [Online]. Available: http://kaiamcorp.com/?page_id=7994, (Jan. 15, 2016).
- [11] Centera Photonics, Inc., [Online]. Available: http://www.centera-photonics.com/pages/page_company_en, (Jan. 15, 2016).
- [12] VLC Photonics S.L., [Online]. Available: <http://www.vlcphotonics.com/technology-2/>, (Jan. 15, 2016).
- [13] Compass-EOS, "Silicon Photonics and the Future of Core Routing," [Online]. Available: <http://compassnetworks.com/wp-content/uploads/Compass-EOS-Technology-White-Paper.pdf>, (Jan. 15, 2016).
- [14] APIC Corp., [Online]. Available: <http://www.apichip.com/next.html>, (Jan. 15, 2016).
- [15] PhotonIC Corp., [Online]. Available: <http://www.photonic-corp.com>, (Jan. 15, 2016).
- [16] photonics.com, "Samtec Joins French Silicon Photonics Development Project," [Online]. Available: <http://www.photonics.com/Article.aspx?AID=57434>, (Jan. 15, 2016).
- [17] AEAPONYX, Inc., [Online]. Available: <http://www.aeponyx.com/OCS>, (Jan. 15, 2016).
- [18] Fujitsu Ltd., "Fujitsu, PETRA, and NEDO Achieve World's Lowest Energy Requirements of 5 mW per 1 Gbps for High-Speed Inter-Processor Data Transmissions," [Online]. Available: <http://www.fujitsu.com/global/about/resources/news/press-releases/2015/0223-02.html>, (Jan. 15, 2016).

- [19] Optic2Connect Pte. Ltd., [Online]. Available: <http://www.optic2connect.com>, (Jan. 15, 2016).
- [20] COMSOL, Inc., “Optical ring resonator notch filter,” [Online]. Available: <http://www.comsol.com/model/optical-ring-resonator-notch-filter-22221>, (Jan. 15, 2016).
- [21] Optiwave Systems, Inc., [Online]. Available: <http://optiwave.com>, (Jan. 15, 2016).
- [22] PhoeniX B.V., [Online]. Available: <http://www.phoenixbv.com/index.php>, (Jan. 15, 2016).
- [23] Photon Design, Inc., [Online]. Available: <http://www.photond.com>, (Jan. 15, 2016).
- [24] EM Photonics, Inc., [Online]. Available: <http://www.emphotonics.com/projects/electromagnetics/>, (Jan. 15, 2016).
- [25] Apollo Photonics, Inc., [Online]. Available: <http://www.apollophoton.com/apollo/>, (Jan. 15, 2016).
- [26] Luceda Photonics, [Online]. Available: <http://www.lucedaphotonics.com/en>, (Jan. 15, 2016).
- [27] Synopsys, Inc., [Online]. Available: <https://optics.synopsys.com/rsoft/rsoft-product-applications.html>, (Jan. 15, 2016).
- [28] Mentor Graphics Corp., “Mentor Graphics and Lumerical Unify Optical Design and Simulation Flow,” [Online]. Available: <http://www.mentor.com/company/news/mentor-lumerical-optical-design>, (Jan. 15, 2016).
- [29] Maple Leaf Photonics LLC, [Online]. Available: <http://mapleleafphotonics.com>;
http://www.sos.wa.gov/corps/search_detail.aspx?ubi=603483503, (Apr. 14, 2016).
- [30] Inphi Corp., “Inphi Collaborates to Announce Industry’s First 100G Cloud Platform at IDF 2014,” [Online]. Available: <http://www.inphi.com/media-center/press-room/press-releases-and-media-alerts/inphi-collaborates-to-announce-industrysquos-first-100g-cloud-platform-at-idf-2014.php>, (Jan. 15, 2016).

- [31] Caliopa, [Online]. Available: <http://www.caliopa.com>, (Jan. 15, 2016).
- [32] Novati Technologies, [Online]. Available: <http://www.novati-tech.com/silicon-photonics>, (Jan. 15, 2016).
- [33] Sandia National Laboratories, [Online]. Available: <http://www.sandia.gov/mstc/IPIMI/>, (Jan. 15, 2016).
- [34] F. Boeuf, S. Cremer, E. Temporiti, M. Fere', M. Shaw, N. Vulliet, B. Orlando, D. Ristoiu, A. Farcy, T. Pinguet, A. Mekis, G. Masini, P. Sun, Y. Chi, H. Petiton, S. Jan, J.-R. Manouvrier, C. Baudot, P. Le-Maitre, J. F. Carpentier, L. Salager, M. Traldi, L. Maggi, D. Rigamonti, C. Zaccherini, C. Elemi, B. Sautreuil, and L. Verga, "Recent progress in silicon photonics R&D and manufacturing on 300mm wafer platform," in *Optical Fiber Communication Conference*. Optical Society of America, 2015, p. W3A.1.
- [35] P. Liao, M. Sakib, F. Lou, J. Park, M. Wlodawski, V. Kopp, D. Neugroschl, and O. Liboiron-Ladouceur, "Ultradense silicon photonic interface for optical interconnection," *IEEE Photonics Technology Letters*, vol. 27, no. 7, pp. 725–728, Apr. 2015.
- [36] M/A-COM Technology Solutions Holdings, Inc., [Online]. Available: <http://www.macom.com/technologies/siph>, (Jan. 15, 2016).
- [37] One Silicon Chip Photonics, Inc., [Online]. Available: <http://onesiliconchip Photonics.com/technology>, (Jan. 15, 2016).
- [38] Applied NanoTools, Inc., [Online]. Available: <http://www.appliednt.com>, (Jan. 15, 2016).
- [39] Acacia Communications, Inc., [Online]. Available: <http://acacia-inc.com/acacia-advantage/silicon-photonics-integration/>, (Jan. 15, 2016).
- [40] NEC Corp., "NEC develops silicon integrated optical switch technology with port count extendability according to network size," [Online]. Available: http://www.nec.com/en/press/201503/global_20150319_02.html, (Jan. 15, 2016).
- [41] VTT Memsfab Ltd., [Online]. Available: <http://www.vttmemsfab.fi/services>, (Jan. 15, 2016).

- [42] Markets and Markets, “Silicon Photonics Market by Product, Application and by Geography - Global Trends and Forecasts to 2014 - 2020,” [Online]. Available: http://www.researchandmarkets.com/research/n42dsl/silicon_photonics, (Jan. 15, 2016).
- [43] Omega Optics, Inc., [Online]. Available: <http://www.omegaoptics.com>, (Jan. 15, 2016).
- [44] Rockley Photonics, [Online]. Available: <http://rockleyphotonics.com>, (Jan. 15, 2016).
- [45] Luxmux Technology Corp., [Online]. Available: <http://www.luxmux.com>, (Jan. 15, 2016).
- [46] Lumerical Solutions, Inc., “Unified Design Flow for Silicon Photonics,” [Online]. Available: https://www.lumerical.com/solutions/partners/eda/mentor_graphics/, (Jan. 15, 2016).
- [47] Mellanox Technologies, “Mellanox Introduces Next Generation 100Gb/s Silicon Photonics Transceivers,” [Online]. Available: http://www.mellanox.com/page/press_release_item?id=1504, (Jan. 15, 2016).
- [48] Y. Painchaud, M. Poulin, F. Pelletier, C. Latrasse, J.-F. Gagne, S. Savard, G. Robidoux, M. Picard, S. Paquet, C. Davidson, M. Pelletier, M. Cyr, C. Paquet, M. Guy, M. Morsy-Osman, M. Chagnon, and D. V. Plant, “Silicon-based products and solutions,” *Proc. SPIE*, vol. 8988, p. 89880L, 2014.
- [49] D. M. Calhoun, Q. Li, C. Browning, N. C. Abrams, Y. Liu, R. Ding, L. P. Barry, T. Baehr-Jones, M. Hochberg, and K. Bergman, “Programmable wavelength locking and routing in a silicon-photonic interconnection network implementation,” in *Optical Fiber Communication Conference*. Optical Society of America, 2015, p. Tu2H.3.
- [50] P. Dong, Y.-K. Chen, and L. L. Buhl, “Reconfigurable four-channel polarization diversity silicon photonic WDM receiver,” in *Optical Fiber Communication Conference*. Optical Society of America, 2015, p. W3A.2.

- [51] D. Mahgerefteh and C. Thompson, "Techno-economic comparison of silicon photonics and multimode VCSELs," in *Optical Fiber Communication Conference*. Optical Society of America, 2015, p. M3B.2.
- [52] C.-H. J. Chen, T.-C. Huang, D. Livshit, A. Gubenko, S. Mikhlin, V. Mikhlin, M. Fiorentino, and R. Beausoleil, "A comb laser-driven DWDM silicon photonic transmitter with microring modulator for optical interconnect," in *CLEO: 2015*. Optical Society of America, 2015, p. STu4F.1.
- [53] M. Mazzini, M. Traverso, M. Webster, C. Muzio, S. Anderson, P. Sun, D. Siadat, D. Conti, A. Cervasio, S. Pfner, J. Stayt, M. Nyland, C. Togami, K. Yanushefski, and T. Daugherty, "25GBaud PAM-4 error free transmission over both single mode fiber and multimode fiber in a QSFP form factor based on silicon photonics," in *Optical Fiber Communication Conference Post Deadline Papers*. Optical Society of America, 2015, p. Th5B.3.
- [54] X. Zheng and A. V. Krishnamoorthy, "A WDM CMOS photonic platform for chip-to-chip optical interconnects," in *CLEO: 2014*. Optical Society of America, 2014, p. SM4O.3.
- [55] H.-F. Liu, "Integrated silicon photonics links for high bandwidth data transportation," in *Optical Fiber Communication Conference*. Optical Society of America, 2014, p. Th1D.1.
- [56] A. Ramaswamy, J. E. Roth, E. J. Norberg, R. S. Guzzon, J. H. Shin, J. T. Imamura, B. R. Koch, D. K. Sparacin, G. A. Fish, B. G. Lee, R. Rimolo-Donadio, C. W. Baks, A. Rylyakov, J. Proesel, M. Meghelli, and C. L. Schow, "A WDM 4x28Gbps integrated silicon photonic transmitter driven by 32nm CMOS driver ICs," in *Optical Fiber Communication Conference Post Deadline Papers*. Optical Society of America, 2015, p. Th5B.5.
- [57] Ericsson, "Ericsson-backed research project breaks new ground in silicon photonic integration," [Online]. Available: <http://www.ericsson.com/news/1948557>, (Jan. 15, 2016).
- [58] Analog Photonics LLC, [Online]. Available: <http://www.analogphotonics.com>, (Jan. 15, 2016).
- [59] BrPhotonics Produtos Optoeletrônicos LTDA., [Online]. Available: <http://brphotonics.com/en/>, (Jan. 15, 2016).

- [60] RANOVUS, Inc., [Online]. Available: <http://ranovus.com/technology/>, (Jan. 15, 2016).
- [61] Iris Dorbian, "Target Partners backs Sicoya," [Online]. Available: <https://www.pehub.com/2015/11/target-partners-backs-sicoya/>, (Jan. 15, 2016).
- [62] SiFotonics Technologies Co., Ltd., [Online]. Available: <http://sifotonics.com/en/>, (Jan. 15, 2016).
- [63] Katherine Bourzac, "Magic Leap needs to engineer a miracle," [Online]. Available: <http://www.technologyreview.com/news/538146/magic-leap-needs-to-engineer-a-miracle/>, (Jan. 15, 2016).
- [64] Acorn Technologies, [Online]. Available: <http://acorntech.com/applications/semiconductor/>, (Jan. 15, 2016).
- [65] Luxtera, Inc., "Luxtera Ships One-Millionth Silicon CMOS Photonics Enabled 10Gbit Channel," [Online]. Available: <http://www.luxtera.com/luxtera/201221LuxteraOneMillionthCMOS.pdf>, (Jan. 15, 2016).
- [66] VPIphotonics Inc., [Online]. Available: <http://www.vpiphotonics.com/Tools/PhotonicCircuits/Applications/>, (Jan. 15, 2016).
- [67] PLCC2 LLC, [Online]. Available: <http://www.plccconnections.com/silicon.html>, (Jan. 15, 2016).
- [68] Genalyte, Inc., [Online]. Available: <http://www.genalyte.com/about-us/our-technology/>, (Jan. 15, 2016).
- [69] P. Brown, "Optoelectronics Deal Struck Between Two Chinese Firms," [Online]. Available: <http://electronics360.globalspec.com/article/6132/optoelectronics-deal-struck-between-two-chinese-firms>, (Jan. 15, 2016).
- [70] photonics.com, "Microprocessor Integrates Silicon Photonics," [Online]. Available: <http://www.photonics.com/Article.aspx?AID=58119>, (Jan. 15, 2016).
- [71] DermaLumics S.L., [Online]. Available: <http://www.dermalumics.com/integrated-optics/>, (Jan. 15, 2016).

- [72] JCMwave GmbH, “Simulation of an integrated optical (de)multiplexer / SOI ring resonator,” [Online]. Available: <http://www.jcmwave.com/applications/287-add-drop-multiplexers>, (Jan. 15, 2016).
- [73] GigOptix, Inc., “GigOptix, Inc. and CPqD Announce Signing of Definitive Agreements to Incept BrPhotonics Produtos Optoeletrônicos LTDA., a New Joint Venture Company in Brazil,” [Online]. Available: <http://ir.gigoptix.com/phoenix.zhtml?c=225697&p=irol-newsArticle&ID=1899101>, (Jan. 15, 2016).
- [74] Coriant, “Coriant Begins Independent Path, Starts with Leadership Position in Optical Networking Market,” [Online]. Available: <https://www.coriant.com/company/press-releases/Coriant-Begins-Independent-Path-Starts.asp>, (Jan. 15, 2016).
- [75] HP Inc., “HP Inc. and Hewlett Packard Enterprise to jointly present live audio webcast of Hewlett-Packards fourth quarter earnings conference call,” [Online]. Available: <http://h30261.www3.hp.com/news-and-events/news-library/2015/11-10-2015.aspx>, (Jan. 15, 2016).
- [76] Novati Technologies, “Company profile,” [Online]. Available: <http://www.novati-tech.com/company-profile>, (Jan. 15, 2016).
- [77] iXBlue Photonics, [Online]. Available: <http://www.photonics.ixblue.com/about-us/overview>, (Jan. 15, 2016).
- [78] I. Shubin, X. Zheng, H. Thacker, S. S. Djordjevic, S. Lin, P. Amberg, J. Yao, J. Lexau, E. Chang, F. Liu, N. Park, K. Raj, R. Ho, J. E. Cunningham, and A. V. Krishnamoorthy, “Microring-based multi-chip WDM photonic module,” *Optics Express*, vol. 23, no. 10, pp. 13 172–13 184, May 2015.
- [79] A. Mekis, G. Armijo, J. Balardeta, S. Barabas, B. Chase, Y. Chi, A. Dahl, Y. De Koninck, S. Denton, M. Eker, S. Fathpour, D. Foltz, F. Gholami, S. Gloeckner, K. Hon, S. Hovey, S. Jackson, W. Li, Y. Liang, M. Mack, G. Masini, G. McGee, S. Pang, M. Peterson, T. Pinguet, L. Planchon, K. Roberson, S. Sahn, J. Schramm, M. Sharp, C. Sohn, K. Stechschulte, P. Sun, G. Vastola, S. Wang, G. Wong, K. Xu, K. Yokoyama, S. Yu, R. Zhou, and P. De Dobbelaere, “High-speed silicon photonics optical transceivers,” in *IEEE Summer Topicals Meeting Series (SUM), 2015*, Jul. 2015, pp. 23–24.

- [80] C. R. Doerr, L. Chen, D. Vermeulen, T. Nielsen, S. Azemati, S. Stulz, G. McBrien, X.-M. Xu, B. Mikkelsen, M. Givhchi, C. Rasmussen, and S. Y. Park, “Single-chip silicon photonics 100-Gb/s coherent transceiver,” in *Optical Fiber Communication Conference: Postdeadline Papers*. Optical Society of America, 2014, p. Th5C.1.
- [81] S. Hardy, “Acacia Communications IPO a referendum on optical subsystems space?” [Online]. Available: <http://www.lightwaveonline.com/articles/2016/01/acacia-communications-ipo-a-referendum-on-optical-subsystems-space.html>, (Jan. 15, 2016).
- [82] IRIS Project Consortium, “IRIS Project Deliverable 8.1 First Scientific Report,” [Online]. Available: http://www.ict-iris.eu/IRIS_619194_Deliverable_8.1, (Jan. 15, 2016).
- [83] Fujitsu Ltd., “Fujitsu Laboratories Develops 4-Wavelength Integrated Silicon Laser for Inter-Processor Data Transmission,” [Online]. Available: <http://www.fujitsu.com/global/about/resources/news/press-releases/2013/0321-03.html>, (Jan. 15, 2016).
- [84] R. Boeck, L. Chrostowski, and N. A. F. Jaeger, “Theoretical sensitivity analysis of quadruple Vernier racetrack resonators designed for fabrication on the silicon-on-insulator platform,” *Proc. SPIE*, vol. 9288, p. 928812, 2014.
- [85] R. Boeck, L. Chrostowski, and N. A. F. Jaeger, “Sensitivity analysis of silicon-on-insulator quadruple Vernier racetrack resonators,” *Optical Engineering*, vol. 54, no. 11, p. 117102, Nov. 2015.
- [86] B. Peng, Alliance Fiber Optic Products, Inc. personal communication, May 8, 2012.
- [87] Alliance Fiber Optic Products, Inc., “High isolation OADM (100 GHz),” REV. G, Feb. 23, 2006.
- [88] R. Papannareddy, *Lightwave Communication Systems : A Practical Perspective*. Penram International Publishing (India) Pvt. Ltd., 2004.
- [89] H. Simos, C. Mesaritakis, D. Alexandropoulos, and D. Syvridis, “Dynamic analysis of crosstalk performance in microring-based add/drop filters,” *Journal of Lightwave Technology*, vol. 27, no. 12, pp. 2027–2034, Jun. 2009.

- [90] H. Jayatileka, K. Murray, M. Caverley, N. A. F. Jaeger, L. Chrostowski, and S. Shekhar, "Crosstalk in SOI microring resonator-based filters," *Journal of Lightwave Technology*, vol. PP, no. 99, pp. 1–1, Sep. 2015.
- [91] V. Tandon, M. Volanthen, M. van der Vliet, and J. Bonar, "Standardized parameters for AWGs would ease system design," *Lightwave Online*, 2001.
- [92] D. Minoli, *Telecommunications Technology Handbook*. Norwood: Artech House, Inc., 2003.
- [93] ITU Telecommunication Standardization Sector, "Recommendation ITU-T G.671, Transmission characteristics of optical components and subsystems," 2012.
- [94] ITU Telecommunication Standardization Sector., "Recommendation ITU-T G.692, Optical interfaces for multichannel systems with optical amplifiers," 1998.
- [95] "APSS Apollo Application Note on Array Waveguide Grating (AWG)," [Online]. Available: <http://www.apollophoton.com/apollo/APNT/APN-APSS-AWG.pdf>, Apollo Photonics, Inc. 2003., (Jan. 15, 2016).
- [96] R. Boeck, J. Flueckiger, L. Chrostowski, and N. A. F. Jaeger, "Experimental performance of DWDM quadruple Vernier racetrack resonators," *Optics Express*, vol. 21, no. 7, pp. 9103–9112, Apr. 2013.
- [97] R. Boeck, W. Shi, L. Chrostowski, and N. A. F. Jaeger, "FSR-eliminated Vernier racetrack resonators using grating-assisted couplers," *IEEE Photonics Journal*, vol. 5, no. 5, p. 2202511, Oct. 2013.
- [98] Alliance Fiber Optic Products, Inc., "DWDM and CWDM three port device optical parameter definition and test requirements," REV. C, Feb. 24 2005.
- [99] Photonics-USA, "Optical Add/Drop Multiplexers 100 GHz OADM (1x2)," (Jan. 15, 2016).
- [100] Alliance Fiber Optic Products, Inc., "Single Channel DWDM (100 GHz)," REV. G, Mar. 4 2009.
- [101] AOXC Technologies, "Fiber Optic DWDM Single Add/Drop Device," DWDM-100/200-N1.
- [102] AC Photonics, Inc., "100GHz single channel OADM(2x2)," Apr. 11, 2005.

- [103] B. Collings, F. Heismann, and G. Lietaert, "Reference Guide to Fiber Optic Testing: Volume 2," JDS Uniphase Corporation, 2010.
- [104] ITU Telecommunication Standardization Sector, "ITU-T Recommendation G.680, Physical transfer functions of optical network elements," 2007.
- [105] R. Boeck, M. Caverley, L. Chrostowski, and N. A. F. Jaeger, "Experimental demonstration of a silicon-on-insulator high-performance double microring filter using MZI-based coupling," *Optics Letters*, vol. 40, no. 2, pp. 276–279, Jan. 2015.
- [106] K. Bergman, L. P. Carloni, A. Biberman, J. Chan, and G. Hendry, *Photonic Network-on-Chip Design*. Springer, 2014.
- [107] R. Boeck, "Silicon ring resonator add-drop multiplexers," Master's thesis, University of British Columbia, Oct. 2011.
- [108] M. Popović, T. Barwicz, M. R. Watts, P. T. Rakich, L. Socci, E. P. Ippen, F. X. Kärtner, and H. I. Smith, "Multistage high-order microring-resonator filters with relaxed tolerances for high through-port extinction," in *CLEO: 2005*. Optical Society of America, 2005, p. CMP2.
- [109] M. A. Popović, T. Barwicz, M. R. Watts, P. T. Rakich, L. Socci, E. P. Ippen, F. X. Kärtner, and H. I. Smith, "Multistage high-order microring-resonator add-drop filters," *Optics Letters*, vol. 31, no. 17, pp. 2571–2573, Sep. 2006.
- [110] ITU Telecommunication Standardization Sector, "ITU-T Recommendation G.694.1, Spectral grids for WDM applications: DWDM frequency grid," Feb. 2012.
- [111] R. Boeck, J. Flueckiger, H. Yun, L. Chrostowski, and N. A. F. Jaeger, "High performance Vernier racetrack resonators," *Optics Letters*, vol. 37, no. 24, pp. 5199–5201, Dec. 2012.
- [112] M. Popović, "Theory and design of high-index-contrast microphotonic circuits," PhD thesis, Massachusetts Institute of Technology, Feb. 2008.
- [113] M. Romagnoli, L. Socci, L. Bolla, S. Ghidini, P. Galli, C. Rampinini, G. Mutinati, A. Nottola, A. Cabas, S. Doneda, M. Di Muri, R. Morson, T. Tomasi, G. Zuliani, S. Lorenzotti, D. Chacon, S. Marinoni, R. Corsini, F. Giacometti, S. Sardo, M. Gentili, and G. Grasso, "Silicon photonics in Pirelli," *Proc. SPIE*, vol. 6996, p. 699611, 2008.

- [114] L. Socci, S. Ghidini, P. Galli, L. Bolla, and F. Boffi, “Method and device for tunable optical filtering using Vernier effect,” European Union Patent EP 2 181 348 B1, Jan. 18, 2012.
- [115] M. A. Popović, T. Barwicz, M. S. Dahlem, F. Gan, C. W. Holzwarth, P. T. Rakich, H. I. Smith, E. P. Ippen, and F. X. Kärtner, “Tunable, fourth-order silicon microring-resonator add-drop filters,” *33rd European Conference and Exhibition of Optical Communication (ECOC)*, pp. 1–2, 2007.
- [116] C. Ferrari, A. Canciamilla, F. Morichetti, M. Sorel, and A. Melloni, “Penalty-free transmission in a silicon coupled resonator optical waveguide over the full C-band,” *Optics Letters*, vol. 36, no. 19, pp. 3948–3950, Sep. 2011.
- [117] P. Chen, S. Chen, X. Guan, Y. Shi, and D. Dai, “High-order microring resonators with bent couplers for a box-like filter response,” *Optics Letters*, vol. 39, no. 21, pp. 6304–6307, Oct. 2014.
- [118] F. Xia, L. Sekaric, M. O’Boyle, and Y. Vlasov, “Coupled resonator optical waveguides based on silicon-on-insulator photonic wires,” *Applied Physics Letters*, vol. 89, no. 4, p. 041122, Jul. 2006.
- [119] J. R. Ong, R. Kumar, and S. Mookherjea, “Ultra-high-contrast and tunable-bandwidth filter using cascaded high-order silicon microring filters,” *IEEE Photonics Technology Letters*, vol. 25, no. 16, pp. 1543–1546, Aug. 2013.
- [120] F. Xia, M. Rooks, L. Sekaric, and Y. Vlasov, “Ultra-compact silicon WDM optical filters with flat-top response for on-chip optical interconnects,” *2007 Conference on Lasers and Electro-Optics*, p. CTuG3, May 2007.
- [121] S. H. Tao, J. Song, Q. Fang, M. B. Yu, G. Q. Lo, and D. L. Kwong, “50th order series-coupled micro-ring resonator,” *PhotonicsGlobal@Singapore*, pp. 1–3, Dec. 2008.
- [122] Q. Li, M. Soltani, S. Yegnanarayanan, and A. Adibi, “Design and demonstration of compact, wide bandwidth coupled-resonator filters on a silicon-on-insulator platform,” *Optics Express*, vol. 17, no. 4, pp. 2247–2254, Apr. 2009.
- [123] A. Rohit, R. Stabile, and K. A. Williams, “Dynamic routing in a fifth-order ring resonator switch array,” *2012 38th European Conference and Exhibition on Optical Communications (ECOC)*, p. Tu.1.E.1, Sep. 2012.

- [124] P. Prabhathan, V. M. Murukeshan, and J. Zhang, “Optimal detuning combinations in a series coupled silicon micro ring resonator thermo optic-wavelength selective switch,” *Optical Engineering*, vol. 51, no. 4, p. 044604, Apr. 2012.
- [125] M. L. Cooper, G. Gupta, M. A. Schneider, W. M. J. Green, S. Assefa, F. Xia, Y. A. Vlasov, and S. Mookherjea, “Statistics of light transport in 235-ring silicon coupled-resonator optical waveguides,” *Optics Express*, vol. 18, no. 25, pp. 26 505–26 516, Dec. 2010.
- [126] O. Schwelb and I. Frigyes, “Vernier operation of series-coupled optical microring resonator filters,” *Microwave Optical Technology Letters*, vol. 39, no. 4, pp. 257–261, Nov. 2003.
- [127] O. Schwelb, “The nature of spurious mode suppression in extended FSR microring multiplexers,” *Optics Communications*, vol. 271, no. 2, pp. 424–429, Mar. 2007.
- [128] C. Chaichuay, P. P. Yupapin, and P. Saeung, “The serially coupled multiple ring resonator filters and Vernier effect,” *Optica Applicata*, vol. 39, no. 1, pp. 175–194, 2009.
- [129] R. Boeck, N. A. F. Jaeger, N. Rouger, and L. Chrostowski, “Series-coupled silicon racetrack resonators and the Vernier effect: theory and measurement,” *Optics Express*, vol. 18, no. 24, pp. 25 151–25 157, Nov. 2010.
- [130] S. Srinivasan, M. Davenport, T. Komljenovic, J. Hulme, D. T. Spencer, and J. E. Bowers, “Coupled-ring-resonator-mirror-based heterogeneous III-V silicon tunable laser,” *IEEE Photonics Journal*, vol. 7, no. 3, p. 2700908, Jun. 2015.
- [131] T. Claes, W. Bogaerts, and P. Bienstman, “Experimental characterization of a silicon photonic biosensor consisting of two cascaded ring resonators based on the Vernier-effect and introduction of a curve fitting method for an improved detection limit,” *Optics Express*, vol. 18, no. 22, pp. 22 747–22 761, Oct. 2010.
- [132] J. A. Thorsveen and K. Blotekjaer, “High-resolution fringe-counting sensor utilizing the Vernier effect,” *Proc. SPIE*, vol. 3483, pp. 169–173, 1998.
- [133] Y. Yanagase, S. Suzuki, Y. Kokubun, and S. T. Chu, “Vertical triple series-coupled microring resonator filter for passband flattening and

expansion of free spectral range,” *Japanese Journal of Applied Physics*, vol. 41, no. 2A, pp. L141–L143, Feb. 2002.

- [134] S. T. Chu, B. E. Little, V. Van, J. V. Hryniewicz, P. P. Absil, F. G. Johnson, D. Gill, O. King, F. Seiferth, M. Trakalo, and J. Shanton, “Compact full C-band tunable filters for 50 GHz channel spacing based on high order micro-ring resonators,” *Optical Fiber Communication Conference*, p. PD9, 2004.
- [135] L. Zhu, M. Li, J. Ye, and J.-J. He, “Highly-sensitive optical waveguide sensor based on SiON using two cascaded-microring resonators,” in *2012 Asia Communications and Photonics Conference (ACP)*, Nov. 2012, pp. 1–3.
- [136] S. A. Miller, Y. Okawachi, S. Ramelow, K. Luke, A. Dutt, A. Farsi, A. L. Gaeta, and M. Lipson, “Tunable frequency combs based on dual microring resonators,” *Optics Express*, vol. 23, no. 16, pp. 21 527–21 540, Aug. 2015.
- [137] B. Timotijevic, G. Mashanovich, A. Michaeli, O. Cohen, V. M. N. Passaro, J. Crnjanski, and G. T. Reed, “Tailoring the spectral response of add/drop single and multiple resonators in silicon-on-insulator,” *Chinese Optics Letters*, vol. 7, no. 4, pp. 291–295, Apr. 2009.
- [138] M. Popović, “Wide free-spectral-range, widely tunable and hitless-switchable optical channel add-drop filters,” U.S. Patent US8 032 027 B2, Oct. 4, 2011.
- [139] K. Vahala, *Optical Microcavities*. Singapore: World Scientific Publishing Co. Pte. Ltd., 2004.
- [140] Y. Kokubun and T. Kato, “Series-coupled and parallel-coupled add/drop filters and FSR extension,” in *Photonic Microresonator Research and Applications*, ser. Springer Series in Optical Sciences, I. Chremmos, O. Schwelb, and N. Uzunoglu, Eds. Springer US, 2010, no. 156, pp. 87–113.
- [141] A. Sayarath, “Silicon microring resonator-based devices for wavelength-division-multiplexing optical communications,” Master’s thesis, The Hong Kong University of Science and Technology, Dec. 2011.
- [142] D. Zhang, Y. Huang, X. Ren, X. Duan, B. Shen, Q. Wang, X. Zhang, and S. Cai, “Add-drop filters based on asymmetric high-order microring resonators,” *Proc. SPIE*, vol. 8555, p. 85550U, 2012.

- [143] Y. Goebuchi, T. Kato, and Y. Kokubun, "Optimum arrangement of high-order series-coupled microring resonator for crosstalk reduction," *Japanese Journal of Applied Physics*, vol. 45, no. 7, pp. 5769–5774, Jul. 2006.
- [144] S. Dey and S. Mandal, "Modeling and analysis of quadruple optical ring resonator performance as optical filter using Vernier principle," *Optics Communications*, vol. 285, no. 4, pp. 439–446, Feb. 2012.
- [145] I. Bhar, T. Jha, P. Priya, and S. Dey, "Design and simulation of integrated optic ring resonator based devices," *2012 International Conference on Communications, Devices and Intelligent Systems (CODIS)*, pp. 453–456, 2012.
- [146] S. Ghosh, T. Bandyopadhyay, S. Ghosh, A. Bondyopadhyay, and S. Dey, "Comparative analysis of quadruple optical ring resonator based filter using SOI waveguides," *2012 National Conference on Computing and Communication Systems (NCCCS)*, pp. 1–5, 2012.
- [147] S. B. Dey, S. Mandal, and N. N. Jana, "Optical signal processing using linear system theory," *2nd International Conference on Power, Control and Embedded Systems (ICPCES)*, pp. 1–6, 2012.
- [148] S. B. Dey, S. Mandal, and N. N. Jana, "Quadruple optical ring resonator based filter on silicon-on-insulator," *Optik*, vol. 124, no. 17, pp. 2920–2927, Sep. 2013.
- [149] R. Boeck, L. Chrostowski, and N. A. F. Jaeger, "Thermally tunable quadruple Vernier racetrack resonators," *Optics Letters*, vol. 38, no. 14, pp. 2440–2442, Jul. 2013.
- [150] R. Boeck, M. Caverley, L. Chrostowski, and N. A. F. Jaeger, "Silicon quadruple series-coupled Vernier racetrack resonators: experimental signal quality," in *Optical Fiber Communication Conference*. Optical Society of America, 2015, p. W2A.8.
- [151] I. P. Kaminow, P. P. Iannone, J. Stone, and L. W. Stulz, "FDM-FSK star network with a tunable optical filter demultiplexer," *Electronics Letters*, vol. 23, no. 21, pp. 1102–1103, Oct. 1987.
- [152] P. Urquhart, "Compound optical-fiber-based resonators," *Journal of the Optical Society of America A*, vol. 5, no. 6, pp. 803–812, Jun. 1988.

- [153] I. P. Kaminow, P. P. Iannone, J. Stone, and L. W. Stulz, "FDMA-FSK star network with a tunable optical filter demultiplexer," *Journal of Lightwave Technology*, vol. 6, no. 9, pp. 1406–1414, Sep. 1988.
- [154] P. Barnsley, P. Urquhart, C. Millar, and M. Brierley, "Fiber Fox-Smith resonators: application to single-longitudinal-mode operation of fiber lasers," *Journal of the Optical Society of America A*, vol. 5, no. 8, pp. 1339–1346, Aug. 1988.
- [155] I. P. Kaminow, P. P. Iannone, J. Stone, and L. W. Stulz, "A tunable Vernier fiber Fabry-Perot filter for FDM demultiplexing and detection," *IEEE Photonics Technology Letters*, vol. 1, no. 1, pp. 24–26, Jan. 1989.
- [156] A. Frenkel and C. Lin, "Angle-tuned etalon filters for optical channel selection in high density wavelength division multiplexed systems," *Journal of Lightwave Technology*, vol. 7, no. 4, pp. 615–624, Apr. 1989.
- [157] K. Oda, N. Takato, and H. Toba, "A wide-FSR waveguide double-ring resonator for optical FDM transmission systems," *Journal of Lightwave Technology*, vol. 9, no. 6, pp. 728–736, Jun. 1991.
- [158] Y. H. Ja, "A Vernier fiber double-ring resonator with a 3*3 fiber coupler and degenerate two-wave mixing," *IEEE Photonics Technology Letters*, vol. 4, no. 7, pp. 743–745, Jul. 1992.
- [159] H. Okamura and K. Iwatsuki, "Proposal of ultra-high finesse, bi-directional Vernier based on Er-doped fiber ring resonator," in *Optical Fiber Sensors*, ser. Collected Papers of the International Conferences on Optical Fiber Sensors 1983-1997. Optical Society of America, Jan. 1992, p. TH35.
- [160] Y. H. Ja, "Vernier fiber double-ring resonator using degenerate two-wave mixing," *Microwave and Optical Technology Letters*, vol. 5, no. 4, pp. 181–183, Apr. 1992.
- [161] Y. H. Ja, "A Vernier S-shaped fiber double-loop resonator with double couplers and degenerate two-wave mixing," *Journal of Lightwave Technology*, vol. 11, no. 2, pp. 258–264, Feb. 1993.
- [162] G. Barbarossa, M. N. Armenise, and A. M. Matteo, "Novel architecture for wide free-spectral range optical resonator for frequency division multiplexing transmission systems," *Proc. SPIE*, vol. 2150, pp. 211–219, 1994.

- [163] J. Zhang and J. W. Y. Lit, "All-fiber compound ring resonator with a ring filter," *Journal of Lightwave Technology*, vol. 12, no. 7, pp. 1256–1262, Jul. 1994.
- [164] J. Capmany, "Amplified double recirculating delay line using a 3x3 coupler," *Journal of Lightwave Technology*, vol. 12, no. 7, pp. 1136–1143, Jul. 1994.
- [165] K. Oda, S. Suzuki, H. Takahashi, and H. Toba, "An optical FDM distribution experiment using a high finesse waveguide-type double ring resonator," *IEEE Photonics Technology Letters*, vol. 6, no. 8, pp. 1031–1034, Aug. 1994.
- [166] Y. H. Ja, "Optical vernier filter with two single 3x3 planar coupler fiber ring resonators in tandem," *Applied optics*, vol. 33, no. 27, pp. 6409–6411, Sep. 1994.
- [167] S. Suzuki, K. Oda, and Y. Hibino, "Integrated-optic double-ring resonators with a wide free spectral range of 100 GHz," *Journal of Lightwave Technology*, vol. 13, no. 8, pp. 1766–1771, Aug. 1995.
- [168] Y. H. Ja, "Optical vernier filter with fiber grating Fabry-Perot resonators," *Applied Optics*, vol. 34, no. 27, pp. 6164–6167, Sep. 1995.
- [169] G. Barbarossa, A. M. Matteo, and M. N. Armenise, "Theoretical analysis of triple-coupler ring-based optical guided-wave resonator," *Journal of Lightwave Technology*, vol. 13, no. 2, pp. 148–157, Feb. 1995.
- [170] S. Shimada, *Coherent Lightwave Communications Technology*. Springer-Science+Business Media, B.V., 1995.
- [171] W. Weiershausen and R. Zengerle, "Photonic highway switches based on ring resonators used as frequency-selective components," *Applied Optics*, vol. 35, no. 30, pp. 5967–5978, Oct. 1996.
- [172] J. Zhang, C.-Y. Yue, G. Schinn, W. R. L. Clements, and J. W. Y. Lit, "Stable single-mode compound-ring erbium-doped fiber laser," *Journal of Lightwave Technology*, vol. 14, no. 1, pp. 104–109, Jan. 1996.
- [173] J. Martin and J. Capmany, "Transfer functions of double- and multiple-cavity Fabry-Perot filters driven by Lorentzian sources," *Applied Optics*, vol. 35, no. 36, pp. 7108–7111, Dec. 1996.

- [174] Y. Zhao and C. Shu, "Multi-wavelength lasing oscillation of a Vernier-type unidirectional Er^{3+} -doped fiber compound ring," *Applied Physics Letters*, vol. 70, no. 25, pp. 3344–3346, Jun. 1997.
- [175] G. Barbarossa and A. M. Matteo, "Novel double-ring optical-guided-wave Vernier resonator," *IEE Proceedings - Optoelectronics*, vol. 144, no. 4, pp. 203–208, Aug. 1997.
- [176] K. Blotekjaer, "Theoretical concepts of a novel Vernier-based fringe-counting fibre optic sensor," *IEE Proceedings - Optoelectronics*, vol. 144, no. 3, pp. 126–129, Jun. 1997.
- [177] O. Schwelb, "Generalized analysis for a class of linear interferometric networks. part II: simulations," *IEEE Transactions on Microwave Theory and Techniques*, vol. 46, no. 10, pp. 1409–1418, Oct. 1998.
- [178] H. A. Haus, "Microwaves and photonics," in *Symposium on Electro-Optics: Present and Future*, ser. OSA Trends in Optics and Photonics, T. Li, Ed., vol. 23. Optical Society of America, Apr. 1998, p. CB1.
- [179] C.-C. Lee, Y.-K. Chen, and S.-K. Liaw, "Single-longitudinal-mode fiber laser with a passive multiple-ring cavity and its application for video transmission," *Optics Letters*, vol. 23, no. 5, pp. 358–360, Mar. 1998.
- [180] S.-T. Chu, B. E. Little, W. Pan, T. Kaneko, and Y. Kokubun, "Cascaded microring resonators for crosstalk reduction and spectrum cleanup in add-drop filters," *IEEE Photonics Technology Letters*, vol. 11, no. 11, pp. 1423–1425, Nov. 1999.
- [181] G. Lenz and C. K. Madsen, "General optical all-pass filter structures for dispersion control in WDM systems," *Journal of Lightwave Technology*, vol. 17, no. 7, pp. 1248–1254, Jul. 1999.
- [182] M. Sorel, S. Gluck, and P. J. R. Laybourn, "Semiconductor double ring waveguide resonators," *Electronics Letters*, vol. 35, no. 18, pp. 1551–1552, Sep. 1999.
- [183] B. Ortega, J. Capmany, and J. L. Cruz, "Wavelength division multiplexing all-fiber hybrid devices based on Fabry-Perot's and gratings," *Journal of Lightwave Technology*, vol. 17, no. 7, pp. 1241–1247, Jul. 1999.
- [184] Z. Hu, L. Zheng, Y. Zhang, and Q. Tang, "Composite cavity semiconductor fiber ring laser," *Optics Letters*, vol. 25, no. 7, pp. 469–471, Apr. 2000.

- [185] I. Ribet, A. Godard, C. Ventalon, C. Simonneau, E. Rosencher, and M. Lefebvre, "Pulsed single-mode doubly resonant optical parametric oscillator based on the Vernier effect," in *2000 Conference on Lasers and Electro-Optics Europe. Conference Digest*, Sep. 2000, p. CThH4.
- [186] Y. Yanagase, S. Suzuki, Y. Kokubun, and S.-T. Chu, "Box-like filter response by vertically series coupled microring resonator filter," in *27th European Conference on Optical Communication, 2001. ECOC '01*, vol. 4, 2001, pp. 634–635.
- [187] O. Schwelb, "Interferometric circuits: analysis, configurations, applications," *Proc. SPIE*, vol. 4417, pp. 131–141, 2001.
- [188] D. H. Geuzebroek, E. J. Klein, H. Kelderman, F. S. Tan, D. J. W. Klunder, and A. Driessen, "Thermally tuneable, wide FSR switch based on micro-ring resonators," *Proc. Symp. IEEE/LEOS Benelux Chapter*, pp. 155–158, 2002.
- [189] I. S. Hidayat, Y. Toyota, O. Torigoe, O. Wada, and R. Koga, "Application of transfer matrix method with signal flow-chart to analyze optical multi-path ring-resonator," *Memoirs of the Faculty of Engineering, Okayama University*, vol. 36, no. 2, pp. 73–82, Mar. 2002.
- [190] Y. Yanagase, S. Suzuki, Y. Kokubun, and S. T. Chu, "Box-like filter response and expansion of FSR by a vertically triple coupled microring resonator filter," *Journal of Lightwave Technology*, vol. 20, no. 8, pp. 1525–1529, Aug. 2002.
- [191] F. Rana, C. Manolatu, and R. J. Ram, "Microring resonator based widely tunable semiconductor lasers," in *Integrated Photonics Research*, ser. OSA Trends in Optics and Photonics, A. Sawchuk, Ed., vol. 78. Optical Society of America, Jul. 2002, p. IFH3.
- [192] Y. Meng, Z. Huang, and L. Wang, "Multifunction double-ring resonant optical comb filter," *Proc. SPIE*, vol. 4906, pp. 81–89, 2002.
- [193] S. T. Chu, T. Kaneko, Y. Kokubun, B. E. Little, W. Pan, and S. Sato, "Optical waveguide wavelength filter with ring resonator and 1xN optical waveguide wavelength filter," European Patent Application EP1 176 438 A1, Jan. 30, 2002.
- [194] B. Liu, A. Shakouri, and J. E. Bowers, "Wide tunable double ring resonator coupled lasers," *IEEE Photonics Technology Letters*, vol. 14, no. 5, pp. 600–602, May 2002.

- [195] D. G. Rabus, "Realization of optical filters using ring resonators with integrated semiconductor optical amplifiers in GaInAsP / InP," Ph.D. dissertation, Technical University Berlin, 2002.
- [196] L. R. Dalton, B. H. Robinson, R. Nielsen, A. K. Jen, D. Casmier, P. Rabiei, and W. H. Steier, "Organic electro-optics: exploiting the best of electronics and photonics," *Proc. SPIE*, vol. 4991, pp. 508–519, 2003.
- [197] Y. Kokubun, "Three-dimensional integration of vertically coupled microring resonator filters: fabrication and wavelength trimming technologies," *Proc. SPIE*, vol. 4944, pp. 1–14, 2003.
- [198] O. Schwelb and I. Frigyes, "A design for a high finesse parallel-coupled microring resonator filter," *Microwave and Optical Technology Letters*, vol. 38, no. 2, pp. 125–129, Jul. 2003.
- [199] B. Little, "Advances in microring resonators," in *Integrated Photonics Research*, ser. OSA Trends in Optics and Photonics, A. Sawchuk, Ed., vol. 91. Optical Society of America, Jun. 2003, p. ITuE6.
- [200] W. H. Steier, H.-C. Song, Y.-H. Kuo, P. Rabiei, S.-W. Ahn, M.-C. Oh, H. R. Fetterman, C. Zhang, L. R. Dalton, and A. K. Y. Jen, "Advances in polymer waveguide devices," in *The 16th Annual Meeting of the IEEE Lasers and Electro-Optics Society, 2003. LEOS 2003*, vol. 2, Oct. 2003, pp. 748–749.
- [201] P. Rabiei and W. H. Steier, "Tunable double micro-ring (DMR) filters for widely tunable lasers," *11th European Conference on Integrated Optics*, p. FrB3.1, 2003.
- [202] I. S. Hidayat, Y. Toyota, O. Torigoe, O. Wada, and R. Koga, "Multipath structure for FSR expansion in waveguide-based optical ring resonator," *Electronics Letters*, vol. 39, no. 4, pp. 366–367, Feb. 2003.
- [203] P. Rabiei and W. H. Steier, "Tunable polymer double micro-ring filters," *IEEE Photonics Technology Letters*, vol. 15, no. 9, pp. 1255–1257, Sep. 2003.
- [204] L. Bach, J. P. Reithmaier, A. Forchel, J.-L. Gentner, and L. Goldstein, "Wavelength stabilized single-mode lasers by coupled micro-square resonators," *IEEE Photonics Technology Letters*, vol. 15, no. 3, pp. 377–379, Mar. 2003.

- [205] S.-J. Choi, Z. Peng, Q. Yang, S.-J. Choi, and P. D. Dapkus, "All-buried active microring resonators using vernier effects for free spectral range expansion and optical channel configuration," in *2004 Digest of the LEOS Summer Topical Meetings Biophotonics/Optical Interconnects and VLSI Photonics/WBM Microcavities*, Jun. 2004, p. 2.
- [206] B. Liu and A. Shakouri, "Narrow linewidth, low frequency chirping and broad wavelength tunable ring resonator coupled lasers," U.S. Patent US6 680 962 B2, Jan. 20, 2004.
- [207] J. K. S. Poon, J. Scheuer, and A. Yariv, "Wavelength-selective reflector based on a circular array of coupled microring resonators," *IEEE Photonics Technology Letters*, vol. 16, no. 5, pp. 1331–1333, May 2004.
- [208] S. Srivastava and K. Srinivasan, "Signal flow graphs in the analysis and design of fiber optical resonating structures," 2004.
- [209] L. Binh, "A Venier double ring shape-8 optically amplified resonator," *Department of Electrical and Computer Systems Engineering Technical Report MECSE-33-2004*, 2004.
- [210] S. T. Chu, B. E. Little, J. V. Hryniewicz, F. G. Johnson, O. King, D. Gill, W. Chen, and W. Chen, "High index contrast photonics platform," *Proc. SPIE*, vol. 6014, p. 60140E, 2005.
- [211] S.-J. Choi, Z. Peng, Q. Yang, E. H. Hwang, and P. D. Dapkus, "A semiconductor tunable laser using a wavelength selective reflector based on ring resonators," in *Optical Fiber Communication Conference and Exposition and The National Fiber Optic Engineers Conference*, ser. Technical Digest (CD). Optical Society of America, Mar. 2005, p. PDP20.
- [212] Y. Goebuchi, T. Kato, and Y. Kokubun, "Expansion of tuning range of wavelength selective switch using Vernier effect of series coupled microring resonator," *The 18th Annual Meeting of the IEEE Lasers and Electro-Optics Society (LEOS)*, pp. 734–735, 2005.
- [213] A. A. Savchenkov, V. S. Ilchenko, A. B. Matsko, and L. Maleki, "High-order tunable filters based on a chain of coupled crystalline whispering gallery-mode resonators," *IEEE Photonics Technology Letters*, vol. 17, no. 1, pp. 136–138, Jan. 2005.
- [214] S. June, Choi, P. D. Dapkus, Q. Yang, Z. Peng, S.-J. Choi, and E. H. Hwang, "High-Q buried heterostructure resonators for photonic integrated

- circuits,” in *Conference on Lasers and Electro-Optics, 2005. (CLEO)*, vol. 1, May 2005, pp. 553–555.
- [215] A. Driessen, R. Dekker, M. B. J. Diemeer, D. H. Geuzebroek, H. J. W. M. Hoekstra, E. J. Klein, and A. Leinse, “Microresonators as promising building blocks for VLSI photonics,” *Proc. SPIE*, vol. 5956, p. 59560Q, 2005.
- [216] S. J. Choi, Z. Peng, Q. Yang, S. J. Choi, and P. D. Dapkus, “Tunable narrow linewidth all-buried heterostructure ring resonator filters using Vernier effects,” *IEEE Photonics Technology Letters*, vol. 17, no. 1, pp. 106–108, Jan. 2005.
- [217] T. Barwicz, “Accurate Nanofabrication Techniques for High-Index-Contrast Microphotonic Devices,” PhD thesis, Massachusetts Institute of Technology, 2005.
- [218] L. Kolodziejski and G. S. Petrich, “Tunable optical add/drop multiplexer with multi-function optical amplifiers,” U.S. Patent US6 888 973 B2, May 3, 2005.
- [219] Y. Kokubun, “Vertically coupled microring resonator filter for integrated add/drop node,” *IEICE TRANSACTIONS on Electronics*, vol. E88-C, no. 3, pp. 349–362, Mar. 2005.
- [220] G. T. Reed, W. R. Headley, F. Y. Gardes, B. D. Timotijevic, S. P. Chan, and G. Z. Mashanovich, “Characteristics of rib waveguide racetrack resonators in SOI,” *Proc. SPIE*, vol. 6183, p. 61830G, 2006.
- [221] O. Schwelb, “Phase-matched lossy microring resonator add/drop multiplexers,” *Proc. SPIE*, vol. 6343, p. 63433P, 2006.
- [222] P. Koonath, T. Indukuri, and B. Jalali, “3-D integrated Vernier filters in silicon,” in *Integrated Photonics Research and Applications/Nanophotonics*, ser. Technical Digest (CD). Optical Society of America, Apr. 2006, p. IMG1.
- [223] S. Mandal, K. Dasgupta, T. K. Basak, and S. K. Ghosh, “A generalized approach for modeling and analysis of ring-resonator performance as optical filter,” *Optics Communications*, vol. 264, no. 1, pp. 97–104, Aug. 2006.

- [224] Z. Bian, W. J. He, D. G. Rabus, and A. Shakouri, "A wavelength-tunable monolithically integrated double ring resonator coupled laser," in *Conference on Lasers and Electro-Optics, 2006 and 2006 Quantum Electronics and Laser Science Conference. CLEO/QELS 2006*, May 2006, pp. 1–2.
- [225] Y. Goebuchi, T. Kato, and Y. Kokubun, "Fast and stable wavelength-selective switch using double-series coupled dielectric microring resonator," *IEEE Photonics Technology Letters*, vol. 18, no. 3, pp. 538–540, Feb. 2006.
- [226] Y. Kokubun, "Integrated microring resonator circuits for large-scale optical cross-connects," *Proc. SPIE*, vol. 6352, p. 635201, 2006.
- [227] B. D. Timotijevic, G. T. Reed, R. Jones, A. Liu, A. Michaeli, and G. Z. Mashanovich, "Optical filters in silicon-on-insulator: design considerations for devices based upon strip and rib waveguides," *Proc. SPIE*, vol. 6350, p. 63500K, 2006.
- [228] J. Scheuer, M. Margalit, and D. Bortman-Arbiv, "Integrated optical filters utilizing resonators," U.S. Patent US7 065 276 B2, Jun. 20, 2006.
- [229] M. Margalit, M. Yasin, and M. Orenstein, "Optical filtering device and method," U.S. Patent US7 149 381 B2, Dec. 12, 2006.
- [230] Y. Chung, D.-G. Kim, and N. Dagli, "Reflection properties of coupled-ring reflectors," *Journal of Lightwave Technology*, vol. 24, no. 4, pp. 1865–1874, Apr. 2006.
- [231] M. A. Popović, E. P. Ippen, and F. X. Kärtner, "Universally balanced photonic interferometers," *Optics Letters*, vol. 31, no. 18, pp. 2713–2715, Aug. 2006.
- [232] M. Ishizaka and H. Yamazaki, "Wavelength tunable laser using silica double ring resonators," *Electronics and Communications in Japan (Part II: Electronics)*, vol. 89, no. 3, pp. 34–41, Mar. 2006.
- [233] B. D. Timotijevic, G. T. Reed, R. Jones, A. Michaeli, A. Liu, and G. Z. Mashanovich, "Small optical filters in silicon-on-insulator," in *3rd IEEE International Conference on Group IV Photonics, 2006*, Sept 2006, pp. 25–27.

- [234] B. D. Timotijevic, D. Thomson, F. Y. Gardes, S. Howe, A. Michaeli, J. V. Crnjanski, V. M. N. Passaro, G. Z. Mashanovich, G. T. Reed, and D. Ikuesan, "Tailoring the response and temperature characteristics of multiple serial-coupled resonators in silicon on insulator," *Proc. SPIE*, vol. 6477, p. 64770B, 2007.
- [235] O. Schwelb, "An overview of recent developments in microring resonator based photonic circuits," *Mikrotalasna revija*, vol. 13, no. 2, pp. 26–33, Dec. 2007.
- [236] Y. Kokubun, "High index contrast optical waveguides and their applications to microring filter circuit and wavelength selective switch," *IEICE TRANSACTIONS on Electronics*, vol. E90-C, no. 5, pp. 1037–1045, May 2007.
- [237] D. G. Rabus, *Integrated Ring Resonators - The Compendium*. Berlin Heidelberg: Springer-Verlag, 2007.
- [238] O. Schwelb, "Invariant resonance splitting in stand-alone multiring resonators," in *Integrated Photonics and Nanophotonics Research and Applications / Slow and Fast Light*, ser. OSA Technical Digest (CD). Optical Society of America, Jul. 2007, p. ITuA5.
- [239] T. T. Le and L. W. Cahill, "Photonic signal processing using MMI coupler-based microring resonators," in *The 20th Annual Meeting of the IEEE Lasers and Electro-Optics Society, 2007. LEOS 2007, 2007*, pp. 395–396.
- [240] O. Schwelb, "Resonance splitting and its invariance in coupled optical microring resonators," *Proc. SPIE*, vol. 6796, p. 67962P, 2007.
- [241] T. Kakitsuka, S. Matsuo, T. Segawa, and H. Suzuki, "Semiconductor tunable lasers based on integrated waveguide filters for wavelength routing applications," in *Integrated Photonics and Nanophotonics Research and Applications / Slow and Fast Light*, ser. OSA Technical Digest (CD). Optical Society of America, Jul. 2007, p. IMA1.
- [242] Z. Peng, "Coupled multiple micro-resonators design and active semiconductor micro-resonator fabrication," PhD thesis, University of Southern California, 2007.
- [243] R. Todt, S. Watanabe, Y. Deki, M. Takahashi, T. Takeuchi, S. Takaesu, T. Miyazaki, M. Horie, H. Yamazaki, and H. Yamazaki, "Widely tunable

resonated-ring-reflector lasers covering C- and L-bands,” in *2007 33rd European Conference and Exhibition of Optical Communication - Post-Deadline Papers (published 2008)*, Sep. 2007, pp. 1–2.

- [244] G. Sun, D. S. Moon, and Y. Chung, “Theoretical analysis of feedback high birefringence fiber loop mirror with dramatically enhanced free spectral range,” *Proc. SPIE*, vol. 6781, p. 678131, 2007.
- [245] T. Segawa, S. Matsuo, T. Kakitsuka, T. Sato, Y. Kondo, and H. Suzuki, “Tunable double-ring-resonator-coupled laser over full C-band with low tuning current,” in *IEEE 19th International Conference on Indium Phosphide Related Materials, 2007. IPRM '07*, May 2007, pp. 598–601.
- [246] M. Takahashi, T. Takeuchi, Y. Deki, S. Takaesu, M. Horie, T. Miyazaki, M. Kurihara, S. Watanabe, K. Suzuki, N. Sakuma, A. Kawauchi, and H. Yamazaki, “Tunable lasers based on silica waveguide ring resonators,” in *Conference on Optical Fiber Communication and the National Fiber Optic Engineers Conference, 2007. OFC/NFOEC 2007*, Mar. 2007, pp. 1–3.
- [247] P. Saeung and P. P. Yupapin, “Vernier effect of multiple-ring resonator filters modeling by a graphical approach,” *Optical Engineering*, vol. 46, no. 7, p. 075005, Jul. 2007.
- [248] Y. Deki, T. Hatanaka, M. Takahashi, T. Takeuchi, S. Watanabe, S. Takaesu, T. Miyazaki, M. Horie, and H. Yamazaki, “Wide-wavelength tunable lasers with 100 ghz fsr ring resonators,” *Electronics Letters*, vol. 43, no. 4, pp. 225–226, Feb. 2007.
- [249] H. Lee, G.-W. Kim, J.-O. Park, S.-H. Kim, and Y.-C. Chung, “Widely tunable wavelength-selective reflector using polymer waveguide double-ring-resonator add/drop filter and loop-back mirror,” *Journal of the Optical Society of Korea*, vol. 12, no. 3, pp. 157–161, Sept. 2008.
- [250] L. Zhang, M. Song, T. Wu, L. Zou, R. G. Beausoleil, and A. E. Willner, “Embedded ring resonators for microphotonic applications,” *Optics Letters*, vol. 33, no. 17, pp. 1978–1980, Sep. 2008.
- [251] L. Y. M. Tobing, D. C. S. Lim, P. Dumon, R. Baets, and M.-K. Chin, “Experimental verification of finesse enhancement scheme in two-ring resonator system,” *Proc. SPIE*, vol. 6996, p. 69960B, 2008.
- [252] L. Y. M. Tobing, D. C. S. Lim, P. Dumon, R. Baets, and M.-K. Chin, “Finesse enhancement in silicon-on-insulator two-ring resonator system,” *Applied Physics Letters*, vol. 92, no. 10, p. 101122, Mar. 2008.

- [253] J. E. Heebner, R. Grover, and T. Ibrahim, *Optical microresonators: theory, fabrication, and applications*. Springer, 2008.
- [254] Y.-W. Choi and D.-G. Kim, “Micro resonator sensor,” U.S. Patent Application US 2008/0 266 573 A1, Oct. 30, 2008.
- [255] T. Segawa, S. Matsuo, T. Kakitsuka, Y. Shibata, T. Sato, Y. Kondo, and R. Takahashi, “Monolithically integrated filter-free wavelength converter with widely tunable double-ring resonator coupled laser,” in *20th International Conference on Indium Phosphide and Related Materials, 2008. IPRM 2008*, May 2008, pp. 1–4.
- [256] L. Y. M. A. L. Tobing and M.-K. Chin, “Optical buffering scheme based on two-ring resonator system,” *Proc. SPIE*, vol. 6996, p. 69961G, 2008.
- [257] L. Y. Mario, S. Darmawan, P. Dumon, R. Baets, and M.-K. Chin, “Transmission properties and application of a two-ring one-bus building block,” in *2nd IEEE International Nanoelectronics Conference, 2008. INEC 2008.*, Mar. 2008, pp. 217–221.
- [258] J. Park, T. Lee, D. Lee, S. Kim, W. Hwang, and Y. Chung, “Widely tunable coupled-ring-reflector filter based on planar polymer waveguide,” *IEEE Photonics Technology Letters*, vol. 20, no. 12, pp. 988–990, Jun. 2008.
- [259] T. Chu, N. Fujioka, S. Nakamura, M. Tokushima, and M. Ishizaka, “Compact, low power consumption wavelength tunable laser with silicon photonic-wire waveguide micro-ring resonators,” in *35th European Conference on Optical Communication, 2009. ECOC '09*, Sep. 2009, pp. 1–2.
- [260] T. Chu, N. Fujioka, and M. Ishizaka, “Compact, lower-power-consumption wavelength tunable laser fabricated with silicon photonic-wire waveguide micro-ring resonators,” *Optics Express*, vol. 17, no. 16, pp. 14 063–14 068, Jul. 2009.
- [261] T. Segawa, S. Matsuo, T. Kakitsuka, Y. Shibata, T. Sato, Y. Kawaguchi, Y. Kondo, and R. Takahashi, “Dynamic operation of a monolithic wavelength-routing switch using double-ring-resonator-coupled tunable laser diodes,” in *International Conference on Photonics in Switching, 2009. PS '09*, Sep. 2009, pp. 1–2.
- [262] D. Dai, “Highly sensitive digital optical sensor based on cascaded high-Q ring-resonators,” *Optics Express*, vol. 17, no. 26, pp. 23 817–23 822, Dec. 2009.

- [263] L. Jin, M. Li, and J.-J. He, "Highly-sensitive optical sensor using two cascaded-microring resonators with Vernier effect," in *2009 Asia Communications and Photonics Conference and Exhibition (ACP)*, Nov. 2009, p. AS4E.2.
- [264] S. Matsuo and T. Segawa, "Microring-resonator-based widely tunable lasers," *IEEE Journal of Selected Topics in Quantum Electronics*, vol. 15, no. 3, pp. 545–554, May 2009.
- [265] H. Lee, G. Kim, S. Kim, and Y. Chung, "Widely tunable PLC-based polymer double-ring-resonator add/drop reflection filter," in *Conference on Lasers Electro Optics The Pacific Rim Conference on Lasers and Electro-Optics, 2009. CLEO/PACIFIC RIM '09.*, Aug. 2009, pp. 1–2.
- [266] T. Segawa, S. Matsuo, T. Kakitsuka, T. Sato, Y. Kondo, and R. Takahashi, "Semiconductor double-ring-resonator-coupled tunable laser for wavelength routing," *IEEE Journal of Quantum Electronics*, vol. 45, no. 7, pp. 892–899, Jul. 2009.
- [267] A. Kapsalis, D. Syvridis, M. Hamacher, and H. Heidrich, "Broadly tunable laser using double-rings vertically coupled to a passive waveguide," *IEEE Journal of Quantum Electronics*, vol. 46, no. 3, pp. 306–312, Mar. 2010.
- [268] T. Chu, N. Fujioka, M. Tokushima, S. Nakamura, and M. Ishizaka, "C and L bands wavelength tunable laser with silicon photonic-wire waveguide micro-ring resonators," in *Integrated Photonics Research, Silicon and Nanophotonics and Photonics in Switching*, ser. OSA Technical Digest (CD). Optical Society of America, Jul. 2010, p. IME1.
- [269] N. Fujioka, T. Chu, and M. Ishizaka, "Compact and low power consumption hybrid integrated wavelength tunable laser module using silicon waveguide resonators," *Journal of Lightwave Technology*, vol. 28, no. 21, pp. 3115–3120, Nov. 2010.
- [270] R. Boeck, N. A. F. Jaeger, and L. Chrostowski, "Experimental demonstration of the Vernier effect using series-coupled racetrack resonators," *2010 International Conference on Optical MEMS and Nanophotonics (OPT MEMS)*, pp. 1–2, 2010.
- [271] L. Jin, M. Li, and J.-J. He, "Experimental investigation of waveguide sensor based on cascaded-microring resonators with Vernier effect," in *Conference on Lasers and Electro-Optics 2010*, ser. OSA Technical Digest (CD). Optical Society of America, May 2010, p. JWA84.

- [272] T. Chu, N. Fujioka, M. Tokushima, S. Nakamura, and M. Ishizaka, "Full C and L bands wavelength tunable laser module with silicon micro-ring resonators," in *2010 15th OptoElectronics and Communications Conference (OECC)*, July 2010, pp. 866–867.
- [273] M. Popovic and M. R. Watts, "Hitless tuning and switching of optical resonator amplitude and phase responses," U.S. Patent Application US20 100 209 038 A1, Aug. 19, 2010.
- [274] T. Okamoto, K. Mizutani, K. Tsuruoka, S. Sudo, M. Sato, K. Kudo, T. Kato, and K. Sato, "Monolithic integration of a 10 Gb/s Mach-Zehnder modulator and a widely tunable laser based on a 2-ring loop-filter," in *2010 International Conference on Indium Phosphide Related Materials (IPRM)*, May 2010, pp. 1–4.
- [275] T. Segawa and S. Matsuo, "Monolithically integrated wavelength-routing switch with double-ring-resonator-coupled tunable lasers," in *Integrated Photonics Research, Silicon and Nanophotonics and Photonics in Switching*, ser. OSA Technical Digest (CD). Optical Society of America, Jul. 2010, p. ITuC2.
- [276] T. Matsumoto, A. Suzuki, M. Takahashi, S. Watanabe, S. Ishii, K. Suzuki, T. Kaneko, H. Yamazaki, and N. Sakuma, "Narrow spectral linewidth full band tunable laser based on waveguide ring resonators with low power consumption," in *Optical Fiber Communication Conference*, ser. OSA Technical Digest (CD). Optical Society of America, Mar. 2010, p. OThQ5.
- [277] K. Lee, S. D. Lim, C. H. Kim, J. H. Lee, Y.-G. Han, and S. B. Lee, "Noise reduction in multiwavelength SOA-based ring laser by coupled dual cavities for WDM applications," *Journal of Lightwave Technology*, vol. 28, no. 5, pp. 739–745, Mar. 2010.
- [278] W. Li and J. Sun, "Optical vernier filter with cascaded double-coupler compound fiber loop resonators," *Optik - International Journal for Light and Electron Optics*, vol. 121, no. 15, pp. 1370–1375, Sep. 2010.
- [279] K. S. Hyun, "Single mode lasing in MMI coupled square semiconductor ring resonators," in *2010 12th International Conference on Transparent Optical Networks (ICTON)*, Jun. 2010, pp. 1–4.
- [280] G. Sun, Y. Zhou, Y. Hu, and Y. Chung, "Theoretical analysis of Sagnac loop mirror with an inline high birefringence fiber ring resonator:

Application in single-frequency fiber lasers,” *Optical Fiber Technology*, vol. 16, no. 2, pp. 86–89, Mar. 2010.

- [281] H. Yamazaki, “Tunable laser with multiple ring resonator and mode filter,” European Patent EP1 708 323 B1, Jan. 6, 2010.
- [282] K. Suzuki and H. Yamazaki, “Tunable resonator, tunable light source using the same, and method for tuning wavelength of multiple resonator,” U.S. Patent US7 701 983 B2, Apr. 20, 2010.
- [283] H. Lee, Y. Lee, G. Kim, S. Kim, and Y. Chung, “Widely tunable double-ring resonator add/drop reflection filter based on polymer PLC,” *Microwave and Optical Technology Letters*, vol. 52, no. 4, pp. 852–855, Apr. 2010.
- [284] A. Sayarath and A. W. Poon, “Proposed high-speed electro-optical hitless reconfigurable demultiplexer using feedback-waveguides coupled to microring resonators,” *The 12th IEEE Photonics Society Hong Kong Chapter Postgraduate Conference*, pp. 1–3, 2011.
- [285] K. Kasai, M. Nakazawa, and H. Yamazaki, “Absolute frequency stabilization of a laser diode based on triple ring resonators to an C2H2 absorption line,” in *17th Microoptics Conference (MOC)*, Oct. 2011, pp. 1–2.
- [286] J. Hu and D. Dai, “Cascaded-ring optical sensor with enhanced sensitivity by using suspended Si-nanowires,” *IEEE Photonics Technology Letters*, vol. 23, no. 13, pp. 842–844, Jul. 2011.
- [287] G. Ren, T. Cao, and S. Chen, “Design and analysis of a cascaded microring resonator-based thermo-optical tunable filter with ultralarge free spectrum range and low power consumption,” *Optical Engineering*, vol. 50, no. 7, p. 074601, Jul. 2011.
- [288] L. Jin, M. Li, and J.-J. He, “Highly-sensitive silicon-on-insulator sensor based on two cascaded micro-ring resonators with vernier effect,” *Optics Communications*, vol. 284, no. 1, pp. 156–159, Jan. 2011.
- [289] L. S. Stewart and P. D. Dapkus, “In-plane thermally tuned silicon on insulator wavelength selective reflector,” in *2011 IEEE Winter Topicals (WTM)*, Jan. 2011, pp. 123–124.

- [290] M. Mancinelli, R. Guider, P. Bettotti, M. Masi, M. R. Vanacharla, J. Fedeli, D. V. Thourhout, and L. Pavesi, "Optical characterization of silicon-on-insulator-based single and coupled racetrack resonators," *Journal of Nanophotonics*, vol. 5, no. 1, p. 051705, Jun. 2011.
- [291] L. Jin, M. Li, and J.-J. He, "Optical waveguide double-ring sensor using intensity interrogation with a low-cost broadband source," *Optics Letters*, vol. 36, no. 7, pp. 1128–1130, Mar. 2011.
- [292] J.-J. He, L. Jin, and M. Li, "The 'Lord of the Rings' of optical biosensors," *SPIE Newsroom*, Sep. 2011.
- [293] T. Claes, W. Bogaerts, and P. Bienstman, "Vernier-cascade silicon photonic label-free biosensor with very large sensitivity and low-cost interrogation," *Proc. SPIE*, vol. 8099, p. 80990R, 2011.
- [294] Y. Lee, H. Lee, G. Kim, S. Lee, and Y. Chung, "Widely tunable optical source hybrid-integrated with wavelength-selective double-ring-resonator reflector," *Microwave and Optical Technology Letters*, vol. 53, no. 4, pp. 924–927, Apr. 2011.
- [295] Y. Li and A. W. Poon, "Analytical methods of strong-coupled microring coupled-resonator optical waveguides," *The 12th IEEE Photonics Society Hong Kong Chapter Postgraduate Conference*, pp. 1–2, 2011.
- [296] V. M. N. Passaro, B. Troia, and F. De Leonardis, "A generalized approach for design of photonic gas sensors based on Vernier-effect in mid-IR," *Sensors and Actuators B: Chemical*, vol. 168, pp. 402–420, Jun. 2012.
- [297] T. Segawa, T. Sato, R. Iga, S. Matsuo, and R. Takahashi, "A novel tunable laser with flat-output wideband tuning based on parallel ring resonators," in *2012 International Conference on Photonics in Switching (PS)*, Sep. 2012, pp. 1–3.
- [298] L. Jin, M. Li, and J.-J. He, "Analysis of wavelength and intensity interrogation methods in cascaded double-ring sensors," *Journal of Lightwave Technology*, vol. 30, no. 12, pp. 1994–2002, Jun. 2012.
- [299] C. Sirawattananon, M. Bahadoran, J. Ali, S. Mitatha, and P. P. Yupapin, "Analytical Vernier effects of a PANDA ring resonator for microforce sensing application," *IEEE Transactions on Nanotechnology*, vol. 11, no. 4, pp. 707–712, Jul. 2012.

- [300] B. Troia, V. M. N. Passaro, F. D. Leonardis, and A. V. Tsarev, "Design of efficient photonic sensors based on vernier effect in near-IR," *16th European Conference on Integrated Optics (ECIO 2012)*, 2012.
- [301] P. Prabhathan, Z. Jing, V. M. Murukeshan, Z. Huijuan, and C. Shiyi, "Discrete and fine wavelength tunable thermo-optic WSS for low power consumption C+L band tunability," *IEEE Photonics Technology Letters*, vol. 24, no. 2, pp. 152–154, Jan. 2012.
- [302] S. B. Dey, S. Mandal, and N. N. Jana, "Enhancement of free spectral range using pentuple microresonator," *Applied Optics*, vol. 51, no. 29, pp. 6901–6912, Oct. 2012.
- [303] R. Xu, S. Liu, Q. Sun, P. Lu, and D. Liu, "Experimental characterization of a Vernier strain sensor using cascaded fiber rings," *IEEE Photonics Technology Letters*, vol. 24, no. 23, pp. 2125–2128, Dec. 2012.
- [304] K. Kulrod, C. Sirawattananon, S. Mitatha, K. Srinuanjan, and P. P. Yupapin, "Force sensing device design using a modified add-drop filter," *Procedia Engineering*, vol. 32, pp. 291–298, Mar. 2012.
- [305] S. Dey and S. Mandal, "Enhancement of free spectral range in optical triple ring resonator: A Vernier principle approach," *1st International Conference on Recent Advances in Information Technology (RAIT)*, pp. 246–250, 2012.
- [306] X. Jiang, J. Song, L. Jin, and J.-J. He, "High-sensitivity silicon photonic biosensors based on cascaded resonators," *Proc. SPIE*, vol. 8564, p. 85640Y, 2012.
- [307] J.-J. He, "Intensity interrogated planar waveguide biosensors," in *International Photonics and Optoelectronics Meetings*, ser. OSA Technical Digest (online). Optical Society of America, Nov. 2012, p. IF3B.1.
- [308] J. Song, L. Wang, L. Jin, X. Xia, Q. Kou, S. Bouchoule, and J.-J. He, "Intensity-interrogated sensor based on cascaded Fabry Perot laser and microring resonator," *Journal of Lightwave Technology*, vol. 30, no. 17, pp. 2901–2906, Sep. 2012.
- [309] B. Troia, V. M. N. Passaro, and F. D. Leonardis, "Investigation of wide-FSR SOI optical filters operating in C and L bands," *Telfor Journal*, vol. 4, no. 1, pp. 37–42, 2012.

- [310] B. Troia, F. D. Leonardis, and V. M. N. Passaro, "Design of integrated photonic sensor based on Vernier effect for very sensitive chemical surface sensing," in *Proceedings of the 2012 Annual Symposium of the IEEE Photonics Society Benelux Chapter*, Nov. 2012, pp. 1–4.
- [311] S. Mandal and S. Dey, "Modeling and analysis of multiple ring resonator performance as optical filter," *Proc. SPIE*, vol. 8264, p. 82640J, 2012.
- [312] K. Nemoto, T. Kita, and H. Yamada, "Narrow spectral linewidth wavelength tunable laser with Si photonic-wire waveguide ring resonators," in *2012 IEEE 9th International Conference on Group IV Photonics (GFP)*, Aug. 2012, pp. 216–218.
- [313] J.-J. He, L. Jin, and M. Li, "Optical sensor based on a broadband light source and cascaded waveguide filters," U.S. Patent Application US2012/0 298 849 A1, Nov. 29, 2012.
- [314] L. Qin, L. Wang, M. Li, and J.-J. He, "Optical sensor based on Vernier-cascade of ring resonator and echelle diffraction grating," *IEEE Photonics Technology Letters*, vol. 24, no. 11, pp. 954–956, Jun. 2012.
- [315] T. Segawa, W. Kobayashi, S. Matsuo, T. Sato, R. Iga, and R. Takahashi, "Parallel-ring-resonator tunable laser integrated with electroabsorption modulator for 100-Gb/s (25-Gb/s x 4) optical packet switching," in *European Conference and Exhibition on Optical Communication*, ser. OSA Technical Digest (online). Optical Society of America, Sep. 2012, p. Mo.1.E.1.
- [316] I. Khan, "Design consideration analysis of optical filters based on multiple ring resonator," *International Journal of Electronics & Informatics*, vol. 1, no. 1, pp. 8–13, Aug. 2012.
- [317] W. S. Fegadolli, G. Vargas, X. Wang, F. Valini, L. A. M. Barea, J. E. B. Oliveira, N. Frateschi, A. Scherer, V. R. Almeida, and R. R. Panepucci, "Reconfigurable silicon thermo-optical ring resonator switch based on Vernier effect control," *Optics Express*, vol. 20, no. 13, pp. 14 722–14 733, Jun. 2012.
- [318] Y. Lu, C. Hao, B. Lu, X. Huang, B. Wu, and J. Yao, "Transmission and group delay in a double microring resonator reflector," *Optics Communications*, vol. 285, no. 21-22, pp. 4567–4570, Oct. 2012.

- [319] R. D. Mansoor, H. Sasse, and A. P. Duffy, "Analysis of optical ring resonator add/drop filters," *Proc. of the 62nd IWCS Conference*, pp. 471–475, 2013.
- [320] V. Zamora, P. Lutzow, M. Weiland, and D. Pergande, "A highly sensitive refractometric sensor based on cascaded SiN microring resonators," *Sensors*, vol. 13, no. 11, pp. 14 601–14 610, Oct. 2013.
- [321] V. Zamora, P. Lutzow, D. Pergande, and H. Heidrich, "Cascaded microring resonators for biomedical applications: improved sensitivity at large tuning range," *Proc. SPIE*, vol. 8570, p. 857002, 2013.
- [322] X. Jiang, J. Ye, J. Zou, M. Li, and J.-J. He, "Cascaded silicon-on-insulator double-ring sensors operating in high-sensitivity transverse-magnetic mode," *Optics Letters*, vol. 38, no. 8, pp. 1349–1351, Apr. 2013.
- [323] V. Raghunathan, "Athermal Photonic Devices and Circuits on a Silicon Platform," PhD thesis, Massachusetts Institute of Technology, 2013.
- [324] J. C. Hulme, J. K. Doylend, and J. E. Bowers, "Widely tunable Vernier ring laser on hybrid silicon," *Optics Express*, vol. 21, no. 17, pp. 19 718–19 722, 2013.
- [325] J. Dong, L. Liu, D. Gao, Y. Yu, A. Zheng, T. Yang, and X. Zhang, "Compact notch microwave photonic filters using on-chip integrated microring resonators," *IEEE Photonics Journal*, vol. 5, no. 2, p. 5500307, Apr. 2013.
- [326] H. Yan, X. Feng, D. Zhang, K. Cui, F. Liu, and Y. Huang, "Compact optical add-drop multiplexers with parent-sub ring resonators on SOI substrates," *IEEE Photonics Technology Letters*, vol. 25, no. 15, pp. 1462–1465, Aug. 2013.
- [327] C. Gentry and M. Popovic, "Dark state lasers," in *CLEO: 2013*, ser. OSA Technical Digest (online). Optical Society of America, Jun. 2013, p. CM3F.1.
- [328] R. Dey, J. Doylend, J. Ackert, A. Evans, P. Jessop, and A. Knights, "Demonstration of a wavelength monitor comprised of racetrack-ring resonators with defect mediated photodiodes operating in the C-band," *Optics Express*, vol. 21, no. 20, pp. 23 450–23 458, Sep. 2013.

- [329] M. Bahadoran, J. Ali, and P. P. Yupapin, “Graphical approach for nonlinear optical switching by PANDA Vernier filter,” *IEEE Photonics Technology Letters*, vol. 25, no. 15, pp. 1470–1473, Aug. 2013.
- [330] S. Tan, L. Xiang, J. Zou, Q. Zhang, Z. Wu, Y. Yu, J. Dong, and X. Zhang, “High-order all-optical differential equation solver based on microring resonators,” *Optics Letters*, vol. 38, no. 19, pp. 3735–3738, Oct. 2013.
- [331] H. Yan, X. Feng, D. Zhang, and Y. Huang, “Integrated optical add-drop multiplexer based on a compact parent-sub microring-resonator structure,” *Optics Communications*, vol. 289, pp. 53–59, Feb. 2013.
- [332] V. Zamora, P. Lutzow, M. Weiland, and D. Pergande, “Investigation of cascaded SiN microring resonators at 1.3 μm and 1.5 μm ,” *Optics Express*, vol. 21, no. 23, pp. 27 550–27 557, Nov. 2013.
- [333] S. Qin, P. Cho, D. H. Park, V. Yun, Y. Leng, P.-T. Ho, J. Goldhar, W. N. Herman, and J. T. Fourkas, “MAP-fabricated acrylic double ring resonators (DRRs) with expanded free spectral range (FSR),” *2013 Conference on Lasers and Electro-Optics (CLEO)*, p. CF2I.3, 2013.
- [334] T. Kita, K. Nemoto, and H. Yamada, “Narrow spectral linewidth and high output power Si photonic wavelength tunable laser diode,” in *2013 IEEE 10th International Conference on Group IV Photonics (GFP)*, Aug. 2013, pp. 152–153.
- [335] E. H. W. Chan, “Noise investigation of a large free spectral range high-resolution microwave photonic signal processor,” *IEEE Photonics Journal*, vol. 5, no. 6, pp. 5 502 109–5 502 109, 2013.
- [336] D. Bachman, Z. Chen, R. Fedosejevs, Y. Y. Tsui, and V. Van, “Permanent fine tuning of silicon microring devices by femtosecond laser surface amorphization and ablation,” *Optics Express*, vol. 21, no. 9, pp. 11 048–11 056, Apr. 2013.
- [337] D. Bachman, Z. Chen, R. Fedosejevs, Y. Y. Tsui, and V. Van, “Permanent tuning of high-Q silicon microring resonators by Fs laser surface modification,” in *2013 Conference on Lasers and Electro-Optics Pacific Rim (CLEO-PR)*, Jun. 2013, pp. TuPM–8.
- [338] M. H. M. Salleh, A. Glidle, M. Sorel, J. Reboud, and J. M. Cooper, “Polymer dual ring resonators for label-free optical biosensing using microfluidics,” *Chemical Communications*, vol. 49, no. 30, pp. 3095–3097, Apr. 2013.

- [339] Z. Huang and Y. Wang, "Selectable heterogeneous integrated III-V /SOI single mode laser based on Vernier effect," in *2013 Conference on Lasers and Electro-Optics Pacific Rim (CLEO-PR)*, Jun. 2013, pp. TuPM-3.
- [340] T. Kita, K. Nemoto, K. Watanabe, H. Yamazaki, and H. Yamada, "Si photonic wavelength tunable laser diode for digital coherent optical communication," in *2013 18th OptoElectronics and Communications Conference held jointly with 2013 International Conference on Photonics in Switching (OECC/PS)*, Jun. 2013, pp. WM1-3.
- [341] C. Ciminelli, C. E. Campanella, F. Dell'Olio, C. M. Campanella, and M. N. Armenise, "Theoretical investigation on the scale factor of a triple ring cavity to be used in frequency sensitive resonant gyroscopes," *Journal of the European Optical Society Rapid Publications*, vol. 8, p. 13050, Jul. 2013.
- [342] L. Ding, X. Jiang, C. Yang, and J.-J. He, "Thermally-tuned silicon double ring resonator for external cavity tunable laser," in *PIERS Proceedings*, Aug. 2014, pp. 822-825.
- [343] X. Zhang, L. Zhou, L. Lu, J. Xie, X. Sun, X. Li, and J. Chen, "Tunable Vernier microring optical filters using p-i-p resistor-based micro-heaters," *Optical Fiber Communication Conference/National Fiber Optic Engineers Conference*, p. OTu3C.7, 2013.
- [344] L. Zhou, X. Zhang, L. Lu, and J. Chen, "Tunable Vernier microring optical filters with p-i-p-type microheaters," *IEEE Photonics Journal*, vol. 5, no. 4, p. 6601211, Aug. 2013.
- [345] M. La Notte and V. M. N. Passaro, "Ultra high sensitivity chemical photonic sensing by Mach-Zehnder interferometer enhanced Vernier-effect," *Sensors and Actuators B: Chemical*, vol. 176, pp. 994-1007, Jan. 2013.
- [346] "Vernier effect based dual-micro-ring resonator optical biochemical sensing chip," Patent Application CN103 308 476 A, Sep. 18, 2013. [Online]. Available: <http://www.google.com/patents/CN103308476A?cl=en>
- [347] S. Chiangga, S. Pitakwongsaporn, T. D. Frank, and P. P. Yupapin, "Optical bistability investigation in a nonlinear silicon microring circuit," *Journal of Lightwave Technology*, vol. 31, no. 7, pp. 1101-1105, Apr. 2013.

- [348] P. Bienstman, T. Claes, and W. Bogaerts, “Vernier photonic sensor data-analysis,” U.S. Patent Application US20 130 094 029 A1, Apr. 18, 2013.
- [349] X. Zhang, Z. quan Li, and K. Tong, “A compact cascaded microring filter with two master rings and two slave rings for sensing application,” *Optoelectronics Letters*, vol. 10, no. 1, pp. 16–20, Jan. 2014.
- [350] M. Ren, H. Cai, Y. D. Gu, P. Kropelnicki, A. B. Randles, and A. Q. Liu, “A tunable laser based on nano-opto-mechanical system,” in *2014 IEEE 27th International Conference on Micro Electro Mechanical Systems (MEMS)*, Jan. 2014, pp. 1143–1146.
- [351] L. Liu, J. Dong, T. Yang, X. Zhang, and D. Gao, “Comparison analysis of microwave photonic filter using SOI microring and microdisk resonators,” *Proc. SPIE*, vol. 8985, p. 898515, 2014.
- [352] C. M. Gentry and M. A. Popović, “Dark state lasers,” *Optics Letters*, vol. 39, no. 14, pp. 4136–4139, Jul. 2014.
- [353] V. D. Ta, R. Chen, and H. Sun, “Flexible microresonators: lasing and sensing,” *Proc. SPIE*, vol. 8960, p. 89600E, 2014.
- [354] T. Kita, K. Nemoto, and H. Yamada, “Silicon photonic wavelength-tunable laser diode with asymmetric Mach-Zehnder interferometer,” *IEEE Journal of Selected Topics in Quantum Electronics*, vol. 20, no. 4, pp. 344–349, Jul. 2014.
- [355] V. Zamora, P. Lutzow, M. Weiland, D. Pergande, and H. Schroder, “Highly sensitive integrated optical biosensors,” *Proc. SPIE*, vol. 8933, p. 893307, 2014.
- [356] B. Troia and V. M. N. Passaro, “Investigation of a novel silicon-on-insulator rib-slot photonic sensor based on the vernier effect and operating at 3.8 μm ,” *Journal of the European Optical Society Rapid Publications*, vol. 9, p. 14005, Jan. 2014.
- [357] S. Lakra and S. Mandal, “Modeling and performance analysis of vertically coupled triple microring resonator in the Z domain,” *Applied Optics*, vol. 53, no. 36, pp. 8381–8388, Dec. 2014.
- [358] D. Dai and J. E. Bowers, “Silicon-based on-chip multiplexing technologies and devices for peta-bit optical interconnects,” *Nanophotonics*, vol. 3, no. 4-5, pp. 283–311, Aug. 2014.

- [359] K. Sato, N. Kobayashi, M. Namiwaka, K. Yamamoto, T. Kita, H. Yamada, and H. Yamazaki, "High output power and narrow linewidth silicon photonic hybrid ring-filter external cavity wavelength tunable lasers," in *2014 European Conference on Optical Communication (ECOC)*, Sept. 2014, p. PD.2.3.
- [360] B. Troia, V. M. N. Passaro, A. Z. Khokhar, M. Nedeljkovic, J. S. Penades, and G. Z. Mashanovich, "Design and fabrication of silicon cascade-coupled ring resonators operating in mid infrared," in *2014 Fotonica AEIT Italian Conference on Photonics Technologies*, May 2014, pp. 1–4.
- [361] H. Debregeas, C. Ferrari, M. A. Cappuzzo, F. Klemens, R. Keller, F. Pardo, C. Bolle, C. Xie, and M. P. Earnshaw, "2kHz Linewidth C-Band Tunable Laser by Hybrid Integration of Reflective SOA and SiO₂ PLC External Cavity," in *2014 International Semiconductor Laser Conference (ISLC)*, Sept. 2014, pp. 50–51.
- [362] G. Fan, Y. Li, C. Hu, L. Lei, D. Zhao, H. Li, Y. Luo, and Z. Zhen, "Model of Vernier devices in silicon-on-insulator technology," *Infrared Physics & Technology*, vol. 65, pp. 83–86, 2014.
- [363] M. Ren, H. Cai, J. F. Tao, Y. D. Gu, K. Radhakrishnan, Z. C. Yang, D. L. Kwong, and A. Q. Liu, "An integrated tunable laser using nano-silicon-photonic circuits," in *2014 IEEE International Electron Devices Meeting (IEDM)*, Dec. 2014, pp. 15.6.1–15.6.4.
- [364] R. Tang, T. Kita, and H. Yamada, "Narrow spectral linewidth Si photonic wavelength tunable laser diode for digital coherent optical communication," in *2014 International Semiconductor Laser Conference (ISLC)*, Sept. 2014, pp. 96–97.
- [365] T. Segawa, W. Kobayashi, T. Nakahara, and R. Takahashi, "Wavelength-Routed Switching for 25-Gbit/s Optical Packets Using a Compact Transmitter Integrating a Parallel-Ring-Resonator Tunable Laser and an InGaAlAs EAM," *IEICE TRANSACTIONS on Electronics*, vol. E97-C, no. 7, pp. 719–724, Jul. 2014.
- [366] T. Kita, R. Tang, and H. Yamada, "Wide-band wavelength tunable laser diode with Si photonic filter," in *2014 International Semiconductor Laser Conference (ISLC)*, Sept. 2014, pp. 149–150.

- [367] T. Kita, K. Nemoto, and H. Yamada, "Long external cavity Si photonic wavelength tunable laser diode," *Japanese Journal of Applied Physics*, vol. 53, no. 4S, p. 04EG04, Jan. 2014.
- [368] M. La Notte, B. Troia, T. Muciaccia, C. E. Campanella, F. De Leonardis, and V. M. N. Passaro, "Recent advances in gas and chemical detection by Vernier effect-based photonic sensors," *Sensors*, vol. 14, no. 3, pp. 4831–4855, Mar. 2014.
- [369] J. Xie, L. Zhou, X. Sun, Z. Zou, L. Lu, H. Zhu, X. Li, and J. Chen, "Selective excitation of microring resonances using a pulley-coupling structure," *Applied Optics*, vol. 53, no. 5, pp. 878–884, Feb. 2014.
- [370] Y. Liu, J.-L. Yu, W.-R. Wang, H.-G. Pan, and E.-Z. Yang, "Single longitudinal mode Brillouin fiber laser with cascaded ring Fabry-Perot resonator," *IEEE Photonics Technology Letters*, vol. 26, no. 2, pp. 169–172, 2014.
- [371] T. Kita, R. Tang, and H. Yamada, "Compact silicon photonic wavelength-tunable laser diode with ultra-wide wavelength tuning range," *Applied Physics Letters*, vol. 106, no. 11, p. 111104, Mar. 2015.
- [372] S. Mandal and S. Lakra, "Z-domain modeling and analysis of vertically coupled triple asymmetrical optical micro ring resonator (VCTAOMRR)," *Proc. SPIE*, vol. 9598, p. 95980F, 2015.
- [373] M. Sun, L. Wu, X. Xiong, X. Liao, and J.-J. He, "Double half-wave-coupled rectangular ring-FP semiconductor laser with 19-nm quasi-continuous tuning range," in *CLEO: 2015*. Optical Society of America, 2015, p. SF11.5.
- [374] A. Ouariach, K. Ghoumid, R. Malek, A. E. Moussati, A. Nougououi, and T. Gharbi, "Multiband filter at adjustable free spectral range by convolution of transfer functions according to the Vernier effect," *IET Optoelectronics*, Sep. 2015.
- [375] H. Gevorgyan, K. A. Qubaisi, M. Dahlem, and A. Khilo, "Time-wavelength pulse interleaver on a silicon platform," in *Advanced Photonics 2015*. Optical Society of America, 2015, p. IM2A.2.
- [376] M. Bahadoran, A. F. A. Noorden, K. Chaudhary, M. S. Aziz, J. Ali, and P. Yupapin, "Nano force sensing using symmetric double stage micro resonator," *Measurement*, vol. 58, pp. 215–220, Dec. 2014.

- [377] R. Tang, T. Kita, and H. Yamada, "Narrow-spectral-linewidth silicon photonic wavelength-tunable laser with highly asymmetric Mach-Zehnder interferometer," *Optics Letters*, vol. 40, no. 7, pp. 1504–1507, Apr. 2015.
- [378] Y. Chen, F. Yu, C. Yang, J. Song, L. Tang, M. Li, and J.-J. He, "Label-free biosensing using cascaded double-microring resonators integrated with microfluidic channels," *Optics Communications*, vol. 344, pp. 129–133, Jun. 2015.
- [379] T.-R. Kim, H.-S. Kim, J. Li, G.-Y. Oh, D.-G. Kim, and Y.-W. Choi, "Ultra-high sensitivity optical biosensor based on Vernier effect in triangular ring resonators (TRRs) with SPR," *Proc. SPIE*, vol. 9357, p. 93571A, 2015.
- [380] G. Z. Mashanovich, M. Nedeljkovic, J. Soler Penades, C. J. Mitchell, A. Z. Khokhar, C. J. Littlejohns, S. Stankovic, B. Troia, Y. Wang, S. Reynolds, V. M. N. Passaro, L. Shen, N. Healy, A. C. Peacock, C. Alonso-Ramos, A. Ortega-Monux, G. Wanguemert-Perez, I. Molina-Fernandez, D. J. Rowe, J. S. Wilkinson, P. Cheben, J. J. Ackert, A. P. Knights, D. J. Thomson, and F. Y. Gardes, "Group IV mid-infrared photonics," *Proc. SPIE*, vol. 9367, p. 93670Q, 2015.
- [381] G. Z. Mashanovich, F. Y. Gardes, D. J. Thomson, Y. Hu, K. Li, M. Nedeljkovic, J. Soler Penades, A. Z. Khokhar, C. J. Mitchell, S. Stankovic, R. Topley, S. A. Reynolds, Y. Wang, B. Troia, V. M. N. Passaro, C. G. Littlejohns, T. Dominguez Bucio, P. R. Wilson, and G. T. Reed, "Silicon photonic waveguides and devices for near- and mid-IR applications," *IEEE Journal of Selected Topics in Quantum Electronics*, vol. 21, no. 4, pp. 407–418, Jul. 2015.
- [382] X. Xiao, X. Li, X. Feng, K. Cui, F. Liu, and Y. Huang, "Eight-channel optical add-drop multiplexer with cascaded parent-sub microring resonators," *IEEE Photonics Journal*, vol. 7, no. 4, p. 7801307, Aug. 2015.
- [383] X. Gu, D. Zhu, S. Li, Y. Zhao, and S. Pan, "Photonic RF channelization based on series-coupled asymmetric double-ring resonator filter," in *2014 IEEE 7th International Conference on Advanced Infocomm Technology (ICAIT)*, Nov. 2014, pp. 240–244.
- [384] M. Ren, H. Cai, L. K. Chin, K. Radhakrishnan, Y. Gu, G.-Q. Lo, D. L. Kwong, and A. Q. Liu, "Coupled-ring reflector in an external-cavity tunable laser," *Optica*, vol. 2, no. 11, pp. 940–943, Nov. 2015.

- [385] C. Errando-Herranz, F. Niklaus, G. Stemme, and K. B. Gylfason, "Low-power microelectromechanically tunable silicon photonic ring resonator add-drop filter," *Optics Letters*, vol. 40, no. 15, pp. 3556–3559, Aug. 2015.
- [386] G. de Valicourt, G. Levaufre, Y. Pointurier, A. Le Liepvre, J.-C. Antona, C. Jany, A. Accard, F. Lelarge, D. Make, and G.-H. Duan, "Direct modulation of hybrid-integrated InP/Si transmitters for short and long reach access network," *Journal of Lightwave Technology*, vol. 33, no. 8, pp. 1608–1616, Apr. 2015.
- [387] Y. Li, Q. Li, Y. Liu, T. Baehr-Jones, M. Hochberg, and K. Bergman, "Integrated on-chip C-band optical spectrum analyzer using dual-ring resonators," in *CLEO: 2015*. Optical Society of America, 2015, p. SM11.4.
- [388] B. Dong, H. Cai, M. Tang, Y. D. Gu, Z. C. Yang, Y. F. Jin, Y. L. Hao, D. L. Kwong, and A. Q. Liu, "NEMS integrated photonic system using nano-silicon-photonic circuits," in *2015 Transducers - 2015 18th International Conference on Solid-State Sensors, Actuators and Microsystems (TRANSDUCERS)*, Jun. 2015, pp. 997–1000.
- [389] J. C. Hulme, J. K. Doyle, M. J. R. Heck, J. D. Peters, M. L. Davenport, J. T. Bovington, L. A. Coldren, and J. E. Bowers, "Fully integrated hybrid silicon two dimensional beam scanner," *Optics Express*, vol. 23, no. 5, pp. 5861–5874, Mar. 2015.
- [390] G.-M. Parsanasab, M. Moshkani, and A. Gharavi, "Femtosecond laser direct writing of single mode polymer micro ring laser with high stability and low pumping threshold," *Optics Express*, vol. 23, no. 7, pp. 8310–8316, Apr. 2015.
- [391] R. Bruck, B. Mills, D. J. Thomson, B. Troia, V. M. N. Passaro, G. Z. Mashanovich, G. T. Reed, and O. L. Muskens, "Picosecond optically reconfigurable filters exploiting full free spectral range tuning of single ring and Vernier effect resonators," *Optics Express*, vol. 23, no. 9, pp. 12 468–12 477, May 2015.
- [392] L. Liu, J. Dong, and X. Zhang, "Chip-integrated all-optical 4-bit Gray code generation based on silicon microring resonators," *Optics Express*, vol. 23, no. 16, pp. 21 414–21 423, Aug. 2015.

- [393] B. Troia, A. Z. Khokhar, M. Nedeljkovic, S. A. Reynolds, Y. Hu, G. Z. Mashanovich, and V. M. N. Passaro, "Design procedure and fabrication of reproducible silicon Vernier devices for high-performance refractive index sensing," *Sensors*, vol. 15, no. 6, p. 13548, 2015.
- [394] L. Liu, J. Dong, D. Gao, A. Zheng, and X. Zhang, "On-chip passive three-port circuit of all-optical ordered-route transmission," *Scientific Reports*, vol. 5, p. 10190, 2015.
- [395] T. Baehr-Jones, Y. Liu, R. Ding, and M. J. Hochberg, "Operation and stabilization of mod-mux WDM transmitters based on silicon microrings," U.S. Patent Application US 2015/0 104 176 A1, Apr. 16, 2015.
- [396] T. Komljenovic, M. Davenport, S. Srinivasan, J. Hulme, and J. E. Bowers, "Narrow linewidth tunable laser using coupled resonator mirrors," in *Optical Fiber Communication Conference*. Optical Society of America, 2015, p. W2A.52.
- [397] S. Dey, "Microring resonator for WDM filter applications," in *2015 International Conference on Industrial Instrumentation and Control (ICIC)*, May 2015, pp. 133–138.
- [398] K. R. Oh, "Resonator, variable wavelength optical filter, and variable wavelength laser diode," U.S. Patent US 9 008 134 B2, Apr. 14, 2015.
- [399] S. Addya and S. Dey, "Design and analysis of optical filter using series coupled racetrack resonator," in *2015 IEEE 2nd International Conference on Recent Trends in Information Systems (ReTIS)*, Jul. 2015, pp. 76–80.
- [400] T. Komljenovic and J. Bowers, "Monolithically integrated high-Q rings for narrow linewidth widely tunable lasers," *IEEE Journal of Quantum Electronics*, vol. 51, no. 11, pp. 1–10, Nov. 2015.
- [401] R. Mansoor and A. Duffy, "Review of progress in optical ring resonators with crosstalk modelling in OADMS," *2015 IWCS Conference*, 2015.
- [402] J. W. Hicks, Jr., "Adscitious resonator," U.S. Patent US4 676 583 A, Jun. 30, 1987.
- [403] D. R. Huber and J. B. Carroll, "Time domain response of an optically frequency swept Fabry-Perot interferometer," *Applied Optics*, vol. 25, no. 14, pp. 2386–2390, Jul. 1986.

- [404] K. L. Belsley, J. B. Carroll, L. A. Hess, D. R. Huber, and D. Schmadel, “Optically multiplexed interferometric fiber optic sensor system,” *Proc. SPIE*, vol. 0566, pp. 257–264, 1986.
- [405] R. Mock, B. Hillebrands, and R. Sandercock, “Construction and performance of a Brillouin scattering set-up using a triple-pass tandem Fabry-Perot interferometer,” *Journal of Physics E: Scientific Instruments*, vol. 20, no. 6, p. 656, Jan. 1987.
- [406] L. W. Bin, “Signal Flow Graph Theory and Its Applications in the Analysis of Optical Ring Resonator,” PhD thesis, Huazhong University of Science and Technology, 2009.
- [407] L. Zhuang, M. Hoekman, W. Beeker, A. Leinse, R. Heideman, P. van Dijk, and C. Roeloffzen, “Novel low-loss waveguide delay lines using Vernier ring resonators for on-chip multi- λ microwave photonic signal processors,” *Laser & Photonics Reviews*, vol. 7, no. 6, pp. 994–1002, Nov. 2013.
- [408] J. T. Kindt and R. C. Bailey, “Biomolecular analysis with microring resonators: applications in multiplexed diagnostics and interaction screening,” *Current Opinion in Chemical Biology*, vol. 17, no. 5, pp. 818 – 826, Oct. 2013.
- [409] R. Bruck, B. Mills, B. Troia, D. J. Thomson, F. Y. Gardes, Y. Hu, G. Z. Mashanovich, V. M. N. Passaro, G. T. Reed, and O. L. Muskens, “Device-level characterization of the flow of light in integrated photonic circuits using ultrafast photomodulation spectroscopy,” *Nature Photonics*, vol. 9, no. 1, pp. 54–60, Jan. 2015.
- [410] O. A. Mrayat and M. S. Rasras, “A digital-like on-chip photonics sensor,” in *Frontiers in Optics 2015*. Optical Society of America, 2015, p. JW2A.78.
- [411] L. Wu, X. Liao, Z. Hu, and J.-J. He, “Double half-wave-coupled rectangular ring-FP laser with 35 x 100 GHz wavelength tuning,” *IEEE Photonics Technology Letters*, vol. 27, no. 10, pp. 1076–1079, May 2015.
- [412] D. V. Orden, A. Mizrahi, T. Creazzo, and S. B. Krasulick, “Tunable reflectors based on multi-cavity interference,” U.S. Patent Application US 2015/0 331 184 A1, Nov. 19, 2015.
- [413] H. Chandralalim and X. Fan, “Reconfigurable solid-state dye-doped polymer ring resonator lasers,” *Scientific Reports*, vol. 5, p. 18310, 2015.

- [414] Y. Liu, Y. Hsu, C.-W. Hsu, L.-G. Yang, C.-W. Chow, C.-H. Yeh, Y.-C. Lai, and H.-K. Tsang, "Narrow line-width single-longitudinal-mode fiber laser using silicon-on-insulator based micro-ring-resonator," *Laser Physics Letters*, vol. 13, no. 2, p. 025102, 2015.
- [415] E. J. Klein, "Densely integrated microring-resonator based components for fiber-to-the-home applications," PhD thesis, University of Twente, 2007.
- [416] X. Jiang, "Silicon nanowire waveguide sensor based on two cascaded ring resonators," in *Asia Communications and Photonics Conference*, ser. OSA Technical Digest (online). Optical Society of America, Nov. 2012, p. AS4E.3.
- [417] B. Troia, A. Z. Khokhar, M. Nedeljkovic, J. S. Penades, V. M. N. Passaro, and G. Z. Mashanovich, "Cascade-coupled racetrack resonators based on the Vernier effect in the mid-infrared," *Optics Express*, vol. 22, no. 20, pp. 23 990–24 003, Oct. 2014.
- [418] J. H. Lee, I. Shubin, J. Yao, J. Bickford, Y. Luo, S. Lin, S. S. Djordjevic, H. D. Thacker, J. E. Cunningham, K. Raj, X. Zheng, and A. V. Krishnamoorthy, "High power and widely tunable Si hybrid external-cavity laser for power efficient Si photonics WDM links," *Optics Express*, vol. 22, no. 7, pp. 7678–7685, Apr. 2014.
- [419] X. Gu, D. Zhu, Y. Zhao, and S. Pan, "Series-coupled double-ring resonators with asymmetric radii for use in channelizer," *Proc. SPIE*, vol. 9270, p. 927010, 2014.
- [420] N. Feng, X. Sun, and D. Zheng, "Tunable optical system with hybrid integrated laser," U.S. Patent US 8,831,049 B2, Sept. 9, 2014.
- [421] A. V. Krishnamoorthy, X. Zheng, G. Li, and J. E. Cunningham, "Optical device with reduced thermal tuning energy," U.S. Patent US 8,768,170 B2, Jul. 1, 2014.
- [422] H. Tanaka, T. Ishikawa, and T. Machida, "Method for tuning semiconductor laser," U.S. Patent US 8,681,826 B2, Mar. 25, 2014.
- [423] M. Bahadoran, J. Ali, and P. Yupapin, *Vernier effect for optical microring resonator*. Lap Lambert Academic Publishing GmbH KG, 2013.
- [424] L. Vivien and L. Pavesi, *Handbook of Silicon Photonics*. CRC Press, 2013.

- [425] P. Yupapin and J. Ali, *Small Scale Optics*. CRC Press, 2013.
- [426] P. Yupapin, C. Teeka, and J. Ali, *Nanoscale Nonlinear PANDA Ring Resonator*. CRC Press, 2012.
- [427] L. A. Coldren, S. W. Corzine, and M. L. Masanovic, *Diode Lasers and Photonic Integrated Circuits*. John Wiley & Sons, Inc., 2012.
- [428] D. Mahmudin, T. T. Estu, P. Daud, I. D. P. Hermida, G. Sugandi, Y. N. Wijayanto, P. S. Menon, and S. Shaari, "Sensitivity improvement of multipath optical ring resonators using silicon-on-insulator technology," in *2015 IEEE Regional Symposium on Micro and Nanoelectronics (RSM)*, Aug 2015, pp. 1–4.
- [429] C.-C. Lee, Y. K. Chen, S.-K. Liaw, F. Tsai, C. S. Wang, and Y. K. Tu, "Single-longitudinal-mode fiber laser using passive multiple-ring-cavity technique," *Proc. SPIE*, vol. 3420, pp. 253–257, 1998.
- [430] H. Jayatilleka, R. Boeck, K. Murray, J. Flueckiger, L. Chrostowski, N. A. F. Jaeger, and S. Shekhar, "Automatic wavelength tuning of series-coupled Vernier racetrack resonators on SOI," in *Optical Fiber Communication Conference*. Optical Society of America, 2016, p. Th3J.5.
- [431] P. Dong, W. Qian, H. Liang, R. Shafiiha, N.-N. Feng, D. Feng, X. Zheng, A. V. Krishnamoorthy, and M. Asghari, "Low power and compact reconfigurable multiplexing devices based on silicon microring resonators," *Optics Express*, vol. 18, no. 10, pp. 9852–9858, May 2010.
- [432] M. R. Watts, T. Barwicz, M. A. Popović, P. T. Rakich, L. Socci, E. P. Ippen, H. I. Smith, and F. Kaertner, "Microring-resonator filter with doubled free-spectral-range by two-point coupling," *Conference on Lasers and Electro-Optics/Quantum Electronics and Laser Science and Photonic Applications Systems Technologies*, p. CMP3, 2005.
- [433] H. L. R. Lira, C. B. Poitras, and M. Lipson, "CMOS compatible reconfigurable filter for high bandwidth non-blocking operation," *Optics Express*, vol. 19, no. 21, pp. 20 115–20 121, Oct. 2011.
- [434] W. Shi, "Silicon photonic filters for wavelength-division multiplexing and sensing applications," PhD thesis, University of British Columbia, Aug. 2012.

- [435] R. Boeck, M. Caverley, L. Chrostowski, and N. A. F. Jaeger, "Process calibration method for designing silicon-on-insulator contra-directional grating couplers," *Optics Express*, vol. 23, no. 8, pp. 10 573–10 588, Apr. 2015.
- [436] W. Shi, H. Yun, C. Lin, M. Greenberg, X. Wang, Y. Wang, S. T. Fard, J. Flueckiger, N. A. F. Jaeger, and L. Chrostowski, "Ultra-compact, flat-top demultiplexer using anti-reflection contra-directional couplers for CWDM networks on silicon," *Optics Express*, vol. 21, no. 6, pp. 6733–6738, Mar. 2013.
- [437] P. Orlandi, P. Velha, M. Gnan, P. Bassi, A. Samarelli, M. Sorel, M. J. Strain, and R. D. L. Rue, "Microring resonator with wavelength selective coupling in SOI," *8th IEEE International Conference on Group IV Photonics*, pp. 281–283, 2011.
- [438] W. Shi, X. Wang, W. Zhang, H. Yun, N. A. F. Jaeger, and L. Chrostowski, "Integrated microring add-drop filters with contradirectional couplers," in *Conference on Lasers and Electro-Optics 2012*. Optical Society of America, 2012, p. JW4A.91.
- [439] W. Shi, X. Wang, W. Zhang, H. Yun, C. Lin, L. Chrostowski, and N. A. F. Jaeger, "Grating-coupled silicon microring resonators," *Applied Physics Letters*, vol. 100, no. 12, p. 121118, Mar. 2012.
- [440] R. Boeck, M. Caverley, L. Chrostowski, and N. A. F. Jaeger, "Grating-assisted silicon-on-insulator racetrack resonator reflector," *Optics Express*, vol. 23, no. 20, pp. 25 509–25 522, Oct. 2015.
- [441] R. Boeck, M. Caverley, L. Chrostowski, and N. A. F. Jaeger, "An FSR-free silicon resonator reflector using a contra-directional coupler and a Bragg reflector," in *Photonics North, 2015*, June 2015, p. 1.
- [442] N. Zhang, "Forward and Backward Grating-Assisted Directional Couplers in Silicon for Wavelength Multiplexing Tunable Add-Drop Applications," Master's thesis, University of Cincinnati, Sep. 2005.
- [443] D. T. Tan, K. Ikeda, and Y. Fainman, "On-chip group velocity dispersion compensation using coupled chirped vertical gratings," in *Advances in Optical Sciences Congress*. Optical Society of America, 2009, p. JTuB12.
- [444] D. T. H. Tan, K. Ikeda, and Y. Fainman, "Coupled chirped vertical gratings for on-chip group velocity dispersion engineering," *Applied Physics Letters*, vol. 95, no. 14, p. 141109, Oct. 2009.

- [445] D. T. H. Tan, K. Ikeda, A. Mizrahi, M. Nezhad, and Y. Fainman, “Coupled vertical gratings on silicon for applications in wavelength division multiplexing,” *Proc. SPIE*, vol. 7607, p. 760705, 2010.
- [446] D. T. H. Tan, K. Ikeda, S. Zamek, A. Mizrahi, M. Nezhad, and Y. Fainman, “Wavelength selective coupler on silicon for applications in wavelength division multiplexing,” in *2010 IEEE Photonics Society Summer Topical Meeting Series*, Jul. 2010, pp. 203–204.
- [447] W. Shi, X. Wang, C. Lin, H. Yun, Y. Liu, T. Baehr-Jones, M. Hochberg, N. A. F. Jaeger, and L. Chrostowski, “Electrically tunable resonant filters in phase-shifted contra-directional couplers,” in *2012 IEEE 9th International Conference on Group IV Photonics (GFP)*, Aug. 2012, pp. 78–80.
- [448] W. Shi, V. Veerasubramanian, D. V. Plant, N. A. F. Jaeger, and L. Chrostowski, “Silicon photonic bragg-grating couplers for optical communications,” *Proc. SPIE*, vol. 9010, p. 90100F, 2014.
- [449] W. Shi, V. Veerasubramanian, D. Patel, and D. V. Plant, “Tunable nanophotonic delay lines using linearly chirped contradirectional couplers with uniform Bragg gratings,” *Optics Letters*, vol. 39, no. 3, pp. 701–703, Feb. 2014.
- [450] D. T. H. Tan, A. Grieco, and Y. Fainman, “Silicon-based optical interconnects for dense wavelength division multiplexing with 100GHz Spacing,” in *Advanced Photonics for Communications*. Optical Society of America, 2014, p. PT4B.3.
- [451] H. Qiu, T. Hu, P. Yu, Y. Wang, and X. Jiang, “A nonreciprocal add-drop multiplexer based on grating assisted couplers,” *Optik - International Journal for Light and Electron Optics*, vol. 126, no. 23, pp. 3959 – 3961, Dec. 2015.
- [452] G. F. R. Chen, T. Wang, K. J. A. Ooi, A. K. L. Chee, L. K. Ang, and D. T. H. Tan, “Wavelength selective mode division multiplexing on a silicon chip,” *Optics Express*, vol. 23, no. 6, pp. 8095–8103, Mar. 2015.
- [453] H. Qiu, Y. Su, P. Yu, T. Hu, J. Yang, and X. Jiang, “Compact polarization splitter based on silicon grating-assisted couplers,” *Optics Letters*, vol. 40, no. 9, pp. 1885–1887, Apr. 2015.
- [454] J. St-Yves, H. Bahrami, S. LaRochelle, and W. Shi, “Widely bandwidth-tunable broadband optical filter on silicon,” in *Optical Fiber*

Communication Conference. Optical Society of America, 2015, p. Th1F.2.

- [455] M. Caverley, "Silicon photonic modulators and filters for optical interconnects," Master's thesis, University of British Columbia, Aug. 2015.
- [456] L. Chrostowski and K. Iniewski, *High-Speed Photonics Interconnects*. CRC Press, 2013.
- [457] N. Zhang and J. T. Boyd, "Forward and backward grating-assisted directional couplers in silicon for wavelength-division multiplexing tunable add-drop applications," *Optical Engineering*, vol. 45, no. 5, p. 054603, 2006.
- [458] K. Ikeda, H. C. Kim, M. Nezhad, A. Krishnamoorthy, J. Cunningham, and Y. Fainman, "Wavelength selective coupler with vertical gratings on silicon chip," in *Frontiers in Optics 2007/Laser Science XXIII/Organic Materials and Devices for Displays and Energy Conversion*. Optical Society of America, 2007, p. FTuB2.
- [459] K. Ikeda, M. Nezhad, and Y. Fainman, "Wavelength selective coupler with vertical gratings on silicon chip," *Applied Physics Letters*, vol. 92, no. 20, p. 201111, May 2008.
- [460] D. T. H. Tan, K. Ikeda, S. Zamek, A. Mizrahi, M. P. Nezhad, A. V. Krishnamoorthy, K. Raj, J. E. Cunningham, X. Zheng, I. Shubin, Y. Luo, and Y. Fainman, "Wide bandwidth, low loss 1 by 4 wavelength division multiplexer on silicon for optical interconnects," *Optics Express*, vol. 19, no. 3, pp. 2401–2409, Jan. 2011.
- [461] W. Shi, X. Wang, W. Zhang, L. Chrostowski, and N. A. F. Jaeger, "Contradirectional couplers in silicon-on-insulator rib waveguides," *Optics Letters*, vol. 36, no. 20, pp. 3999–4001, Oct. 2011.
- [462] W. Shi, X. Wang, H. Yun, W. Zhang, L. Chrostowski, and N. A. F. Jaeger, "Add-drop filters in silicon grating-assisted asymmetric couplers," in *Optical Fiber Communication Conference*. Optical Society of America, 2012, p. OTh3D.3.
- [463] Q. Huiye, T. Hu, P. Yu, J. Yang, and X. Jiang, "Add-drop filter with asymmetric vertical gratings in silicon-on-insulator rib waveguides," in *Asia Communications and Photonics Conference*. Optical Society of America, 2012, p. AF4A.10.

- [464] W. Shi, H. Yun, C. Lin, X. Wang, J. Flueckiger, N. A. F. Jaeger, and L. Chrostowski, "Silicon CWDM demultiplexers using contra-directional couplers," in *CLEO: 2013*. Optical Society of America, 2013, p. CTu3F.5.
- [465] W. Shi, X. Wang, C. Lin, H. Yun, Y. Liu, T. Baehr-Jones, M. Hochberg, N. A. F. Jaeger, and L. Chrostowski, "Silicon photonic grating-assisted, contra-directional couplers," *Optics Express*, vol. 21, no. 3, pp. 3633–3650, Feb. 2013.
- [466] H. Qiu, G. Jiang, T. Hu, H. Shao, P. Yu, J. Yang, and X. Jiang, "FSR-free add-drop filter based on silicon grating-assisted contradirectional couplers," *Optics Letters*, vol. 38, no. 1, pp. 1–3, Jan. 2013.
- [467] W. Shi, H. Yun, C. Lin, J. Flueckiger, N. A. F. Jaeger, and L. Chrostowski, "Coupler-apodized Bragg-grating add-drop filter," *Optics Letters*, vol. 38, no. 16, pp. 3068–3070, Aug. 2013.
- [468] D. T. H. Tan, A. Grieco, and Y. Fainman, "Towards 100 channel dense wavelength division multiplexing with 100GHz spacing on silicon," *Optics Express*, vol. 22, no. 9, pp. 10 408–10 415, May 2014.
- [469] M. Caverley, R. Boeck, L. Chrostowski, and N. A. F. Jaeger, "High-speed data transmission through silicon contra-directional grating coupler optical add-drop multiplexers," in *CLEO: 2015*. Optical Society of America, 2015, p. JTh2A.41.
- [470] L. Chrostowski and M. Hochberg, *Silicon Photonics Design: From Devices to Systems*. Cambridge University Press, 2015.
- [471] J. St-Yves, H. Bahrami, P. Jean, S. LaRochelle, and W. Shi, "Widely bandwidth-tunable silicon filter with an unlimited free-spectral range," *Optics Letters*, vol. 40, no. 23, pp. 5471–5474, Dec. 2015.
- [472] T. Baehr-Jones, R. Ding, A. Ayazi, T. Pinguet, M. Streshinsky, N. Harris, J. Li, L. He, M. Gould, Y. Zhang, A. E.-J. Lim, T.-Y. Liow, S. H.-G. Teo, G.-Q. Lo, and M. Hochberg, "A 25 Gb/s silicon photonics platform," *arXiv:1203.0767 [physics.optics]*, 2012.
- [473] N. Rouger, L. Chrostowski, and R. Vafaei, "Temperature effects on silicon-on-insulator (SOI) racetrack resonators: a coupled analytic and 2-D finite difference approach," *Journal of Lightwave Technology*, vol. 28, no. 9, pp. 1380–1391, May 2010.

- [474] H. Fukuda, K. Yamada, T. Tsuchizawa, T. Watanabe, H. Shinjima, and S. ichi Itabashi, “Ultrasmall polarization splitter based on silicon wire waveguides,” *Optics Express*, vol. 14, no. 25, pp. 12 401–12 408, Dec. 2006.
- [475] S. Bandyopadhyay, *Dissemination of Information in Optical Networks: From Technology to Algorithms*. Springer, 2008.
- [476] P. Dumon, “Ultra-compact integrated optical filters in silicon-on-insulator by means of wafer-scale technology,” PhD thesis, Universiteit Gent, 2007.
- [477] F. Dell’Olio, V. M. N. Passaro, G. Z. Mashanovich, and F. De Leonardis, “Micro-racetrack coupled-resonator optical waveguides in silicon photonic wires,” *Journal of Optics A: Pure and Applied Optics*, vol. 10, no. 6, p. 064003, Apr. 2008.
- [478] X. Wang, W. Shi, H. Yun, S. Grist, N. A. F. Jaeger, and L. Chrostowski, “Narrow-band waveguide Bragg gratings on SOI wafers with CMOS-compatible fabrication process,” *Optics Express*, vol. 20, no. 14, pp. 15 547–15 558, Jun. 2012.
- [479] A. V. Krishnamoorthy, R. Ho, X. Zheng, H. Schwetman, J. Lexau, P. Koka, G. Li, I. Shubin, and J. E. Cunningham, “Computer systems based on silicon photonic interconnects,” *Proc. IEEE*, vol. 97, no. 7, pp. 1337–1361, 2009.
- [480] P. Matavulj and T. Keča, “Influence of geometric parameters on the SOI racetrack resonator properties,” *PIERS Proc. Moscow*, pp. 13–17, 2012.
- [481] A. V. Krishnamoorthy, X. Zheng, G. Li, J. Yao, T. Pinguet, A. Mekis, H. Thacker, I. Shubin, Y. Luo, K. Raj, and J. E. Cunningham, “Exploiting CMOS manufacturing to reduce tuning requirements for resonant optical devices,” *IEEE Photonics Journal*, vol. 3, no. 3, pp. 567–579, Jun. 2011.
- [482] D. Dai and S. He, “Proposal of a coupled-microring-based wavelength-selective $1 \times N$ power splitter,” *IEEE Photonics Technology Letters*, vol. 21, no. 21, pp. 1630–1632, Nov. 2009.
- [483] J. D. Doménech, P. Muñoz, and J. Capmany, “The longitudinal offset technique for apodization of coupled resonator optical waveguide devices: concept and fabrication tolerance analysis,” *Optics Express*, vol. 17, no. 23, pp. 21 050–21 059, Nov. 2009.

- [484] L. Chrostowski, X. Wang, J. Flueckiger, Y. Wu, Y. Wang, and S. Talebi Fard, "Impact of fabrication non-uniformity on chip-scale silicon photonic integrated circuits," *Optical Fiber Communication Conference*, p. Th2A.37, 2014.
- [485] A. Prinzen, J. Bolten, M. Waldow, and H. Kurz, "Study on fabrication tolerances of SOI based directional couplers and ring resonators," *Microelectronic Engineering*, vol. 121, pp. 51–54, Jun. 2014.
- [486] J. C. Mikkelsen, W. D. Sacher, and J. K. S. Poon, "Dimensional variation tolerant silicon-on-insulator directional couplers," *Optics Express*, vol. 22, no. 3, pp. 3145–3150, Feb. 2014.
- [487] A. Prinzen, M. Waldow, and H. Kurz, "Fabrication tolerances of SOI based directional couplers and ring resonators," *Optics Express*, vol. 21, no. 14, pp. 17 212–17 220, Jul. 2013.
- [488] S. K. Selvaraja, G. Winroth, S. Locorotondo, G. Murdoch, A. Milenin, C. Delvaux, P. Ong, S. Pathak, W. Xie, G. Sterckx, G. Lepage, D. Van Thourhout, W. Bogaerts, J. Van Campenhout, and P. Absil, "193nm immersion lithography for high-performance silicon photonic circuits," *Proc. SPIE*, vol. 9052, p. 90520F, 2014.
- [489] T. Keča, P. Matavulj, W. Headley, and G. Mashanovich, "Free spectral range adjustment of a silicon rib racetrack resonator," *Physica Scripta*, vol. 2012, no. T149, p. 014031, Apr. 2012.
- [490] D.-X. Xu, J. H. Schmid, G. T. Reed, G. Z. Mashanovich, D. J. Thomson, M. Nedeljkovic, X. Chen, D. Van Thourhout, S. Keyvaninia, and S. K. Selvaraja, "Silicon photonic integration platform - have we found the sweet spot?" *IEEE Journal of Selected Topics in Quantum Electronics*, vol. 20, no. 4, pp. 1–17, Jul. - Aug. 2014.
- [491] F. Boeuf, S. Crémer, N. Vulliet, T. Pinguet, A. Mekis, G. Masini, L. Verslegers, P. Sun, A. Ayazi, N. K. Hon, S. Sahni, Y. Chi, B. Orlando, D. Ristoiu, A. Farcy, F. Leverd, L. Broussous, D. Pelissier-Tanon, C. Richard, L. Pinzelli, R. Beneyton, O. Gourhant, E. Gourvest, Y. Le-Friec, D. Monnier, P. Brun, M. Guillermet, D. Benoit, K. Haxaire, J. R. Manouvrier, S. Jan, H. Petiton, J. F. Carpentier, T. Quémerais, C. Durand, D. Gloria, M. Fourel, F. Battegay, Y. Sanchez, E. Batail, F. Baron, P. Delpech, L. Salager, P. De Dobbelaere, and B. Sautreuil, "A multi-wavelength 3D-compatible silicon photonics platform on 300mm

SOI wafers for 25Gb/s applications,” *IEEE International Electron Devices Meeting (IEDM)*, pp. 13.3.1–13.3.4, 2013.

- [492] R. Ding, T. Baehr-Jones, T. Pinguet, J. Li, N. C. Harris, M. Streshinsky, L. He, A. Novack, E.-J. Lim, T.-Y. Liow, H.-G. Teo, G.-Q. Lo, and M. Hochberg, “A silicon platform for high-speed photonics systems,” *Optical Fiber Communication Conference*, p. OM2E.6, 2012.
- [493] R. J. Bojko, J. Li, L. He, T. Baehr-Jones, M. Hochberg, and Y. Aida, “Electron beam lithography writing strategies for low loss, high confinement silicon optical waveguides,” *Journal of Vacuum Science & Technology B*, vol. 29, no. 6, p. 06F309, Nov. 2011.
- [494] R. S. Romaniuk, “Optical fiber transmission with wavelength multiplexing: faster or denser?” *Proc. SPIE*, vol. 5484, pp. 19–28, Jul. 2004.
- [495] C. Manolatou, M. A. Popovic, P. T. Rakich, T. Barwicz, H. A. Haus, and E. P. Ippen, “Spectral anomalies due to coupling-induced frequency shifts in dielectric coupled-resonator filters,” in *Optical Fiber Communication Conference*, ser. Technical Digest (CD). Optical Society of America, Feb. 2004, p. TuD5.
- [496] N. Sherwood-Droz, H. Wang, L. Chen, B. G. Lee, A. Biberman, K. Bergman, and M. Lipson, “Optical 4x4 hitless silicon router for optical networks-on-chip (NoC),” *Optics Express*, vol. 16, no. 20, pp. 15 915–15 922, Sep. 2008.
- [497] M. Geng, L. Jia, L. Zhang, L. Yang, P. Chen, T. Wang, and Y. Liu, “Four-channel reconfigurable optical add-drop multiplexer based on photonic wire waveguide,” *Optics Express*, vol. 17, no. 7, pp. 5502–5516, Mar. 2009.
- [498] Y. Wang, J. Flueckiger, C. Lin, and L. Chrostowski, “Universal grating coupler design,” *Proc. SPIE*, vol. 8915, p. 89150Y, 2013.
- [499] M.-C. N. Dicaire, J. Upham, I. D. Leon, S. A. Schulz, and R. W. Boyd, “Group delay measurement of fiber Bragg grating resonances in transmission: Fourier transform interferometry versus Hilbert transform,” *Journal of the Optical Society of America B*, vol. 31, no. 5, pp. 1006–1010, May 2014.
- [500] The MathWorks, Inc., “Discrete-time analytic signal using Hilbert transform - MATLAB hilbert,” [Online]. Available: <http://www.mathworks.com/help/signal/ref/hilbert.html>, (Jan. 15, 2016).

- [501] A. Melloni, M. Martinelli, G. Cusmai, and R. Siano, "Experimental evaluation of ring resonator filters impact on the bit error rate in non return to zero transmission systems," *Optics Communications*, vol. 234, no. 1-6, pp. 211 – 216, Apr. 2004.
- [502] Photonics-USA, "Optical Add/Drop Multiplexers 200 GHz OADM (1x2)."
- [503] Alliance Fiber Optic Products, Inc., "Single Channel DWDM (200 GHz)," REV. H, Mar. 4, 2009.
- [504] S. Mason, "Feedback theory-further properties of signal flow graphs," *Proc. IRE*, vol. 44, pp. 920–926, 1956.
- [505] Y. Wang, X. Wang, J. Flueckiger, H. Yun, W. Shi, R. Bojko, N. A. F. Jaeger, and L. Chrostowski, "Focusing sub-wavelength grating couplers with low back reflections for rapid prototyping of silicon photonic circuits," *Optics Express*, vol. 22, no. 17, pp. 20 652–20 662, Aug. 2014.
- [506] W. Bogaerts, R. Baets, P. Dumon, V. Wiaux, S. Beckx, D. Taillaert, B. Luyssaert, J. Van Campenhout, P. Bienstman, and D. Van Thourhout, "Nanophotonic waveguides in silicon-on-insulator fabricated with CMOS technology," *Journal of Lightwave Technology*, vol. 23, no. 1, pp. 401–412, Jan. 2005.
- [507] X. Wang, "Silicon photonic waveguide Bragg gratings," PhD thesis, University of British Columbia, Dec. 2013.
- [508] D. Marcuse, "Bandwidth of forward and backward coupling directional couplers," *Journal of Lightwave Technology*, vol. 5, no. 12, pp. 1773–1777, Dec. 1987.
- [509] M. R. Shenoy, K. Thyagarajan, V. Priye, and N. S. Madhavan, "Estimation of the characteristic parameters of fiber Bragg gratings from spectral measurements," *Proc. SPIE*, vol. 3666, pp. 94–99, 1999.
- [510] R. Kashyap, *Fiber Bragg Gratings*. Academic, 1999.
- [511] X. Wang, Y. Wang, J. Flueckiger, R. Bojko, A. Liu, A. Reid, J. Pond, N. A. F. Jaeger, and L. Chrostowski, "Precise control of the coupling coefficient through destructive interference in silicon waveguide Bragg gratings," *Optics Letters*, vol. 39, no. 19, pp. 5519–5522, Oct. 2014.
- [512] J. P. Weber, "Spectral characteristics of coupled-waveguide Bragg-reflection tunable optical filter," *IEE Proceedings J. Optoelectronics*, vol. 140, no. 5, pp. 275–284, Oct. 1993.

- [513] A. Yariv and P. Yeh, *Photonics: optical electronics in modern communications*. Oxford University Press, 2007.
- [514] D. Marcuse, "Directional couplers made of nonidentical asymmetric slabs. Part II: Grating-assisted couplers," *Journal of Lightwave Technology*, vol. 5, no. 2, pp. 268–273, Feb. 1987.
- [515] R. Marz and H. P. Nolting, "Spectral properties of asymmetrical optical directional couplers with periodic structures," *Optical and Quantum Electronics*, vol. 19, no. 5, pp. 273–287, Sep. 1987.
- [516] S. Nacer, A. Aissat, K. Ferdjani, and M. Bensebti, "Influence of dispersion on spectral characteristics of GADC optical filters," *Optical and Quantum Electronics*, vol. 38, no. 8, pp. 701–710, Jun. 2006.
- [517] D. T. H. Tan, K. Ikeda, and Y. Fainman, "Cladding-modulated Bragg gratings in silicon waveguides," *Optics Letters*, vol. 34, no. 9, pp. 1357–1359, May 2009.
- [518] S. Xiao, M. H. Khan, H. Shen, and M. Qi, "Modeling and measurement of losses in silicon-on-insulator resonators and bends," *Optics Express*, vol. 15, no. 17, pp. 10 553–10 561, Aug. 2007.
- [519] The MathWorks, Inc., "Solve nonlinear curve-fitting (data-fitting) problems in least-squares sense - MATLAB lsqcurvefit," [Online]. Available: <http://www.mathworks.com/help/optim/ug/lscurvefit.html>, (Jan. 15, 2016).
- [520] J. Willems, K. David, G. Morthier, and R. Baets, "Filter characteristics of DBR amplifier with index and gain coupling," *Electronics Letters*, vol. 27, no. 10, pp. 831–833, May 1991.
- [521] L. Poladian, "Group-delay reconstruction for fiber Bragg gratings in reflection and transmission," *Optics Letters*, vol. 22, no. 20, pp. 1571–1573, Oct. 1997.
- [522] J. Skaar and H. E. Engan, "Phase reconstruction from reflectivity in fiber Bragg gratings," *Optics Letters*, vol. 24, no. 3, pp. 136–138, Feb. 1999.
- [523] A. Melloni, R. Costa, P. Monguzzi, and M. Martinelli, "Ring-resonator filters in silicon oxynitride technology for dense wavelength-division multiplexing systems," *Optics Letters*, vol. 28, no. 17, pp. 1567–1569, Sep. 2003.

- [524] A. Canciamilla, F. Morichetti, and A. Melloni, “Full characterization of integrated optical ring-resonators by phase-sensitive time-domain interferometry,” *Proc. SPIE*, vol. 7138, p. 71381L, 2008.
- [525] O. Schwelb, “Transmission, group delay, and dispersion in single-ring optical resonators and add/drop filters - a tutorial overview,” *Journal of Lightwave Technology*, vol. 22, no. 5, pp. 1380–1394, May 2004.
- [526] P. Pintus, P. Contu, N. Andriolli, A. D’Errico, F. Di Pasquale, and F. Testa, “Analysis and design of microring-based switching elements in a silicon photonic integrated transponder aggregator,” *Journal of Lightwave Technology*, vol. 31, no. 24, pp. 3943–3955, Dec. 2013.
- [527] S. K. Selvaraja, P. D. Heyn, G. Winroth, P. Ong, G. Lepage, C. Cailler, A. Rigny, K. Bourdelle, W. Bogaerts, D. VanThourhout, J. V. Campenhout, and P. Absil, “Highly uniform and low-loss passive silicon photonics devices using a 300mm CMOS platform,” in *Optical Fiber Communication Conference*. Optical Society of America, 2014, p. Th2A.33.
- [528] H. Jayatileka, K. Murray, M. Ángel Guillén-Torres, M. Caverley, R. Hu, N. A. F. Jaeger, L. Chrostowski, and S. Shekhar, “Wavelength tuning and stabilization of microring-based filters using silicon in-resonator photoconductive heaters,” *Optics Express*, vol. 23, no. 19, pp. 25 084–25 097, Sep. 2015.

Appendix A

Derivation of the Transfer Functions of a Quadruple Series-Coupled Racetrack Resonator Filter

¹Here, we will derive the drop port and through port transfer functions of quadruple series-coupled racetrack resonators using Mason's rule [504]. In [144], Dey *et al.* derived the drop port transfer function using Mason's rule [504] but did not derive nor present the through port transfer function. For completeness, here we have re-derived the drop port transfer function as well as derived the through port transfer function. Since in our configuration, there are four racetrack resonators coupled in series, there are 33 loop gains. There are 10 loop gains of the 10 possible

¹A version of Appendix A has been published in [96].

combinations of 1 non-touching loop,

$$P_{11} = t_1 t_2 X_a, \quad (\text{A.1})$$

$$P_{21} = t_2 t_3 X_b, \quad (\text{A.2})$$

$$P_{31} = t_3 t_4 X_c, \quad (\text{A.3})$$

$$P_{41} = t_4 t_5 X_d, \quad (\text{A.4})$$

$$P_{51} = \kappa_2^2 \kappa_3^2 t_1 t_4 X_a X_b X_c, \quad (\text{A.5})$$

$$P_{61} = \kappa_3^2 \kappa_4^2 t_2 t_5 X_b X_c X_d, \quad (\text{A.6})$$

$$P_{71} = -\kappa_3^2 t_2 t_4 X_b X_c, \quad (\text{A.7})$$

$$P_{81} = -\kappa_4^2 t_3 t_5 X_c X_d, \quad (\text{A.8})$$

$$P_{91} = -\kappa_2^2 \kappa_3^2 \kappa_4^2 t_1 t_5 X_a X_b X_c X_d, \quad (\text{A.9})$$

$$P_{101} = -\kappa_2^2 t_1 t_3 X_a X_b \quad (\text{A.10})$$

where $X_{a,b,c,d} = \exp(-j\beta_{a,b,c,d}L_{a,b,c,d} - \alpha_{a,b,c,d}L_{a,b,c,d})$, where the field loss coefficients and propagations constants for the racetrack resonators are represented by $\alpha_{a,b,c,d}$, and $\beta_{a,b,c,d}$, respectively. κ_1 , κ_2 , κ_3 , κ_4 , and κ_5 are the symmetric (real) point field coupling factors. t_1 , t_2 , t_3 , t_4 , and t_5 are the straight through (real) point field transmission factors. There are 15 loop gains of the 15 possible combinations of 2 non-touching loops,

$$P_{12} = P_{11}P_{21}, \quad (\text{A.11})$$

$$P_{22} = P_{21}P_{31}, \quad (\text{A.12})$$

$$P_{32} = P_{31}P_{41}, \quad (\text{A.13})$$

$$P_{42} = P_{11}P_{31}, \quad (\text{A.14})$$

$$P_{52} = P_{11}P_{41}, \quad (\text{A.15})$$

$$P_{62} = P_{21}P_{41}, \quad (\text{A.16})$$

$$P_{72} = P_{41}P_{51}, \quad (\text{A.17})$$

$$P_{82} = P_{11}P_{71}, \quad (\text{A.18})$$

$$P_{92} = P_{41}P_{71}, \quad (\text{A.19})$$

$$P_{102} = P_{81}P_{101}, \quad (\text{A.20})$$

$$P_{112} = P_{31}P_{101}, \quad (\text{A.21})$$

$$P_{122} = P_{41}P_{101}, \quad (\text{A.22})$$

$$P_{132} = P_{11}P_{81}, \quad (\text{A.23})$$

$$P_{142} = P_{21}P_{81}, \quad (\text{A.24})$$

$$P_{152} = P_{11}P_{61}. \quad (\text{A.25})$$

There are 7 loop gains of the 7 possible combinations of 3 non-touching loops,

$$P_{13} = P_{11}P_{21}P_{31}, \quad (\text{A.26})$$

$$P_{23} = P_{21}P_{31}P_{41}, \quad (\text{A.27})$$

$$P_{33} = P_{31}P_{41}P_{101}, \quad (\text{A.28})$$

$$P_{43} = P_{11}P_{41}P_{71}, \quad (\text{A.29})$$

$$P_{53} = P_{11}P_{21}P_{81}, \quad (\text{A.30})$$

$$P_{63} = P_{11}P_{21}P_{41}, \quad (\text{A.31})$$

$$P_{73} = P_{11}P_{31}P_{41}. \quad (\text{A.32})$$

There is 1 loop gain of the 1 possible combination of 4 non-touching loops,

$$P_{14} = P_{11}P_{21}P_{31}P_{41}. \quad (\text{A.33})$$

The gain and co-factor of the first forward path that is used to determine the drop port transfer function is,

$$G_1 = -j\kappa_1\kappa_2\kappa_3\kappa_4\kappa_5\sqrt{X_aX_bX_cX_d}, \quad (\text{A.34})$$

$$\Delta_1 = 1. \quad (\text{A.35})$$

The determinant for the entire system is given by,

$$\begin{aligned} \Delta = 1 - & (P_{11} + P_{21} + P_{31} + P_{41} + P_{51} + P_{61} + P_{71} + P_{81} + P_{91} + P_{101}) + \\ & (P_{12} + P_{22} + P_{32} + P_{42} + P_{52} + P_{62} + \\ & P_{72} + P_{82} + P_{92} + P_{102} + P_{112} + P_{122} + P_{132} + P_{142} + P_{152}) - \\ & (P_{13} + P_{23} + P_{33} + P_{43} + P_{53} + P_{63} + P_{73}) + P_{14}. \end{aligned} \quad (\text{A.36})$$

Thus, the transfer function for the drop port is given by [144],

$$TF_{drop} = \frac{G_1\Delta_1}{\Delta}. \quad (\text{A.37})$$

The gains of the second to sixth forward path that are used to determine the through port transfer function are,

$$G_2 = t_1, \quad (\text{A.38})$$

$$G_3 = -\kappa_1^2 t_2 X_a, \quad (\text{A.39})$$

$$G_4 = \kappa_1^2 \kappa_2^2 t_3 X_a X_b, \quad (\text{A.40})$$

$$G_5 = -\kappa_1^2 \kappa_2^2 \kappa_3^2 t_4 X_a X_b X_c, \quad (\text{A.41})$$

$$G_6 = \kappa_1^2 \kappa_2^2 \kappa_3^2 \kappa_4^2 t_5 X_a X_b X_c X_d, \quad (\text{A.42})$$

and the corresponding co-factors are,

$$\Delta_2 = \Delta, \quad (\text{A.43})$$

$$\begin{aligned} \Delta_3 = 1 - (P_{21} + P_{31} + P_{41} + P_{61} + P_{71} + P_{81}) \\ + (P_{22} + P_{32} + P_{62} + P_{92} + P_{142}) - P_{23}, \end{aligned} \quad (\text{A.44})$$

$$\Delta_4 = 1 - (P_{31} + P_{41} + P_{81}) + P_{32}, \quad (\text{A.45})$$

$$\Delta_5 = 1 - P_{41}, \quad (\text{A.46})$$

$$\Delta_6 = 1. \quad (\text{A.47})$$

Thus, the transfer function for the through port is given by,

$$TF_{through} = \frac{G_2\Delta_2 + G_3\Delta_3 + G_4\Delta_4 + G_5\Delta_5 + G_6\Delta_6}{\Delta}. \quad (\text{A.48})$$

Appendix B

Derivation of the Transfer Functions of a Double Microring Resonator Filter with MZI-Based Coupling

The drop port and through port transfer functions of a double microring resonator filter with MZI-based coupling (which are used in [105]) are determined using the same method used in Appendix A, which is Mason's rule [96, 107, 504]. There are 8 loop gains of the 8 possible combinations of 1 non-touching loops,

$$P_{11} = t_{mzi}^2 t_r X_r X_{mzi-2}, \quad (\text{B.1})$$

$$P_{21} = t_{mzi}^2 t_r X_r X_{mzi-2}, \quad (\text{B.2})$$

$$P_{31} = -t_{mzi}^4 \kappa_r^2 X_r^2 X_{mzi-2}^2, \quad (\text{B.3})$$

$$P_{41} = -t_r \kappa_{mzi}^2 X_r X_{mzi-1}, \quad (\text{B.4})$$

$$P_{51} = -t_r \kappa_{mzi}^2 X_r X_{mzi-1}, \quad (\text{B.5})$$

$$P_{61} = \kappa_{mzi}^2 t_{mzi}^2 \kappa_r^2 X_{mzi-1} X_r^2 X_{mzi-2}, \quad (\text{B.6})$$

$$P_{71} = t_{mzi}^2 \kappa_r^2 \kappa_{mzi}^2 X_{mzi-2} X_r^2 X_{mzi-1}, \quad (\text{B.7})$$

$$P_{81} = -\kappa_{mzi}^4 \kappa_r^2 X_r^2 X_{mzi-1}^2, \quad (\text{B.8})$$

where

$$X_r = e^{-j\beta_r L_r - \alpha L_r}, \quad (\text{B.9})$$

$$X_{mzi-2} = e^{-j\beta_r L_{mzi-2} - \alpha L_{mzi-2}}, \quad (\text{B.10})$$

$$X_{mzi-1} = e^{-j\beta_r L_{mzi-1} - \alpha L_{mzi-1}}, \quad (\text{B.11})$$

α is the field propagation loss coefficient, L_r is the length of the microring resonator that does not include the portion within the MZI section. β_r is the propagation constant of the microring resonator and the MZI-bus waveguide branch. The length L_{mzi-2} is the MZI-ring waveguide branch length [105]. The length L_{mzi-1} is the total length of the MZI-bus waveguide branch [105]. κ_r and t_r are the inter-ring real point field coupling factor and transmission factor, respectively, κ_{mzi} and t_{mzi} are the real point field coupling factor and transmission factor for the MZI regions, respectively [105]. There are 4 loop gains of the 4 possible combinations of 2 non-touching loops,

$$P_{12} = P_{11}P_{21}, \quad (\text{B.12})$$

$$P_{22} = P_{41}P_{21}, \quad (\text{B.13})$$

$$P_{32} = P_{41}P_{51}, \quad (\text{B.14})$$

$$P_{42} = P_{51}P_{11}, \quad (\text{B.15})$$

The determinant, Δ , for the filter is,

$$\Delta = 1 - (P_{11} + P_{21} + P_{31} + P_{41} + P_{51} + P_{61} + P_{71} + P_{81}) + (P_{12} + P_{22} + P_{32} + P_{42}). \quad (\text{B.16})$$

The forward path gains and their, respective, co-factors for the drop port transfer function are,

$$G_1 = j\kappa_r \kappa_{mzi}^2 t_{mzi}^2 X_r X_{mzi-1} X_{mzi-2}, \quad (\text{B.17})$$

$$\Delta_1 = 1, \quad (\text{B.18})$$

$$G_2 = j\kappa_r \kappa_{mzi}^2 t_{mzi}^2 X_r X_{mzi-1} X_{mzi-2}, \quad (\text{B.19})$$

$$\Delta_2 = 1, \quad (\text{B.20})$$

$$G_3 = j\kappa_r \kappa_{mzi}^2 t_{mzi}^2 X_r X_{mzi-2}^2, \quad (\text{B.21})$$

$$\Delta_3 = 1, \quad (\text{B.22})$$

$$G_4 = j\kappa_r \kappa_{mzi}^2 t_{mzi}^2 X_r X_{mzi-1}^2, \quad (\text{B.23})$$

$$\Delta_4 = 1. \quad (\text{B.24})$$

Therefore, the drop port transfer function is,

$$TF_{drop} = \frac{G_1\Delta_1 + G_2\Delta_2 + G_3\Delta_3 + G_4\Delta_4}{\Delta}. \quad (\text{B.25})$$

The forward path gains and their, respective, co-factors for the through port transfer function are,

$$G_5 = t_{mzi}^2 X_{mzi-1}, \quad (\text{B.26})$$

$$\Delta_5 = 1 - (P_{11} + P_{21} + P_{31} + P_{41} + P_{61}) + (P_{12} + P_{22}), \quad (\text{B.27})$$

$$G_6 = -\kappa_{mzi}^2 X_{mzi-2}, \quad (\text{B.28})$$

$$\Delta_6 = 1 - (P_{11} + P_{41} + P_{51} + P_{71} + P_{81}) + (P_{32} + P_{42}), \quad (\text{B.29})$$

$$G_7 = \kappa_r^2 \kappa_{mzi}^2 t_{mzi}^4 X_r^2 X_{mzi-1} X_{mzi-2}^2, \quad (\text{B.30})$$

$$\Delta_7 = 1, \quad (\text{B.31})$$

$$G_8 = -\kappa_{mzi}^2 t_r t_{mzi}^2 X_r X_{mzi-1} X_{mzi-2}, \quad (\text{B.32})$$

$$\Delta_8 = 1 - (P_{11} + P_{41}), \quad (\text{B.33})$$

$$G_9 = -\kappa_{mzi}^2 t_r t_{mzi}^2 X_r X_{mzi-1} X_{mzi-2}, \quad (\text{B.34})$$

$$\Delta_9 = 1 - (P_{11} + P_{41}), \quad (\text{B.35})$$

$$G_{10} = -\kappa_r^2 \kappa_{mzi}^4 t_{mzi}^2 X_r^2 X_{mzi-1}^2 X_{mzi-2}, \quad (\text{B.36})$$

$$\Delta_{10} = 1, \quad (\text{B.37})$$

$$G_{11} = -\kappa_r^2 \kappa_{mzi}^4 t_{mzi}^2 X_r^2 X_{mzi-1}^2 X_{mzi-2}, \quad (\text{B.38})$$

$$\Delta_{11} = 1, \quad (\text{B.39})$$

$$G_{12} = \kappa_r^2 \kappa_{mzi}^2 t_{mzi}^4 X_r^2 X_{mzi-1} X_{mzi-2}^2, \quad (\text{B.40})$$

$$\Delta_{12} = 1. \quad (\text{B.41})$$

Therefore, the through port transfer function is,

$$TF_{through} = \frac{G_5 \Delta_5 + G_6 \Delta_6 + G_7 \Delta_7 + G_8 \Delta_8 + G_9 \Delta_9 + G_{10} \Delta_{10} + G_{11} \Delta_{11} + G_{12} \Delta_{12}}{\Delta}. \quad (\text{B.42})$$

Appendix C

Derivation of the Average Propagation Constant Mismatch of a Contra-Directional Grating Coupler

¹Here, we will derive the equation for the average propagation constant mismatch, $\delta\beta_{avg}$. The first step in determining $\delta\beta_{avg}$ is to calculate the propagation constant difference, $\delta\beta_H$, which is defined as the difference between the propagation constant mismatch, $\Delta\beta(f_H)$, at the frequency, f_H , corresponding to the intensity at FWHM at the higher frequency and the propagation constant mismatch, $\Delta\beta(f_0)$, at the centre frequency, f_0 , (see Figure C.1) as shown in Eq. C.1.

$$\delta\beta_H = \Delta\beta(f_H) - \Delta\beta(f_0) \quad (C.1)$$

Next, we substitute into Eq. C.1 the propagation constant mismatch equation, $\Delta\beta = \beta_a + \beta_b - m\frac{2\pi}{\Lambda}$, where β_a and β_b are the propagation constants of waveguide “a” and waveguide “b” in isolation, respectively, m is the grating order which is equal to 1 for our first-order contra-DCs, and Λ is the grating period [513] as shown in

¹A version of Appendix C has been published in [435].

Eq. C.2.

$$\delta\beta_H = \beta_a(f_H) + \beta_b(f_H) - \frac{2\pi}{\Lambda} - \beta_a(f_0) - \beta_b(f_0) + \frac{2\pi}{\Lambda} \quad (\text{C.2})$$

The next steps involve simplifying Eq. C.2, substitutions for the propagation constants, and rearrangements of the terms,

$$\delta\beta_H = \beta_a(f_H) + \beta_b(f_H) - \beta_a(f_0) - \beta_b(f_0) \quad (\text{C.3})$$

$$= \left(\frac{2\pi}{c}\right) (n_a(f_H)f_H + n_b(f_H)f_H - n_a(f_0)f_0 - n_b(f_0)f_0) \quad (\text{C.4})$$

$$= \left(\frac{2\pi}{c}\right) (n_a(f_H)f_H - n_a(f_0)f_0 + n_b(f_H)f_H - n_b(f_0)f_0) \quad (\text{C.5})$$

where n_a and n_b are the effective indices of waveguide “a” and waveguide “b”, respectively, and c is the speed of light in a vacuum. Since the effective indices are frequency dependent due to dispersion, we will express $n_a(f_H)$ as $n_a(f_0) + \Delta f_H \left. \frac{dn_a}{df} \right|_{f_0}$ and $n_b(f_H)$ as $n_b(f_0) + \Delta f_H \left. \frac{dn_b}{df} \right|_{f_0}$ where $\Delta f_H = f_H - f_0$ [107]. After simplification by grouping terms, $\delta\beta_H$ becomes,

$$\delta\beta_H = \left(\frac{2\pi\Delta f_H}{c}\right) \left(n_a(f_0) + f_H \left. \frac{dn_a}{df} \right|_{f_0} + n_b(f_0) + f_H \left. \frac{dn_b}{df} \right|_{f_0} \right). \quad (\text{C.6})$$

In Eq. C.6, the terms, $n_a(f_0) + f_H \left. \frac{dn_a}{df} \right|_{f_0}$ and $n_b(f_0) + f_H \left. \frac{dn_b}{df} \right|_{f_0}$ correspond approximately to the group indices of waveguide “a” and waveguide “b,” respectively, since $\Delta f_H \ll f_0$ [107]. Therefore, the final equation for $\delta\beta_H$ is,

$$\delta\beta_H = \left(\frac{2\pi\Delta f_H}{c}\right) (n_{g,a}(f_0) + n_{g,b}(f_0)) \quad (\text{C.7})$$

where $n_{g,a}$ and $n_{g,b}$ are the group indices of waveguide “a” and waveguide “b”, respectively.

Next, we show the equation for the propagation constant difference, $\delta\beta_L$, [see Eq. C.8 where $\Delta f_L = f_0 - f_L$] which is defined as the difference between the propagation constant mismatch, $\Delta\beta(f_L)$, at the frequency, f_L , corresponding to the intensity at FWHM at the lower frequency and the propagation constant mismatch,

$\Delta\beta(f_0)$, at the center frequency, f_0 (see Figure C.1). $\delta\beta_L$ was derived using the same procedure as used to derive $\delta\beta_H$.

$$\delta\beta_L = - \left(\frac{2\pi\Delta f_L}{c} \right) (n_{g,a}(f_0) + n_{g,b}(f_0)) \quad (\text{C.8})$$

We are now able to determine $\delta\beta_{avg}$,

$$\delta\beta_{avg} = \frac{|\delta\beta_H| + |\delta\beta_L|}{2} \quad (\text{C.9})$$

$$\delta\beta_{avg} = \left(\frac{2\pi}{2c} \right) (n_{g,a}(f_0) + n_{g,b}(f_0)) (\Delta f_H + \Delta f_L) \quad (\text{C.10})$$

$$\delta\beta_{avg} = \left(\frac{\pi}{c} \right) (n_{g,a}(f_0) + n_{g,b}(f_0)) (f_H - f_L) \quad (\text{C.11})$$

$$\delta\beta_{avg} = \left(\frac{\pi}{c} \right) (n_{g,a}(f_0) + n_{g,b}(f_0)) \left(\frac{c}{\lambda_L} - \frac{c}{\lambda_H} \right) \quad (\text{C.12})$$

$$\delta\beta_{avg} = \frac{\pi\Delta\lambda_{bw}}{\lambda_L\lambda_H} (n_{g,a}(\lambda_0) + n_{g,b}(\lambda_0)) \quad (\text{C.13})$$

where the wavelengths λ_0 , λ_L , and λ_H correspond to the frequencies f_0 , f_H , and f_L , respectively, and $\Delta\lambda_{bw} = \lambda_H - \lambda_L$. Equations C.7 and C.8 are similar to Eq. 13.5-22 in [513] and Eq. C.13 is similar to Eq. 31 in [508] except that we have taken dispersion into account.

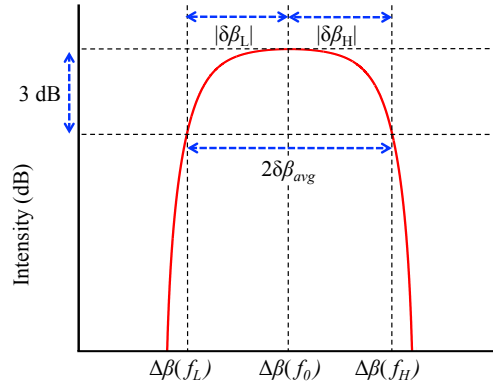


Figure C.1: Diagram depicting some of the relevant parameters used in our derivation. ©Optical Society of America, 2015, by permission [435].

Appendix D

Derivation of the Minimum Bandwidth of a Contra-Directional Grating Coupler

¹Here, we present the derivation for the minimum bandwidth of a contra-DC, $\Delta\lambda_{bw-min}$ as $|\kappa|$ goes to zero. First, we rearrange the terms in Eq. 6.7 as shown below,

$$\frac{2|\kappa|^2 \sinh^2(sL)}{\tanh^2(|\kappa|L)} = s^2 \cosh^2(sL) + \left(\frac{\delta\beta_{avg}}{2}\right)^2 \sinh^2(sL). \quad (D.1)$$

¹A version of Appendix D has been published in [435].

Next, we take the limit of the left side and the right side of Eq. D.1,

$$\lim_{\kappa \rightarrow 0} \frac{2|\kappa|^2 \sinh^2(sL)}{\tanh^2(|\kappa|L)} = \lim_{\kappa \rightarrow 0} \left[s^2 \cosh^2(sL) + \left(\frac{\delta\beta_{avg}}{2} \right)^2 \sinh^2(sL) \right] \quad (D.2)$$

$$\frac{\cos(\delta\beta_{avg}L) - 1}{L^2} = -\frac{\delta\beta_{avg}^2}{4} \quad (D.3)$$

$$\cos(\delta\beta_{avg}L) + \frac{(\delta\beta_{avg}L)^2}{4} - 1 = 0. \quad (D.4)$$

The numerically determined solution to Eq. D.4 is $\delta\beta_{avg}L = 2.783115$ (we neglect the trivial solution which is zero). Therefore, for a contra-DC with a given L , $\delta\beta_{avg}L$ needs to be greater than 2.783115. Therefore, substituting $\delta\beta_{avg}L = 2.783115$ into Eq. C.13, we get (similar to [520]),

$$\Delta\lambda_{bw-min} = \frac{2.783115\lambda_L\lambda_H}{\pi L [n_{g,a}(\lambda_0) + n_{g,b}(\lambda_0)]} \quad (D.5)$$

which is approximately equal to,

$$\Delta\lambda_{bw-min} \approx \frac{2.783115\lambda_0^2}{\pi L [n_{g,a}(\lambda_0) + n_{g,b}(\lambda_0)]}. \quad (D.6)$$